UNIVERSIDAD DE GRANADA

Tesis Doctoral

X-ray Emission from Hot Bubbles in nebulae around Evolved Stars

Jesús Alberto Toalá Sánz
Instituto de Astrofísica de Andalucía - CSIC

Memoria de Tesis
presentada en la Universidad de Granada
para obtener el grado de Doctor en Física y Matemáticas

Directores de Tesis:
Dr. Martín A. Guerrero
Instituto de Astrofísica de Andalucía - CSIC
&
Dra. S. Jane Arthur
Centro de Radioastronomía y Astrofísica - UNAM

Editor: Editorial de la Universidad de Granada
Autor: Jesús Alberto Toalá Sánz
D.L.: GR 2333-2014
ISBN: 978-84-9083-378-0

UNIVERSIDAD DE GRANADA

Tesis Doctoral

X-ray Emission from Hot Bubbles in nebulae around Evolved Stars

Jesús Alberto Toalá Sánz
Instituto de Astrofísica de Andalucía - CSIC

Memoria de Tesis
presentada en la Universidad de Granada
para obtener el grado de Doctor en Física y Matemáticas

ABSTRACT

This thesis presents an observational and numerical study on the X-ray emission related to the formation and evolution from hot bubbles in nebulae around evolved stars. The observational part of this study consists mainly in observations obtained from the X-ray satellites *X-ray Multi Mirror Mission* (*XMM-Newton*) and *Chandra X-ray Observatory* (*CXO*). We have made use of optical, infrared, and ultraviolet observations that have complemented our results and analysis. These observations have allowed us to study the Wolf-Rayet (WR) nebulae S 308 and NGC 6888 and that around the WR star WR 16. We have also studied the planetary nebulae (PNe) NGC 6543 and Abell 78 (A 78).

The X-ray telescopes, *XMM-Newton* and *CXO*, have allowed us to study the distribution and physical characteristics of the hot and diffuse gas in the WR nebulae S 308 and NGC 6888 with exquisite detail. Even though the *CXO* observations do not map entirely NGC 6888, we are able to estimate global parameters of the X-ray emission making use of *ROSAT* observations. Previous observations performed with were hampered by *Suzaku*, *ROSAT*, and *ASCA* were hampered by a large number of point sources in the line of sight of the nebulae. S 308 was observed with *XMM-Newton* with four pointings. We have made use of the most up-to-date tools for the analysis of soft and diffuse X-ray emission (the ESAS tasks). We found that in both nebulae the hot gas has a plasma temperature of 1–1.5$\times10^6$ K and it is delineated by the [O III] emission and not the Hα as stated in previous studies. A notable difference between these two WR nebulae is that S 308 has a limb-brightened morphology in the distribution of its hot gas, while NGC 6888 displays three maxima.

We have studied the WR nebula around WR 16 with archived *XMM-Newton* observations. Even though it was expected that diffuse X-ray emission should be detected from a spherical, non-disrupted WR nebula, by comparison with S 308 and NGC 6888, we are not able to detect such emission within this WR nebula. It is possible that hot gas exist inside the nebula, but with emissivity below detectable limits of the present generation of X-ray satellites.

The Cat's Eye PN (a.k.a. NGC 6543) was also studied with *XMM-Newton* observations. We focused our analysis on observations from the Reflecting Grating Spectrometers (RGS1 and RGS2). We have been able to detect emission lines of ionized species of carbon, oxygen, and nitrogen. This makes NGC 6543 the second PN with high resolution spectroscopy observations apart from BD+30°3639.

Finally, on observational grounds, we studied the born-again PN A 78 with observations

obtained during the realization of this thesis. This is the second born-again PNe to harbor a point-like X-ray emission plus a diffuse component. Such diffuse X-ray emission is the result of the complex interaction of the current fast stellar wind with the hydrogen-poor knots ejected in the born-again event.

On the other hand, this thesis has been enriched with the realization of two-dimension (2D) radiative-hydrodynamic simulations. These simulations hace been used to study the formation, evolution, and X-ray emission from PNe. With this, we have shown that the wind-wind interaction during the formation of PNe creates hydrodynamical instabilities that change the dynamics and observables (optical and X-ray) from the hot bubbles in PNe. This effect has been downplayed by previous 1D (and analytical) works that have addressed the X-ray emission from PNe. As a result of such instabilities, we have shown that there is a difference in the hot bubble's size between models with and without thermal conduction. In the cases without such physical effect, the hot gas can leak through the gaps between clumps and filaments in the broken swept-up shell and this depressurises the bubble. The inclusion of thermal conduction evaporates and heats material from the clumpy shell, which expands to seal the gaps, preventing a loss in bubble pressure. The pressure in bubbles without conduction is dominated by the photoionized shell, while for bubbles with thermal conduction it is dominated by the hot, shocked wind.

We extended this work by computing the synthetic X-ray emission from our numerical results. We find that even models without thermal conduction can mix material into the hot bubble via instabilities, which raises the emissivity of the bubbles to observable values. This is contrary to 1D models which need thermal conduction in order for the PN to be detected in X-rays. Furthermore, we can reproduce the temperatures as observed from X-ray studies.

RESUMEN

En esta tesis presentamos un estudio observacional y numérico sobre la emisión de rayos X relacionada con la formación y evolución de burbujas calientes en nebulosas alrededor de estrellas evolucionadas. La parte observacional de este estudio consiste principalmente de observaciones obtenidas con los satélites de rayos X *X-ray Multi-Mirror Mission* (*XMM-Newton*) y el *Chandra X-ray Observatory* (*CXO*). Sin embargo, los resultados se han complementado con observaciones ópticas, infrarrojas y ultravioleta que han facilitado el análisis de las regiones referidas en la presente tesis. Estas observaciones han permitido estudiar las nebulosas Wolf-Rayet (WR) S 308, NGC 6888 y la nebulosa alrededor de la estrella WR 16. Así mismo hemos estudiado las nebulosas planetarias (NPs) NGC 6543 y Abell 78 (A 78).

Los telescopios espaciales de rayos X, *XMM-Newton* y *CXO*, han permitido estudiar la distribución y caracteristicas físicas del gas caliente dentro de las nebulosas WR S 308 y NGC 6888 con exquisito detalle. Aunque las observaciones hechas con *CXO* no mapean por completo NGC 6888, somos capaces estimar los parámetros globales de la emisión de rayos X haciendo uso de las observaciones del satélite *ROSAT*. Estas observaciones han demostrado una superioridad ante las observaciones previas hechas con los satélites *Suzaku*, *ROSAT* y *ASCA* al poder identificar un gran numero de fuentes puntuales que caen en la línea de visión dentro de la nebulosa. En el caso de S 308 observado con *XMM-Newton*, hemos hecho uso de las herramientas recientemente desarrolladas para el estudio del gas difuso y extenso (las tareas ESAS). Como resultados principales podemos resaltar que para el caso de ambas nebulosas se puede estimar que la temperatura del gas caliente que las llena es de 1-1.5$\times 10^6$ K y que dicho gas está delimitado por la contraparte de oxígeno dos veces ionizado ([O III]) y no por la emisión de hidrógeno ionizado (Hα). Una diferencia importante entre estas dos nebulosas WR, es que S 308 muestra una distribución del gas caliente con una morfología de abrillantamiento al limbo, mientras que NGC 6888 no. Esta última, muestra tres diferentes máximos en la distribusión del gas caliente.

Hemos estudiado la nebulosa WR alrededor de la estrella WR 16 con observaciones de archivo realizadas con *XMM-Newton*. El resultado principal del análisis es que, aunque era de esperase que una nebulosa con morfología esférica emitiera en rayos X por comparación con S308 y NGC 6888, no se ha detectado gas difuso. Aunque es muy probable que el gas caliente sí exista pero con baja densidad. Esto es, que su emisividad no esté dentro de los límites observables por los satélites de rayos X modernos.

La NP del ojo de gato o NGC 6543 fue estudiada con observaciones hechas con el satélite

espacial *XMM-Newton*. Nos concentramos principalmente en las observaciones realizadas con los espectrómetros *Reflecting Grating Spectrometer* (RGS1 y RGS2). Con estas observaciones hemos sido capaces de detectar líneas de especies ionizadas de carbono, oxígeno y nitrógeno. Esto posiciona a NGC 6543 como la segunda NP en ser observada con espectroscopía de alta resolución después de BD+30° 3639.

Finalmente en el lado observacional, la NP A 78 fue estudiada con observaciones *XMM-Newton* obtenidas durante la realización de esta tesis. Esta es la segunda NP *nacida de nuevo* (*born-gain*) en ser reportada en emitir en rayos X, después de Abell 30 (A 30). La emisión en rayos X en ambas nebulosas proviene de la estrella central rica en carbono y de gas difuso. Dicho emisión en rayos X es el resultado de la compleja interacción del viento de la estrella contra el gas pobre en hidrógeno eyectado durante el evento de *born-again*.

Por otro lado, esta tesis se ha enriquecido por el lado teórico con el uso de un código radiativo-hidrodinámico en dos dimensiones (2D) escrito en FORTRAN. Dicho código ha sido utilizado para estudiar la formación, evolución y emisión en rayos X de NPs. Hemos demostrado que la interación de vientos durante la formación de las NPs crean inestabilidades hidrodinámicas importantes que cambian la dinámica y observables (ópticas y en rayos X) de las burbujas calientes en NPs, incluso para modelos en donde el efecto conductivo no es aplicado. Dicho efecto ha sido ignorado por trabajos numéricos en 1D (y analíticos) que tratan la emisión en rayos X de NPs. Así mismo, hemos demostrado que existe una diferencia en presión (i.e., tamaño) dentro de la burbuja caliente entre los casos sin y con conducción térmica. En los casos sin condución, la presión de la burbuja caliente disminuye debido a que el gas caliente se expande hacia regiones creadas por la interacción entre los vientos. Cuando se incluye este efecto, las cavidades entre las inestabilidades son ocupadas por gas inyectado a la burbuja caliente, esto es, la burbuja es *autosellada*, lo cual hace que en estos casos la burbuja se expanda un poco más que sus correspondientes sin conducción.

Hemos estudiado la emisión de rayos X proveniente de nuestros resultados numéricos. El resultado principal es que las inestabilidades hidrodinánicas mezclan material a la burbuja caliente, haciendo que sean un efecto importante aumentando la emisividad en rayos X de la burbuja caliente hasta para casos en que la condución térmica no es includida. Los valores estimados para las temperatures del plasma emisor y las luminosidades están dentro de los rangos observables en ambos casos. Esto muestra una superioridad contra modelos en 1D en donde el efecto conductivo es primordial y el único que puede explicar la emisión de rayos X de burbujas calientes en NPs.

The world rarely shrieks its meaning at you.
It whispers, in private languages and obscure modalities,
in arcane and quixotic imagery, through symbols
in which every element has multiple meanings
determined by juxtaposition.

– Gregory Maguire

TABLE OF CONTENTS

List of Tables

List of Figures

CHAPTER 1

INTRODUCTION

All stars influence the interstellar medium (ISM) in different ways throughout their formation and evolution. Once the star has formed, i.e., once it can be located in the main sequence (MS) track on the Hertzsprung-Russel (HR) diagram, it can affect the ISM by different mechanisms; for example, winds (i.e., mass injection of isotropic or bipolar outflows into the ISM), photoionization flux, magnetic fields, and/or proper motions. Stellar winds are characterized by two main parameters: the terminal wind velocity (v_∞) and the mass-loss rate ($\dot{M}$). With these parameters we can define the stellar wind mechanical luminosity, L_w, as

$$L_\mathrm{w} = \frac{1}{2}\dot{M}v_\infty^2. \tag{1.1}$$

The stellar parameters change as the star evolves, as well as the impact that the star has into the surroundings. These changes are linked directly to the initial mass, metallicity, and whether the star has an initial rotation or not. For this, we will separate in the following sections the description of the generalities of massive stars, those that create Wolf-Rayet (WR) stars, and sections dedicated to low- and intermediate-mass stars, that create planetary nebulae (PNe). Hot bubbles within WR nebulae and PNe will be the main objects studied in this thesis.

1.1 Massive star evolution

For simplicity, we will refer as massive stars to those stars that start their lives with masses greater than $M_\mathrm{i} \gtrsim 25{-}30\ M_\odot$, as these are the progenitors of WR stars (e.g., Meynet & Maeder 2003; Ekström et al. 2012; Georgy et al. 2012). As soon as they are formed, they start ionizing the ISM with their powerful UV photon flux ($S_\star$=10^{47}–10^{49} s^{-1}) creating the so-called H II regions (e.g., Dyson & Williams 1997). At the same time, these stars display a fast stellar wind, with terminal wind velocity $v_\infty \gtrsim 10^3$ km s^{-1} and mass-loss rate of $\dot{M} \approx 10^{-6}\ M_\odot$ yr^{-1} that sweeps up the

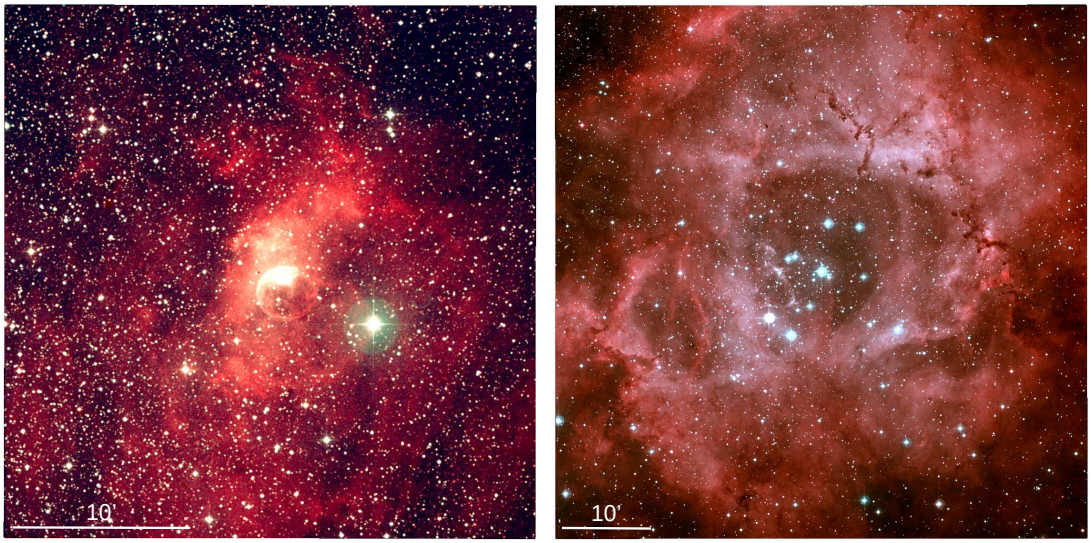

Figure 1.1: Color-composite image of NGC 7635 (left panel) and NGC 2239 (right panel). NGC 7635 is located at 2.4 kpc (Berghöfer & Christian, 2002) and its main bubble has a radius of 1.1 pc, while NGC 2239 has an inner radius of 4.4 pc at a distance of 1.5 kpc (Moore et al., 2002). Red and blue colors correspond to the Red and Blue bands of the STScI Digitalized Sky Survey. North is up, east to the left.

photoionized region. These effects can be clearly seen in the case of NGC 7635 and NGC 2239 (a.k.a. the Bubble and Rosette nebulae, respectively; see Figure 1.1).

By the end of the MS phase, after a few 10^6 yr, these stars will be surrounded by a low-density, hot bubble of tens of parsec, delimited by a thick shell of swept-up neutral material expanding at a few km s^{-1} (e.g., Cappa et al. 2005; Arthur 2007). In the case that the ISM is not homogeneous or in the case of a non-single star, the general picture still prevales (see Arthur et al. 2011; Rogers & Pittard 2013).

When the star evolves off the MS phase, its mass-loss rate increases ($\dot{M}$=10^{-4}–10^{-3} $M_\odot$ yr^{-1}) and its velocity diminishes considerably (v_∞=10–100 km s^{-1}). Depending on the initial mass, the star may undergo different episodes of mass ejections becoming a red or yellow supergiant (RSG or YSG) or a luminous blue variable (LBV) star. During this phase, the star expels a great amount of its mass (up to half its initial mass) via a slow and dense wind into the circumstellar medium (CSM). In general these massive eruptions of material will be episodic and non-spherical (Humphreys, 2010). Figure 1.2 shows the most recognized example of a star in the LBV phase, η Car (see Artigau et al. 2011 and references therein).

To illustrate the differences, figure 1.3 presents the evolutionary models of stars with initial masses of 40 and 85 $M_\odot$ at solar abundances (Z=0.014) from Ekström et al. (2012). The area colored in yellow illustrates the region in which the models become a YSG as defined by Drout et al. (2009), 4800 < $T_{\rm eff}$ < 7500 K, temperatures below this value define the RSG upper limit. As can be seen, the 40 $M_\odot$ model oscillates between the YSG and RSG phases once it has evolved off

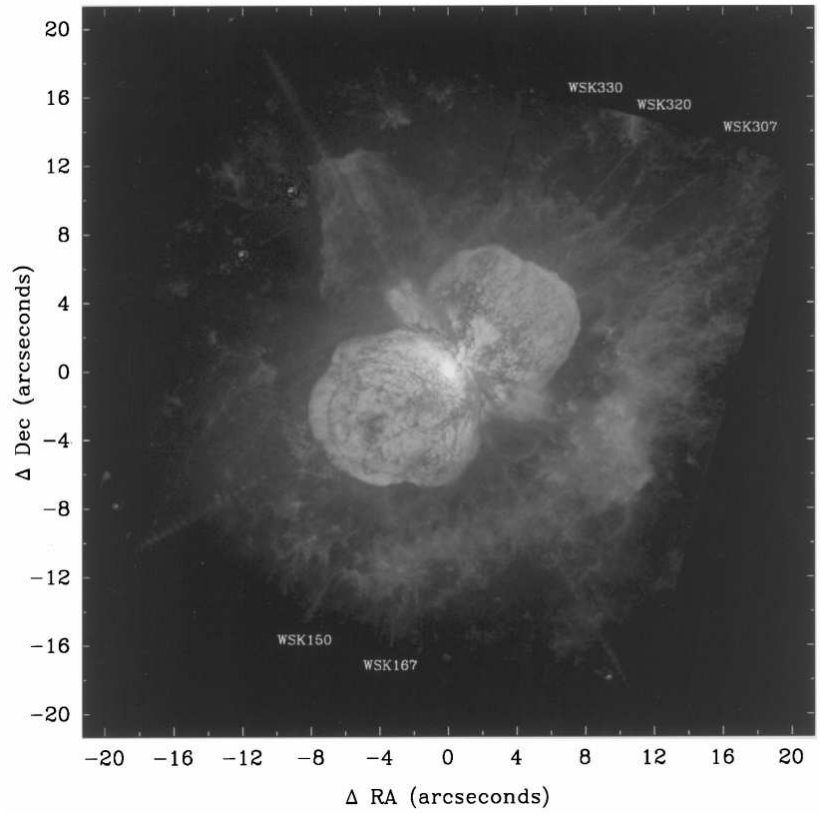

Figure 1.2: Narrow band [N II] image of η Car as seen by the *Hubble Space Telescope* WFPC2 taken from Morse et al. (1998). The dusty ejecta and the *homumculus* are clearly seen in the image. The central star in η Car is a binnary system (80+30 $M_\odot$) with a 5.52 yr period located at a distance of 2.3 kpc (Damineli, 1996).

the MS phase. This will make the star to present eruptive, non-steady ejections of mass. In the case of the 85 $M_\odot$ model, its temperature diminish as low as the YSG limit and never becomes a RSG star, i.e., it spends most if its time in the blue part of the HR diagram creating a LBV star.

1.1.1 Formation of WR Nebulae

As a result of the copious mass-loss rate in the previous evolutive stage (RSG/YSG or LBV), the star's core is stripped and exposed creating a WR star (Conti, 1975). As soon as a WR star is created, a new ionizing photon flux is developed as well as a powerful wind (v_∞=1000–3000 km s^{-1} and $\dot{M}$=10^{-5} $M_\odot$ yr^{-1}). As a result, this new fast stellar wind interacts with the previously ejected slow and dense CSM, whilst is photoionized by the central star. This creates the so-called WR nebulae. This formation mechanism was first proposed by García-Segura & Mac Low (1995) with their analytical *three-wind model*.

These nebulae are observable basically in all frequencies of the electromagnetic spectrum: ra-

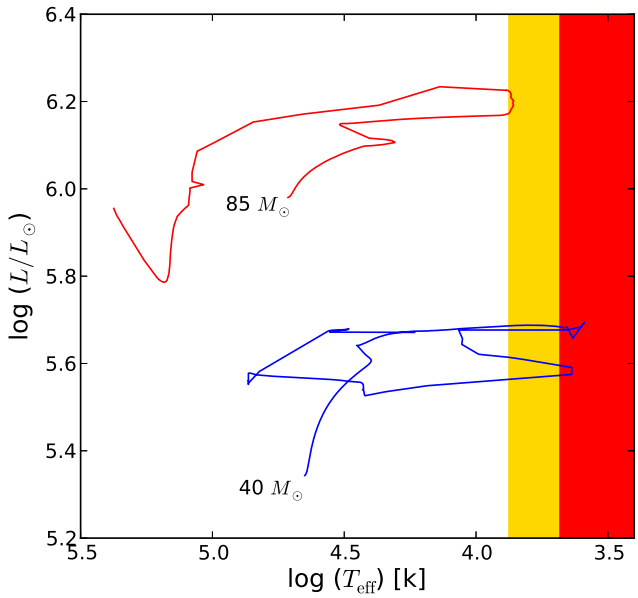

Figure 1.3: Evolutinary tracks for the cases of the 40 and 85 $M_\odot$ stars from Ekström et al. (2012). The yellow and red regions show the regions in which the star becomes a YSG or RSG. The YSG region correspond to effective temperatures between 4800 and 7500 K as defined by Drout et al. (2009).

dio (e.g., Arnal & Cappa 1996; Arnal et al. 1999; Cappa et al. 2002,2008,2009), infrared (IR; e.g., van Buren & McCray 1988; Gvaramadze et al. 2010; Mauerhan et al. 2010; Wachter et al. 2010; Flagey et al. 2011; Stringfellow et al. 2011; Wachter et al. 2011), optical (e.g., Chu 1982; Treffers & Chu 1982a; Chu et al. 1983; Gruendl et al. 2000; Stock & Barlow 2010), and X-rays (e.g., Bochkarev 1988; Wrigge et al. 1994; Wrigge, 1999; Chu et al. 2003; Wrigge & Wendker 2002; Wrigge et al. 2005; Zhekov & Park 2011; this thesis). Figure 1.4 presents two examples of different views of the WR nebulae S 308 and NGC 2359 around WR 6 and WR 7, respectively.

These WR nebulae present different morphological characteristics such as bubbles, clumps, filaments, diffuse matter, or a combination of those features. A series of papers addressing the characteristics and proposing a morphological classification scheme was started by Chu (1981). The classification was divided into three major groups: (1) *R* - Radiatively Excited H II regions, (2) *E* - Stellar Ejecta, and (3) *W* - Wind Blown Bubble (see Chu 2003, for an updated review of the morphology of WR nebulae). The *R*-type nebulae present optical emission lines with widths comparable to those in ordinary H II regions, and are further divided into amorphous H II regions (*R*a) and shell-structured H II regions (*R*s). The *E*-type nebulae were characterized by their highly clumpy appearance and irregular velocity field. These nebulae were proposed to form through sudden episodes of mass ejection. Finally, the *W*-type nebulae present a thin sheet

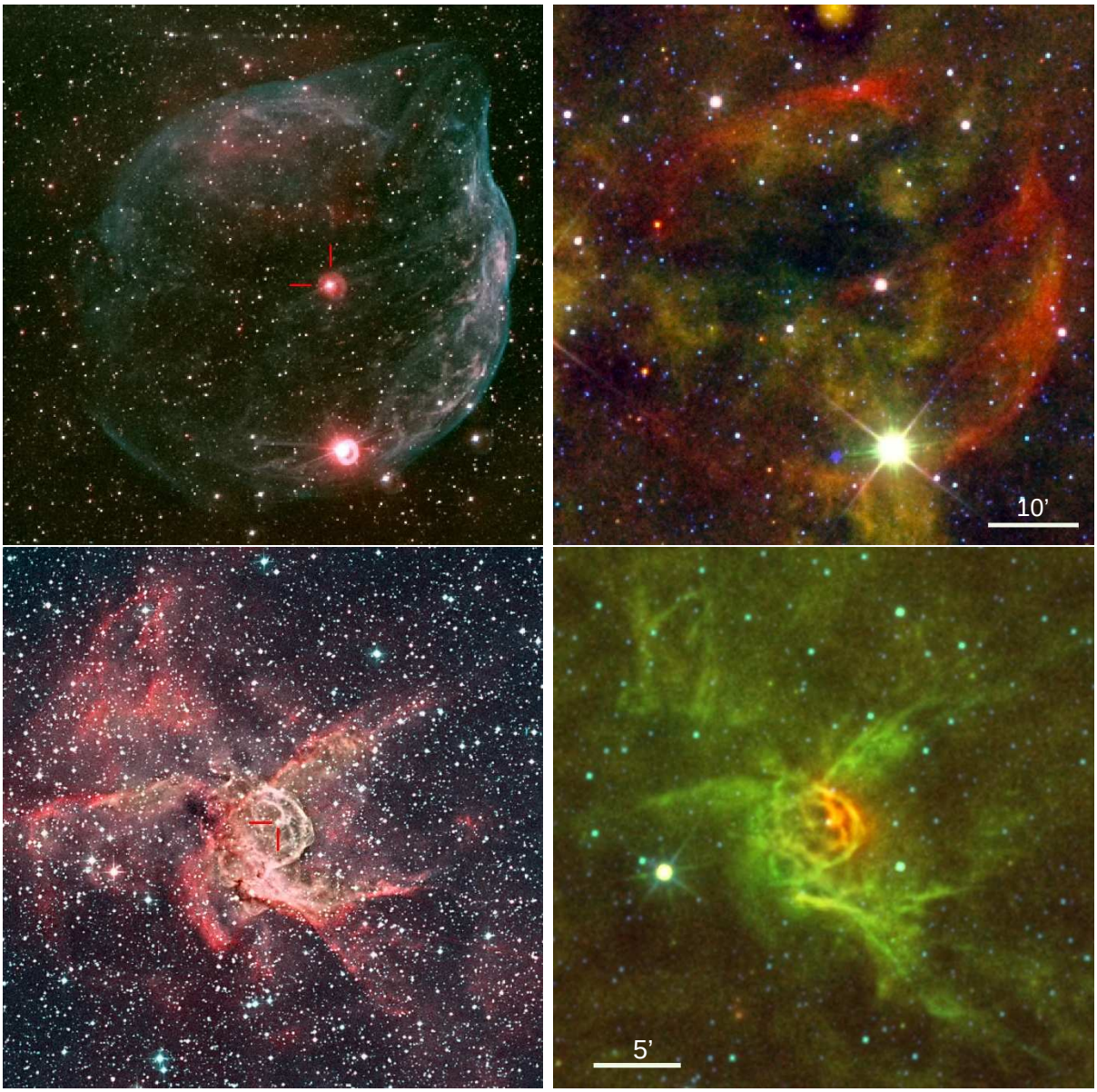

Figure 1.4: Examples of WR nebulae as seen in optical and mid-IR wavelengths. Top panels: S 308 around WR 6. Bottom panels: NGC 2359 around WR 7. The left panels show the optical Hα (red) and [O III] (blue) images, while the right panels show *WISE* W2 4.6μm (blue),W3 12 μm (green), and W4 22μm (red) bands. The red lines show the position of the central star. S 308 and NGC 2359 are at distances of 1.5 kpc and 3.7 kpc, respectively, i.e., their bubbles have physical sizes of 9 and 2.4 pc, i.e., their physical sizes are 9 and 2.4 pc, respectively.

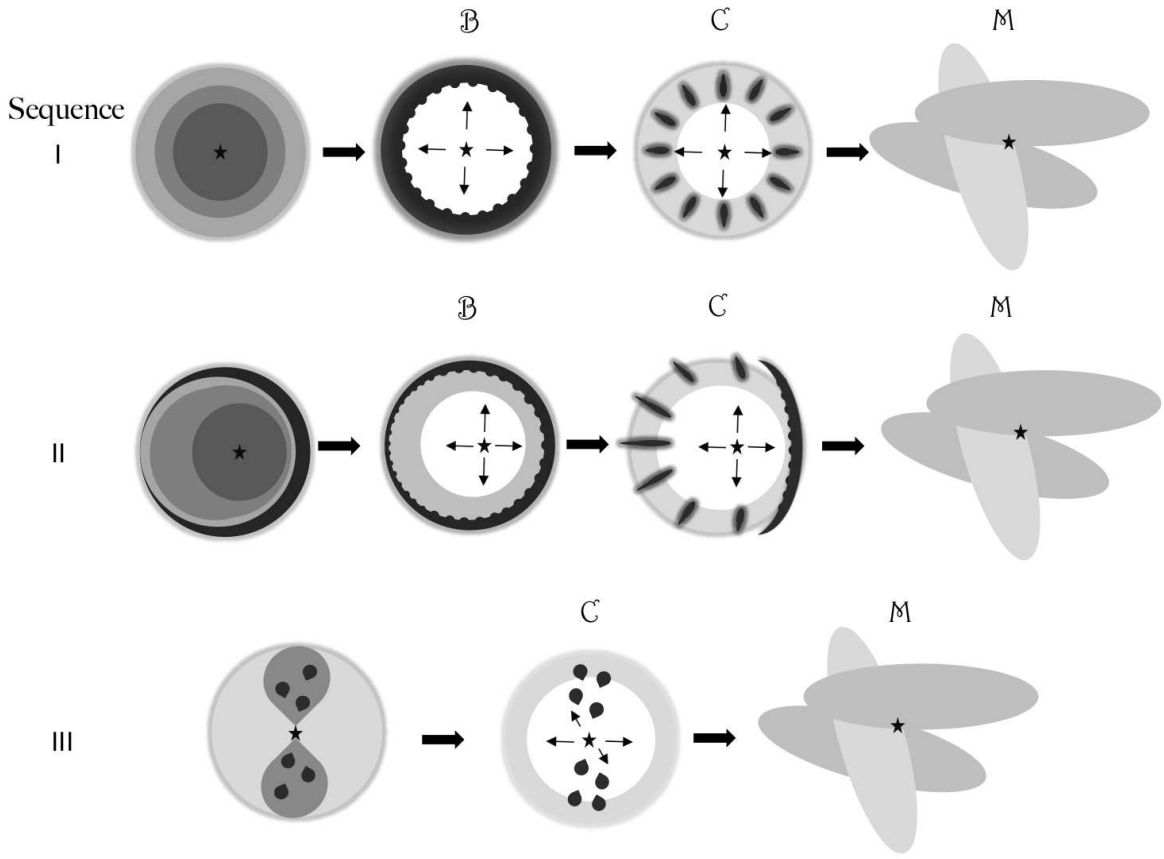

Figure 1.5: Illustration of the formation and evolution of WR nebulae. The letters *B*, *C*, and *M* correspond to bubble, clumpy, and mixed morphologies.

of gas and filaments curving around a WR star which is close to the geometric center of the nebula or offset toward the brightest rim. *W*-type nebulae are found in numerical simulations of the circumstellar medium (CSM) around WR stars (e.g., García-Segura et al. 1996a,b; Freyer et al. 2003,2006; Toalá & Arthur 2011). Using this classification scheme, Stock & Barlow (2010) extended and revised the morphologies of a sample of southern WR nebulae.

The most important characteristics that will shape the WR nebula will be the configuration of the CSM by the end of the RSG/LBV phase. If this material is ejected by non isotropic episodes of mass-loss and/or the star has a proper motion, the WR nebulae may not have the simple round morphology. This is further illustrated in Figure 1.5. Sequence I illustrates the classic formation and evolution of spherical (or elliptical) WR nebula with time. Sequence II illustrates the case of a WR star with a proper motion or interaction with the ISM. Finally, sequence III illustrates the case in which the WR star evolved throught a bipolar LBV phase. In all cases, after the WR nebula is disrupted it evolves further to mix with the ISM.

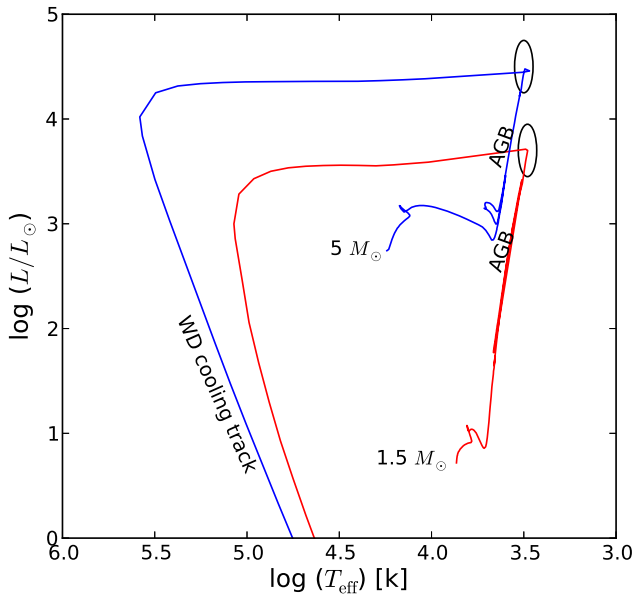

Figure 1.6: Evolutinary tracks for the cases of the 1.5 and 5 $M_\odot$ stars from Girardi et al. (2000). The ellipses show the position of the top of the thermally pulsing AGB phase (TP-AGB), where the thermal flashes take place.

1.2 Low- and intermediate-mass star evolution

In this section we will describe the evolution of those stars that end up their lives forming PNe, low- and intermediate-mass stars (LIMS). The limit between the massive and LIMS is between 8–10 $M_\odot$, and depends on several factors as metallicity. By simplicity we will keep this limit as 8 $M_\odot$. On the other hand, the lower limit for stars to create a PN is set to 0.8 $M_\odot$, as stars with masses below this limit do not ignite the helium in their nucleus to further proceed with the evolution towards a white dwarf (WD) and do not create a PN.

The limit between low- and intermediate-mass stars is around ~2.3 $M_\odot$ (see Bisnovatyi-Kogan 2002). This defines the low-mass stars limit as $0.8 \leqslant M_{\rm i} \lesssim 2.3 M_\odot$. These stars harbor a degenerate helium core where the onset of the helium burning triggers a thermal flash. The thermal flash makes the helium core non-degenerate, and an evolutionary phase with core helium burning returns, similar as that occuring in intermediate-mass stars ($2.3 \lesssim M_{\rm i} \lesssim 8 M_\odot$). In the case of intermediate-mass stars this degeneracy occurs after the formation of the carbon core (i.e., after the hydrogen and helium burning phase).

In general, LIMS spend most of their lives in the MS phase. For example, according to Ekström et al. (2012) a 1.5 $M_\odot$ star spends 2.24×10^9 yr in the MS phase (hydrogen burning) and a 5 $M_\odot$ star lasts for 8.8×10^7 yr for models with solar abundance (Z=0.014) without stellar

rotation.

After the LIMS have exhausted their helium in the core, forming a degenerate core of carbon and outer helium- and hydrogen-burning shells, it will be positioned in the asymptotic giant branch (AGB) region of the HD diagram (see Figure 1.6). In this evolutionary phase the stars present the so-called *thermal pulses*, i.e., the star becomes a thermally pulsing AGB (TP-AGB) star. These stars have compact CO cores with masses between 0.5–1.5 $M_{\odot}$ and are mantained in quasi-isothermal equilibrium. The outer H-rich envelope becomes convective and presents a strong mass-loss (up to 10^{-5} $M_{\odot}$ yr^{-1}). The intermediate He-rich intershell is the more interesting region in these stars (see Cristallo et al. 2009).

The energy irradiated by these stars is mainly provided by the H-burning outer envelope. As a result, the He-intershell increase and periodic TPs are driven by violent helium ignitions everytime it reaches a critical mass and the conditions in order to burn itself via the 3α thermonuclear process. This makes the He-intershell to become unstable, while the external layes expand and cool down. This results in the carbon enrichment of the He-intershell. This process repeats until the star looses a great amount of material into the ISM within a few 10^5–10^6 yr (e.g., Vassiliadis & Wood 1993). For example a star with an initial mass of 3.5 $M_{\odot}$ can lose up to $\gtrsim$2 $M_{\odot}$ during this phase (see Figure 1 in Villaver et al. 2002a).

As the effective temperature of the AGB stars in this phase is low ($T_{\rm eff}$ ~10^3–10^4 K), they produce dense and dusty envelopes that expand a slow velocities (v_{∞}=10–20 km s^{-1}), as reported in optical and infrared works (Cox et al. 2012; Mauron et al. 2013; and references therein).

1.2.1 PN formation

The intermediate transition between the AGB and the post-AGB phase is short ($\lesssim 10^4$ yr). To this point the star displays a powerful wind known as the *superwind* with mass-loss rates as high as 10^{-4} $M_{\odot}$ yr^{-1}. The H-rich envelope detaches from the nucleus of the star and is expelled into the CSM. At the same time the effective radius of the nucleus of the star is reduced while increasses its temperature to form a white dwaft (WD). When the temperature of the central star overcomes 10^4 K it developes a strong ionizing photon flux and a fast wind ($v_{\infty} \lesssim$1000 km s^{-1}).

The interaction between the ionizing photon flux and the fast stellar wind with the dense and dusty envelope creates a PN. This scenario was first described by Kwok et al. (1978) with the introduction of the *Interacting stellar winds* (ISW) model. This pioneer work described the interaction of the newly developed fast wind with the previosly ejected dense and slow shell of AGB material whilst it is photoionized by the strong UV flux from the central star (CSPN). This model was furthered discussed by Balick (1987) with the generalization of the ISW (GISW).

The GISW describes how the shapes of PNe could depend on different factors. For example, in the case that the AGB wind was not expelled isotropically, forming a latitude-dependent density gradient would create elliptical or bipolar PNe. The picture becomes more complex if we also take into account the multiplicity of the CSPN or the proper motions during the AGB

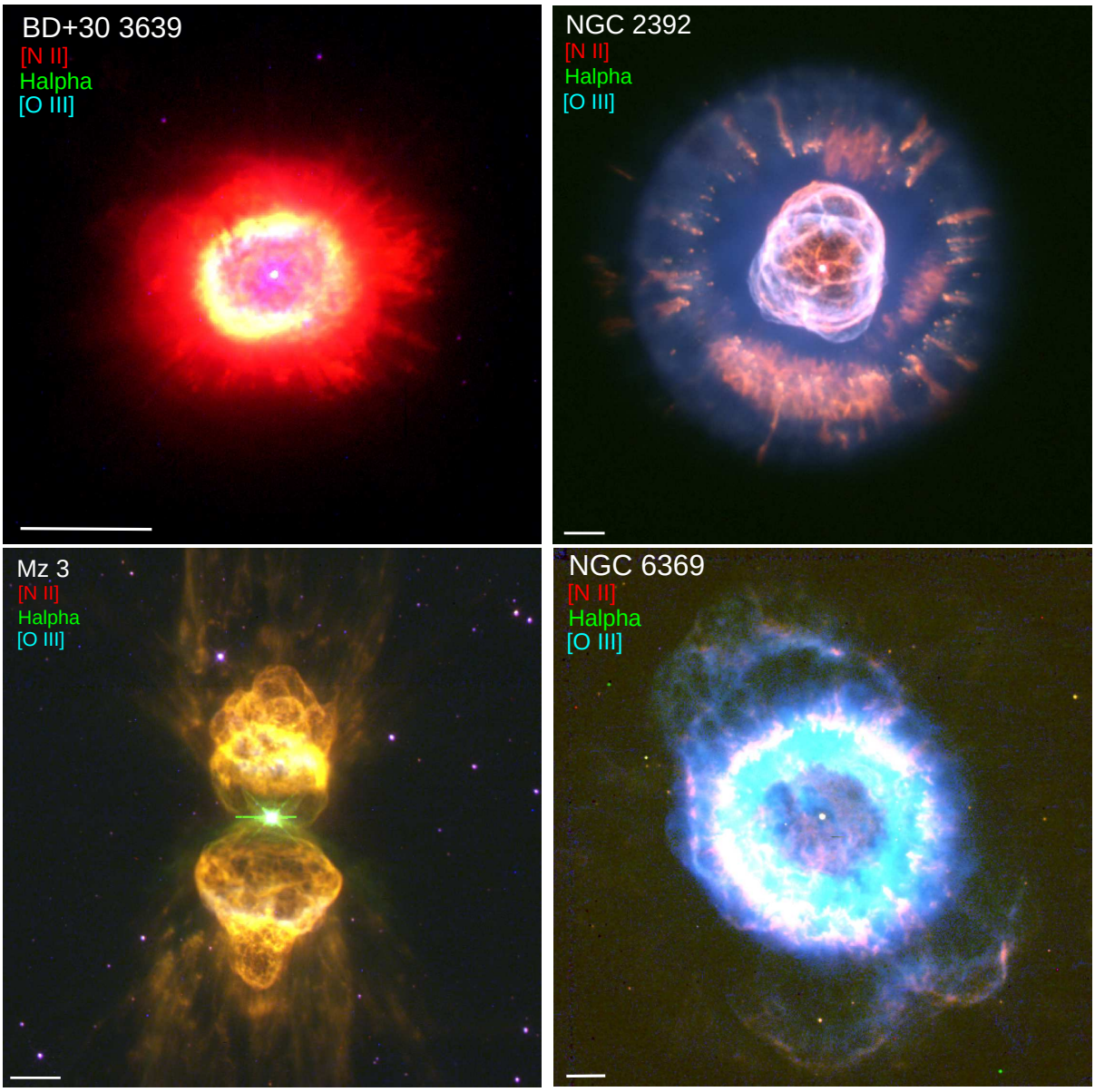

Figure 1.7: PNe examples as seen by *Hubble Space Telescope*. The CSPNs are at the center of each figure.

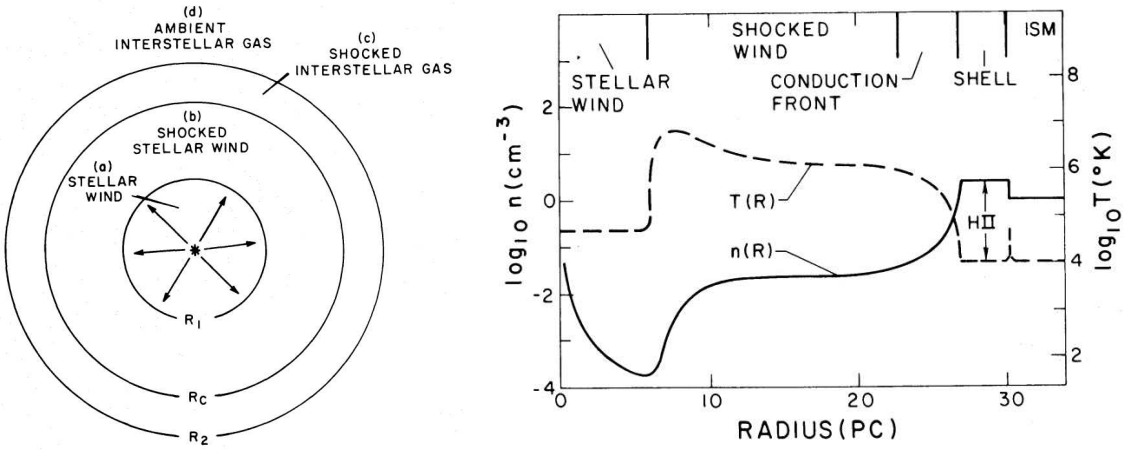

Figure 1.8: Structure of an idealized bubble as presented in Weaver et al. (1977). The different regions can be identify on each panel.

phase (Esquivel et al. 2010; Mohamed et al. 2012; Villaver et al. 2012). Some examples of PNe as observed by the *Hubble Space Telescope* are presented in Figure 1.7.

1.3 The physics of hot bubbles: Justification

In this section we describe the observational and theoretical scenarios at the time before the realization of this thesis to finally introduce the justification of the present work.

The formation and evolution of WR nebulae and PNe are similar. They correpond to the evolution of the CSM as a result of the evolution of a star that developes a fast wind ($v_\infty \gtrsim 10^3$ km s^{-1}) that interacts with a previously ejected, dense, and slow material (RSG/LBV or AGB), while the central star photoionizes this material.

Both types of nebulae will experience the formation of a hot and diffuse bubble in their interiors pushing outwards the ionized region, i.e., the PN or WR nebula.

1.3.1 The formation of a hot bubble

Pikel'Ner (1968) was the first to study the interaction of a fast stellar wind with an outer diffuse nebula via analytical solutions of an adiabatic shock. He concluded that the outer nebula must compress to a thin layer and the inner part of this shock must create a region filled with shocked wind.

The term *bubble*, as applied to diffuse cavities in the ISM, was first coined by the leading analytical works presented by Castor et al. (1975) and Weaver et al. (1977). Castor et al. (1975) described that these bubbles must be filled with low density plasmas ($n \approx 0.01$ cm^{-3}) at temperatures $\gtrsim 10^6$ K, while Weaver et al. (1977) presented the solution for the structure of an idealized

model of adiabatic flow (see Figure 1.8). The proposed structure (which is still the accepted scenario of a bubble) of the configuration of the medium around a star that exhibits a fast wind is: (a) the free streaming wind, (b) a hot bubble of diffuse material form by shocked stellar wind, (c) the shocked interstellar material, (d) the undisrupted ISM. In the case of the WR nebulae and PNe, the shocked interstellar material corresponds to the RSG/LBV or AGB material, respectively.

The formation of the hot and diffuse bubble is the result of this fast-wind-slow-wind interaction. A double shock pattern is created: a shock wave sweeping out the photoionized material interacting with the CSM, and a rarefied shock wave termalizing the fast stellar wind. The generalities of the physics of this adiabatic shock is well know and studied in textbooks (e.g., Dyson & Williams, 1997). The temperature (T) of the hot bubble can be estimated as

$$T = \frac{3}{16}\frac{\mu}{k_{\rm B}} m_{\rm H} v_{\infty}^2 = 2.3\times10^7 \mu \left(\frac{v_{\infty}}{1000\,{\rm km\,s^{-1}}}\right)^2 [{\rm K}], \tag{1.2}$$

where μ is the mean particle mass for fully ionized gas, $m_{\rm H}$ is the hydrogen mass, and $k_{\rm B}$ is the Bolztmann constant. Thus, it is expected that all WR nebulae and PNe would be filled with a termalized gas with temperatures $T \gtrsim 10^8$ K as computed from terminal wind velocities from WR stars and CSPN (e.g., Hamann et al. 2006 and Guerrero & de Marco 2013). Furthermore, this means that WR nebulae and PNe should be detected in diffuse X-rays from these hot bubbles.

1.3.2 X-ray emission from hot bubbles

Indeed, diffuse X-ray emission from hot bubbles in WR nebulae and PNe has been detected in the past. The first report of X-ray emission associated to a PN (NGC 1360) was done by de Korte et al. (1985) with the *EXOSAT* satellite. Since then, many works addresing the X-ray emission from these objects using the previous X-ray facilities (*Einstein*, *EXOSAT*, *ROSAT*, and *ASCA*) have been reported (see Chu et al. 2003 for a review). For all cases, the temperature of the diffuse X-ray emission was found to be two orders of magnitude below theorerical predictions.

In the case of WR nebulae, Bochkarev (1988) reported the first detection of diffuse X-ray emission from NGC 6888 with the *Einstein* observatory. Since then the only WR nebulae reported to harbor diffuse X-ray emission (with the previous facilities) were NGC 6888 and S 308 (Wrigge et al. 1994,1998; Wrigge 1999 Wrigge & Wendker 2002; Wrigge et al. 2005). All these works concluded that the temperature of the hot plasma in S 308 and NGC 6888 was of 1-2$\times10^6$ K with abundances as those as from the optical WR nebula. Again, two orders of magnitude below predictions.

The unprecedent sensitivity and angular resolution of *CXO* and *XMM-Newton* X-ray observatories allowed to obtain better analysis of the hot gas in WR nebulae and PNe with admirable detail. Chu et al. (2001) presented the first resolved X-ray image of the hot interior of the Cat Eye's nebula (a.k.a. NGC 6543) as observed with *CXO* (see Figure 1.9). They confirmed a soft plasma temperature of 1.7$\times10^6$ K and estimated an X-ray luminosity of $L_{\rm X}$=10^{32} erg s^{-1}. By

Figure 1.9: The PN NGC 6543 as seen by *CXO* and the *HST*. Blue is the X-ray emission, green is Hα, and red is [N II] emission. The image taken from the *CXO* webpage, is based on X-ray observations obtaied by Y.-H. Chu (Chu et al. 2001).

2009, soft diffuse X-ray emission delimited by bright optical bubbles had been reported for 10 PNe (Kastner et al. 2008, and references therein) with similar temperatures and X-ray luminosities. More recently, Kastner et al. (2012) reported that of the 35 PNe observed to that time with *CXO*, ~30% display diffuse X-ray emission.

The first high resolution X-ray observation of a WR nebula was done with *XMM-Newton* and reported by Chu et al. (2003). Due to the large angular size of S 308 (~40′ in diameter) as compared to the field of view of *XMM-Newton* ($\lesssim$30′), they only presented the analysis of the northwest quadrant of that nebula. They estimated a plasma temperature of 1.1×10^6 K and an X-ray luminosity of $L_{\rm X} \leqslant 10^{34}$ erg s^{-1}. Unfortunately, the number of WR nebulae observed in X-rays has not increased much in the past few years. NGC 6888 was further studied by *Suzaku* and confirmed the findins of previous works (Zhekov & Parks 2011). Only one more WR nebula was added to the list of observed ones, RCW 58 around WR 40. The *XMM-Newton* observations presented by Gosset et al. (2005) dit not detected any signature of diffuse emission, thus, they estimated an X-ray luminosity assuming that the nebula harbors hot gas similar as in S 308 and NGC 6888, of $L_{\rm X}$=6×10^{32}–10^{33} erg s^{-1}.

Since the proposition of the *three wind model* by García-Segura & Mac Low (1995a) there have been a great number of numerical studies related to this subject. The purely 2D hydrody-

namic simulations of García-Segura et al. (1996a,1996b) set the basis of the differences on the instabilities created in the wind-wind interaction zone between stars that go throught a RSG phase and those that evolve throught a LBV phase. These results were extended by the works of Freyer et al. (2003,2006) with the inclusion of radiative transfer (photoionization due to the cental star). Even though, the temperature discrepancy found between analytical estimations and those obtained from observations was initially assumed to be due to thermal conduction between the cold (10^4 K), outer photoionized nebula between the hot (10^7–10^8 K) interior (Weaver et al. 1977), simulations presented by Toala & Arthur (2011) and Dwarkadas & Rosenberg (2013) have proved that the instabilities created in the wind-wind interaction zone are also important into reducing the temperature of the hot bubble and producing soft X-ray spectra. It is important to mention here that all these works take into account the detailed evolution of the central star, making use of the most up-to-date stellar evolutionary models. The main issue is the limited number of WR observed with X-ray satellites, which makes very hard to create an observational scheme.

On the other hand, there are plenty X-ray observations of PNe, and the number is increasing because of the *Chandra* X-ray Survey of Planetary Nebulae (CHANPLANS) papers I, II, and III (see Kastner et al.2012; Freeman et al., in prep.; Montez et al., in prep.). Contrary to the case of the WR nebulae, most of the theoretical works on the X-ray emission from PNe are analytical or obtained from 1D numerical results. For example, the illustrative works of Stute & Sahai (2006) and Akashi et al. (2007) study the influence of the stellar wind parameters during the post-AGB phase with purely hydrodynamical, 1D models. They concluded that in this phase the fast wind velocity must be below 10^3 km s^{-1} in order to explain such low temperatures in the X-ray-emitting plasma. However, this is not consistent with the results from the observed P Cygni profiles of UV lines of central star winds (Guerrero & de Marco 2013), which indicate that CSPN wind velocities are generally above 1000 km s^{-1} and can be as high as 4000 km s^{-1}. Another difficulty in these works is that they do not take into account the time evolution of the stellar wind parameters (velocity and mass-loss rate) and the ionizing photon rate from the star.

The most used model to study the soft X-ray emission in PNe is the numerical results presented by the AIP group in Steffen et al. (2008). Their 1D radiative-hydrodinami simulations generally agree with the observational results, but in order to do so, they have to include a new (more *aggressive*) formulation of the thermal conduction according to an interpolation formula. It is done in order to inject more mass from the AGB outer shell into the hot bubble, which reduces the hot bubble's temperature. But these models fail in cases in which even a weak magnetic field is present as it will suppress the conductive effect. For example, in the cases of the proto PNe CRL 618 and OH 231.8+4.2 there is evidence of the presence of a magnetic field (Sabin et al., 2014) that could be also present after the PN has formed (Asensio Ramos et al., 2014; Leone et al., 2014, see).

1.4 Motivations of the present thesis

With all these in mind, we intend to responde to the following question/issues in the present thesis.

- What is the distribution and physical characteristics of the hot gas in S 308 and NGC 6888 as seen by high spatial resolution observations (*XMM-Newton* and *CXO*)?
- Are there more WR nebulae that harbor diffuse X-ray emission?
- How similar are those WR nebulae detected in X-rays?
- Is there any relation between the stellar wind parameters and the X-ray emission in WR nebulae? How important is the enviroment in which the star evolves?
- What are the predictions of 2D models on the formation of hot bubbles in PNe?
- Are the instabilities created in the wind-wind interaction zone in PNe important in reducing the temperature of the hot bubble?
- How importan is the modification of the classic formulation of the thermal conduction in order to explain the soft X-ray emission?
- Does PNe modeled with thermal conduction have the same dynamics than those without this physical effect?

All these questions are discussed in the different chapters throghout the thesis. The presentation is as follows. In Chapter 2 we present the complete mapping and analysis of the hot gas in the WR nebula S 308 with *XMM-Newton* observations. This took 4 different pointings to complete. In Chapter 3 we present the report of the third WR nebula observed with the newest generation of X-ray satellites, the nebula around WR 16. Chapter 4 describe the *CXO* observations of NGC 6888 and presents the estimations of the physical conditions of the hot gas. Chapter 5 presents *XMM-Newton* RGS observations of the Cat's Eye nebula. This makes this PN the second PN to be observed with high resolution spectroscopy. Chapter 6 presents the analysis of the *XMM-Newton* observations of the born-again PN A 78, and we compare the results to its *twin*, A 30. Finally, Chapters 7 and 8 describe the results from our radiative-hydrodynamical numerical simulations on the formation, evolution, and X-ray emission from hot bubbles in PNe. We summarize our findings in Chapter 9.

1.5 List of publications

The work presented in this thesis has resulted in the following publications:

- *X-ray emission from the Wolf-Rayet bubble S 308*
  Toalá, J.A., Guerrero, M.A., Chu, Y.-H., Gruendl, R.A., Arthur, S.J., Smith, R.C., and Snowden, S.L., 2012, ApJ, 755, 77

- *Absence of hot gas within the Wolf-Rayet bubble around WR 16*
  Toalá, J.A., and Guerrero, M.A., 2013, A&A, 559, 52

- *X-ray emission from the Wolf-Rayet bubble NGC 6888. I.* Chandra *ACIS-S Observations*
  Toalá, J.A., Guerrero, M.A., Gruendl, R.A., and Chu, Y.-H., 2014, ApJ, 147, 30

- *Formation and X-ray emission from hot bubbles in Planetary Nebulae. I. Hot bubble formation*
  Toalá, J.A., and Arthur, S.J., 2014, MNRAS, accepted for publication

- *Formation and X-ray emission from hot bubbles in Planetary Nebulae. II. Synthetic X-ray emission*
  Toalá, J.A., and Arthur, S.J., in preparation

- *The Born-again planetary nebula A 78: an X-ray twin of A 30*
  Toalá, J.A., Guerrero, M.A., Todt, H., Hamann, W.-R., Chu, Y.-H., Gruendl, R.A., Schönberner, D., Steffen, M., and Oskinova, L., 2014, submitted to ApJ

- XMM-Newton *RGS view of the Cat's eye nebula*
  Toalá, J.A., Guerrero, M.A., Chu, Y.-H., Gruendl, R.A., and A.M.T. Pollock, in preparation

Other publications related to this thesis are:

- *Unveiling shocks in planetary nebulae*
  Guerrero, M.A., **Toalá, J.A.**, Medina, J.A., Luridiana, V., Miranda, L.F., Riera, A., Velázquez, P.F., 2013, A&A, 557, 121

- *Rebirth of X-ray Emission from the Born-again planetary nebula A 30*
  Guerrero, M.A., Ruiz, N., Hamann, W.-R., Chu, Y.-H., Todt, H., Schönberner, D., Oskinova, L., Gruendl, R.A., Steffen, M., Blair, W.P., and **Toalá, J.A.**, 2012, ApJ, 755, 129

- *Expansion of hydrogen-poor knots in the born-again planetary nebulae A 30 and A 78*
  Fang, X., Guerrero, M.A., Márquez-Lugo, R.A., **Toalá, J.A.**, Chu, Y.-H., Gruendl, R.A., Arthur, S.J., Blair, W.P., Hamann, W.-R., Oskinova, L., Todt, H., 2014, in preparation

- *The* Chandra *Planetary Nebula Survey (*CHANPLANS*). II. X-ray emission from Compact Planetary Nebulae*
  Freeman, M., and the CHANPLANS Team, submitted to ApJ

- *The* Chandra *Planetary Nebula Survey (*CHANPLANS*). III. X-ray emission from the Central Stars of Planetary Nebulae*
  Montez, R. Jr. and the CHANPLANS Team, submitteed to ApJ

CHAPTER 2

X-RAY EMISSION FROM THE WOLF-RAYET BUBBLE S 308

The Wolf-Rayet (WR) bubble S 308 around the WR star HD 50896 is one of the only two WR bubbles known to possess X-ray emission. We present XMM-Newton *observations of three fields of this WR bubble that, in conjunction with an existing observation of its Northwest quadrant, map most of the nebula. The X-ray emission from S 308 displays a limb-brightened morphology, with a central cavity ~22′ in size and a shell thickness of ~8′. This X-ray shell is confined by the optical shell of ionized material. The spectrum is dominated by the He-like triplets of N* VI *at 0.43 keV and O* VII *at 0.57 keV, and declines towards high energies, with a faint tail up to 1 keV. This spectrum can be described by a two-temperature optically thin plasma emission model (T_1 ~1.1×10^6 K, T_2 ~13×10^6 K), with a total X-ray luminosity ~ 2×10^{33} erg s^{-1} at the assumed distance of 1.5 kpc.*

2.1 Introduction

Wolf-Rayet (WR) bubbles are the final result of the evolution of the circumstellar medium (CSM) of massive stars with initial masses $M \gtrsim 35\,M_\odot$. These stars exhibit high mass-loss rates throughout their lives, peaking during their post-main-sequence evolution that involves a Red or Yellow Supergiant (RSG or YSG) or Luminous Blue Variable (LBV) stage (e.g., Meynet & Maeder, 2003) during which the mass-loss rate can be as high as 10^{-4}–$10^{-3}\,M_\odot$ yr^{-1} (Nugis & Lamers, 2000), although the stellar wind velocity is low (10-10^2 km s^{-1}). The final WR stage is characterized by a fast stellar wind ($v_\infty \gtrsim 10^3$ km s^{-1}), which sweeps up, shocks, and compresses the RSG/LBV material. Thin-shell and Rayleigh-Taylor instabilities lead to the corrugation and eventual fragmentation of the swept-up shell (Freyer et al., 2003, 2006; García-Segura et al., 1996a,b; Toalá & Arthur, 2011). Clumpy WR wind-blown bubbles have been detected at optical wavelengths around ~10 WR stars in our Galaxy (Chu et al., 1983; Gruendl et al., 2000;

Stock & Barlow, 2010). Their optical emission is satisfactorily modeled as photoionized dense clumps and shell material (Esteban et al., 1993).

X-ray emission has been detected so far in only two WR bubbles, NGC 6888 and S 308 (Bochkarev, 1988; Chu et al., 2003a; Wrigge, 1999; Wrigge et al., 1994, 1998; Wrigge & Wendker, 2002; Wrigge et al., 2005; Zhekov & Park, 2011). The most sensitive X-ray observations of a WR bubble are those of the northwest (NW) quadrant of S 308 presented by Chu et al. (2003a). Their *XMM-Newton* EPIC-pn X-ray spectrum of S 308 revealed very soft X-ray emission dominated by the N VI He-like triplet at ~0.43 keV and declining sharply toward higher energies. This spectrum was fit with a two-temperature optically thin MEKAL plasma emission model, with a cold main component at $kT_1 = 0.094$ keV (i.e., $T_{\rm X} \sim 1.1 \times 10^6$ K), and a hot secondary component at $kT_2 \sim 0.7$ keV contributing ≤6% of the observed X-ray flux. The comparison of the X-ray and optical Hα and [O III] images of S 308 showed that the X-ray emission is confined by the ionized shell.

In this chapter, we present the analysis of three additional *XMM-Newton* observations of S 308, which, in conjunction with those of the NW quadrant presented by Chu et al. (2003a), map 90% of this WR bubble (see §2). In §3 and §4 we discuss the spatial distribution and spectral properties of the X-ray-emitting plasma in S 308, respectively. In §5 we present our results of the X-ray emission from the central star in the WR bubble. A discussion is presented in §6 and summary and conclusions in §7.

2.2 *XMM-Newton* Observations

The unrivaled sensitivity of the *XMM-Newton* EPIC cameras to large-scale diffuse emission makes them the preferred choice for the observation of S 308. Chu et al. (2003a) presented *XMM-Newton* observations of the brightest NW quadrant of S 308 (Wrigge, 1999), but the large angular size of S 308 (~40′ in diameter) exceeds the field of view of the EPIC camera and a significant fraction of the nebula remained unobserved. To complement these observations, additional *XMM-Newton* observations of three overlapping fields covering the northeast (NE), southwest (SW), and southeast (SE) quadrants of the nebula have been obtained. The previous and new observations result in the coverage of ~90% of the area of S 308. The pointings, dates and revolutions of the observations, and their exposure times are listed in Table 2.1. In the following, we will refer to the individual observations by the quadrant of S 308 that is covered, namely the NW, NE, SW, and SE quadrants. All observations were obtained using the Medium Filter and the Extended Full-Frame Mode for EPIC-pn and Full-Frame Mode for EPIC-MOS.

The *XMM-Newton* pipeline products were processed using the *XMM-Newton* Science Analysis Software (SAS) Version 11.0, and the Calibration Access Layer available on 2011-09-13. In order to analyze the diffuse and soft X-ray emission from S 308, the *XMM-Newton* Extended Source Analysis Software (XMM-ESAS) package (Kuntz & Snowden, 2008; Snowden et al., 2008) has

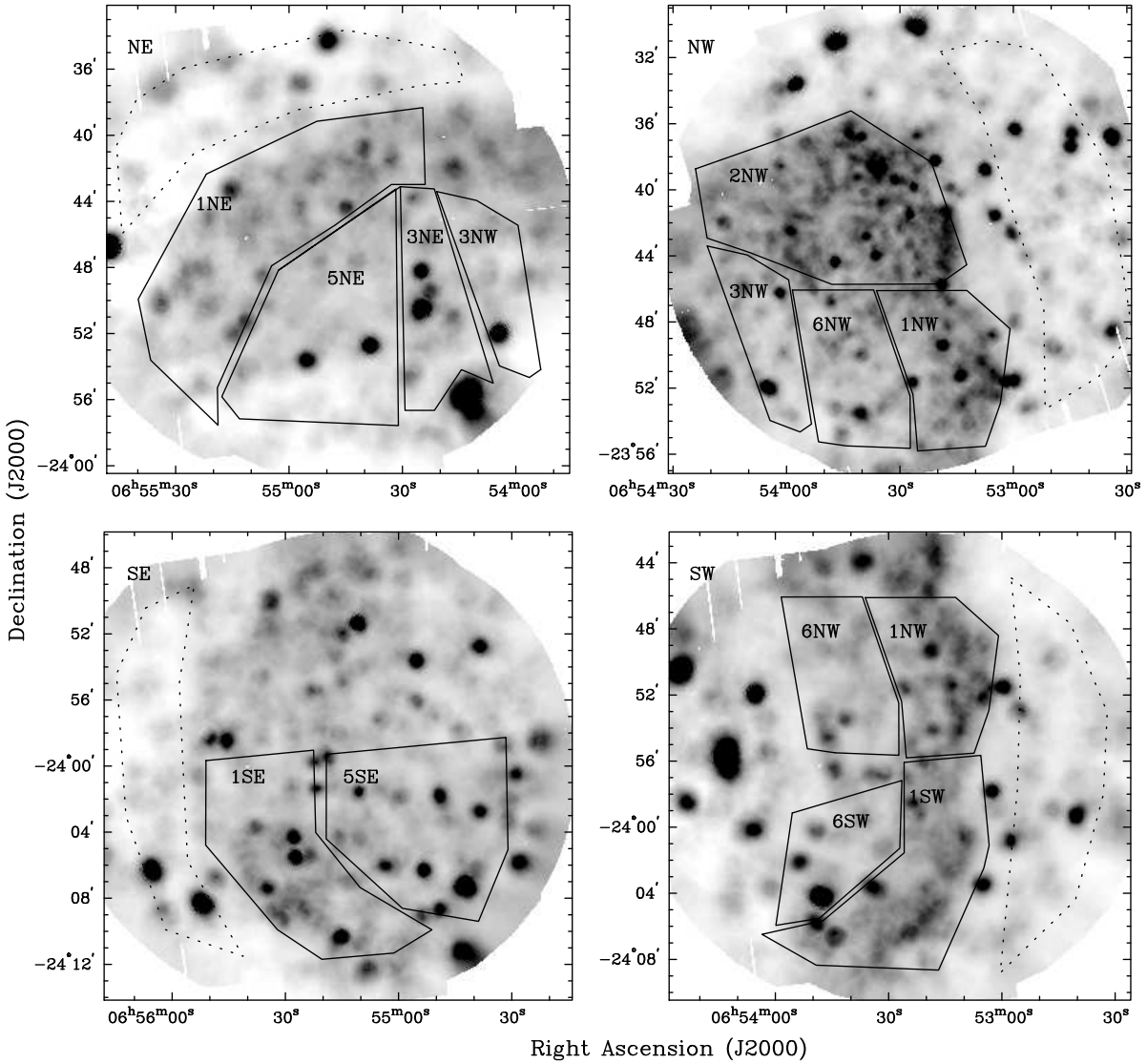

Figure 2.1: *XMM-Newton* EPIC images of the four observations of S 308 in the 0.3–1.15 keV band. The images have been extracted using a pixel size of 2″ and adaptively smoothed using a Gaussian kernel between 5″ and 30″. The source regions used for spectral analysis are indicated by solid lines and the background regions by dotted lines. Note that the point sources that are present in the images were excised for the spectral analysis.

Table 2.1: *XMM-Newton* Observations of S 308

Pointing	R.A. (J2000)	Dec. (J2000)	Obs. ID	Rev.	Observation start UTC	Total exposure time			Net exposure time		
						pn [ks]	MOS1 [ks]	MOS2 [ks]	pn [ks]	MOS1 [ks]	MOS2 [ks]
NW	06:53:30	−23:43:00	0079570201	343	2001-10-23T22:00:09	43.5	47.6	47.5	11.9	19.6	19.9
SW	06:53:24	−23:56:18	0204850401	781	2004-03-15T14:30:41	20.0	23.3	23.4	6.4	9.0	9.2
SE	06:55:16	−24:00:00	0204850501	781	2004-03-14T23:00:41	22.0	25.4	25.4	8.2	12.4	12.7
NE	06:54:47	−23:46:18	0204850601	781	2004-03-15T06:45:41	22.0	25.4	25.4	5.4	8.9	8.4

been used. This procedure applies very restrictive selection criteria for the screening of bad events registered during periods of high background to ensure a reliable removal of the background and instrumental contributions, particularly in the softest energy bands. As a result, the final net exposure times resulting from the use of the XMM-ESAS tasks, as listed in Table 2.1, are noticeably shorter than the original exposure times. Since we are interested in the best time coverage of the central WR star to assess its possible X-ray variability and given that its X-ray emission level is much brighter than that of a mildly enhanced background, we applied less restrictive criteria in selecting good time intervals for this star. For this particular analysis, the 10–12 keV energy band is used to assess the charged particle background, and we excised periods of high background with EPIC-pn count rates ≥1.5 counts s^{-1} and EPIC-MOS count rates ≥0.3 counts s^{-1}.

2.3 Spatial Distribution of the Diffuse X-ray Emission

2.3.1 Image processing

Following Snowden & Kuntz' cookbook for analysis procedures for *XMM-Newton* EPIC observations of extended objects and diffuse background, Version 4.3 (Snowden & Kuntz, 2011), the XMM-ESAS tasks and the associated Current Calibration Files (CCF), as obtained from
`ftp://xmm.esac.esa.int/pub/ccf/constituents/extras/esas_caldb`,
have been used to remove the contributions from the astrophysical background, soft proton background, and solar wind charge-exchange reactions, which have contributions at low energies (<1.5 keV). The resulting exposure-map-corrected, background-subtracted EPIC images of each observed quadrant of S 308 in the 0.3–1.15 keV band are presented in Figure 2.1. The new observations of the NE, SW, and SE quadrants of S 308 detect diffuse emission, as well as a significant number of point sources superimposed on this diffuse emission. With the single exception of HD 50896 (a.k.a. WR 6), the WR star progenitor of this bubble registered in the SW and NE observations, all point sources are either background or foreground sources that we have removed prior to our analysis.

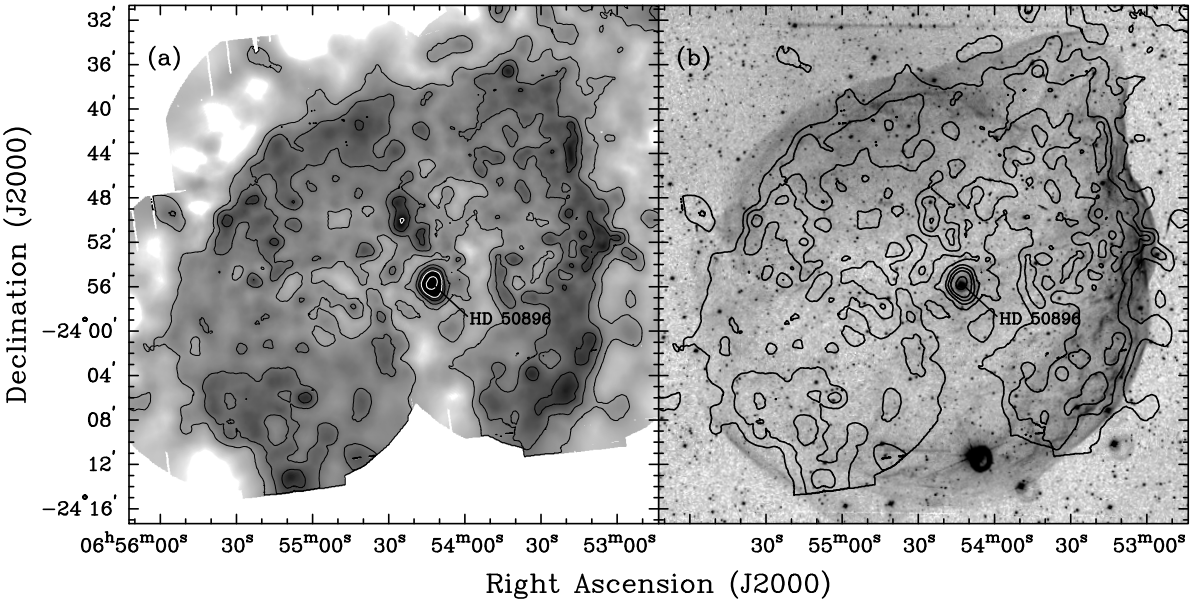

Figure 2.2: *(left)* Adaptively smoothed *XMM-Newton* EPIC Image of S 308 in the 0.3–1.15 keV band. All point sources, except for the central star HD 50896 (WR 6), have been excised. *(right)* Ground-based [O III] image of S 308 obtained with the Michigan Curtis Schmidt telescope at Cerro Tololo Inter-American Observatory (CTIO) with superimposed X-ray emission contours. The position of the central star HD 50896 is indicated in both panels.

2.3.2 Analysis of the diffuse X-ray emission

In order to analyze the spatial distribution of the diffuse X-ray emission in S 308, the four individual observations have been mosaicked using the XMM-ESAS tasks and all point sources removed using the *Chandra* Interactive Analysis of Observations (CIAO) Version 4.3 *dmfilth* routine, except the one corresponding to WR 6. The final image (Figure 2.2-*left*), extracted in the 0.3–1.15 keV energy band with a pixel size of $3''$, has been adaptively smoothed using the ESAS task *adapt-2000* requesting 100 counts of the original image for each smoothed pixel, with typical smoothing kernel scales $\leqslant 1'$ in the brightest regions and $1'-2'$ in the faintest ones. This image reveals that the diffuse X-ray emission from S 308 has a limb-brightened morphology, with an irregular inner cavity $\sim 22'$ in size. The surface brightness distribution displayed by this image confirms and adds further details to the results of previous X-ray observations (Chu et al., 2003a; Wrigge, 1999). The X-ray emission from the bubble is brighter towards the northwest blowout and the western rim, and fainter towards the east. The bubble seems to lack detectable X-ray emission towards the central regions around the WR star.

The limb-brightened spatial distribution of the X-ray emission from S 308 is further illustrated by the surface brightness profiles along the SE–NW and NE–SW directions shown in Figure 2.3. The emission in the innermost regions, close to the central WR star, falls to levels comparable to those of a background region to the west of S 308 shown in the bottom panel of

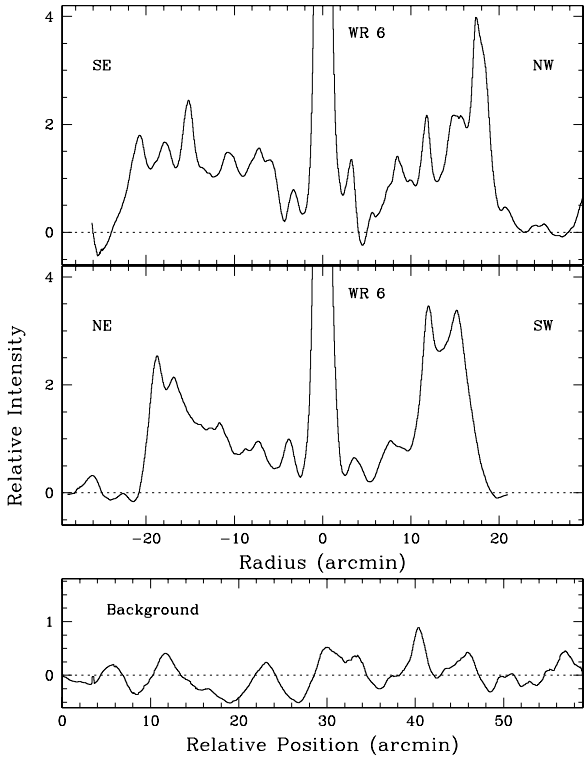

Figure 2.3: S 308 X-ray surface brightness profiles along the SE–NW (PA=135°) and SW–NE (PA=45°) directions extracted from the smoothed *XMM-Newton* EPIC image presented in Figure 2.2-*left*. For comparison, a surface brightness profile of a representative background region towards the West of S 308 is shown at the same intensity and spatial scales.

Fig. 2.3. Besides the SE region, whose surface brightness distribution is best described by a plateau, the X-ray emission along the other directions increases steadily with radial distance, peaking near the shell rim and declining sharply outwards. The thickness of the X-ray-emitting shell is difficult to quantify; along the SW direction, it has a FWHM ~5′, whereas it has a FWHM ~8′ along the NE direction. Figure 2.3 also illustrates that the X-ray-emitting shell is larger along the SE–NW direction (~44′ in size) than along the NE–SW direction (~40′ in size).

Finally, the spatial distribution of the diffuse X-ray emission from S 308 is compared to the [O III] emission from the ionized optical shell in Figure 2.2-*right*. The X-ray emission is interior to the optical emission not only for the NW quadrant but for the entire bubble. This is also illustrated in the color composite picture shown in Figure 2.4, in which the distribution of the X-ray emission is compared to the optical Hα and [O III] images. This image shows that the diffuse X-ray emission is closely confined by the filamentary emission in the Hα line, whereas the smooth emission in the [O III] line extends beyond both the Hα and X-ray rims.

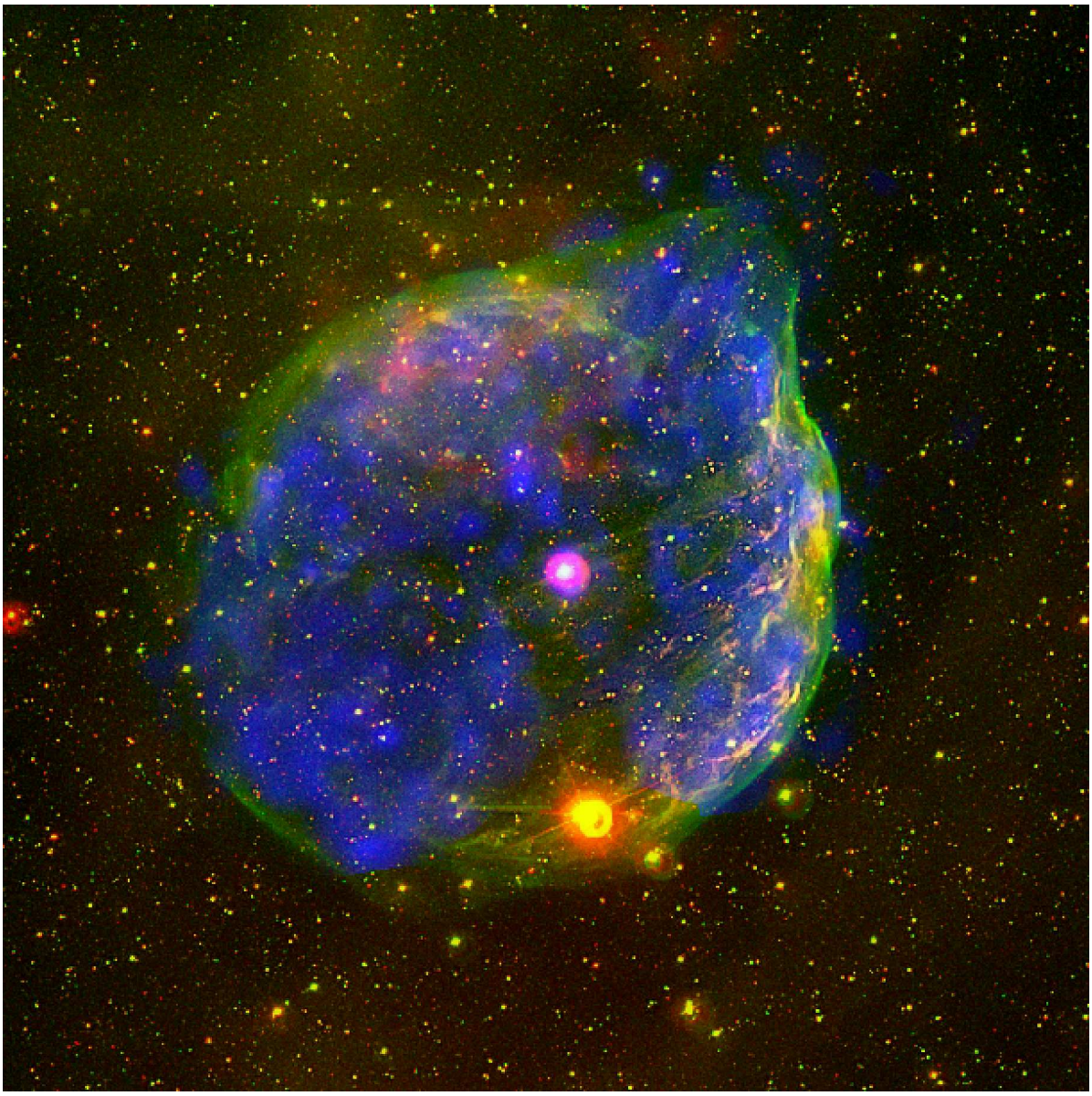

Figure 2.4: Color-composite picture of the *XMM-Newton* EPIC image (blue) and CTIO [O III] (green) and Hα (red) images of S 308. The apparent X-ray emission outside the optical shell is caused by large fluctuations in the background in regions near the EPIC cameras edge where the net exposure is much shorter than at the aimpoint.

2.4 Physical Properties of the Hot Gas in S 308

The spectral properties of the diffuse X-ray emission from S 308 can be used to investigate the physical conditions and chemical abundances of the hot gas inside this nebula. In order to proceed with this analysis, we have defined several polygonal aperture regions, as shown in Figure 2.1, which correspond to distinct morphological features of S 308: regions with #1 designations correspond to the rim revealed by the limb-brightened morphology, #2 the NW blowout, #3, #5, and #6 shell interior, and #4 the central star HD 50896. We note that any particular morphological feature may have been registered in more than one quadrant, in which case several spectra can have the same numerical designation (for instance, there are four spectra for the rim of the shell, namely 1NE, 1NW, 1SE, and 1SW).

2.4.1 Spectra Extraction and Background Subtraction

Perhaps the most challenging problem associated with the analysis of the X-ray spectra of S 308 is a reliable subtraction of the background contribution. The diffuse X-ray emission from S 308 fills a significant fraction of the field of view of the EPIC-pn and EPIC-MOS cameras, making the selection of suitable background regions difficult because the instrumental spectral response of the cameras close to their edges may not be the same as those for the source apertures.

The background contribution to the diffuse emission from clusters of galaxies that fills the field of view is typically assessed from high signal-to-noise ratio observations of blank fields. In the case of S 308, however, the comparison of spectra extracted from background regions with those extracted from the same detector regions of the most suitable EPIC Blank Sky observations (Carter & Read, 2007) clearly indicates that they have different spectral shapes. The reason for this discrepancy lies in the typical high Galactic latitude of the EPIC Blank Sky observations, implying low hydrogen absorption column densities and Galactic background emission, while S 308 is located in regions close to the Galactic Plane where extinction and background emission are significant. We conclude that EPIC Blank Sky observations, while suitable for the analysis of the diffuse emission of a large variety of extragalactic objects, cannot be used in our analysis of S 308.

Alternatively, the different contributions to the complex background emission in *XMM-Newton* EPIC observations can be modeled, taking into account the contributions from the astrophysical background, solar wind charge-exchange reactions, high-energy (soft protons) particle contributions, and electronic noise. This is the procedure recommended by the XMM-ESAS in the release of SAS v11.0, following the background modeling methodology devised by Snowden et al. (2004) and Kuntz & Snowden (2008). Even though the modeling of the different contributions is a complex task, it can be routinely carried out. Unfortunately, S 308 is projected close to the Galactic

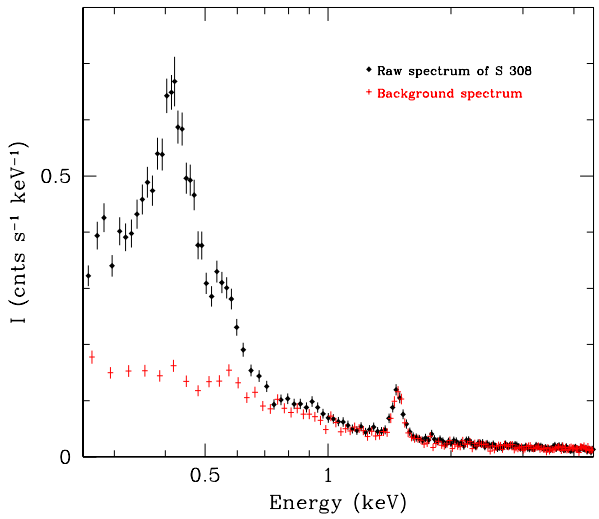

Figure 2.5: Comparison of the background-unsubtracted raw EPIC-pn spectrum of S 308 (black) and scaled EPIC-pn background spectrum (red). The Al-K line at ~1.5 keV is an instrumental line.

Plane and the *ROSAT* All Sky Survey (RASS) reveals that it is located in a region of strong soft background emission with small-scale spatial variations. As shown in Figure 2.5, the X-ray emission from this background is soft and shows lines in the 0.3-1.0 keV energy band from thermal components as the emission from S 308. Therefore, it is not possible to model independently the emission from the S 308 bubble and that from the soft background.

The only viable procedure for the analysis seems the use of background spectra extracted from areas near the camera edges of the same observations. It can be expected that the spectral properties of these background spectra differ from those of the background registered by the central regions of the cameras, given the varying spectral responses of the peripheral and central regions of the cameras to the various background components. To assess these differences, we have used EPIC Blank Sky observations to extract spectra from source and background regions identical in detector units to those used for S 308. Two typical examples of blank sky background-subtracted spectra are presented in Figure 2.6. While these spectra are expected to be flat, several deviations can be noticed: (1) clear residuals at ~ 7.5 and ~ 8.1 keV, which can be attributed to the defective removal of the strong instrumental Cu lines that affect the EPIC-pn spectra (Kuntz & Snowden, 2008), (2) a noticeable deviation at ~ 0.65 keV of the O-K line, and (3) most notably, deviations at energies below 0.3 keV, which is indicative of the faulty removal of the electronic noise component of the background (Carter & Read, 2007). Note that the Al-K line at ~ 1.5 keV and the Si-K line at ~ 1.8 keV, which may be expected to be strong in the background EPIC-pn spectra, are correctly removed. Consequently, we have chosen to use

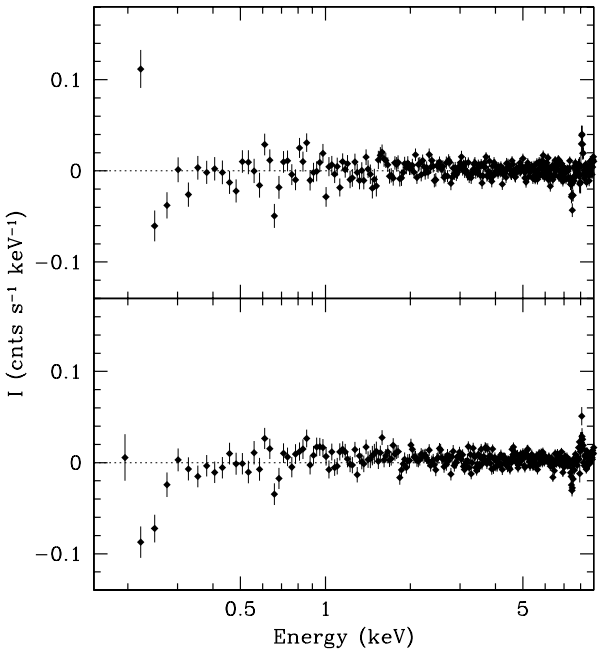

Figure 2.6: Background-subtracted blank sky spectra extracted from source and background regions equal in detector coordinates to the regions 1NW (*top*) and 1SW (*bottom*) of S 308.

the background spectra extracted from the observations of S 308, but restrict our spectral fits to the 0.3–1.3 keV band.

2.4.2 Spectral properties

The individual background-subtracted EPIC-pn spectra of the diffuse emission of S 308 are presented in Figure 2.7. This figure also includes spectra of the whole nebula, its rim, and central cavity obtained by combining all spectra, those of regions #1 and #2 (the rim or limb-brightened shell), and those of regions #3, #5, and #6 (the central cavity), respectively. Spectra and response and ancillary calibrations matrices from different observations of the same spatial regions were merged using the *mathpha*, *addarf*, and *addrmf* HEASOFT tasks according to the prescriptions of the SAS threads. The EPIC-MOS spectra have also been examined and found to be consistent with the EPIC-pn ones although, due to the lower sensitivity of the EPIC-MOS cameras, they have fewer counts. Therefore, our spectral analysis of the diffuse X-ray emission will concentrate on the EPIC-pn spectra.

The spectra shown in Figure 2.7 are all soft, with a prominent peak near $\gtrsim 0.4$ keV, and a rapid decline in emission towards higher energies. Some spectra (e.g., 1NE, 1NW, 1SW, 5NE, and 5SE) show a secondary peak near $\lesssim 0.6$ keV that is only hinted in other spectra. There is little emission above ~ 0.7 keV, although some spectra (e.g., 1SE, 1SW, 2NW, 3NE, 5SE, and 6SW) appear to present a hard component between 0.8 and 1.0 keV.

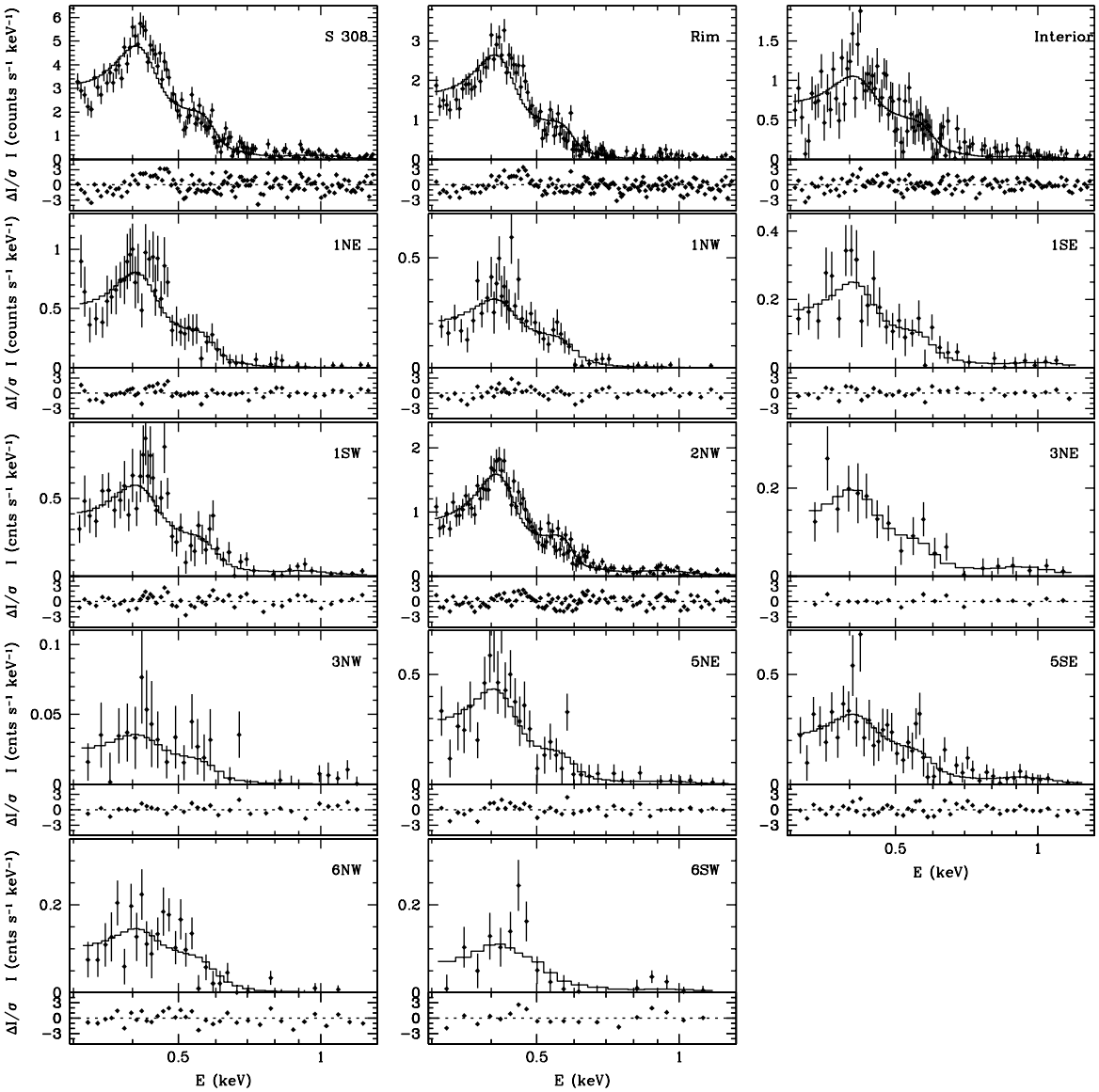

Figure 2.7: Background-subtracted *XMM-Newton* EPIC-pn spectra of S 308 corresponding to the 11 individual source regions shown in Figure 2.1, as well as the combined spectra of the entire nebula, its shell or rim (regions #1 and #2) and the interior region of the shell (#3, #5, and #6). Each spectrum is overplotted with its best-fit two-temperature APEC model in the energy range 0.3–1.3 keV, assuming fixed abundances, while the lower panel displays the residuals of the fit.

Table 2.2: Spectral Fits of the Diffuse X-ray Emission of S 308

Region	Counts	$N_{\rm H}$ [10^{20}cm^{-2}]	kT_1 [keV]	EM$_1$[a] [cm^{-3}]	f_1[b] [erg cm^{-2}s^{-1}]	kT_2 [keV]	EM$_2$[a] [cm^{-3}]	f_2[b] [erg cm^{-2}s^{-1}]	f_2/f_1	χ^2/DoF
S 308	10290±19	6.2	0.096±0.002	7.6×10^{56}	2.7×10^{-12}	1.12±0.22	1.2×10^{55}	2.4×10^{-13}	0.090	2.01 (=319.6/159)
Shell	7920±23	6.2	0.092±0.003	4.9×10^{56}	1.5×10^{-12}	…	…	…	…	1.54 (=233.9/151)
Interior	2390±120	6.2	0.116±0.011	8.3×10^{55}	5.6×10^{-13}	0.95	4.8×10^{54}	7.5×10^{-14}	0.134	1.35 (=188.2/139)
1NE	965±10	6.2	0.094±0.010	1.7×10^{56}	5.1×10^{-13}	0.95	1.1×10^{53}	2.5×10^{-15}	0.005	0.82 (=46.9/57)
1NW	1000±60	6.2	0.102±0.009	4.7×10^{55}	2.0×10^{-13}	0.95	4.4×10^{50}	1.0×10^{-17}	$<10^{-3}$	1.13 (=57.9/51)
1SE	540±50	6.2	0.094±0.010	1.8×10^{56}	5.1×10^{-13}	0.95	1.1×10^{53}	2.5×10^{-15}	0.005	0.82 (=46.9/57)
1SW	1100±50	6.2	0.097±0.012	1.0×10^{56}	3.9×10^{-13}	0.95	2.3×10^{54}	5.2×10^{-14}	0.135	1.31 (=69.3/53)
2NW	4620±100	6.2	0.095±0.003	2.2×10^{56}	7.4×10^{-13}	0.96±0.21	4.3×10^{54}	9.8×10^{-14}	0.130	1.30 (=137.9/106)
3NE	300±33	6.2	0.095±0.023	3.5×10^{55}	1.2×10^{-13}	0.95	1.4×10^{54}	3.1×10^{-14}	0.262	0.55 (=9.4/17)
3NW	160±25	6.2	0.11±0.04	5.0×10^{54}	2.5×10^{-14}	0.95	5.6×10^{51}	1.2×10^{-16}	0.005	0.91 (=27.4/30)
5NE	530±50	6.2	0.090±0.015	7.6×10^{55}	2.1×10^{-13}	0.95	9.0×10^{53}	1.8×10^{-14}	0.083	1.06 (=44.5/42)
5SE	820±60	6.2	0.103±0.016	4.4×10^{55}	1.9×10^{-13}	0.95	2.2×10^{54}	5.1×10^{-14}	0.268	1.05 (=54.5/52)
6NW	400±50	6.2	0.112±0.015	1.8×10^{55}	1.0×10^{-13}	…	…	…	…	1.42 (=50.0/35)
6SW	210±32	6.2	0.12±0.05	8.3×10^{54}	5.7×10^{-14}	0.95	9.7×10^{53}	1.5×10^{-14}	0.270	1.69 (=27.0/16)
W99[c]	4560	35	0.129	1.0×10^{56}	6.5×10^{-12}	2.4	4.3×10^{55}	1.2×10^{-12}	0.185	20 (=40/2)
C03[d]	…	11	0.094±0.009	8.2×10^{56}	7.2×10^{-12}	$0.7^{+1.5}_{-0.5}$	5.1×10^{54}	1.1×10^{-13}	0.015	1.02

[a] EM = $\int n_{\rm e}^2 dV$.

[b] Observed (absorbed) fluxes for the two-temperature models components in the energy range 0.3-1.3 keV.

[c] Wrigge (1999).

[d] Chu et al. (2003a).

The feature at ~ 0.4 keV can be identified with the 0.43 keV N VI triplet, while the fainter feature at ~ 0.6 keV can be associated with the 0.57 keV O VII triplet. The occurrence of spectral lines is suggestive of optically thin plasma emission, confirming previous X-ray spectral analyses of S 308 (Chu et al., 2003a; Wrigge, 1999). The predominance of emission from the He-like species of nitrogen and oxygen over their corresponding H-like species implies a moderate ionization stage of the plasma. Furthermore, the relative intensity of the N VI and O VII lines suggests nitrogen enrichment, since the intensity of the O VII lines from a plasma with solar abundances would be brighter than that of the N VI lines.

In accordance with their spectral properties and previous spectral fits of the NW regions of S 308 (Chu et al., 2003a), all the X-ray spectra of S 308 have been fit with XSPEC v12.7.0 (Arnaud, 1996) for an absorbed two-temperature APEC optically thin plasma emission model. The absorption model uses Balucińska-Church & McCammon (1992) cross-sections. A low temperature component is used to model the bulk of the X-ray emission, while a high temperature component is used to model the faint emission above 0.7 keV. We have adopted the same chemical abundances as Chu et al. (2003a), i.e., C, N, O, Ne, Mg, and Fe to be 0.1, 1.6, 0.13, 0.22, 0.13, and 0.13 times their solar values (Anders & Grevesse, 1989), respectively, which correspond to the nebular abundances. The simulated two-temperature APEC model spectra were then absorbed by an interstellar absorption column and convolved with the EPIC-pn response matrices. The resulting spectra were then compared to the observed spectrum in the 0.3–1.3 keV energy range and χ^2 statistics are used to determine the best-fit models. A minimum of 50 counts per bin was required for the spectral fit. The foreground absorption ($N_{\rm H}$), plasma temperatures (kT_1, kT_2) with 1-σ uncertainties, and emission measures ($\rm EM_1$, $\rm EM_2$) of the best-fit models are listed in Table 2.2. The best-fit models are overplotted on the background-subtracted spectra in Figure 2.7, together with the residuals of the fits. Multi-temperature models do not provide a substantial reduction of the value of the reduced χ^2 of the fit. We note that the values of the reduced χ^2 differ the most from unity for large regions, implying inconsistencies of the relative calibrations across the FoV, but the spectral fits still provide a fair description of the observed spectrum. In the following sections we discuss the spectral fits of the emission from the different morphological components of S 308 in more detail.

Spectral fits using models with varying chemical abundances of C, N, and O were also attempted, but they did not provide any statistical improvement of the fit. In particular, models with N/O abundance ratios different from those of the nebula resulted in notably worst quality spectral fits. As noted by other authors (see Chu et al., 2003a; Zhekov & Park, 2011), an X-ray-emitting plasma with chemical abundances similar to those of the optical nebulae seems at this moment to be the most adequate model for the soft X-ray emission from WR bubbles.

2.4.2.1 Properties of the Global X-ray Emission from S 308

The best-fit to the combined spectrum of the whole nebula results in unphysically high values of the hydrogen absorption column density, $N_{\rm H}$, well above the range $[0.2-1.05]\times10^{21}$ cm^{-2} implied by the optical extinction values derived from Balmer decrement of the nebula (Esteban et al., 1992). The effects of $N_{\rm H}$ and nitrogen abundance on the χ^2 of the spectral fits appear to be correlated, i.e., models with high $N_{\rm H}$ and low nitrogen abundance fit the spectra equally well as models with low $N_{\rm H}$ and high nitrogen abundance. If we adopt the high absorption column density from the best-fit model ($N_{\rm H} \gtrsim 3\times10^{21}$ cm^{-2}), the elevated nitrogen abundance reported by Chu et al. (2003a) will not be reproduced. As the high absorption column density is not supported by the optical extinction, in the subsequent spectral fits we will adopt a fixed $N_{\rm H}$ of 6.2×10^{20} cm^{-2} that is consistent with the optical extinction measurements. We note that this choice results in an imperfect modeling of the spectral features in the 0.3–0.5 keV range, as indicated by the S-shaped distribution of residuals in this spectral region in Fig. 2.7. If we allow the value of $N_{\rm H}$ to float during the spectral fit, the improvement of the value of the reduced χ^2 is negligible.

The parameters of the best-fit model, listed in the first line of Table 2.2, show two plasma components at temperatures $\sim1.1\times10^6$ K and $\sim1.3\times10^7$ K with an observed flux ratio, $f_2/f_1 \sim0.09$, corresponding to an intrinsic flux ratio $F_2/F_1 \sim0.06$. The total observed flux is $\sim 3\times10^{-12}$ erg cm^{-2} s^{-1}. The intrinsic luminosity at a distance of 1.5 kpc[1], after accounting for a fraction of $\sim$ 1/3 of S 308 which is not included in the source apertures considered here, is $\sim 2\times10^{33}$ erg s^{-1}. The emission measure of the best-fit to the combined spectrum, along with the spatial distribution of the X-ray-emitting gas in a spherical thick shell with a thickness $\sim8'$ and inner radius of $\sim11'$, implies an average electron density $n_e \sim 0.1$ cm^{-3}. We note that the quality of the spectral fit is not exceptionally good, but more sophisticated fits using multi-temperature models failed to improve the quality of the fit. The proposed 2-T model, providing a fair description of the spectral shape, should be considered as a first approximate of the hot gas content and its physical conditions.

2.4.2.2 Northwest Blowout (Region #2)

The northwest blowout of S 308 has the brightest X-ray emission, with a surface brightness $\sim 2.0\times10^{-18}$ erg cm^{-2} s^{-1} arcsec^{-2} and its individual spectrum has a high signal-to-noise ratio. The spectral shape is consistent with those of the shell spectra, with a prominent 0.43 keV N VI line, a weaker O VII line, and a clear detection of X-ray emission to energies of 0.8–1.0 keV. The best-fit parameters are rather similar to those of the spectrum of the entire nebula, with a marginally lower temperature for the hard component. We will adopt this value of the hard

[1]See discussion about the distance to WR 6 of Chu et al. (2003a).

component temperature for those regions whose spectra do not have an adequate count number to fit this parameter.

2.4.2.3 The Limb-Brightened Shell

The diffuse X-ray emission from S 308 has a clear limb-brightened morphology surrounding a cavity of diminished X-ray surface brightness. The emission from regions at the rim of this shell (1NE, 1NW, 1SE, and 1SW) is relatively bright, with an averaged surface brightness of the rim $\sim 1.2 \times 10^{-18}$ erg cm^{-2} s^{-1} arcsec^{-2}. All individual spectra of the rim regions show the bright 0.43 keV N VI emission line and indications of the weaker 0.57 keV O VII emission line. The hard component is faint, except for the spectrum of region 1SW. The fit to the combined spectrum confirms the temperature of the soft component, but it is not possible to provide statistical proof of the detection of the hard component. The fits to the individual spectra only provide upper limits for this component, except for region 1SW where it seems relatively bright.

2.4.2.4 The Central Cavity

The level of X-ray emission from the innermost regions of the optical shell of S 308 is lower than that of its edge, with an averaged surface brightness of 5×10^{-19} erg cm^{-2} s^{-1} arcsec^{-2}, i.e., $\sim$ 2.5–4.0 times fainter than the shell and blowout regions. The combined X-ray spectrum of the interior regions shown in Figure 2.7 indicates a stronger relative contribution from the hard component. This is indeed confirmed by the spectral fit: on average, the hard X-ray component has a flux $\sim$ 13% that of the soft component. There is a noticeable lack of emission from this component in the region 6NW, but otherwise the average contributions derived from the individual fits are higher than for the spectra of apertures on the shell rim.

2.4.2.5 Comparison with Previous X-ray Studies

Table 2.2 also lists the best-fit parameters of the spectral fits to the diffuse X-ray emission from S 308 obtained by Wrigge (1999) and Chu et al. (2003a). It is worthwhile discussing some of the differences with these previous X-ray analyses. The Chu et al. (2003a) joint fit of our regions 1NW, 2NW, 3NW and 6NW yields very similar results to the ones shown in Table 2.2. For the second thermal component, the derived temperatures from our spectral fits and those of Chu et al. (2003a) are consistent with each other, but Wrigge (1999) provides a much higher temperature for this component. This discrepancy highlights the difficulty of fitting the hard component using *ROSAT* PSPC data given its low spectral resolution, as well as the very likely contamination of the *ROSAT* PSPC spectrum of S 308 by unresolved hard point sources superposed on the diffuse emission.

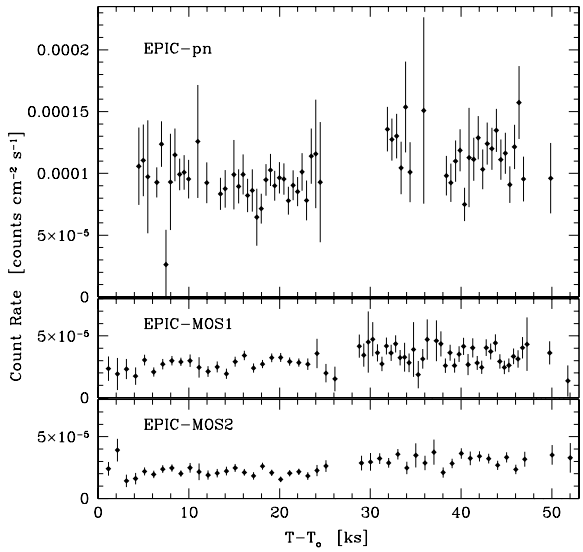

Figure 2.8: EPIC-pn (top), MOS1 (center), and MOS2 (bottom) exposure-map-corrected light curves of WR 6 in the 0.2–9.0 keV energy band. The time is referred to the starting time of the NE observation, 2004-03-15T06:45:41 UTC.

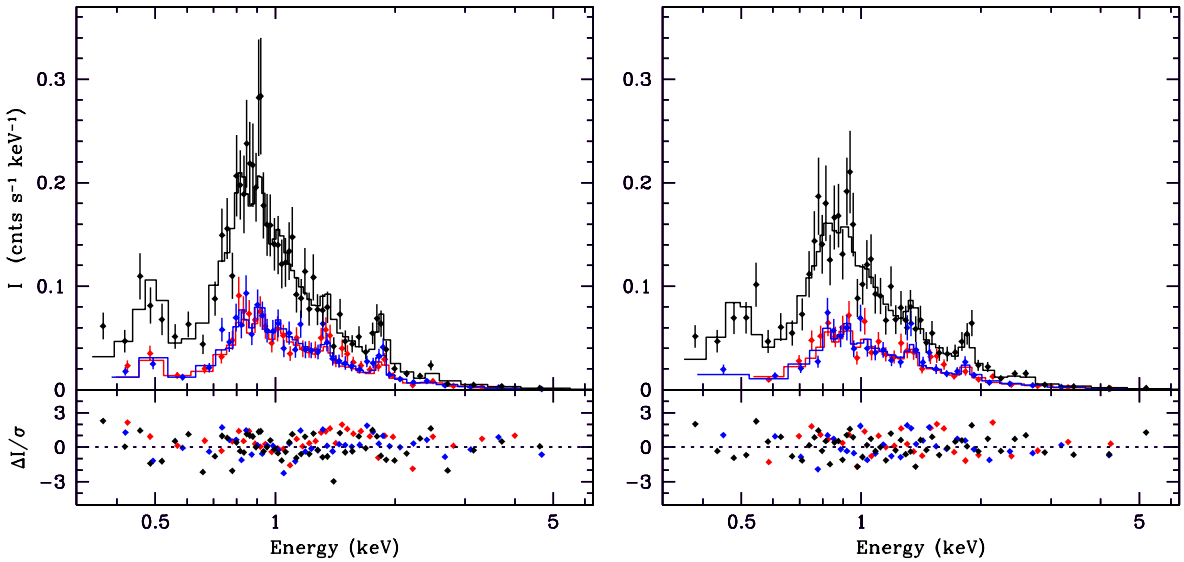

Figure 2.9: Background-subtracted *XMM-Newton* EPIC-pn (black), MOS1 (red), and MOS2 (blue) spectra of WR 6 obtained during the observation of the NE (*left*) and SW (*right*) pointings of S 308.

Table 2.3: Spectral Fits of HD 50896

Parameter	NE Spectrum	SW Spectrum	Skinner et al. (2002)
N_H [$\times 10^{21}$ cm^{-2}]	$6.4^{+1.0}_{-0.9}$	$5.9^{+1.2}_{-0.9}$	$4.0^{+0.4}_{-0.6}$
kT_1 [keV]	$0.28^{+0.03}_{-0.04}$	0.28	$0.6^{+0.4}_{-0.4}$
A_1 [cm^{-5}]	7.1×10^{-3}	5.9×10^{-3}	3.4×10^{-5}
kT_2 [keV]	$2.5^{+1.5}_{-0.5}$	2.48	$3.5^{+0.7}_{-0.5}$
A_2 [cm^{-5}]	1.8×10^{-4}	2.2×10^{-4}	1.0×10^{-5}
χ^2/DoF	1.10=137.0/124	1.10=113.2/103	1.08=234.5/217
f_1 (0.2–10 keV) [$\times10^{-12}$ erg cm^{-2} s^{-1}]	1.14	1.23	0.97
f_1 (2.5–10 keV) [$\times10^{-12}$ erg cm^{-2} s^{-1}]	0.33	0.39	0.31
f_2 (0.2–10 keV) [$\times10^{-12}$ erg cm^{-2} s^{-1}]	0.58	0.70	0.49
F_1 (0.2–10 keV) [$\times10^{-12}$ erg cm^{-2} s^{-1}]	19.8	17.6	2.90
F_1 (2.5–10 keV) [$\times10^{-12}$ erg cm^{-2} s^{-1}]	0.35	0.41	0.33
F_2 (0.2–10 keV) [$\times10^{-12}$ erg cm^{-2} s^{-1}]	1.10	1.35	0.78

2.5 The Central Star WR6 (HD 50896)

The central star of S 308 is WR 6 (a.k.a. HD 50896), which has a spectral subtype WN4 (van der Hucht et al., 1988). The star is detected by the *XMM-Newton* EPIC cameras in the NE and SW pointings of the nebula. The EPIC-pn, EPIC-MOS1, and EPIC-MOS2 count rates are 160±4 counts ks^{-1}, 65±2 counts ks^{-1}, and 65±2 counts ks^{-1}, respectively, from the NE observation, and 141±4 counts ks^{-1}, 53±2 counts ks^{-1}, and 52±2 counts ks^{-1}, respectively, from the SW observation using a source aperture of 50″ in radius. These count rates appear to imply that the X-ray luminosity of WR 6 diminished by 10–20% from the NE to the SW observations, which were only ~ 8 hours apart[2]. We note, however, that these count rates are largely affected by vignetting due to the offset position of WR 6 on the EPIC cameras. Indeed, the light curves shown in Figure 2.8, after accounting for the effects of vignetting, may imply the opposite, i.e., that the X-ray flux of WR 6 was slightly higher in the second (SW) observation than in the first (NE) observation.

In Figure 2.9 we present the EPIC background-subtracted spectra for the two different epochs. Following Skinner et al. (2002), we have modeled these spectra with a two-temperature VAPEC model with initial abundances set to those shown in Table 1 of van der Hucht et al. (1986). The fit allowed the foreground absorption column density, temperatures, and abundances of N, Ne, Mg, Si, and Fe to vary (Skinner et al., 2002). Table 2.3 displays the parameters resulting from our best-fit models: absorption column densities $N_{\rm H}$, plasma temperatures T, normalization parameters A[3], observed (absorbed) fluxes f, and intrinsic (unabsorbed) fluxes F. Model fits for the spectra from the NE and SW observations are listed separately alongside those from

[2] The on-axis *XMM-Newton* images presented by Skinner et al. (2002) revealed a faint X-ray source at a radial distance of ~57″ from WR 6. The flux from this source is (2 ± 1)% that of WR 6 and thus it is not likely that fraction of the emission from this source entering into the aperture used for WR 6 would contribute significantly to the observed X-ray variability.

[3] $A = 1\times10^{-14}\int n_e^2 dV/4\pi d^2$, where d is the distance, n_e is the electron density, and V the volume in cgs units.

Skinner et al. (2002) for comparison. The column density and temperatures of the two components are within 1-σ of one another among the three different models. The observed fluxes are also consistent, although the Skinner et al. (2002) flux seems to be a bit lower, while our fluxes are closer to the ones derived from the October 1995 *ASCA* observations of WR 6 (Skinner et al., 1996). The total observed fluxes and the observed fluxes of the hot thermal component, f_2, listed in Table 2.3 may indicate a hardening of the X-ray emission from WR 6 during the last observation. To assess this issue, we performed statistical evaluation of the lightcurves showed in Figure 2.8 using the HEASOFT task *lcstats* and found no significant variations. Thus, WR 6 does not show evidence of variability in time-scales of hours.

We would like to point out that the absorption column density obtained from our best fits are in good agreement with the values obtained from Skinner et al. (2002), which are higher than that used to fit the soft X-ray emission from the nebula. Such higher column density values are commonly observed towards massive stars such as WR stars and are recognized to be caused by absorption at the base of the wind (Cassinelli et al., 1981; Corcoran et al., 1994; Gosset et al., 2011; Nazé, 2009; Skinner et al., 2010).

2.6 Discussion

The *XMM-Newton* images and spectra analyzed in the previous sections reveal that the hot plasma in S 308 is spatially distributed in a thick shell plus the northwest blowout, with most emission being attributable to a hot plasma at $\sim 1.1\times10^6$ K. For an adiabatically shocked stellar wind, its temperature is determined by the stellar wind velocity, $kT = 3\mu m_{\rm H} V_w^2/16$, where μ is the mean particle mass for fully ionized gas (Dyson & Williams, 1997). Therefore, the temperature expected for the shocked stellar wind of WR 6, with a terminal wind velocity of 1700 km s^{-1} (Hamann & Koesterke, 1998) and $\mu \gtrsim 1.3$ (van der Hucht et al., 1986), would be $T > 8\times10^7$ K, in sharp contrast with the observed temperature. The same issue has been pointed out for the WR bubble NGC 6888 by several authors (see Zhekov & Park, 2011, and references therein), and it is also a common issue in planetary nebulae (e.g., NGC 6543; Chu et al., 2001).

Electron thermal conduction has been proposed as a mechanism capable of reducing the temperature of the hot plasma in shocked stellar wind bubbles. Thermal conduction was applied by Weaver et al. (1977) to stellar wind bubbles to produce a self-similar solution for the density and temperature structure in bubbles. The soft X-ray luminosities predicted by Weaver et al.'s model for the Omega Nebula and the Rosette Nebula, according to the stellar wind parameters of their associated young clusters (M 17 and NGC 2244, respectively), are several orders of magnitude higher than those observed (Dunne et al., 2003; Townsley et al., 2003). Thus, the standard Weaver et al. model for a stellar wind bubble with thermal conduction cannot be taken

at face value. Recent work by Steffen et al. (2008) in the context of planetary nebulae, which are produced in a very similar manner to WR wind bubbles, has calculated the time-dependent radiation-hydrodynamic evolution of planetary nebula wind bubbles including thermal conduction in 1D models with spherical symmetry. In these models, the cold shell material from the previous AGB superwind phase is evaporated into the hot bubble. Saturated conduction was taken into account in these calculations by limiting the electron mean free path and it was found that thermal conduction was able to lower the temperature and raise the density at the edge of the hot bubble enough to explain the soft X-ray emission and low X-ray luminosities observed in some planetary nebulae (e.g., Chu et al., 2001).

In the case of WR bubbles, Toalá & Arthur (2011) presented time-dependent 2D radiation-hydrodynamic models of the evolution of the CSM around massive stars, including classical and saturated thermal conduction. They found that thermal conduction does not seem to play in important role in shaping WR bubbles, but that models with thermal conduction have slightly greater soft-band luminosities than those without thermal conduction. They suggested that the morphology of S 308 could result from a star with initial mass of 40 $M_{\odot}$ whose stellar evolution model includes stellar rotation (Meynet & Maeder, 2003). They obtained that ~20,000 yr after the onset of the WR phase, the X-ray-emitting gas will present a clump-like morphology with an electron density of $n_e \sim 0.1$ cm^{-3} inside an optical ($T \sim 10^4$ K) shell with radius of ~ 9 pc.

2.7 Summary and conclusions

We present *XMM-Newton* observations of three fields of the WR bubble S 308 which, in conjunction with the observation of its NW quadrant presented by Chu et al. (2003a), map most of the nebula except for its southernmost section. We have used these observations to study the spatial distribution of the X-ray-emitting material within this bubble, to derive global values for its physical conditions (T_e, n_e), and to search for their spatial variations among different morphological components of the nebula.

The X-ray emission from S 308 is found to have a limb-brightened morphology, with a shell thickness 5–8′, and extend to the northwest blowout region. The X-ray-emitting shell is notably larger along the SE-NW direction than along the SW-NE direction, and it is always confined by the optical shell of ionized material. The X-ray surface brightness decreases notably from the blowout region and the western rim shell to the shell interior, where the X-ray emission falls to background levels. The western quadrants are also brighter than the eastern quadrants.

The X-ray emission from S 308 shows prominent emission from the He-like triplet of N VI at 0.43 keV and fainter emission of the O VII 0.57 keV triplet, and declines towards high energies, with a faint tail up to 1 keV. This spectrum can be described by a two-temperature optically thin plasma emission model with temperatures $\sim 1.1 \times 10^6$ K and $\sim 1.3 \times 10^7$ K. The latter component is notably fainter than the former by at least a factor of ~ 6. There is an appreciable difference

in the relative contributions of the hot component to the X-ray-emitting gas between the rim and the nebula interior, of which the latter has a higher contribution from the hard component. The total X-ray luminosity is estimated to be $\sim 2 \times 10^{33}$ erg s^{-1} for a distance of 1.5 kpc.

CHAPTER 3

NO HOT GAS WITHIN THE WOLF-RAYET BUBBLE AROUND WR 16

We present the analysis of XMM-Newton *archival observations towards the Wolf-Rayet (WR) bubble around WR 16. Despite the closed bubble morphology of this WR nebula, the* XMM-Newton *observations show no evidence of diffuse emission in its interior as in the similar WR bubbles NGC 6888 and S 308. We use the present observations to estimate a 3-σ upper limit to the X-ray luminosity in the 0.3–1.5 keV energy band equal to 7.4×10^{32} erg s^{-1} for the diffuse emission from the WR nebula, assuming a distance of 2.37 kpc. The WR nebula around WR 16 is the fourth observed by the current generation of X-ray satellites and the second not detected. We also examine* FUSE *spectra to search for nebular O* VI *absorption lines in the stellar continuum of WR 16. The present far-UV data and the lack of measurements of the dynamics of the optical WR bubble do not allow us to confirm the existence of a conductive layer of gas at $T\sim3\times10^5$ K between the cold nebular gas and the hot gas in its interior. The present observations result in an upper limit of $n_e<0.6$ cm^{-3} on the electron density of the X-ray emitting material within the nebula.*

3.1 Introduction

When massive stars reach the Wolf-Rayet (WR) stage in their late evolution, powerful stellar winds carve the circumstellar medium and produce WR nebulae. X-ray emission from these objects is expected to arise from shock-heated plasma that is produced when the WR stellar wind rams into material previously ejected during the red supergiant (RSG) or luminous blue variable (LBV) phase (García-Segura & Mac Low, 1995). To date, there are only three WR nebulae reported in the literature that had been observed with the latest generation of X-ray satellites (*Chandra*, *Suzaku*, and *XMM-Newton*): S 308, RCW 58, and NGC 6888 around WR 6, WR 40, and WR 136, respectively (Chu et al., 2003a, 2006; Gosset et al., 2005; Toalá et al., 2012; Zhekov & Park, 2011).

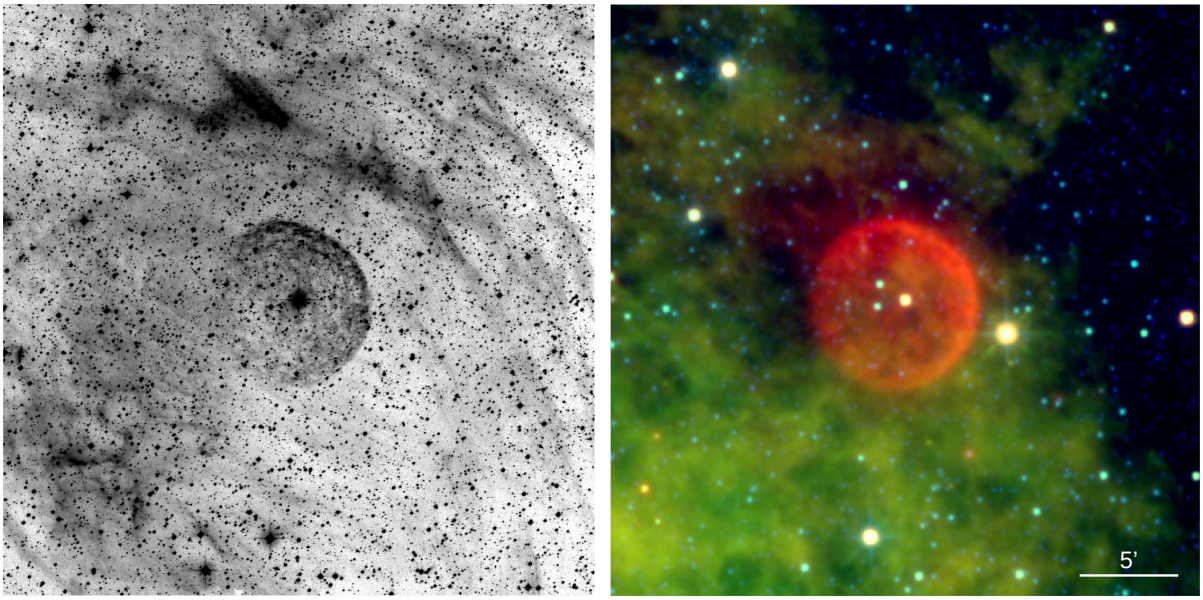

Figure 3.1: *(left)* Narrow-band Hα image of the WR nebula around WR 16 taken from the Super COSMOS Sky Survey (Parker et al., 2005). *(right)* Color-composite mid-infrared *WISE* W2 4.6 μm (blue), W3 12 μm (green), and W4 22 μm (red) picture of the WR nebula around WR 16. The central star, WR 16, is located at the center of each image. North is up, east to the left.

The most recent observations towards S 308 and NGC 6888 show a dominant X-ray-emitting plasma component with a temperature $\gtrsim 10^6$ K and abundances similar to those of the optical nebulae (Toalá et al., 2012; Zhekov & Park, 2011). The temperature and abundances of the dominant X-ray-emitting plasma can be explained by means of mixing between the outer cold material and the shocked fast stellar wind. On the other hand, RCW 58 has not been detected by *XMM-Newton* (Gosset et al., 2005). The cause of this non-detection of hot gas may be twofold. First, WR nebulae lay within the Galactic Plane, and their soft X-ray emission may be highly affected by absorption (RCW 58 has a Galactic latitude ~5°, and the hydrogen column towards it is 5×10^{21} cm^{-2}.). Secondly, RCW 58 presents a disrupted shell morphology (Gruendl et al., 2000), which can imply that the hot gas has already escaped outside the nebula, greatly reducing the X-ray emissivity (Toalá & Arthur, 2011). The limited number of X-ray observations of WR nebulae makes it still an exploration field. It is thus highly important to increase the number of observed WR nebulae with good spatial coverage, high sensitivity, and suitable energy resolution for spectral analyses.

The soft nature of the X-ray emission detected in S 308 and NGC 6888 needs further discussion. Theoretical models of adiabatic shocked winds predict high plasma temperatures, $>10^7$ K (e.g., Dyson & Williams, 1997), which are not reported by observations. The relatively low temperature of the X-ray-emitting plasma is often attributed to mixing in the wind-wind interaction zone, such as, thermal conduction. The hot gas will be cooled down to temperatures of 10^6 K

when in contact with the outer cold (~10^4 K) RSG or LBV material. As a result, a so-called conductive layer with intermediate temperatures, ~10^5 K, is created between the hot and cool gas, as has been first suggested by Castor et al. (1975) and Weaver et al. (1977) in wind-blown bubbles. Observationally, the conductive layer can be revealed by the presence of highly ionized species (Castor et al., 1975; Weaver et al., 1977). Indeed, this conductive layer has been detected in other wind-blown bubbles, such as those of planetary nebulae (PNe; Ruiz et al., 2013) using far-UV *FUSE* observations of the O VI doublet. At least in PNe, the conductive layer at ~10^5 K coexists with diffuse hot gas at X-ray-emitting temperatures $\gtrsim 10^6$ K (Gruendl et al., 2004).

The WR nebula around WR 16 was first discovered by Marston et al. (1994), who described it as a round main nebula with multiple arc-like features towards the northwest (see Figure 3.1-left). The main nebula is classified as a wind-blown bubble (a *W*-type nebula according to the classification scheme developed by Chu, 1981), whereas the outer features have been associated with multiple mass ejection episodes (Marston, 1995). The rim of the main nebula is sharper towards the northwest direction. The diminished optical emission towards the southeast may be associated with extinction due to the molecular material along that direction that is revealed by radio observations (Duronea et al., 2013; Marston et al., 1999). Alternatively, this morphology may have resulted from the large proper motion of the central star along this direction (Duronea et al., 2013).

The optical and radio morphologies of the nebula around WR 16 are consistent with the mid-infrared morphology revealed by *WISE* observations (see Figure 3.1-right). In particular, the W4 band (red in Figure 3.1-right) shows a complete round shell with enhanced, limb-brightened emission towards the northwest direction. The round WR nebula seen in this *WISE* band matches that of the *IRAS* 60 μm image presented by Marston et al. (1999).

According to Toalá & Arthur (2011), the closed nebular shell and limb-brightened morphology of a WR nebula make it a promising candidate for its detection in X-rays, since a complete WR nebula is able to confine the highly pressurized X-ray-emitting gas, as is the case for S 308 and NGC 6888. Such hot gas can be expected to be in contact with the cold nebular shell throughout a conductive layer. In this chapter, we have searched for the different components of hot gas in the WR bubble around WR 16 using archival *XMM-Newton* and *FUSE* observations towards this WR bubble. Section 2 describes the observations and data processing, whereas we briefly describe our findings in Section 3. We discuss our results in Section 4, and finally we summarize them in Section 5.

3.2 Observations

3.2.1 *XMM-Newton* Observations

The *XMM-Newton* observations of the nebula around WR 16 were performed on 2009 Dec 28-29 (Obs. ID 0602020301; PI: S. Skinner) during revolution 1841. The observations were obtained in

the framework of a survey to study single nitrogen-rich stars to determine their X-ray properties and to characterize the emission processes. The data have been presented by Skinner et al. (2012), who focused on the analysis of the X-ray emission from the central star, WR 16. No further analysis of the potential diffuse X-ray emission was performed, and thus we will concentrate in the search and analysis of extended emission.

The two EPIC-MOS and pn cameras were operated in the full-frame mode for a total exposure time of 33 and 30 ks, respectively. The medium optical blocking filter was used. The observations were processed using the *XMM-Newton* Science Analysis Software (SAS Ver. 12.0.1) and the XMM-ESAS tasks for the analysis of the X-ray emission of extended objects and diffuse background (Snowden & Kuntz, 2011), as required for the analysis of *XMM-Newton* observations of WR nebulae (Toalá et al., 2012). The associated Current Calibration Files (CCF) available on June 2013, as obtained from `ftp://xmm.esac.esa.int/pub/ccf/constituents/extras/esas_caldb`, have been used to remove the contribution from the astrophysical background, soft proton background, and solar wind charge-exchange reactions with contributions at low energies ($<$ 1.5 keV).

The net exposure times after processing the data are 27.5, 28.9, and 14 ks for the EPIC/MOS1, MOS2, and pn cameras, respectively. We extracted images in four energy bands, namely 0.3-1.15 keV (soft), 1.15-2.5 keV (medium), 2.5-10 keV (hard), and 0.3-10 keV (total). The combined EPIC X-ray image in the total energy band is shown in Figure 3.2-*left*. Smoothed exposure-corrected images of the soft, medium, and hard images were created using the ESAS task *adapt-900* requesting 20 counts of the original image for each smoothed pixel, and these were combined to create the false-color picture shown in Figure 3.2-*right*.

3.2.2 *FUSE* Observations

To complement the X-ray observations towards the WR bubble around WR 16, we have searched *Far Ultraviolet Spectroscopic Explorer* (*FUSE*) observations on the Mikulski Archive for Space Telescopes (MAST) of WR 16. The *FUSE* observations have a spectral coverage between 920–1190Å with spectral resolution of R$\sim$ 20 000 (Moos et al., 2000; Sahnow et al., 2000). Two sets of observations were used to create a far-UV spectrum of WR 16, namely Obs. ID G9271501 (start time 2006-07-10 05:18:34; exposure time 30.6 ks) and G9271502 (start time 2006-07-11 12:34:37; exposure time 30.7 ks). The data were reprocessed with the CalFUSE calibration pipeline software package, CalFUSE 3.2.3 (Dixon et al., 2007).

The resultant spectrum will be used to analyze the O VI $\lambda\lambda$1032,1037 doublet. The presence of these lines may imply a conductive layer of gas at $T \sim 3\times10^5$ K between the outer cold (10^4 K) nebular material and the interior hot content, as in the case of star forming regions (e.g. Pathak et al., 2011) and PNe (Ruiz et al., 2013). The O VI lines are registered by the LiF2B (979–1075 Å), and Å) and SiC2B (1016–1103 Å) telescopes, gratings, and detector segments combinations. After processing, the observation ID G9271501 has net exposure times of 28.4 ks for

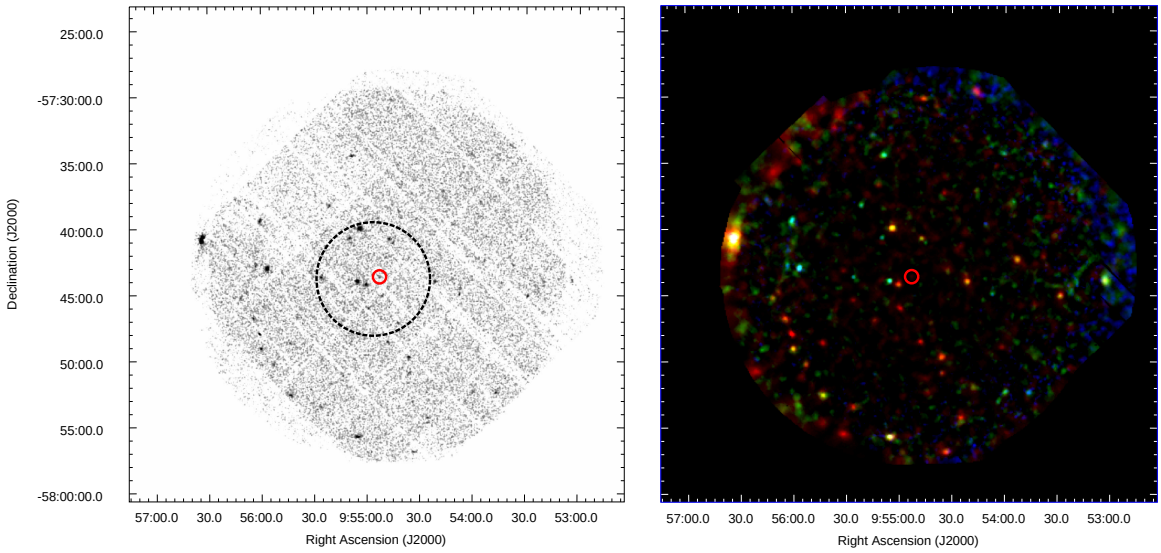

Figure 3.2: *(left) XMM-Newton* EPIC (MOS1, MOS2, and pn) X-ray image of the field of view of WR 16 for the total energy range 0.3–10 keV. *(right) XMM-Newton* EPIC smoothed exposure-corrected, color-composite X-ray picture of WR 16, where the red color corresponds to the soft 0.3–1.15 keV energy band, green to the medium 1.15–2.5 keV band, and blue to the hard 2.5–10 keV band. The small red circle in both images shows the location of the central star, WR 16, whereas the dashed-line circle in the left image encompasses the optical WR nebula.

LiF1A and 30.5 ks for LiF2B, whereas the observation ID G9271502 has net exposure times of 25.2 ks for LiF1A, 26.5 ks for LiF2B, and 7.2 ks for SiC1A. For both observations, the quality of the spectrum registered by SiC2B was limited and the resulting spectrum was not used. Details of the data processing and merging are similar as those described by Guerrero & De Marco (2013).

Figure 3.3 shows the final spectrum obtained from the *FUSE* observations. The O VI doublet lines are marked at 1031.93 Å and 1037.62 Å. Additional absorption lines from material in the interstellar medium and Earth atmosphere are also shown. Details and discussion on this spectrum will be presented in Section 4.

3.3 Results

A preliminary inspection of the images presented in Figure 3.2 does not reveal any diffuse X-ray emission within the nebula around WR 16, although a significant number of point sources are detected in the field of view of the EPIC cameras. Even though there is no detection of diffuse X-ray emission within this WR bubble, we can estimate an upper limit from the present observations. To derive this upper limit, we have extracted background-subtracted spectra from

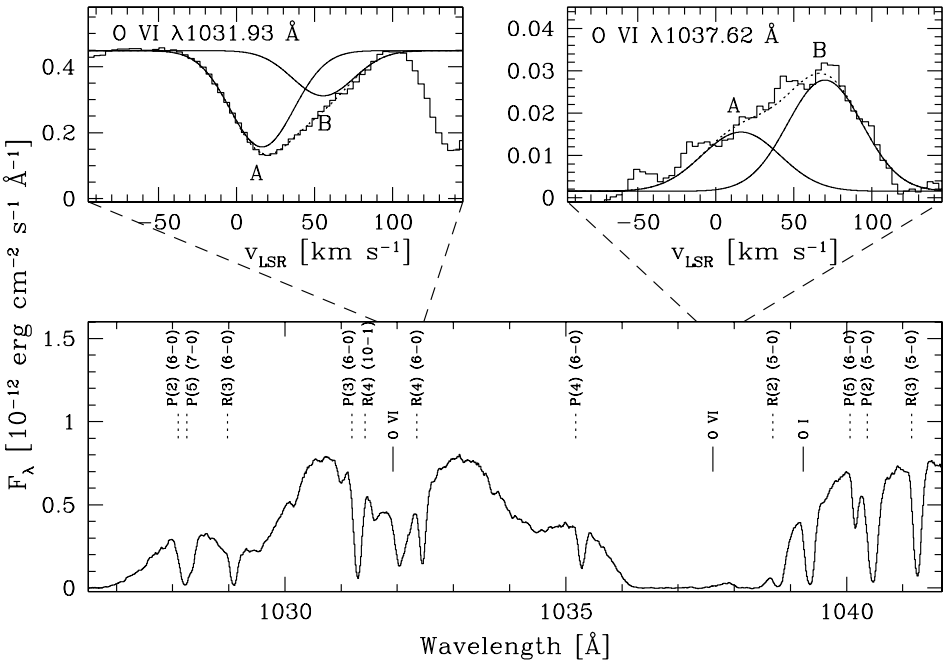

Figure 3.3: *FUSE* far-UV spectrum towards WR 16. The bottom panel shows the spectral range around the O VI lines. Vertical solid lines mark the position of the O VI doublet and O I atomic line, whereas dotted lines mark the position of H_2 absorption lines. The upper panels show enlargements of the O VI lines in the LSR velocity frame with multiple Gaussian fits to their profiles, which include components A and B as described in the text.

the three EPIC instruments corresponding to the source region shown in Figure 3.2-left, which encloses the optical nebula with a radius of 4.3′. Point sources were carefully excised from either the source and background regions. The spectral analysis allowed us to derive 3-σ upper limits to the EPIC-pn, EPIC-MOS1, and EPIC-MOS2 count rates in the 0.3–1.5 keV energy range <28 counts ks^{-1}, <14 counts ks^{-1}, and <13 counts ks^{-1}, respectively.

The X-ray flux and luminosity upper limits for the WR 16 nebula can be estimated from the count rates given above using the count rate simulator WebPIMMS (version 4.6)[1]. To derive these values, we have adopted an optically-thin APEC plasma emission model absorbed by a column density of 4.1×10^{21} cm^{-2}, as implied by Bohlin et al.'s (1978) relation for an optical extinction A_V of 2.14 mag where the average of the values is given by van der Hucht (2001). Furthermore, the temperature of the X-ray-emitting gas in the nebula has been assumed to be $\sim1.4\times10^6$ K ($kT \sim 0.122$ keV), i.e., an intermediate value between those reported for the hot gas detected in S 308 and NGC 6888. Accounting for the use of the EPIC-pn camera with the medium filter, the resultant 3-σ upper limit for the absorbed flux in the 0.3–1.5 keV energy band is $f_X \lesssim 3.1\times10^{-14}$ erg cm^{-2} s^{-1} for an intrinsic flux of $F_X \lesssim 1.1\times10^{-12}$ erg cm^{-2} s^{-1}. The

[1] heasarc.gsfc.nasa.gov/Tools/w3pimms.html

corresponding upper limit for the X-ray luminosity is $L_X \lesssim 7.4\times10^{32}$ erg s^{-1} for a distance of d = 2.37 kpc (van der Hucht, 2001).

Using the normalization factor[2] given by WebPIMMS, A =1.38×10^{-3} cm^{-5}, we can estimate an upper limit to the electron density of the hot gas in the nebula. This gives n_e <0.6 cm^{-3}.

The *FUSE* spectrum shows a strong absorption feature at the wavelength of the O VI λ1031.93 Å line and one weak emission feature at the wavelength of the O VI λ1037.62 Å. These are indicative of the presence of hot gas at ~3×10^5 K along the line of sight of WR 16. The detection of one component of the O VI doublet in absorption and the other in emission is certainly puzzling, as the physical conditions for emission and absorption are very different: O VI emission is typically ascribed to narrow, high-density interfaces in the local interstellar medium (Dixon & Sankrit, 2008), whereas O VI absorptions can also be produced in large volumes of low-density hot gas. The two lines have been reported to be detected either in emission or absorption in surveys of the Galaxy and Magellanic Clouds (e.g., Howk et al., 2002), but the simultaneous detection of one component in absorption and the other in emission requires singular observational conditions. This may be the case of WR 16, as the stellar continuum around the O VI λ1037.62 Å line is completely saturated, whereas it is not around the O VI λ1031.93 Å component. The particular shape of the stellar continuum of WR 16 makes the O VI λ1037.62 Å component sensitive to emission from material along the line of sight but insensitively to absorption. On the other hand, the O VI λ1031.93 Å component is sensitive both to emissions and absorptions along the line of sight, but the former dominates the profile of this line, as the absorption component is stronger than the emission.

The profile shape of the O VI lines is not symmetric, implying different velocity components. We find that the most simple fit of both the emission and absorption spectral features involves two Gaussian components with $V_{LSR} \simeq$16 km s^{-1} and 60 km s^{-1}, which are marked as component A and B in the top panels of Figure 3.3, respectively. Component A has the same radial velocity as the H_2 and O I absorption lines overimposed in the spectrum of WR 16, which are visible at the bottom panel of Figure 3.3. Following the measurement of equivalent widths and column densities technique of O VI (Savage & Sembach, 1991), we have computed the column density of the O VI λ1031.93 Å line, N_{OVI} (in cm^{-2}), along the line of sight of WR 16. This technique uses the apparent optical depth in terms of velocity,

$$\tau(v) = \ln[I_o(v)/I_{obs}(v)], \tag{3.1}$$

where $I_o(v)$ and $I_{obs}(v)$ are the continuum intensity and absorption line depth, respectively. The parameter N_{OVI} can be calculated as

$$N_{OVI} = \frac{m_e c \tau(v)}{\pi e^2 f \lambda} \times \Delta V_{FWHM} = 3.768 \times 10^{14} \frac{\tau(v)}{f\lambda} \Delta V_{FWHM}, \tag{3.2}$$

where λ is the wavelength in Åand f is the oscillator strength of the atomic species (for O VI, f=0.1325; see Pathak et al., 2011, for details). The parameters c, m_e, and e are the speed of

[2] A =1×10^{-14} $\int n_e dV/4\pi d^2$, where d is the distance, n_e the electron density, and V the volume.

light, and electron mass, and charge, respectively, where $\Delta V_{\rm FWHM}$ is the full width at half maximum of the line in km s^{-1}. The O VI column density is estimated to be 1.4×10^{14} cm^{-2}, which is consistent with the averaged value expected for a star at 2.37 kpc ($N_{\rm OVI} \lesssim 10^{14}$ cm^{-2}; de Avillez & Breitschwerdt, 2012). This is especially true if we consider the large spatial variations revealed by studies of the O VI content in the local interstellar medium along the line of sight of B-stars (Welsh & Lallement, 2008) and hot DA white dwarfs (Barstow et al., 2010). Therefore, we can conclude that component A is due to the interstellar medium along the line of sight of WR 16.

Component B of the O VI doublet, on the other hand, does not have a molecular or neutral interstellar medium counterpart. The intensity of its absorption in the λ1031.93 Å line implies a column density of 4.5×10^{13} cm^{-2}, which is, about one third that of component A. The conductive layer within the nebula would result in a narrow O VI absorption feature bluewards of the systemic velocity of the WR 16 nebula. There are, however, no measurements of the dynamics (radial velocity and expansion) of the optical main WR bubble around WR 16 to carry out such comparison. Duronea et al. (2013) attributed a molecular component at $V_{\rm LSR} \simeq -9$ km s^{-1} to the main nebular shell around WR 16. If this were indeed the case, then component B could not be ascribed to hot gas inside the WR nebula around WR 16 as its velocity would be redwards of the systemic velocity. We should then conclude that component B is most likely associated with a high excitation component of the interstellar medium along the line of sight towards WR 16.

3.4 Discussion

The WR nebulae can be expected to be filled with hot diffuse gas, as the current WR wind slams the slow and dense, previously ejected RSG or LBV material, which creates a shock wave that thermalizes the interior of the WR nebula. The star WR 16 possesses a stellar wind with terminal velocity, v_∞, of 630 km s^{-1} (van der Hucht, 2001), which would imply a shocked gas temperature $\sim1.2\times10^7$ K (for a mean free particle $\mu \sim 1.3$; van der Hucht et al., 1986). Higher velocities would imply even higher plasma temperatures, but S 308 and NGC 6888 possess plasma with temperatures barely greater than 10^6 K, which contrasts the terminal wind velocities, $\gtrsim$1700 km s^{-1}, of their central stars. This discrepancy is also seen in H II regions and PNe, in which thermal conduction is invoked to explain the low observed plasma temperatures of the shocked stellar wind (Chu, 2008).

The *XMM-Newton* observations described here show that no extended X-ray emission is detected inside the main nebular shell of WR 16, despite the sensitive integration time of these observations. To put this non-detection in context with previous observations of WR nebulae, we show the stellar and nebular parameters (distance, spectral type of the WR star, stellar wind velocity, nebular radius, observed X-ray surface brightness, and luminosity) for the four WR nebulae observed to date in Table 1 by the present generations of X-ray satellites, namely

S 308, NGC 6888, RCW 58, and that around WR 16. The surface brightness and luminosity of RCW 58 in the 0.3–1.5 keV energy range have been computed from the count rate reported by Gosset et al. (2005) for a distance of 2.26 kpc (van der Hucht, 2001) after adopting the same plasma temperature as for the WR nebula around WR 16. The observed surface brightness presented in Table 1, which is obtained by dividing the observed X-ray flux by the area sustained by the nebula, provides a distance independent measurement of the relative X-ray brightness of each nebula. We remark that the X-ray surface brightness and luminosity for RCW 58 and the WR nebula around WR 16 given in this table correspond to upper limits.

We first note that the distances to all WR nebulae in Table 1 are not dramatically different, ranging from 1.26 kpc up to 2.37 kpc. Furthermore, they are all absorbed by similar hydrogen column densities in the range 6×10^{20}–5×10^{21} cm^{-2}. This situation suggests that the detection of extended X-ray emission from these sources does not depend on external factors, such as distance or amount of intervening material but rather points that the nebula around WR 16 is intrinsically fainter than S 308 and NGC 6888 with a surface brightness 6–20 times lower.

In sharp contrast, the stellar properties (spectral type and terminal wind velocity) seem to be correlated with the detectability of extended X-ray emission within these WR nebulae. Both S 308 and NGC 6888 harbor early WN4 and WN6 stars, respectively, with terminal wind velocities $\gtrsim$1700 km s^{-1}. Meanwhile, the non-detected WR nebulae in the X-rays have late WN stars, WN8h, with stellar velocities below 900 km s^{-1}.

The nebular morphology has been claimed in the past to be correlated with X-ray emission: diffuse X-ray emission is present in S 308 and NGC 6888, and possess undisrupted morphologies, whereas RCW 58, which is undetected in X-rays, has a disrupted morphology (Gruendl et al., 2000). The interpretation of this behaviour is that a disrupted shell cannot hold the hot gas which escapes away. Contrary to this trend, the nebula around WR 16 displays a complete shell morphology (Figure 3.1), but we have set a stringent upper limit for the X-ray emission from hot plasma in its interior.

The lack of X-ray emission motivated us to investigate the *FUSE* spectrum of WR 16, to search for spectral features in the O VI lines that could be attributed to gas at temperatures of $\sim3\times10^5$ K (Figure 3.3). Although several O VI absorption and emission components are detected in the *FUSE* spectrum of WR 16, none of them can be unambiguously attributed to a conductive layer in its nebula. This seems to suggest that this bubble has not experienced the effects of thermal conduction or any other equivalent physical processes (e.g., hydrodynamic ablation, photoevaporation; Arthur, 2007a; Pittard, 2007) in the wind-wind interaction zone. As a result, the shocked wind material may still possess temperatures of 1.2×10^7 K but extremely low densities in the range 0.001–0.01 cm^{-3}. If this would be the case, the non-detection of X-ray emission from the WR bubble around WR 16 does not automatically imply the lack of interior hot gas, but its low density has reduced its differential emission measure below the detectability limits.

3.5 Summary and conclusions

We present the analysis of *XMM-Newton* archival observations of the WR nebula around WR 16. These observations show that there is no detection of hot gas within the nebula, but a number of point sources are detected in the field of view. An upper limit to the unabsorbed flux in the 0.3–1.5 keV band has been estimated to be $F_{\rm X} \lesssim 1.1\times10^{-12}$ erg s^{-1} cm^{-2}, which corresponds to a luminosity $L_{\rm X} \lesssim 7.4\times10^{32}$ erg s^{-1} at a distance of 2.37 kpc and an upper limit to the electron density of $n_{\rm e}$ <0.6 cm^{-3}.

Following the hypothesis that thermal conduction takes place between the outer cold (10^4 K) nebular gas and the hot interior of the WR nebula, we have searched for a conductive layer between these two components using *FUSE* observations of the O VI doublet. We find that both lines can be model as the contribution of two components at $V_{\rm LSR}$=16 km s^{-1} and $V_{\rm LSR}$=60 km s^{-1}, respectively. The velocity of the first component is coincident with that of H_2 and low-excitation ions and neutral atoms in the interstellar medium along the line of sight towards WR 16. Its column density is also consistent with the amount of intervening material expected for a star at the distance of WR 16. The second component does not have a counterpart in the low-excitation interstellar medium, but its radial velocity is not consistent with that expected for the expanding nebular shell of WR 16 from radio molecular observations. Unless there is a significant revision of the radial velocity of WR 16, the present observations suggest that this second component can neither be associated with a conductive layer.

The lack of detection of hot gas (10^5–10^7 K) within the WR bubble around WR 16 is puzzling. This nebula is one of the four WR nebulae observed with the latest generation of X-ray satellites, and is the second non-detected. Because the low number statistics, it is important to increase the number of X-ray observations towards these nebulae with better spatial coverage, sensitivity, and energy resolution to define the stellar and nebular properties required for the presence of hot gas in these objects.

Table 3.1: Stellar and nebular parameters for the WR nebulae observed with modern X-ray satellites.

Star	WR Nebula	Distance[a]	WR type[a]	v_∞^a	Radius[b]		N_H^c	S[c]	L_X^c
		(kpc)		(km s^{-1})	(arcmin)	(pc)	($\times10^{21}$ cm^{-2})	(erg cm^{-2} s^{-1} arcmin^{-2})	($\times10^{33}$ erg s^{-1})
WR 6	S 308	1.5	WN4	1800	20	8.8	0.62–1.1	3.5×10^{-15}	2
WR 16		2.37	WN8h	630	4.3	3	4.1	$<5.4\times10^{-16}$	<0.8
WR 40	RCW 58	2.26	WN8h	840	4.9	3.2	5	$<2.2\times10^{-15}$	<6.5
WR 136	NGC 6888	1.26	WN6	1750	8.6	3.2	3.1	1.2×10^{-14}	3.5

[a]Distance, spectral type, and stellar wind velocity taken from van der Hucht (2001), except for the distance of WR 6 that was taken from the kinematic distance estimated by Chu et al. (2003a).

[b]For NGC 6888 this is the semi-major axis.

[c]Column density taken from Toalá et al. (2012) for S 308, Gosset et al. (2005) for RCW 58, and Zhekov & Park (2011) for NGC 6888. The observed X-ray surface brightness and luminosity of these sources have been scaled from these references to the distances used here and extended to the 0.3–1.5 keV energy range in all cases for consistency.

CHAPTER 4

X-RAY EMISSION FROM NGC 6888. I. *Chandra* ACIS-S OBSERVATIONS

We analyze Chandra *observations of the Wolf-Rayet (WR) bubble NGC 6888. This WR bubble presents similar spectral and morphological X-ray characteristics to those of S 308, the only other WR bubble also showing X-ray emission. The observed spectrum is soft, peaking at the N* VII *line emission at 0.5 keV with additional line emission at 0.7–0.9 keV and a weak tail of harder emission up to ~1.5 keV. This spectrum can be described by a two-temperature optically thin plasma emission model ($T_1 \sim 1.4 \times 10^6$ K, $T_2 \sim 7.4 \times 10^6$ K). We confirm the results of previous X-ray observations that no noticeable temperature variations are detected in the nebula. The X-ray-emitting plasma is distributed in three apparent morphological components: two caps along the tips of the major axis and an extra contribution toward the northwest blowout not reported in previous analysis of the X-ray emission toward this WR nebula. Using the plasma model fits of the* Chandra *ACIS spectra for the physical properties of the hot gas and the* ROSAT *PSPC image to account for the incomplete coverage of* Chandra *observations, we estimate a luminosity of $L_X = (7.7 \pm 0.1) \times 10^{33}$ erg s^{-1} for NGC 6888 at a distance of 1.26 kpc. The average rms electron density of the X-ray-emitting gas is $\gtrsim 0.4$ cm^{-3} for a total mass $\gtrsim 1.2 M_\odot$.*

4.1 Introduction

Wolf-Rayet (WR) bubbles are expected to be filled with hot plasma at temperatures of $\sim 10^7$–10^8 K , but previous X-ray observations of hot bubbles have shown that this plasma presents lower temperatures, of the order of $\sim 10^6$ K (see Chu, 2008). The scarcity of X-ray detections among WR nebulae is also intriguing; there are only two WR nebulae detected in diffuse X-rays: S 308 and NGC 6888 (Bochkarev, 1988; Chu et al., 2003a; Toalá et al., 2012; Wrigge, 1999;

Wrigge et al., 1994, 1998; Wrigge & Wendker, 2002; Wrigge et al., 2005; Zhekov & Park, 2011). These two WR bubbles share several characteristics: the X-ray-emitting plasma is confined inside optical shells where the Hα emission presents a clumpy distribution inside an [O III] shell (Gruendl et al., 2000), and both bubbles are nitrogen-rich and surround WN stars with terminal wind velocities of ~1800 km s^{-1} (van der Hucht, 2001). This configuration can be pictured as the WR wind sweeping up the previously ejected Red Supergiant (RSG) wind material whilst the central star photoionizing this material.

NGC 6888 has been the subject of many studies over the years since it was first reported by Sharpless (1959) and associated to its central WR star, WR 136, by Johnson & Hogg (1965). The most recent optical study of this nebula, presented by Fernández-Martín et al. (2012), investigated the ionization, chemical composition, and kinematics in several regions within the nebula. They concluded that NGC 6888 is composed by multiple shells, and its morphology can be interpreted as a sphere with an ellipsoidal cavity inside.

The first map of the diffuse X-ray-emitting gas in NGC 6888 was presented by Bochkarev (1988) using *Einstein* observations; a total flux of ~10^{-12} erg cm^{-2} s^{-1} was detected in the 0.2–3.0 keV band. Wrigge et al. (1994) analyzed *ROSAT* PSPC observations and found a flux of $(1.2\pm0.5)\times10^{-12}$ erg cm^{-2} s^{-1}. Wrigge et al. (2005) made use of the *ASCA* SIS and *ROSAT* PSPC observations to fit a two-temperature model ($T_1 \sim 1.3\times10^6$ K, $T_2 \sim 8.5\times10^6$ K) and measured a total observed flux of ~10^{-12} erg cm^{-2} s^{-1}. The most recent X-ray observations of NGC 6888 are those obtained by Zhekov & Park (2011) using the *Suzaku* satellite. They concluded that the spectrum indicates a relatively cool plasma with $T < 5\times10^6$ K and a small contribution from a much hotter plasma component with temperature greater than 2×10^7 K. No appreciable temperature variations are found between the northern and southern regions of the nebula. The observed flux was reported to be 2×10^{-12} erg cm^{-2} s $^{-1}$ in the 0.3–1.5 keV energy range.

In this chapter we present *Chandra* observations of NGC 6888. A preliminary analysis of this dataset was presented by Chu et al. (2006), where they showed the diffuse X-ray emission coming from the NE quadrant of the nebula (ACIS-S CCD S3). Here we present the analysis of the ACIS-S CCD S3 and CCD S4, covering ~62% of the nebula. The spectral properties of the X-ray-emitting plasma are compared to those derived previously by other authors using observations obtained by other X-ray facilities. The data from CCD S4 show an additional spatial component of X-ray emission which has not been reported in previous observations.

4.2 *Chandra* observations

The superb angular resolution and sensitivity at soft energies of *Chandra*, as compared to previous satellites that have observed NGC 6888, allow a more reliable study of the soft X-ray

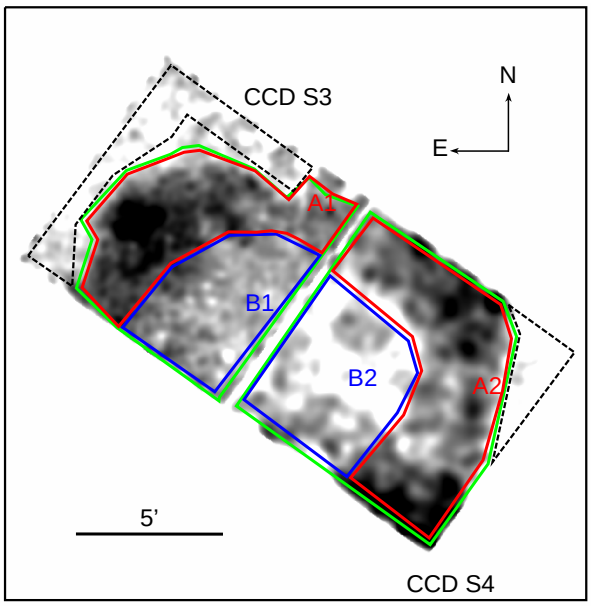

Figure 4.1: *Chandra* ACIS-S image of the diffuse X-ray emission of NGC 6888 in the 0.3-2.0 keV band. Point sources have been excised from this image. The regions used for spectral analysis are indicated with polygonal apertures: green, red, and blue solid lines correspond to source regions, and black dashed lines to background regions.

emission from the hot plasma in this nebula. The *Chandra* observation of NGC 6888 was performed on 2003 February 19-20 (Observation ID 3763; PI: R.A. Gruendl) using the Advanced CCD Imaging Spectrometer (ACIS-S) for a total exposure time of 92.8 ks. The NE quadrant of NGC 6888 was imaged on the back-illuminated ACIS-S CCD S3 while the western region was imaged by CCD S4. The *Chandra* Interactive Analysis of Observations (CIAO) software package version 4.4 was used to analyze the data using CALDB version 3.2.2. Very short periods of high background affected the data and the resulting useful exposure time is 88.0 ks after excising dead time periods. The *Chandra* ACIS-S observation detects diffuse emission from NGC 6888 in the soft energy band below 2.0 keV. No significant emission is detected above this energy limit. The total background-subtracted count rates of the diffuse X-ray emission for CCD S3 and CCD S4 are 0.160 and 0.053 counts s^{-1}, respectively.

4.3 Spatial distribution of the diffuse X-ray emission

In order to analyze the spatial distribution of the hot gas in NGC 6888, we excised all point sources from the observation using the CIAO *dmfilth* routine. The identification of the point sources was made using the CIAO *wavdetect* routine. The image of the diffuse X-ray emission was extracted in the 0.3-2.0 keV energy band and smoothed with the CIAO task *csmooth*, with a Gaussian kernel of 4″ in the brightest regions and 16″ and 24″ in the faintest ones for the

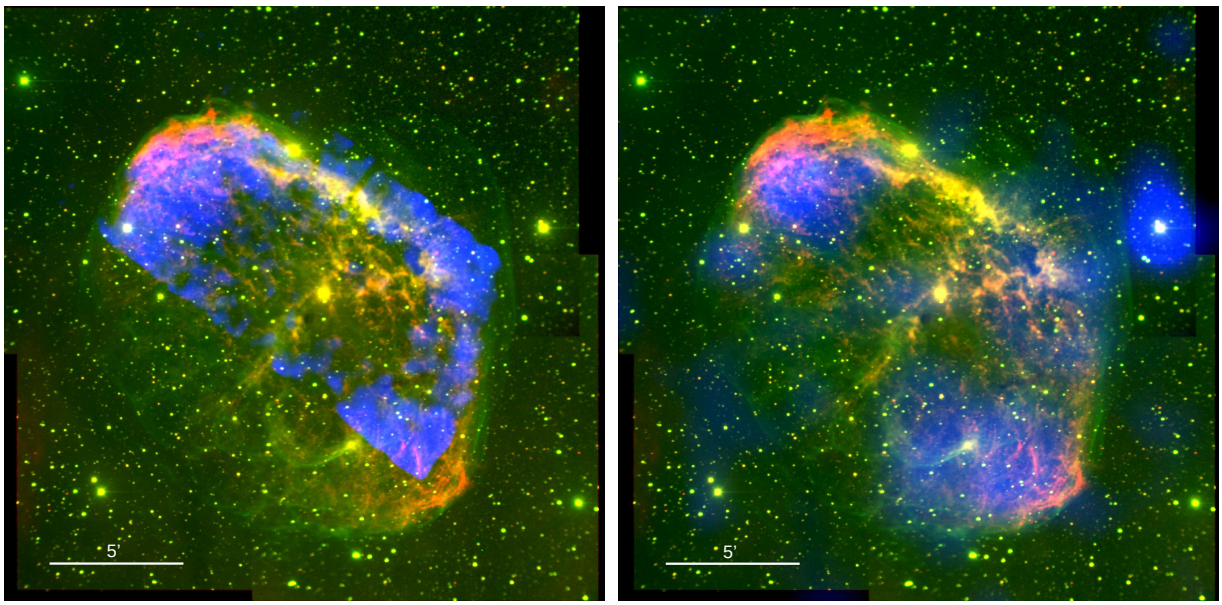

Figure 4.2: Left: Composite color picture of the *Chandra* ACIS-S observation of NGC 6888 (blue) and MLO Hα (red) and [O III] (green) images. Right: Same as in *left* image but with *ROSAT* PSPC image (blue). North is up, East to the left.

CCD S3 and S4, respectively. The resultant image is shown in Figure 4.1.

We compare in Figure 4.2-left the X-ray image with Hα and [O III] optical images of the nebula taken with the 1 m telescope at the Mount Laguna Observatory (Gruendl et al., 2000). This figure shows a limb-brightened spatial distribution of the X-ray emission confined within the optical [O III] shell. In particular the X-ray-emitting gas in the NE region of the nebula (ACIS-S CCD S3) seems to fill all the area within the nebula with a broad emission peak superposed on the Hα clumps, while the emission detected in ACIS-S CCD S4 can be associated with the southwest cap of the nebula, and with emission outside the Hα shell but inside the western [O III] skin.

For comparison, we also present in Figure 4.2-right a composite picture of the same optical images and the X-ray emission detected by *ROSAT* PSPC (Wrigge et al., 1994, 2005). This image demonstrates that the X-ray emission from NGC 6888 is stronger at the caps along the major axis, but an extra contribution can be detected at the westernmost regions of the nebula, just inside the optical [O III] shell. This additional spatial component of X-ray emission, hinted in previous images of the nebula made with *ROSAT* HRI and *ASCA* (Wrigge et al., 1994; Wrigge & Wendker, 2002; Wrigge et al., 2005), is reminiscent of the Northwest blowout in S 308 (Chu et al., 2003a; Toalá et al., 2012).

4.4 Physical properties of the hot gas in NGC 6888

We have carried out the study of the hot gas of NGC 6888 in several steps. First, we have studied the emission from the nebular gas detected in CCD S3 and CCD S4, keeping in mind that the former has more reliable spectral resolution and sensitivity at lower energies than CCD S4. Therefore, we have defined two regions encompassing the diffuse X-ray emission registered in the field of view of the *Chandra* ACIS-S CCD S3 and S4 (green polygonal lines in Figure 4.1).

For further analysis, we have defined several smaller polygonal aperture regions, also shown in Figure 4.1, corresponding to different features presented in NGC 6888: regions labeled as A comprise the apparent shell and caps, and regions labeled with B correspond to the shell interior. We note that both regions are present within each CCD detector, and thus we have extracted two spectra corresponding to each morphological feature. For example, A1 corresponds to a region extracted from CCD S3 and A2 to a region extracted from CCD S4. The same applies to regions B1 and B2.

4.4.1 Spectral Properties

As discussed in Toalá et al. (2012), the extraction of spectra from extended sources, as is the case of WR bubbles, is challenging because the emission fills almost the entire field of view of the instrument. The background contribution can be estimated from high signal-to-noise blank fields, but as mentioned by Toalá et al. (2012), this technique does not produce suitable results because WR bubbles are located in regions close to the Galactic Plane where extinction and background emission are significant (Snowden et al., 1997). To show the contribution of the Galactic background, we plot in Figure 4.3 the background-unsubtracted spectrum from CCD S3 and a background spectrum extracted from the edge of the camera. X-ray emission from the background is soft and show lines in the 0.3–1.0 keV energy band from thermal components (see also figure 5 in Toalá et al., 2012, for the case of S 308). The spectral shape of the background emission certainly differs from that derived from ACIS blank-field observations. Therefore, the most feasible procedure to subtract the background contribution is the use of background spectra extracted from areas near the camera edges, even though the instrumental responses for sources and background regions do not completely match each other.

The individual background-subtracted spectra of the diffuse emission of the NE quadrant and western region of NGC 6888 (namely CCD S3 and CCD S4) are presented in Figure 4.4, as well as the individual spectra extracted from regions A1, A2, B1, and B2. All spectra were extracted using the CIAO task *specextract*, which generates the source and background spectra and their corresponding calibration files. The most notable differences in the spectral shapes are attributed to the differences in sensitivity of the ACIS-S CCD S3 and CCD S4. All spectra are soft and show two main peaks, a narrow peak at 0.5 keV and a broader peak around 0.7–0.9 keV. The feature around 0.5 keV can be identified with the N VII ion, while the feature around ~0.7–

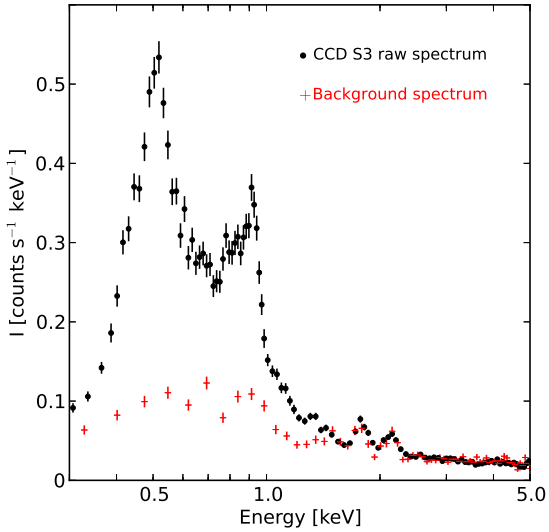

Figure 4.3: Comparison of the raw CCD S3 spectrum (black circles) and scaled background spectrum extracted from the edges of CCD S3 (red crosses). The emission lines around 2 keV in the background spectrum are instrumental lines.

0.9 keV can be associated with the Fe complex and Ne lines. Above 1.0 keV, the emission declines and diminishes at energies ≃1.5 keV. We note that the spectra extracted from CCD S4 show the instrumental Au M complex at 2.2 keV, which has not been properly removed due to the reduced spatial extent of the background region.

In accordance with the spectral properties and previous spectral fits, all X-ray spectra from NGC 6888 have been fit with XSPEC v12.7.0 (Arnaud, 1996) using an absorbed two-temperature *apec* optically thin plasma emission model with an absorption model using Balucińska-Church & McCammon (1992) cross-sections. A low temperature component is used to model the bulk of the X-ray emission, while a high temperature component is added to model the extra emission at and above ~ 0.7 keV. As in previous studies of the X-ray emission from WR bubbles (see Chu et al., 2003a; Toalá et al., 2012; Zhekov & Park, 2011), we have initially adopted nebular abundances for the X-ray-emitting plasma. In particular, we have used abundance values for N, O, and Ne of 3.2, 0.41, and 0.85 times the solar values (Anders & Grevesse, 1989) as averaged from regions X1 and X2 described in Fernández-Martín et al. (2012, see their Table 4), and 0.39 times the solar value for S (Moore et al., 2000). Models with variable C, Mg, Fe, and Ne abundances were also tested. We found that the fitted abundances of Mg and Fe converged to solar values, whereas those of Ne tended to 0.85 times the solar value, i.e., the value determined from optical spectrophotometry (Fernández-Martín et al., 2012). Consequently, we decided to fix the abundances of Mg, Fe, and Ne to these values. As for the carbon abundance, the fits could not converge to specific values because the C VI line at 0.37 keV or C V triplet at 0.3 keV are in the low energy

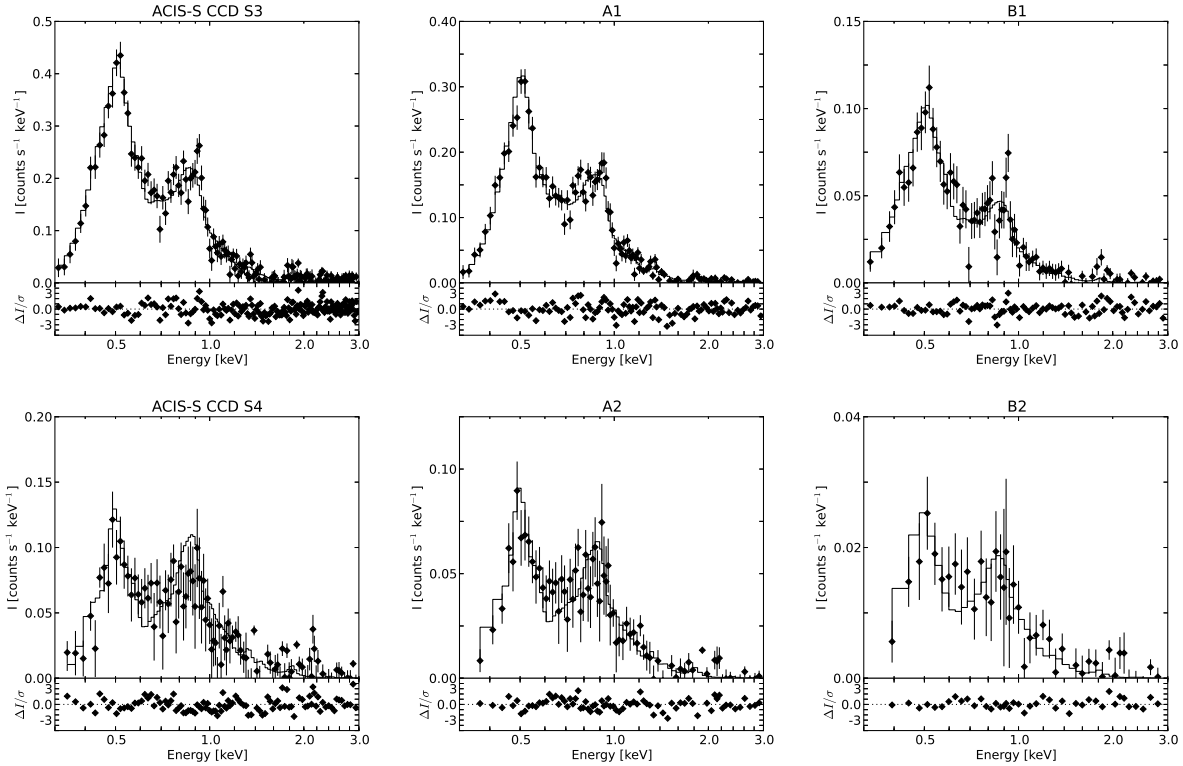

Figure 4.4: Background-subtracted *Chandra* ACIS-S spectra of the NE (top panels) and western (bottom panels) regions of NGC 6888 over-plotted with their best-fit two-temperature *apec* model (solid lines) in the energy range of 0.3 – 3 keV.

range, where absorption is high and the instrument sensitivity is low. Therefore, we fixed the value of the carbon abundance to its solar value. Finally, all spectra were modeled with varying nitrogen abundance (X_N) as the prominent N VII line at 0.5 keV seems to suggest a possible nitrogen enrichment of the X-ray-emitting plasma.

The simulated two-temperature *apec* model spectra obtained were absorbed by the interstellar hydrogen column of 3.13×10^{21} cm^{-2} implied by optical measurements (Hamann et al., 1994). This is the same value used by previous authors (Wrigge et al., 1994, 2005) which was found to be uniform throughout NGC 6888 by Wendker et al. (1975). Models with variable columnar density N_H were also attempted. The absorption column density showed a correlation with the temperature of the main plasma component (T_1), with values 2–4×10^{21} cm^{-2} which is adopted here and is consistent with the value used by Zhekov & Park (2011).

The resultant model spectra were compared with the observed spectra in the 0.3 - 3 keV energy range and the χ^2 statistics was used to determine the best-fit models. A minimum of 60 counts per bin was required for the spectral fit. The plasma temperatures (kT_1, kT_2) with 1σ

uncertainties, normalization factors[1] (A_1, A_2), and nitrogen abundance (X_N) of the best-fit models are listed in Table 4.1. Fluxes and luminosities listed in this table have been computed for the energy range 0.3-2.0 keV. The best-fit models are over-plotted on the background-subtracted spectra, together with the residuals of the fits as solid lines in Figure 4.4.

4.4.1.1 Properties of the NE X-ray Emission

The parameters of the best-fit model of the NE quadrant of NGC 6888 are listed in Table 4.1 as CCD S3. The model presents a low-temperature component of 1.6×10^6 K and a second component of 7.8×10^6 K with an observed flux ratio, $f_1/f_2 \sim 3$, corresponding to an intrinsic flux ratio $F_1/F_2 \sim 14$. The total observed flux in the 0.3–2 keV energy band is $(6.4^{+0.1}_{-0.2}) \times 10^{-13}$ erg cm^{-2} s^{-1} while the total unabsorbed flux is $(8.0^{+0.4}_{-0.2}) \times 10^{-12}$ erg cm^{-2} s^{-1}. The nitrogen abundance of the best-fit model is ≈5.3 times that of the solar value.

In the case of the resultant spectra from regions A1 and B1, the temperatures are consistent with those obtained from the whole region, $T_1 = 1.6 \times 10^6$ K and $T_2 = 7.9 \times 10^6$ K for region A1, and $T_1 = 1.4 \times 10^6$ K and $T_2 = 7.7 \times 10^6$ K for region B1, respectively. Their nitrogen abundances are 5.3 and 3.7 times the solar value for A1 and B1, respectively.

4.4.1.2 Properties of the Western X-ray Emission

The background-subtracted X-ray spectra from the western regions of NGC 6888 are shown in the lower panels of Figure 4.4, which correspond to the total diffuse emission detected by the CCD S4 (left), the emission from the rim registered by region A2 (middle), and the emission from inside the WR nebula registered by region B2 (right). The parameters of the best-fit models overplotted to these spectra are presented in Table 4.1. We remark that the fits of these spectra failed to constrain accurately the nitrogen abundance[2], and therefore we fixed its value to that found for the spectrum of the CCD S3.

The model of the X-ray-emitting plasma detected in the western regions of NGC 6888 (the ACIS CCD S4 spectrum) has a lower dominant temperature of 1.2×10^6 K with a second component of 7.4×10^6 K. The total observed flux is $(8.8 \pm 0.8) \times 10^{-13}$ erg cm^{-2} s^{-1}, while the unabsorbed flux is $(1.5 \pm 0.3) \times 10^{-11}$ erg cm^{-2} s^{-1}, with an unabsorbed flux ratio of $F_1/F_2 \sim 31$.

The resultant spectra from A2 and B2 are consistent from that obtained for the total spectrum extracted from CCD S4. $T_1 = 1.2 \times 10^6$ K and $T_2 = 7.4 \times 10^6$ K for region A2, and $T_1 =$

[1] $A = 1 \times 10^{-14} \int n_e n_H dV / 4\pi d^2$, where d is the distance, n_e is the electron density , and V the volume in cgs units.

[2] At first glance, this may seem perplexing because the CCD S4 and B2 spectra have larger total count numbers than the B1 spectrum from CCD S3 which could be used instead to derive the nitrogen abundance. The cause of this apparent conflict originates in the reduced sensitivity of the front-illuminated (FI) CCD S4 at ~0.5 keV, the energy of the N VII line, which is a few times smaller than that of the back-illuminated (BI) CCD S3. This is clearly illustrated by the differing shapes of the spectra detected by the BI CCD S3 and the FI CCD S4 (Figure 4.4). As a result, the FI CCD S4 detects a count number at the N VII line which is insufficient for a reliable estimate of the nitrogen abundance.

1.4×10^6 K and $T_2 = 7.5 \times 10^6$ K for region B2[3]. The unabsorbed flux ratios are F_1/F_2 ~35 and ~ 26 for A2 and B2, respectively.

4.4.2 Global Properties of the hot gas in NGC 6888

To assess the global properties of the hot gas in NGC 6888, we have derived the parameters of the two-temperature plasma emission model that best describes the total X-ray emission detected by *Chandra*. The CCD S3 and CCD S4 spectra have been fitted simultaneously using the same hydrogen column density and plasma parameters (kT_1, kT_2, $X_{\rm N}$). The results of this joint fit are given in Table 4.1 as CCD S34. The normalization factor of the cold thermal component of both spectra ($A_1^{\rm S3}$, $A_1^{\rm S4}$) were obviously allowed to vary to account for the different volume emission measure of hot gas mapped by each detector. The ratio between the normalization factors of the cold and hot components was also allowed to vary, but it was kept the same for both spectra ($A_2^{\rm S3}/A_1^{\rm S3} \equiv A_2^{\rm S4}/A_1^{\rm S4} \equiv A_2^{\rm S34}/A_1^{\rm S34}$), i.e., it was assumed that the relative contribution of both components of the X-ray-emitting plasma is the same across the nebula. The values of the normalization factors listed for this fit have been obtained by adding the normalization factor of each component for the CCD S3 and CCD S4 spectra ($A_1^{\rm S34} = A_1^{\rm S3} + A_1^{\rm S4}$, $A_2^{\rm S34} = A_2^{\rm S3} + A_2^{\rm S4}$). The temperature of the two components of this model, T_1 =1.4×10^6 K and T_2 =7.4×10^6 K, are enclosed within those obtained for the CCD S3 and S4 spectra. For comparison with all regions, we show in Figure 4.5 the temperature distribution obtained from our fits for the different regions. Accounting for the uncertainties, there is a good agreement for the temperature components of the different regions.

The total observed flux is $f_{\rm X} = (1.5 \pm 0.2) \times 10^{-12}$ erg cm^{-2} s^{-1}, which corresponds to an unabsorbed flux of $F_{\rm X} = (2.5 \pm 0.3) \times 10^{-11}$ erg cm^{-2} s^{-1}. The comparison between *ROSAT* PSPC and *Chandra* ACIS images indicates that the latter includes $\simeq$ 62 % of the total X-ray flux of NGC 6888. With this we can estimate a total X-ray intrinsic flux of $F_{\rm X,TOT} = (4.05 \pm 0.5) \times 10^{-11}$ erg cm^{-2} s^{-1}. Adopting a distance of 1.26 kpc, the total X-ray luminosity of NGC 6888 in the 0.3-2.0 keV energy range is $L_{\rm X} = (7.7 \pm 0.1) \times 10^{33}$ erg s^{-1}.

To proceed to the calculation of the electron density and mass of the X-ray-emitting plasma in NGC 6888 we need to adopt a geometrical model for the nebula in order to estimate the volume occupied by the hot plasma. It is tempting to assume an ellipsoidal geometry, as suggested by the Hα images, however the *Chandra* ACIS-S and *ROSAT* PSPC observations of NGC 6888 have disclosed emission external to the Hα shell, just inside the [O III] skin (see Figure 4.2), that implies a different physical structure. Fernández-Martín et al. (2012) describe a simple morphology for NGC 6888 where an ellipsoidal cavity has been carved inside the almost spherical outer optical shell. We can estimate lower and upper limits of the electron density of the X-ray-emitting gas by adopting spherical and ellipsoidal geometries, respectively. For the spherical model, we have

[3]Due to the low count number of the B2 spectrum, the temperature of the hottest component in this region could not be fitted. Consequently, the temperature of this component was fixed at 0.65 keV.

Table 4.1: Spectral Fits of the Diffuse X-ray Emission from NGC 6888

Region	Counts	$X_{\rm N}$	kT_1 (keV)	A_1 ($\rm cm^{-5}$)	f_1 (erg $\rm cm^{-2}$ $\rm s^{-1}$)	F_1 (erg $\rm cm^{-2}$ $\rm s^{-1}$)	kT_2 (keV)	A_2 ($\rm cm^{-5}$)	f_2 (erg $\rm cm^{-2}$ $\rm s^{-1}$)	F_2 (erg $\rm cm^{-2}$ $\rm s^{-1}$)	F_1/F_2	χ^2/DoF
CCD S3	14000±250	$5.3^{+0.7}_{-0.7}$	$0.140^{+0.003}_{-0.003}$	6.1×10^{-3}	4.7×10^{-13}	7.5×10^{-12}	$0.67^{+0.04}_{-0.03}$	1.7×10^{-4}	1.7×10^{-13}	5.2×10^{-13}	14.4	1.5=170.3/109
A1	10250±200	$5.3^{+0.9}_{-0.9}$	$0.140^{+0.008}_{-0.005}$	3.9×10^{-3}	3.2×10^{-13}	5.0×10^{-12}	$0.68^{+0.02}_{-0.05}$	1.2×10^{-4}	1.2×10^{-13}	3.7×10^{-13}	13.6	1.6=173.5/105
B1	3300 ±120	$3.7^{+1.3}_{-1.0}$	$0.117^{+0.012}_{-0.007}$	3.2×10^{-3}	1.2×10^{-13}	2.5×10^{-12}	$0.66^{+0.08}_{-0.08}$	3.9×10^{-5}	3.9×10^{-14}	1.2×10^{-13}	20.7	1.1=93.0/89
CCD S4	4700±350	5.0	$0.101^{+0.020}_{-0.008}$	2.7×10^{-2}	7.0×10^{-13}	1.5×10^{-11}	$0.64^{+0.07}_{-0.07}$	1.8×10^{-4}	1.8×10^{-13}	4.7×10^{-13}	30.9	1.5=136.6/90
A2	3200±150	5.0	$0.100^{+0.018}_{-0.008}$	2.2×10^{-2}	5.5×10^{-13}	1.4×10^{-11}	$0.64^{+0.08}_{-0.08}$	1.4×10^{-4}	1.3×10^{-13}	4.2×10^{-13}	34.5	1.9=115.9/59
B2	1550±100	5.0	$0.118^{+0.043}_{-0.028}$	3.4×10^{-3}	1.5×10^{-13}	3.1×10^{-12}	0.65	3.8×10^{-5}	3.8×10^{-14}	1.2×10^{-13}	25.7	0.6=20.13/31
CCD S34	...	$4.0^{+0.5}_{-0.6}$	$0.118^{+0.005}_{-0.004}$	3.1×10^{-2}	1.1×10^{-12}	2.4×10^{-11}	$0.64^{+0.04}_{-0.03}$	3.6×10^{-4}	3.5×10^{-13}	1.1×10^{-12}	22.2	1.5=308.1/196

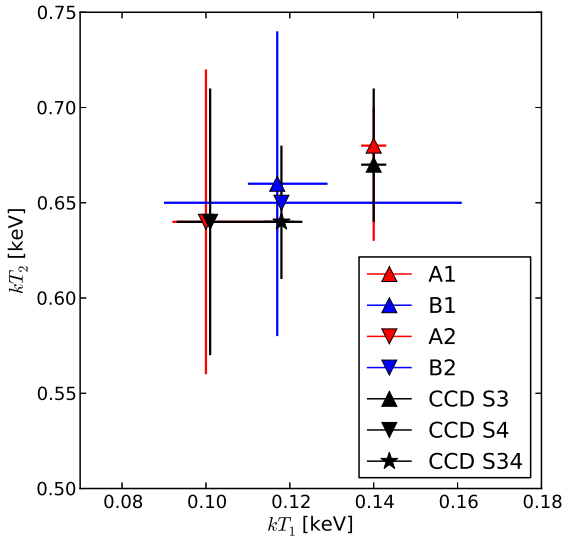

Figure 4.5: Plot of the temperatures of the cold and hot plasma components for the different spatial regions defined for the analysis of NGC 6888. The inset shows a chart of the correspondence between symbols and spatial regions, where the star marks the location of the temperatures derived from the joint fit CCD S34.

adopted a radius of $9'$ to obtain an rms electron density of $n_{\rm e} = 0.4(\epsilon/0.1)^{-1/2}$ cm^{-3}, implying a mass of the X-ray-emitting gas of $m_{\rm X} = 1.7(\epsilon/0.1)^{1/2}\ M_{\odot}$, where ϵ is the gas filling factor. For the ellipsoidal case, we have assumed semiaxes of $9'$, $6'$, and $6'$ to obtain an rms electron density of $n_{\rm e} = 0.6(\epsilon/0.1)^{-1/2}$ cm^{-3} and a mass of the X-ray-emitting gas of $m_{\rm X} = 1.2(\epsilon/0.1)^{1/2}\ M_{\odot}$.

4.5 Discussion

4.5.1 Comparison with previous X-ray studies

All previous X-ray analyses of the diffuse X-ray emission from NGC 6888 agree on the presence of a main plasma component with a temperature $\simeq 1.4\times10^6$ K consistent with that reported in our analysis of the *Chandra* ACIS data. As for the hot component, there are notable discrepancies: Wrigge et al. (1994) did not find evidence of this hot component using *ROSAT* PSPC data, Wrigge et al. (2005) found a hot component with a temperature marginally higher by $\simeq$13% than ours using *ASCA* SIS observations, and Zhekov & Park (2011) reported a second temperature component significantly hotter than ours, $kT \geqslant 2$ keV, using *Suzaku* XIS data. The lack of hot component in the *ROSAT* PSPC data can be attributed to the low sensitivity of this instrument to energies above 1.0 keV. On the other hand, the high temperature for the secondary component reported by Zhekov & Park (2011) originated on the high level of X-ray emission in the range 1.5-4.0 keV found in the *Suzaku* XIS data. The lack of such a hard component in the spectra derived

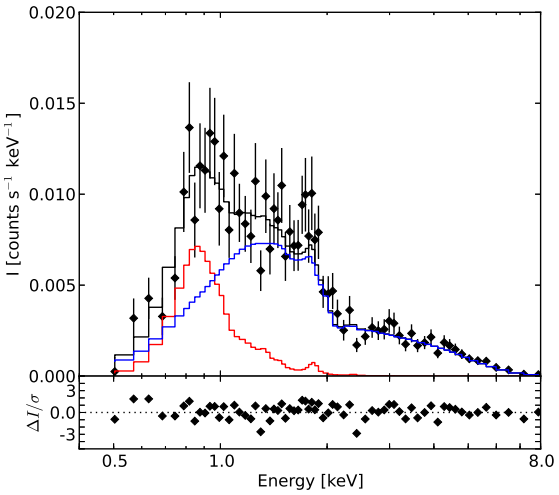

Figure 4.6: (top panel) Background-subtracted spectrum of point sources projected onto the nebula NGC 6888 in the *Chandra* ACIS-S3 detector overplotted with the best-fit model (black histogram) consisting of an absorbed *apec* (red histogram) and a power law (blue histogram) model. See text for details. (Bottom panel) Residuals of the spectral fit.

from the *Chandra* ACIS observations is in sharp contrast with the *Suzaku* XIS data. We present in Figure 4.6 the combined spectrum of point sources projected onto the nebula in the ACIS-S3 detector. The spectrum of the point sources is clearly harder than that of the nebula and shows significant emission above 0.8 keV up to 5-7 keV. Its count rate is 0.0188~0.0005 counts s^{-1}, i.e., ~12% that of the nebular ACIS-S3 region. This emission can be formally fitted using an absorbed model[4] comprising an optically-thin plasma emission component at a temperature of (7.7±1.0)×10^6 K and a power-law component with photon index Γ=1.16±0.08 for a reduced χ^2 of 62.30/63=0.99. The flux of this emission in the 0.3-2.0 keV is (4.1±0.3)×10^{-14} erg cm^{-2} s^{-1}, i.e., it acounts for 6% of the nebular flux measured in the ACIS-S3 spectrum in this band. The total flux in the 0.3-9.0 keV of this component is (2.46±0.24)×10^{-13} erg cm^{-2} s^{-1}. These results demonstrate that the hard, 1.5-4.0 keV component detected by *Suzaku* is an observational artifact caused by its limited spatial resolution (~2′), which makes difficult to identify point sources in the field of view of NGC 6888 and to excise their contribution from the diffuse emission.

The first observations of the X-ray emission toward NGC 6888 reported absorbed fluxes ~10^{-12} erg cm^{-2} s^{-1} (e.g., Bochkarev, 1988; Wrigge et al., 1994, 2005) that were raised up to ~2×10^{-12} erg cm^{-2} s^{-1} by the more recent *Suzaku*'s observations (Zhekov & Park, 2011). Our estimate for the observed flux (2.4 × 10^{-12} erg cm^{-2} s^{-1}) is in good agreement with the latest measurements despite that a fraction of the nebula was not registered by the ACIS-S detectors

[4] For consistency with the spectral fit of the nebular emission from NGC 6888, we have adopted a hydrogen column density of 3.1×10^{21} cm^{-2}.

and we had to rely on *ROSAT* PSPC observations to estimate the total flux. Sensitive observations with a large field of view, as those that would be provided by *XMM-Newton*, are most needed to search for the fainter and more extended X-ray emission in this WR nebula.

Our *Chandra* ACIS-S observation yielded the detection of three peaks in the spatial distribution of the diffuse X-ray emission in NGC 6888: two associated with the caps, and another one toward the NW blowout at the western edge of the ACIS-S field of view in CCD S4. The latter peak in the X-ray emission is hinted in *ROSAT* PSPC and HRI, and *ASCA* SIS observations (Wrigge et al., 1994; Wrigge & Wendker, 2002; Wrigge et al., 2005), but it has not been reported previously to be part of the X-ray-emitting gas associated with the nebula[5]. This additional emission component is located in a region with no Hα counterpart (see Figure 4.2; Gruendl et al., 2000), but it is spatially delineated by the [O III] outer shell. The situation is reminiscent of the northwest blowout in S 308, which can be ascribed to the action of the hot gas carving a cavity towards a low density region of the circumstellar medium (CSM; Chu et al., 2003a; Toalá et al., 2012).

In contrast to the limb-brightened morphology of the X-ray-emitting gas reported for S 308 (Toalá et al., 2012), the current (and previous) X-ray observations of NGC 6888 do not show such a simple morphology, but that the hot gas is distributed in (at least) three maxima. The comparison between infrared images of NGC 6888 and that obtained by *ROSAT* PSPC of the X-ray-emitting gas (see Figure 4.7) is suggestive of a correlation between the regions where the X-ray emission is faintest, toward the southeast region of NGC 6888, and a molecular filament traced in infrared wavelengths. Spatial variations of the amount of intervening material across the nebula, not accounted so far, can be playing an interesting role in the X-ray morphology of NGC 6888.

Finally, it is worth mentioning here that the apparent nitrogen overabundances are still consistent with the values reported by Fernández-Martín et al. (2012) in their region X1. This region is spatially coincident with one of the brightest clumps in the X-ray-emitting region.

4.5.2 Comparison with simulations

There have been several attempts in the past to model the morphology and X-ray emission from NGC 6888 revealed by *ROSAT*, *ASCA*, and *Suzaku* observations. One-dimensional (1D) analytic or hydrodynamic models are an elegant first approximation to the evolution of the CSM of WR stars (e.g., Zhekov & Perinotto, 1998), although they do not include the effects of ionization due to the central star, neither can they reproduce the wealth of structures produced by hydrodynamical instabilities, which seem to trace the X-ray-emitting gas in some regions inside the bubble. Furthermore, those simulations are not able to reproduce simultaneously regions in which instabilities are important (e.g., the caps) and regions where there are no clumps (the blowout). García-Segura et al. (1996b) presented 2D hydrodynamical simulations of the evolving medium

[5]The *Suzaku* observations did not map this nebular region, which was not registered by its detectors.

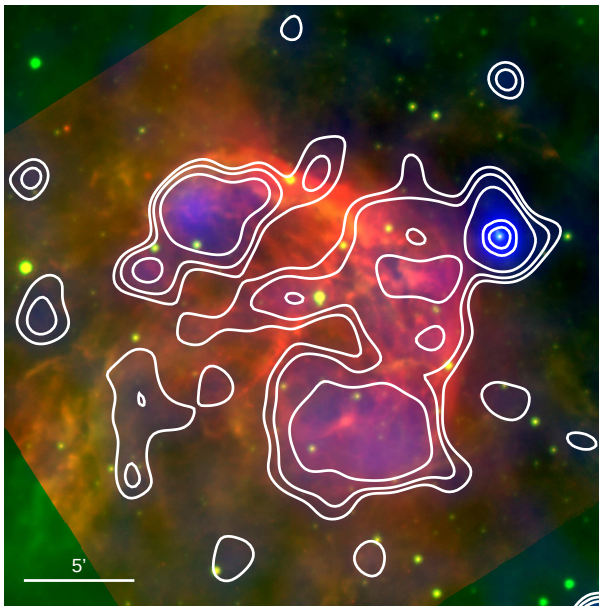

Figure 4.7: *Spitzer* MIPS 24 μm (red), *WISE* 12 μm (green), and *ROSAT* PSPC (blue and contours) colour-composite picture of NGC 6888.

around a star with an initial mass of 35 $M_{\odot}$. The broad morphological properties of NGC 6888 could be reproduced adopting a slow RSG wind of 15 km s^{-1}. These simulations were refined by Freyer et al. (2006) who included the effects of photoionization. Despite the progress achieved by the 2D radiative hydrodynamic models published to date, which have helped us advance our understanding of the formation of NGC 6888, they fail to produce blowout-like features. Blowouts might result from anisotropies in the RSG or non uniformities in the interstellar medium. Simulations recently presented by Rogers & Pittard (2013) explore the evolution of a non uniform initial interstellar medium around massive stars. Specific modeling accounting for these features are needed to understand the morphology and distribution of the X-ray-emitting gas in NGC 6888.

It is often argued that thermal conduction between the cold (10^4 K) outer RSG material and the inner hot ($10^7 - 10^8$ K) bubble causes the temperature of the hot bubble to drop to the observed values of T_X ~10^6 K (e.g., Arthur, 2007a; Pittard, 2007; Zhekov & Perinotto, 1998). Toalá & Arthur (2011) recently presented numerical models including conductive effects (classical and saturated thermal conduction) of WR bubbles that result in a wide range of temperatures capable of generating the soft X-ray emission observed in NGC 6888. Indeed, they present a spectrum corresponding to a nitrogen-rich plasma that shows two main components, one at 0.5 keV and another at ~0.9 keV, very similar to the spectra presented in Figure 4.4 (see also Dwarkadas & Rosenberg, 2013, for a comparison with models without thermal conduction).

Finally, it is interesting to check whether the central star of NGC 6888 can provide the observed X-ray-emitting material. García-Segura et al. (1996b) could match the morphology of

their 2D simulations with that of NGC 6888 at a time ~12,000 yr after the onset of the WR phase. That time-lapse is further reduced to ~8,000 yr when the dynamical effects on the nebular material of the photoionization are accounted (Freyer et al., 2006). For a mass-loss rate of 3.1×10^{-5} $M_\odot$ yr^{-1} (Abbott et al., 1986), the total mass provided by the star amounts up to 0.25–0.37 $M_\odot$, which is smaller than the estimate of >1 $M_\odot$ for the mass of hot plasma inside NGC 6888. Apparently, the WR wind has not had sufficient time to inject all the hot gas inside NGC 6888. This supports the possibility that physical processes such as thermal conduction have transferred material from the outer RSG shell into the hot bubble. The enhanced N/O ratio of the hot plasma, similar to that measured in the cold shell through optical emission lines, is in concordance with this possibility.

4.6 Summary and conclusions

We present *Chandra* ACIS-S observations of the NE quadrant and western regions of NGC 6888. We have used these observations to study the spatial distribution of the diffuse X-ray emission inside the nebula and derived global values of its physical conditions. In particular we find:

- The hot gas in NGC 6888 is distributed inside the optical shell delineated by [O III] emission. The spatial distribution of the X-ray emission shows enhancements towards the caps and a blowout present in the NW region of NGC 6888. This blowout, not discussed in previous studies, has no Hα counterpart, but an outer *skin* of [O III] is detected. The X-ray-emitting gas is, thus, traced by Hα clumps inside the nebular shell and by the blowout. No clear evidence of limb-brightening is detected.

- The X-ray emission is dominated by the N VII 0.5 keV line with additional contributions of the Fe complex and Ne IX line at 0.7–0.9 keV. The spectrum declines with energy, fading at energies higher than 1.5 keV. The X-ray emission from NGC 6888 can be described by a two-temperature optically thin plasma emission model with temperatures of $\sim1.4\times10^6$ K and 7.4×10^6 K.

- The intrinsic total flux emitted by NGC 6888 in the 0.3-2 keV energy band is estimated to be $\sim(4.05\pm0.5)\times10^{-11}$ erg cm^{-2} s^{-1}, and the X-ray luminosity at a distance of 1.26 kpc is $L_{\rm X}=(7.7\pm0.1)\times10^{33}$ erg s^{-1}.

- The estimated rms electron density $n_{\rm e}$ of the X-ray-emitting gas ranges between $0.4\times(\epsilon/0.1)^{-1/2}$ and $0.6\times(\epsilon/0.1)^{-1/2}$ cm^{-3} resulting in an estimated total mass of $1.7\times(\epsilon/0.1)^{1/2}\,M_\odot$ and $1.2\times(\epsilon/0.1)^{1/2}\,M_\odot$, respectively. The density, temperature, and abundance of the X-ray-emitting gas are consistent with the expectation of thermal conduction at the wind-wind interaction zone, where the RSG wind material is mixed in the shocked WR wind in the bubble interior.

Future *XMM-Newton* observations are needed to acquire a complete view of the soft X-ray emission from the hot plasma in NGC 6888 with better spatial coverage, sensitivity, and energy resolution than the existing studies. As the blowout detected in NGC 6888 is at the edge of the cameras of the ACIS-S instrument and a significant section of the bubble remains unobserved, *XMM-Newton* observations could finally unveil the total distribution of the hot gas in this nebula. The soft sensitivity and spatial coverage of such observations would also be very valuable to assess the varying amounts of intervening material across the nebula suggested by optical and infrared observations.

CHAPTER 5

XMM-Newton RGS VIEW OF NGC 6543

We present the analysis of XMM-Newton *observations of the Cat's Eye (NGC 6543) planetary nebula (PN). These observations consist of 26 Reflection Grating Spectrometer (RGS) individual pointings. Although many of these observations were severely affected by high-background energy levels, we have been able to detect emission lines in the RGS spectra from highly ionized species of carbon, nitrogen, and oxygen (C* V*, C* VI*, N* VI*, N* VII*, and O* VII*), whereas other weak lines, as that of Ne* VIII*, can be hinted. This makes NGC 6543 the second PN with high resolution spectroscopy observations apart from BD +30°3639. We conclude that the main features in the RGS spectrum of NGC 6543 can be reproduced by the emission of a plasma with a temperature of* 1.2×10^6 *K (kT=0.10 keV) and abundances similar to those of the central star.*

5.1 Introduction

Since the first discovery of X-ray emission toward NGC 1360 (de Korte et al., 1985), a number of works addressing the X-ray emission in planetary nebulae (PNe) have been published (Guerrero et al., 2000, and references therein). The study of this X-ray emission has taken a strong leap after the advent of *Chandra* and *XMM-Newton* (see Kastner et al., 2012; Ruiz et al., 2013, and references therein). It is now known that the source of this X-ray emission may be twofold, as X-ray emission may arise from a point-like source associated to the central star in the PN (CSPN) or from a diffuse source produced by hot plasma filling the inner cavity. The physics behind the X-ray emission associated to the CSPN is still a matter of discussion, as may be due to binarity (via accretion onto a companion) or shocks originated in the winds as those observed in massive hot stars (Guerrero & De Marco, 2013, Montez et al. in prep.).

The case of diffuse X-ray emission in PNe was actually expected: the fast wind developed in the post-asymptotic giant branch (AGB) sweeps up the previous slow and dense AGB wind

(Balick, 1987; Kwok et al., 1978). This material is adiabatically shocked and produces a hot and diffuse cavity of gas (the so-called hot bubble) whose temperature depends on the terminal wind velocity as $T \sim V_{\infty}^{2}$ (Dyson & Williams, 1997). Since the terminal wind velocities are high, of several thousands km s^{-1} (Patriarchi & Perinotto, 1991), hot bubbles with temperatures higher than 10^8 K can be expected. X-ray observations of PNe seem to show otherwise, as their diffuse X-ray emission is best described by optically-thin plasma emission models with temperatures $\approx 10^6$ K. Obviously, some extra physical effects are taking place into lowering the temperature of material within the hot bubble. Material from the AGB shell must have been injected into the hot bubble via either thermal conduction (e.g., Soker, 1994; Steffen et al., 2008) and/or hydrodynamical mixing at the wind-wind interaction (Toalá & Arthur 2014).

Most of the properties of the diffuse X-ray emission from PNe have been derived from low-resolution CCD spectroscopy. High-dispersion spectroscopic observations revealing individual emission lines are available only for one PN, BD +30°3639 (Yu et al., 2009). The advantages of this observing technique are obvious, but it is restricted to sources with high X-ray photon fluxes untypical of PNe. After BD +30°3639, the next PN in line by its flux is NGC 6543 (aka the Cat's Eye Nebula).

The Cat's Eye nebula was first reported to emit in X-rays by Kreysing et al. (1992) using *ROSAT* All Sky Survey data, but many questions remained unsolved. In particular, *ROSAT*'s low spatial resolution could not determine whether the X-ray emission originated from the photosphere of the central star or from a hot bubble. By comparing the X-ray emission in the Cat's Eye with that of other PNe detected by *ROSAT*, Guerrero et al. (2000) concluded that this X-ray emission could be modeled by an optically thin emission plasma model of a few times 10^6 K. Nevertheless, the diffuse X-ray emission remained spatially unresolved. With the superb angular resolution of the *Chandra* X-ray satellite, Chu et al. (2001) reported that the X-ray emission can be resolved into a point-like emission associated to the central star (CSPN) and a diffuse component within the central cavity. After excising the emission of the central point-like source, the diffuse emission was modeled with an optically thin plasma with stellar wind abundances, i.e., with a N/O ratio three times its solar value, and a plasma temperature $\sim 1.7\times10^6$ K absorbed by a hydrogen column density of $N_{\rm H}$=8×10^{20} cm^{-2}. The revision of the nebular abundances by Bernard-Salas et al. (2003) made Maness & Vrtilek (2003) suggest that the nebular abundances could represent those of the X-ray-emitting material.

The definition of the physical conditions and chemical abundances of the hot gas in NGC 6543 can benefit from high-dispersion X-ray observations. In this chapter we report our *XMM-Newton* Reflection Grating Spectrometer (RGS) observations of NGC 6543. The observations are presented in § 2, the results and their discussion in § 3, and the conclusions in § 4.

Table 5.1: *XMM-Newton* observations details

Label	Observation ID.	Rev.	Total exposure times					Net exposure times				
			MOS1 (ks)	MOS2 (ks)	pn (ks)	RGS1 (ks)	RGS2 (ks)	MOS1 (ks)	MOS2 (ks)	pn (ks)	RGS1 (ks)	RGS2 (ks)
A	0300570101	1143	16.4	16.3	4.9	20.1	20.1	9.8	11.4	2.2	17.9	7.3
B	0300570201	1144	0.3	0.3	8.1	22.5	23.3	0.07	0.04	2.7	4.1	2.5
C	0300570301	1145	21.8	21.8	7.8	22.3	22.2	9.6	6.6	1.7	19.0	16.8
D	0300570401	1146	18.5	18.5	7.2	18.9	18.1	11.8	13.4	4.3	9.4	6.5
E	0300570601	1141	14.4	14.4	5.5	10.9	11.1	4.8	5.7	2.3	6.1	5.9
F	0300570701	1141	5.6	5.6	3.6	...	...	5.6	4.6	2.9	...	...
G	0300570801	1142	13.8	13.8	7.1	14.3	14.1	10.4	10.7	5.3	10.9	5.3
H	0300570901	1142	5.5	5.6	3.5	...	...	4.6	4.3	3.0	...	...
I	0300571001	1143	6.1	6.1	4.0	...	...	5.2	4.2	3.4	...	...
J	0300571101	1144	5.6	5.6	3.4	...	...	5.2	4.4	2.9	...	...
K	0300571201	1145	6.6	6.6	4.4	...	...	6.1	5.1	3.0	...	...
L	0300571301	1146	3.6	3.6	...	...	...	3.0	2.5	...	...	...
M	0300571501	1161	21.1	21.1	12.3	21.6	21.6	16.6	18.4	9.4	17.6	13.9
N	0300571701	1149	0.02	0.02	...	10.4	10.4	0.02	0.01	...	6.2	3.1
O	0300571801	1149	7.3	7.3	5.1	...	...	4.8	6.2	4.0	...	...
P	0300571901	1151	20.9	20.9	12.6	19.9	19.9	16.4	16.9	8.5	18.8	16.6
Q	0300572001	1151	7.1	7.1	4.9	...	...	4.0	4.3	2.5	...	...
R	0300572101	1160	0.2	0.2	0.2	12.9	12.8	...	...	...	5.4	5.4
S	0300572201	1160	8.9	8.9	6.5	...	...	5.4	4.4	3.6	...	...
T	0300572301	1161	9.4	9.4	7.0	...	...	8.7	7.0	5.0	...	...
U	0300572401	1162	0.2	0.2	0.3	13.4	13.4	...	...	...	7.3	8.1
V	0300572501	1162	9.5	9.5	7.1	...	...	7.1	6.0	2.9	...	...
W	0300572601	1163	2.3	2.3	6.5	14.5	7.9	1.5	1.6	0.9	6.8	2.2
X	0300572701	1163	9.5	9.5	7.0	...	...	5.7	5.3	3.5	...	...
Y	0300572801	1164	18.1	18.1	8.8	19.4	19.3	12.4	11.3	3.4	14.2	14.5
Z	0300572901	1164	9.4	9.4	7.0	...	...	9.3	9.0	0.09	...	...
TOTAL			242.1	242.1	144.8	365.9	214.2	168.1	159.1	77.5	143.7	108.1

5.2 *XMM-Newton* Observations

The *XMM-Newton* observations of NGC 6543 consisted of 26 individual pointings obtained on 2006 March and April (PI: M.A. Guerrero). For simplicity, we labeled each observation with letters from A to Z. Details of the different observations are listed in Table 5.1. The European Photon Imaging Camera (EPIC) was used for all of them, but the RGS were not used in the observations labeled as F, H, I, J, K, L, O, S, T, V, X, and Z, although these are kept in Table 5.1 for completeness. In the following, we will focus our analysis in the RGS data.

The observations were reprocessed using the *XMM-Newton* Science Analysis Software (SAS) 13.5.0 with the *XMM-Newton* calibration files available on the Current Calibration File as on 2014 February 20. RGS event files were created using the SAS tool *rgsproc*. In order to identify and excise periods of high background from the observations, we created lightcurves in the 10–12 keV energy range for all RGS observations. An inspections of these lightcurves showed that most of the observations suffered from high background levels as a result of the visibility window of NGC 6543 being close to the satellite orbit perigee. Indeed, some observations did not make use of some of the five instruments (MOS1, MOS2, pn, RGS1, and RGS2) as the result of high

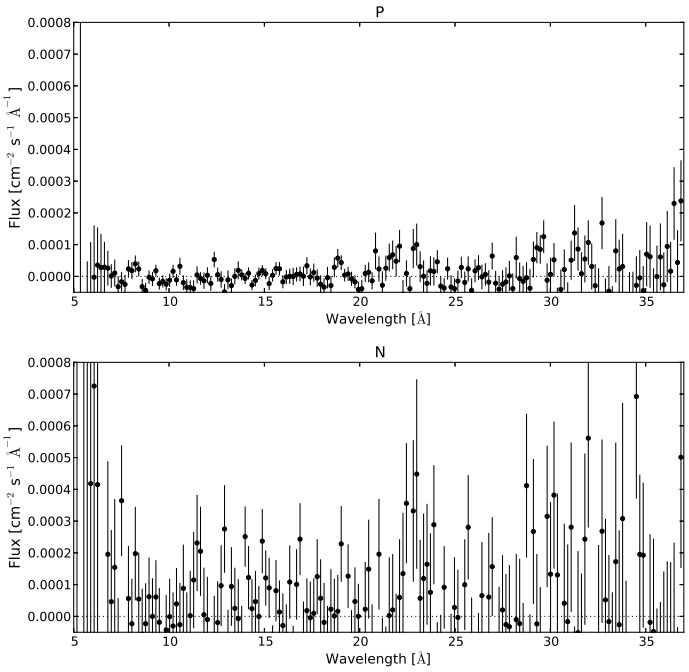

Figure 5.1: Background-subtracted individual RGS spectra. The top panel shows an example of the good quality RGS spectrum derived from observation P ($t_{\rm net}$ = 35.4 ks), whereas the bottom panel represents the bad quality RGS spectrum obtained from observation N ($t_{\rm net}$ = 9.3 ks).

levels of background emission. To clean the observations, we determine the basal level of each background lightcurve and its 1-σ deviation, and excluded those time intervals with background count rates above 3-σ over this basal level. The total and net exposure times after processing are listed in Table 5.1, confirming that the high background levels severely affected the net exposure time; the total RGS1+RGS2 exposure time, 580.1 ks, is reduced to a net exposure time of 251.8 ks, which is ≈43% the total exposure time.

show emission lines at different wavelengths correspondings to ionized species of carbon, nitrogen, oxygen, and probably neon.

5.3 Results and discussion

Each pair of RGS spectra (RGS1 and RGS2) has been used to create a combined background-subtracted spectrum corresponding to each observation with the SAS task *rgsfluxer*. The combined spectrum was requested to be binned into 100 channels. Good-quality spectra are those from observations A, C, D, E, G, M, P, R, and Y, whereas the remaining spectra have low quality. To illustrate the differences between good- and bad-quality spectra, we show two examples of these in Figure 5.1. The good-quality spectrum obtained from observation P (Figure 5.1-top panel) is rather flat, with a hint of emission lines around ~12, 19, 20–22, and ~30 Å. On the

other hand, the low-quality spectrum from observation N (Figure 5.1-bottom panel) is noisier and only the main features seen in spectrum P around ~22 Å can be hinted.

To achieve a better signal-to-noise, we have combined individual good-quality spectra. Figure 5.2 shows how the signal is recovered as more individual spectra are added into the final spectrum. The top panel shows the resultant spectrum obtained by combining the spectra corresponding from observations M and P. This spectrum does not show significant differences with that of the observation P alone (see Figure 5.1-top panel). Other panels in Figure 5.2 show different resultant spectra when adding more spectra, with the bottom panel showing the final, best-quality spectrum. This last spectrum was created by combining observations A, C, D, E, G, M, P, R, and Y, i.e., it has a net exposure time of 211.5 ks. This spectrum shows clearly the emission lines around ~20–22 Å, as that in spectrum of observation P, but the weak spectral features in the wavelength range between 10 and 20 Å, and at ~30 Åhave diminished their intensity.

The main features in all spectra, even in those classified as bad-quality spectra, are always those between 20-22 Å. These features may correspond to the N VII 20.9 Å line and the O VII triplet at 21.6, 21.8, and 22.1 Å. Other weaker lines that seem to be present are those of O VII 18.63 Å, C VI 26.35 Å, N VI 29.08 Å, and N VI 29.53 Å. Some spectra show hints of even weaker lines that can be identified as Ne VIII 12.46 and 13.56 Å, and C V 35.0 Å, but the latter line is almost at the high wavelength end of the spectrum where the sensitivity drops.

Some of the emission lines shown in the RGS spectrum of NGC 6543 are also present in the *Chandra* high resolution spectra of BD+30°3639 presented by Yu et al. (2009). The O VII triplet at ~22 Å is prominent both in BD+30°3639 and NGC 6543, but the brightest Ne IX 13.45 Å line in the former is completely absent in NGC 6543. These spectral variations imply notable differences in the physical conditions and/or chemical abundances of the X-ray-emitting plasma in these two PNe. To investigate the physical conditions and chemical abundances of the hot gas in NGC 6543, we have produced optically thin plasma emission models of the X-ray emission as it is detected by the RGS in the 7–37 Å spectral range. The RGS response matrices as computed using SAS v13.5.0 from the most recent calibrations found in `xmm2.esac.esa.int/external/xmm_sw_cal/calib/rgs_files.shtml` have been used for this purpose.

We initially created an optically thin plasma *apec* model with the chemical abundances, plasma temperature, and column density used by Chu et al. (2001) to fit the *Chandra* ACIS spectrum of NGC 6543. Namely, the column density of this model is $N_{\rm H}$=8×10^{20} cm^{-2}, the plasma temperature kT=0.147 keV (=1.7×10^{6} K), and the abundances of He and N are 60 and 3 times their solar values (Anders & Grevesse, 1989), respectively, and solar for the other elements. This model predicts a N VII 24.78 Å emission line much brighter than the N VI lines (Figure 5.3-dotted line), which is not supported by the observed RGS spectrum. This clearly indicates that the actual temperature of the plasma should be below 0.147 keV, which is also in line with the low O VIII/O VII line ratio.

Accordingly, several models with lower plasma temperatures, in the range 0.1–0.14 keV, and abundances N=2–3, O=1, and C=1 times their solar values were attempted (Figure 5.3-dashed line). These models fail to reproduce the intensity ratio of the O VII ~22 Å triplet and N VI 29.08,29.53 Å lines, $I_{\rm O\,VIII}/I_{\rm N\,VI}$ ~2, and overpredict the intensity of the otherwise weak or absent C VI 33.7 Å line. The most accurate model resulted in a plasma temperature of 0.1 keV (=1.2×10^6 K) and abundances N=1, O=1.0, and C=0.1 times their solar values (Figure 5.3-solid line).

The carbon abundance has to be reduced in order to diminish its contribution at 33.7 Å that does not appear in the observed spectrum. This model is plotted in the bottom panel of Figure 5.2 for comparison with the best RGS spectrum.

Compared to previous studies of the diffuse X-ray emission of NGC 6543 (Chu et al., 2001; Maness & Vrtilek, 2003), the plasma temperature derived from the RGS spectrum is lower as required by the low N VII/N VI and O VIII/O VII line ratios. Further discrepancies result from the determination of the abundances of carbon, nitrogen, and oxygen. These works suggest N/O ratios of $3\times N_\odot/O_\odot$ which seems consistent with the nebular abundances Bernard-Salas et al. (2003); Georgiev et al. (2008). Our N/O abundance ratio is more that six times greater than the values determined by those works ...

5.4 Conclusions

We presented *XMM-Newton* RGS observations towards the planetary nebula NGC 6543. The total exposure time for the RGS spectrometers (RGS1+RGS2) is 580.1 ks (see Table 5.1). Sadly, most of the observations were affected by high-energy background leaves that reduced the net exposure time to 251.8 ks.

We combined the RGS spectra that showed good quality after processing, i.e., those obtained from well-behave lightcurves and good signal-to-noise spectra. The best-quality RGS spectra show emission lines of highly ionized species of carbon, nitrogen, and oxygen: N VII 20.9 Å, N VI 29.08 Å, and N VI 29.53 Å, the O VII triplet at 21.6, 21.8, and 22.1 Å, O VII 18.63 Å, and C VI 26.35 Å. There seem to be some other weaker lines of Ne VIII 12.46 Å, Ne VIII 13.56Å, and C V 35.0 Å, but they are not firm detections. This is the second PN reported with high resolution spectroscopy observations apart from BD +30°3639 (Yu et al., 2009).

We initially modeled the spectrum detected by the RGS using an optically thin plasma model *apec* with parameters and abundances as those found by Chu et al. (2001). But we find that the emission line rations could be best modeled by a cooler plasma temperature of kT=0.1 keV(=1.2×10^6 K). Higher temperatures increase the intensity of the N VII emission line at 24.78 Å that is not present in the spectrum. The abundances that better reproduce our observed spectrum are helium, nitrogen, carbon, and oxygen of 60, 1.0, 1.0, and 0.1 times their solar values.

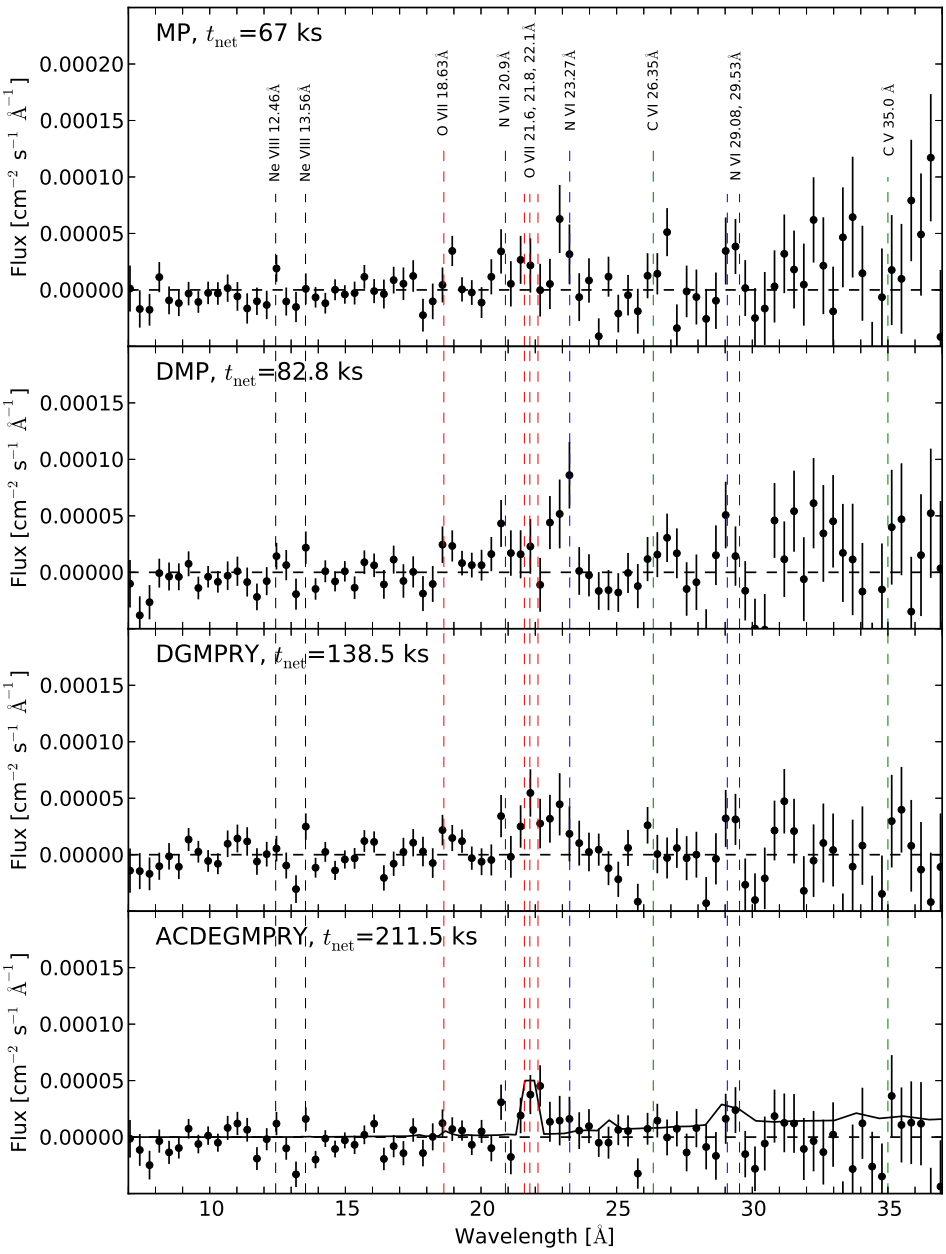

Figure 5.2: Combined background-subtracted RGS spectrum of NGC 6543. Each panel presents spectra obtained from combining the observations labeled on the upper-left corner with the corresponding net exposure time. The solid line in the bottom panel represents the best model that reproduces the lines features of the O VII triplet and N VI doublet at ~22 and 29 Å, respectively.

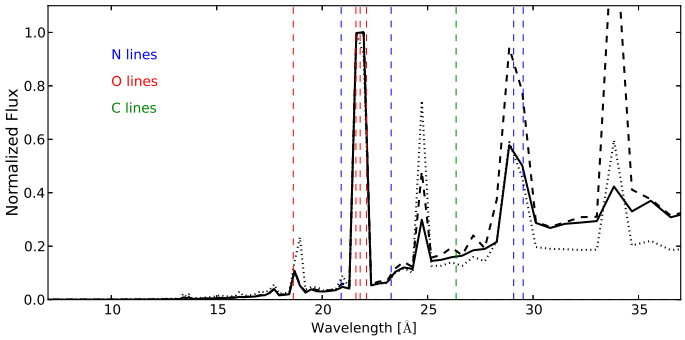

Figure 5.3: Synthetic RGS spectrum of optically thin plasma emission models. The solid line represents the best-fit model with plasma temperature kT=0.1 keV and 0.1×$C_\odot$, $N_\odot$, and $O_\odot$. The dashed line is a plasma model with temperature kT=0.1 keV and abundances $C_\odot$, 2×$N_\odot$, and $O_\odot$. Finally, the dotted line is a plasma model with kT=0.147 keV and abundances $C_\odot$, 3×$N_\odot$, and $O_\odot$. The intensity of each model has been normalized to that of the O VII triplet at 22 Å.

CHAPTER 6

THE BORN-AGAIN PLANETARY NEBULA A78: AN X-RAY TWIN OF A30

We present an XMM-Newton *discovery of X-ray emission from the planetary nebula (PN) A78, the second born-again PN detected in X-rays apart from A 30. These two PNe share similar spectral and morphological characteristics: They harbor diffuse soft X-ray emission associated with the interaction between the H-poor ejecta and the current fast stellar wind, and a point-like source at the position of the central star (CSPN). We present the analysis of the UV and optical spectra of the CSPN, using for the first time a NLTE code for expanding atmospheres which takes line blanketing into account. The obtained abundances are used for the X-ray spectral analysis of the CSPN and the diffuse emission. The X-ray emission from the CSPN in A78 can be modeled by a single C* VI *emission line, while the X-ray emission from its diffuse component is better described by an optically thin plasma emission model with temperature kT=0.11 keV ($T \approx 1.3\times10^6$ K). We estimate X-ray luminosities in the 0.2–2.0 keV energy band of $L_{\rm X,CSPN}=(3.8\pm0.6)\times10^{30}$ erg s^{-1} and $L_{\rm X,DIFF}=(2.0\pm0.1)\times10^{30}$ erg s^{-1} for the CSPN and diffuse components, respectively.*

6.1 Introduction

Born-again planetary nebulae (PNe) are thought to have experienced a *very late thermal pulse* (VLTP) when the central star (CSPN) was on the white dwarf (WD) track. The VLTP event occurs when the thermonuclear burning of hydrogen in the stellar envelope has built up a shell of helium with the critical mass to ignite its fusion into carbon and oxygen (Herwig et al., 1999; Lawlor & MacDonald, 2006; Miller Bertolami & Althaus, 2006; Miller Bertolami et al., 2006). As the WD envelope is shallow, the increase of pressure from this last helium shell flash leads to the ejection of newly processed material inside the old PN, leaving the stellar structure in-

tact. As the stellar envelope expands, its effective temperature decreases and the star goes back to the asymptotic giant branch (AGB) region in the HR diagram. The subsequent stellar evolution is fast and will return the star back to the post-AGB track in the HR diagram (e.g. Miller Bertolami et al., 2006): the envelope of the star contracts, its effective temperature and ionizing photon flux increase, and a new fast stellar wind develops.

The born-again phenomenon is rare, with A30, A58 (Nova Aql 1919), A78, and the Sakurai's object (V 4334 Sgr) the most studied objects of this class. These PNe harbor complex physical processes: the hydrogen-poor material ejected by the star during the born-again event will be photoevaporated by the ionizing photon flux from the CSPN and swept up by the current fast stellar wind (see discussion by Guerrero et al., 2012). These objects evolve very fast after the VLTP, thus, they provide a rare opportunity to study such complex phenomena and their evolution (e.g., Evans et al., 2006; Hinkle & Joyce, 2014; Hinkle et al., 2008).

Among these PNe, A30 and A78 share similar characteristics that suggest they are at a late stage after the born-again event. They exhibit large (~2′ in size) limb-brightened Hα outer shells that surround an ensemble of H-poor clumps that are prominent in [O III] narrow band images (Jacoby, 1979, see Figure 6.1). Their outer hydrogen shells are expanding at ~40 km s^{-1}, with kinematic evidence of ellipsoidal shape, while the H-deficient knots detected in [O III] have velocities up to 200 km s^{-1} (Meaburn & Lopez, 1996; Meaburn et al., 1998). The central parts in A30 and A78 were imaged in detail by the *Hubble Space Telescope* (*HST*; Borkowski et al., 1993). The *HST* WFPC2 [O III] images revealed cometary structures located in an equatorial plane distribution (a few arcsec from the star) with polar features, which, in the case of A78, are more diffuse and are located at ~12–14″ from its CSPN (see Figure 6.1-right panel).

X-ray emission has been detected within a number of PNe, including A30 (e.g., Guerrero et al., 2012; Kastner et al., 2012; Ruiz et al., 2013, and references therein). This born-again PN has been studied with *ROSAT* (PSPC and HRI), *Chandra*, and *XMM-Newton* X-ray satellites (Chu & Ho, 1995; Chu et al., 1997; Guerrero et al., 2012). X-ray emission is detected to originate from the CSPN, but there is also diffuse emission spatially coincident with the cloverleaf-shaped H-poor structure detected in [O III]. The X-ray emission from both the CSPN and the diffuse extended emission are very soft.

The X-ray properties of A30 and the similarities of this nebula to A78 motivated us to obtain *XMM-Newton* observations, as the only previous X-ray observations of A78 by *EINSTEIN* yielded a rather insensitive upper limit (Tarafdar & Apparao, 1988). In this chapter we present the analysis of new *XMM-Newton* observations that reveal the existence of hot gas associated with the H-poor knots inside the eye-shaped inner shell of A78, and also a point-like source of X-ray emission at its CSPN. The outline of this chapter is as follows. The stellar wind properties and abundances of A78 CSPN are discussed in §2. The *XMM-Newton* observations are presented in §3, and the spatial distribution and spectral properties of the X-ray emission in §4 and §5, respectively. A discussion is presented in §6 and we summarize our findings in §7.

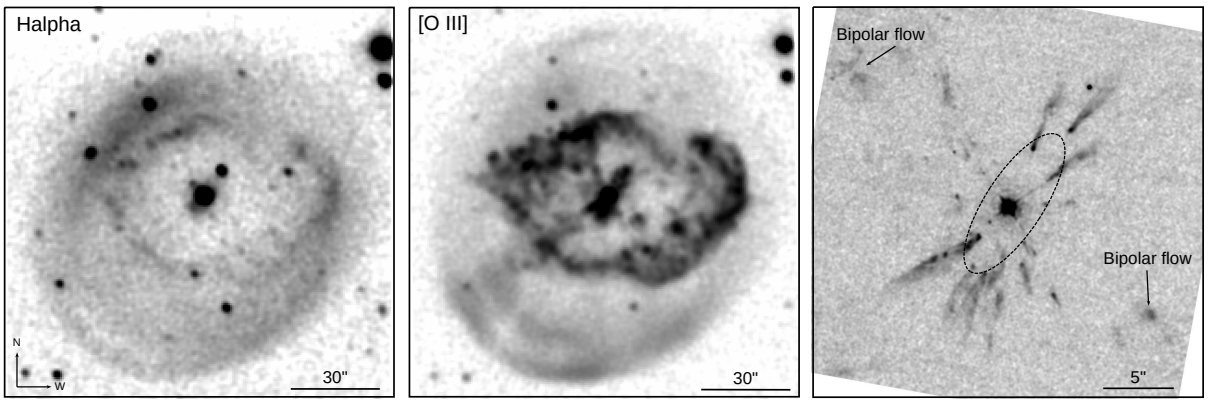

Figure 6.1: Hα (left) and [O III] (center) narrow band images of A78 (images obtained at the 2.1 m San Pedro Mártir UNAM telescope, adapted from Meaburn et al., 1998), and *HST* WFPC2 F502N image of the central part of A78. The equatorial plane and the bipolar flows are marked with a dashed-line ellipse and arrows, respectively.

6.2 NLTE analysis of the central star

We analyzed the optical and UV spectra of CSPN of A78 using the most recent version of the Potsdam Wolf-Rayet (PoWR) model atmosphere[1].

The PoWR solves the NLTE radiative transfer problem in a spherical expanding atmosphere simultaneously with the statistical equilibrium equations and accounts at the same time for energy conservation. Iron-group line blanking is treated by means of the superlevel approach (Gräfener et al., 2002), and a wind clumping in first-order approximation is taken into account (Hamann & Gräfener, 2004). We do not calculate hydrodynamically consistent models, but assume a velocity field following a β-law with $\beta = 1$. We also performed tests with different β-laws, i.e. with $\beta = 0.8$, $\beta = 2$ and a double-β law. We found that the impact of different β-laws is much smaller than the change of other parameters, such as $T_{\rm eff}$ or $\dot{M}$. Therefore we used $\beta = 1$ for our final model. Our computations applied here include complex atomic models for helium, carbon, nitrogen, oxygen, neon, fluorine, hydrogen, and the iron-group elements.

The synthetic spectrum was corrected for interstellar extinction due to dust by the reddening law of Cardelli et al. (1989), as well as for interstellar line absorption for the Lyman series in the UV range.

The UV spectrum of the CSPN of A 78 has been observed by the *Far Ultraviolet Spectroscopic Explorer (FUSE)* and the *International Ultraviolet Explorer (IUE)* satellites. Data from these observations have been retrieved from MAST, the Multimission Archive at the Space Telescope Science Institute[2]. We used the *FUSE* observation with ID e1180101000 (PI: J. Kruk)

[1] `http://www.astro.physik.uni-potsdam.de/PoWR`

[2] STScI is operated by the Association of Universities for Research in Astronomy, Inc., under NASA contract NAS5-26555.

obtained on 2004 November 11 in the spectral range 916-1190 Å for a total exposure time of 58 ks. The *IUE* observations in the spectral range 1150-1975 Å consists of two datasets with IDs SWP19879 and SWP19906, both taken with the large aperture at high dispersion with total exposure times of 25.5 ks and 25.2 ks, respectively. For the range 2000-3300 Å only *IUE* observations with low dispersion are available, we used the data set with ID LWP23314LL with a total exposure time of 600 s for the large aperture. Optical spectra were obtained by K. Werner with the TWIN spectrograph at the 3.5m-telescope at Calar Alto in Oct 1990 and in Sep 1991 (see Werner & Koesterke, 1992).

Since the stellar spectra of the CSPN of A 30 (Guerrero et al., 2012) and A 78 are similar, the spectral fits resulted in similar wind properties and abundances (see Table 6.1).

For the determination of the stellar temperature we used mainly the ratio of the line strengths of O VI vs. O V wind lines. The best fit to these lines was obtained with an effective temperature of $T_* = 116 \pm 5$ kK (see Fig. 6.2 and 6.3).

From the strengths of the emission and P Cygni lines we derived the mass-loss rate under the assumption of a typical central star luminosity and mass of $L = 6000\,L_\odot$ and $M = 0.6\,M_\odot$ (see e.g. Miller Bertolami & Althaus, 2007; Schönberner et al., 2005). The inferred value of $\dot{M} = 1.6 \times 10^{-8}\,M_\odot$/yr is about half of the value from Werner & Koesterke (1992) and Leuenhagen et al. (1993), also because we account for clumping and use a different luminosity, see Table 6.1 for scaling relations. Moreover, the mass-loss rate determined by Koesterke & Werner (1998) is the same as ours, if rescaled to the values of D and $\log L$ that we used in our analysis.

The blue edge of the P Cygni profiles was used to estimate a terminal wind velocity of about 3100 ± 100km/s, which is consistent to that find by Guerrero & De Marco (2013). Additional broadening due to depth dependent microturbulence with $v_\mathrm{D} = 50$ km/s in the photosphere up to $v_\mathrm{D} = 300$ km/s in the outer wind was taken into account and allows to fit the width of the O VI and the C IV resonance lines simultaneously (see Fig. 6.2).

A strong Ne VII line at 973.33 Å (Herald et al., 2005) is observed in the UV spectrum, that can only be reproduced by models with a supersolar Ne abundance.

From the strength of the N V lines we infer also a supersolar nitrogen abundance of 1.5% by mass.

To reproduce the F VI 1139.5 Å line in the observed strength a fluorine abundance of at least 25× the solar value is needed, similar to what was found by Werner et al. (2005) for the same object as as well as for other H-deficient post-AGB stars. They also mentioned an asymmetry of this line meaning that the line is also formed in the wind, as reproduced by our wind models.

We also tried to estimate the hydrogen abundance. The best fit to the Balmer lines is obtained by models without hydrogen. However, at the given resolution and S/N of our optical observation, a hydrogen abundance of below 10% by mass would escape detection (Fig. 6.4).

The absolute flux of the model is diluted by the distance to the central star, which we consider to be a free parameter. We obtain a consistent fit of the spectral energy distribution from the far

Table 6.1: Parameters of the CSPN of A78

Parameter	Value	Comment
$T_{\rm eff}$ (kK)[a]	116	
Log($L/L_\odot$)	3.78	Adopted
R_* ($R_\odot$)[b]	0.19	$R_* \propto L^{1/2}$
$R_{\tau=2/3}$ ($R_\odot$)	0.19	
v_∞ (km s^{-1})	3100	
D (clumping factor)	10	Adopted
Log$\dot{M}$ ($M_\odot$ yr^{-1})	-7.8	$\dot{M} \propto D^{-1/2} L^{3/4}$
d (kpc)	1.40	$d \propto L^{1/2}$
E_{B-V} (mag)	0.12	
Abundances (mass fraction)		
He	0.55	
C	0.30	
N	0.015	
O	0.10	
Ne	0.04	
F	1.3×10^{-5}	
Fe-group	1.4×10^{-3}	solar

[a] $T_{\rm eff}$ is defined as the effective temperature related to the radius R_*.

[b] The stellar radius R_* refers by definition to the point where the radial Rosseland optical depth is 20.

UV up to the near infrared range (see Fig. 6.5) for a reddening of $E_{B-V} = 0.12$ and a distance of $d = 1.4$ kpc.

6.3 *XMM-Newton* Observations

The PN A78 was observed by *XMM-Newton* on 2013 June 3 (Observation ID 0721150101, PI: M.A. Guerrero) using the European Photon Imaging Camera (EPIC). The observations were performed in the Full Frame Mode with the thin optical filter for a total exposure time of 59.4 ks. The observations were reprocessed with the *XMM-Newton* Science Analysis Software (SAS) 13.5 with the most up-to-date *XMM-Newton* calibration files available on the Current Calibration File as of 2014 January 7. The net exposure times were 59.4, 59.1, 59.1, 59.4, and 59.4 ks for the EPIC-pn, EPIC-MOS1, and EPIC-MOS2, RGS1, and RGS2, respectively. After processing the effective times were reduced to 23.9, 43.6, 42.5, 59.0, and 59.1 ks for the EPIC-pn, MOS1, MOS2, RGS1, and RGS2 respectively.

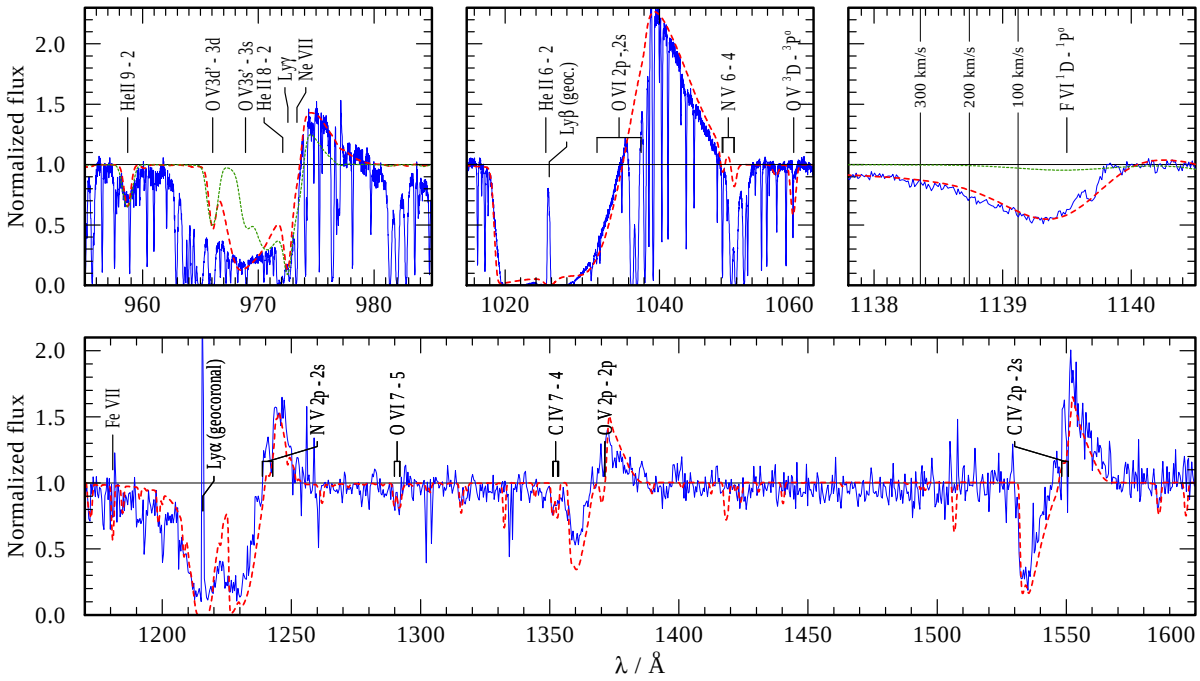

Figure 6.2: Details of the normalized UV spectrum of A 78, observations (blue thin line) from *FUSE* (upper panels) and *IUE* (lower panel) shown together with the synthetic spectrum of our models (dashed lines). *Left upper panel:* A model with 4% Ne (red dashed) compared to a model with only solar Ne abundance (green dashed). *Middle upper panel:* Our best fitting model with v_∞=3100 km s^{-1} plus depth dependent microturbulence (red dashed). *Right upper panel*: Model with $X_\mathrm{F} = 1.3 \times 10^{-5}$ (red dashed), compared to a model with only 2× solar F abundance (green dashed). The vertical lines indicate different Doppler shifts. *Lower panel:* Our best fitting model (red dashed) vs. IUE observation.

6.4 Spatial distribution of the X-ray emission

For direct comparison with the *XMM-Newton* observations of A30, we created EPIC images of A78 in four different energy bands, soft 190-275 eV, medium 275–450 eV, hard 450–600 eV, and total 190–600 eV. Individual EPIC-pn, EPIC-MOS1, and EPIC-MOS2 images were extracted, mosaicked together, and corrected from exposure maps. The final smoothed exposure-corrected images of the four energy bands are show in Figure 6.6.

Figure 6.6 reveals a bright source associated with the CSPN and diffuse X-ray emission within A78. Both the point-like source and diffuse emission seem to fade away at energies >450 eV. Other point-like sources are present in the panels shown in Figure 6.6, in particular there is a point-like X-ray source detected in all energy bands ~37″ North of the CSPN of A78. The latter does not seem to be associated with the PN but to a background source in the field of view.

In Figure 6.7 we compare the spatial extent of the X-ray emission with the optical Hα and [O III] images presented in Figure 6.1. The diffuse X-ray emission in A78 does not fill the nearly

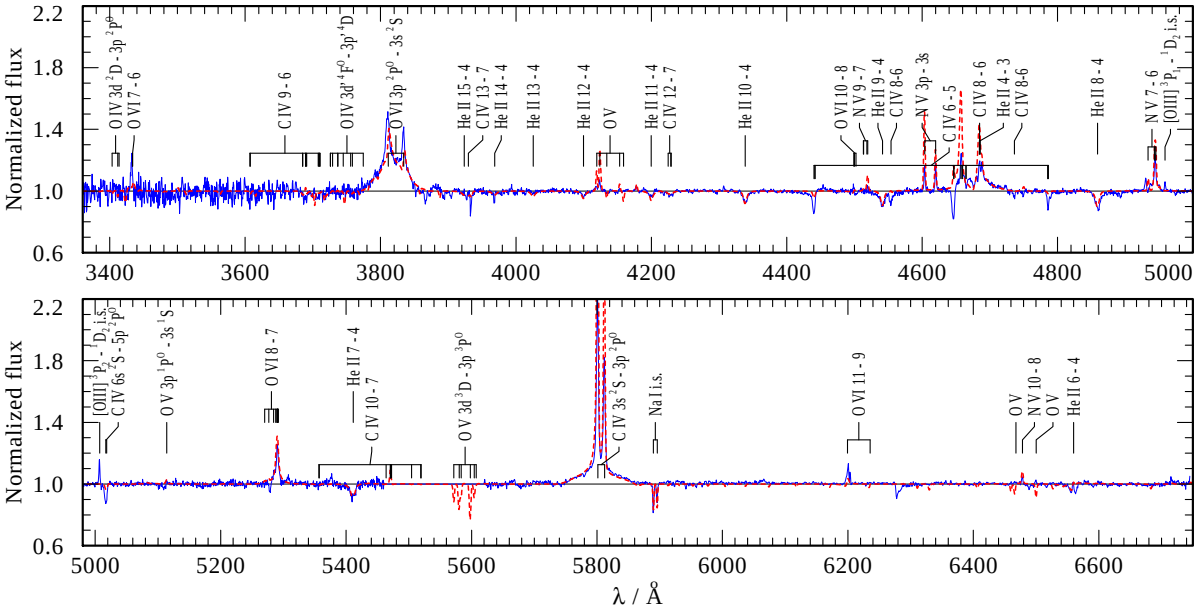

Figure 6.3: Optical spectrum of the central star of A 78. Normalized observation (blue) by K. Werner vs. synthetic spectrum of our best fitting model (red dashed). The model spectrum was convolved with a Gaussian with 2 Å FWHM to match the resolution of the observation, inferred from the interstellar Na I doublet.

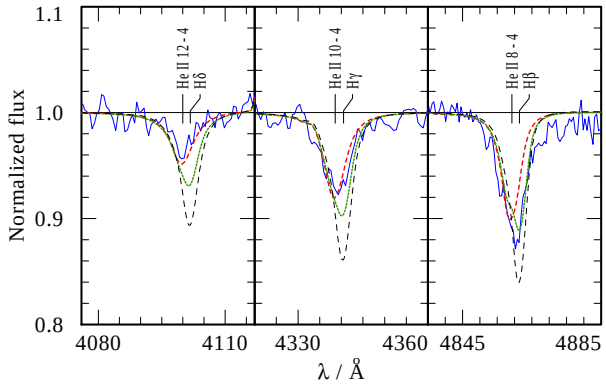

Figure 6.4: Details of the optical spectrum of A 78: Observation (blue thin solid lines) vs. models without hydrogen (red thick dashed), with 10% H (green thick dotted), and with 30% H (black thin dashed).

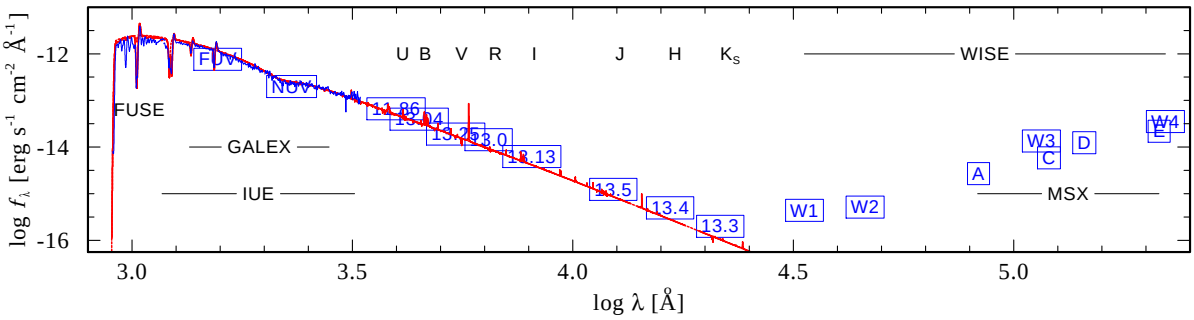

Figure 6.5: Spectral energy distribution (SED) of the central star of A 78 from the UV to the infrared range. Observations (blue) are photometric measurements in the indicated bands and calibrated UV spectra from the *IUE* and *FUSE* satellites. Also shown is the theoretical SED from our stellar model with the parameters compiled in Table 6.1.

spherical H α emission, but it seems to be bounded by the H-poor clumpy distribution shown by the [O III] narrow band image as seen in the case of A30. Furthermore, there is a local peak in the diffuse X-ray emission that seems to be associated with a H-poor clump toward the SW direction from the CSPN. In a similar manner, A30 also presents a maxima in the X-ray emission associated with the H-poor clumps, suggesting that the two born-again PNe may have similar origins o X-ray emission (see §8.5).

To better assess the extent and intensity of the diffuse X-ray emission, we have used the SAS task *eradial* to extract a radial profile of the X-ray emission centered on the CSPN of A78 and compare it to the theoretical point-spread function (PSF) of the observation. This comparison is shown in Figure 6.8, where the PSF scaled to the radial profile fits nicely the emission from the CSPN until a radius of 12″. Diffuse emission is clearly detected between 17–35″, whereas the emission detected beyond this distance is mainly due to the point-like source North of the CSPN as seen in Figures 6.6 and 6.7. It must be recognized, however, the diffuse emission component is present underneath the CSPN's PSF. To estimate this contribution, we have integrated the radial profile emission obtained with *eradial* for distances smaller than 34″, and computed the percentage to the total emission from the CSPN using the PSF model. The contribution of the CSPN to the total emission is 99% for radial distances <12″, 79% for distances <34″, and only 24% between 17″ and 34″.

6.5 Spectral properties of the X-ray emission

To study the global spectral properties of the X-ray emission from A78, we have extracted the EPIC-pn, EPIC-MOS, and a combined RGS1+RGS2 spectra shown in Figure 6.9. The EPIC spectra have been extracted from an elliptical region that encloses the whole emission from A78. These spectra (Figure 6.9-top) are very soft and resemble those presented by Guerrero et al. (2012) for A30. The EPIC-pn spectrum peaks at 0.3-0.4 keV with a rapid decline at energies

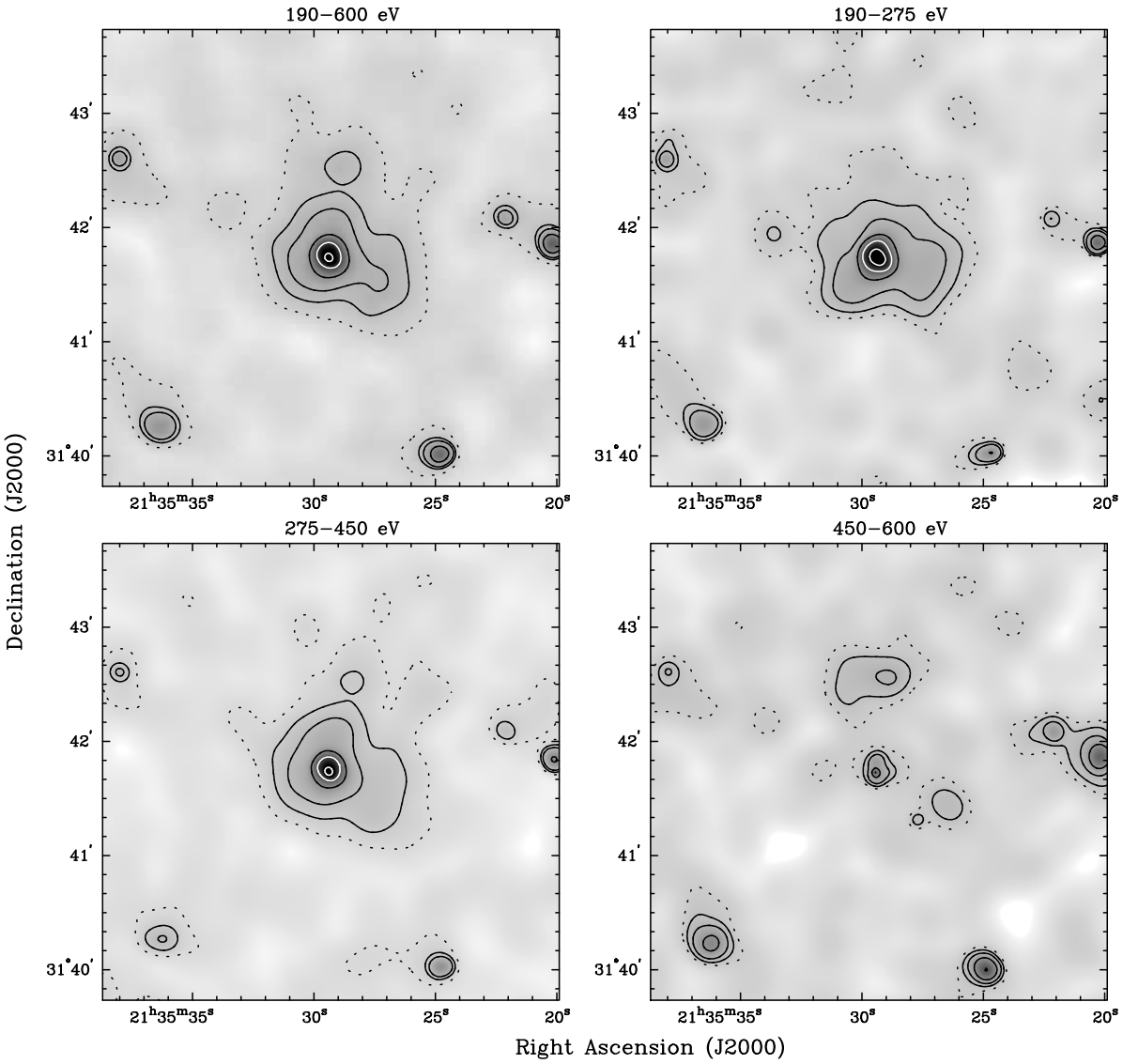

Figure 6.6: Exposure-corrected *XMM-Newton* EPIC images of A78 in different bands. The images have a pixel size $1''$. The images are centered at the central star in A 78. Other point-like sources are presented on the images. The black lower contours correspond to 1, 3, 5, and 10σ over the background level, while the white upper contours represent 20% and 60% of the peak intensity.

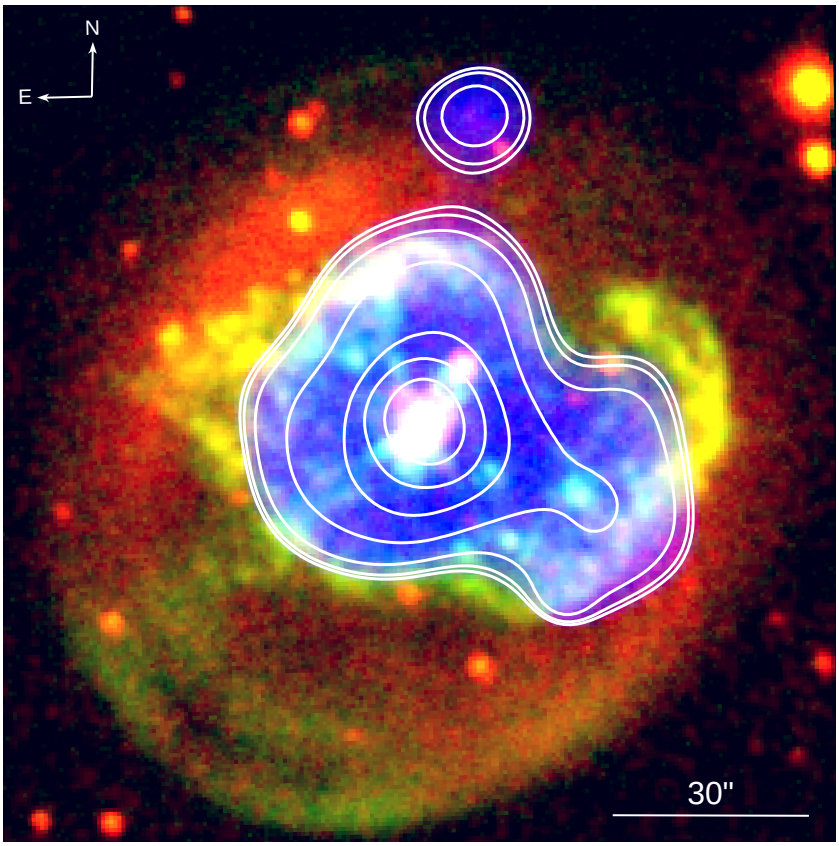

Figure 6.7: Colour-composite picture of A78 in the optical Hα (red) and [O III] (green) emission lines and EPIC 190-600 eV X-ray band (blue). To emphasize the comparison between the spatial distributions of the X-ray-emitting gas and nebular component in A78, X-ray contours of the same energy band have been overplotted. The emission to the north of A 78 corresponds to a point-like X-ray source in the field of view of the observations (see text).

greater than 0.5 keV. This spectrum shows evidence for an emission line at ~0.58 keV, which would correspond to the O VII triplet, which is absent in the EPIC-pn spectrum of A30. The count rates for the EPIC-pn, EPIC-MOS1, and EPIC-MOS2 in the 0.2–2.0 keV energy range are 18.2, 2.4, and 2.1 counts ks^{-1}, respectively.

The combined RGS1+RGS2 background-subtracted spectrum of A78 can help us identify the emission detected around 0.3-0.4 keV in the EPIC-pn camera. Figure 6.9-bottom panel shows that this is mostly due to the C VI emission line at 33.7 Å (=0.37 keV). However, because of the low MOS and RGS count rates, we will focus on the analysis of spectra extracted from the EPIC-pn camera for further discussion.

We have extracted separately EPIC-pn spectra for the CSPN and for the diffuse X-ray emission. The spectrum from the CSPN was extracted using a circular aperture of radius 12″ centered at the position of the star with a background extracted from regions with no contribution of diffuse emission. The spectrum from the diffuse emission was extracted using an elliptical

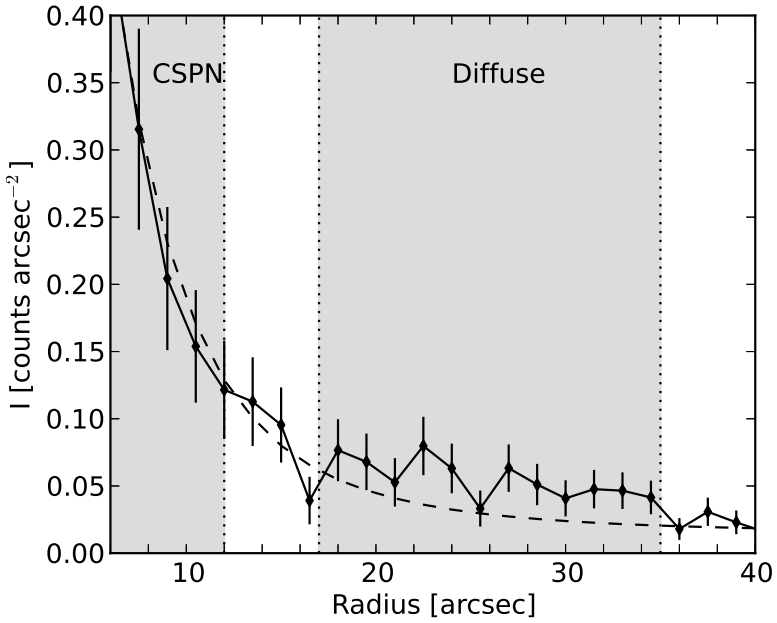

Figure 6.8: EPIC-pn radial profile of the X-ray emission from A78 extracted using *eradial*. The dashed line is the fitted PSF to the radial profile.

aperture that covered the extension of the [O III] filamentary shell with a minor axis of 34″ to avoid contamination from the point-like source to the North. Following the profile analysis in §6.4, a circular region of radius 17″ centered at the position of the CSPN was excised to reduce the contamination from the CSPN. The resultant background-subtracted EPIC-pn spectra of the CSPN and that of the diffuse component, shown in Figure 6.10, have net count rates of 8.8 and 8.0 counts ks^{-1}, respectively.

Figure 6.10 shows subtle differences in the spectral shapes from the CSPN and diffuse emission. For example, the spectrum from the diffuse component (Figure 6.10-right) shows the spectral line at ~0.58 keV, whilst that of the CSPN (Figure 6.10-left) does not. As for A30, both spectra seem to peak at the energy ~0.37 keV of the C VI line.

6.5.1 Spectral analysis

The spectral analysis of the X-ray emission was performed using XSPEC v.12.7.0 (Arnaud, 1996). We used the *apec* optically thin plasma emission model adopting the abundances listed in Table 6.1 to fit the spectra, but we notice that fits were improved by adding an emission line at ~0.37 keV. The distance is assumed to be 1.4 kpc (§2).

We would like to note that, even though the UV extinction toward A78 implies a E_{B-V} = 0.12 mag, which can be translated into an interstellar absorption of $N_{\rm H}$=7×10^{20} cm^{-2}, the origin of the extinction of the X-ray emission in born-again PNe (A30 and A78) has a circum-

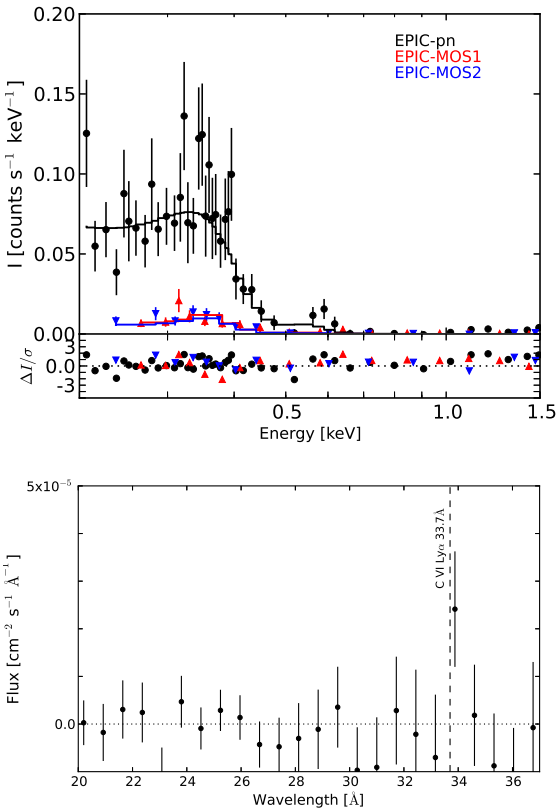

Figure 6.9: *XMM-Newton* EPIC (top) and combined RGS1+RGS2 (bottom) background-subtracted spectra of A78. The best-fit models to the EPIC-pn and MOS cameras are shown with solid lines in the top panel (see § 5.1). Residuals of these fits are also shown.

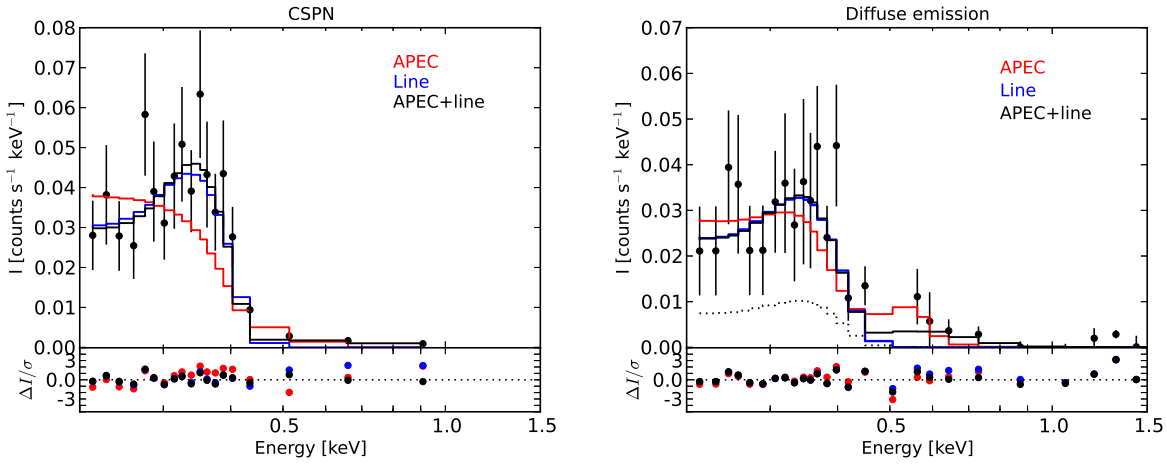

Figure 6.10: EPIC-pn background-subtracted spectra of the CSPN (left) and diffuse emission (right) of A78. Different line colors represent the different fits described in Table 6.2. The dotted histogram in the right panel illustrates the contribution of the CSPN to the diffuse emission.

stellar origin. Indeed the presence of dust in the central regions of A78 has been reported by Kimeswenger et al. (1998) and Phillips & Ramos-Larios (2007). This dust seems to be associated with the central clumps near the CSPN (see Figure 6.1-right), reinforcing the notion that the absorbing material has chemical composition similar to that of the H-poor knots as it was the case of A30 (Guerrero et al., 2012).

We performed a preliminary fit to the EPIC-pn spectrum shown in Figure 6.9 to constrain the hydrogen column density toward A78. The *apec* optically thin plasma emission model gave a reasonable fit (χ^2/dof=70.26/45=1.56) for a plasma temperature of kT=0.086 keV and an absorption column density of 1.9×10^{15} cm^{-2}. For consistency with A30 we adopted $N_{\rm H}=2\times10^{15}$ cm^{-2} for further spectral fits. The plasma temperature (kT), fluxes (f), emission line central energy (E), and normalization factors (A) of the best-fit models are listed in Table 6.2.

We then proceeded to model in more detail the global X-ray emission from A78. This model considered the contribution of the three EPIC cameras using an *apec* component and an emission line at 0.37 keV. This gives a better fit (χ^2=77.44/77=1.0) with a plasma temperature of $kT=0.090^{+0.025}_{-0.017}$ keV and a line width of ΔE=40 eV[3]. The absorbed flux and luminosity in the 0.2–2.0 keV energy range are $f_{\rm TOT}=(2.5\pm0.3)\times10^{-14}$ erg cm^{-2} s^{-1} and $L_{\rm TOT,X}=(5.8\pm0.7)\times10^{30}$ erg s^{-1}. The model is compared to the observed spectra in the 0.2–1.5 keV energy range in Figure 6.9. Another model with the contribution of an *apec* and two emission lines at 0.37 keV and 0.58 keV was attempted but did not give better statistical results than the latter.

In the following subsections we will describe the different models used to study the physical properties of the X-ray emission from the CSPN and that of the diffuse emission. We want to stress that, in the case of the diffuse emission, one third of the emission corresponds to the CSPN, while the spectrum obtained for the central 12″ in radius region corresponds mostly to the CSPN.

6.5.1.1 X-ray emission from the CSPN

The X-ray emission from the central star of A78 was first modeled by an *apec* plasma model. This resulted in a fit with χ^2/dof=1.82 and plasma emission model of $kT=0.086^{+0.004}_{-0.007}$ keV. The absorbed flux in the 0.2–2.0 keV energy range is $f_{\rm X}=(1.6\pm0.2)\times10^{-14}$ erg cm^{-2} s^{-1}.

A second fit was performed using only the contribution of an emission line around ~0.37 keV. This model results in a fit with χ^2=1.30 and an emission line with central energy of $0.37^{+0.01}_{-0.02}$ keV. The corresponding absorbed flux is $(1.1\pm0.1)\times10^{-14}$ erg cm^{-2} s^{-1}.

A third model including the combination of an *apec* model and an emission line at 0.37 keV model was also attempted, but this model did not improve the previous fits (χ^2/dof=0.59). Indeed, XSPEC cannot constrain the temperature of the *apec* component.

[3]It is worth noting that, in the cases in which an emission line is used to model the X-ray emission, its line width is a few tens of eV, which means that the line is not totally resolved.

The three resultant models are compared with the background-subtracted spectrum in the 0.2-1.5 keV energy range in Figure 6.10-left. The parameters of the best-fit models are summarized in Table 6.2.

6.5.1.2 The diffuse and extended X-ray emission

The diffuse X-ray emission in A78 was also studied with the same models used for the CSPN: i) an *apec* plasma model, ii) an emission line at 0.37 keV, and iii) the combination of an *apec* plasma model and an emission line at 0.37 keV.

The first model, with a reduced χ^2 of 1.43, implies a plasma temperature of kT=$0.10^{+0.013}_{-0.012}$ keV and an absorbed flux of $(1.3\pm0.2)\times10^{-14}$ erg cm^{-2} s^{-1}.

The second model resulted in χ^2/dof of 1.36 and the parameters for the emission line are E=$0.37^{+0.01}_{-0.02}$ keV and ΔE=36 eV. The corresponding absorbed flux is $(9.1\pm1.5)\times10^{-15}$ erg cm^{-2} s^{-1}.

The third model gives a χ^2=1.26 with plasma temperature of kT=0.14±0.02 keV and an emission line with central energy of 0.37 keV with ΔE=30 eV. The resultant absorbed flux is $(1.0\pm0.1)\times10^{-14}$ erg cm^{-2} s^{-1}.

Finally, another fit using an *apec* model and an emission line was tried by taking into account that the CSPN contributes significantly to the emission registered in this region (≈1/4 of the total flux). The resultant best-fit model has a similar quality as the last one described above (χ^2/dof=33.53/26=1.29) but the *apec* plasma temperature is reduced to kT=$0.11^{+0.02}_{-0.02}$ keV, which is more consistent with the lower values found for other models. The total corresponding flux in this region is $(1.1\pm0.1)\times10^{-14}$ erg cm^{-2} s^{-1}, but only $(8.5\pm0.2)\times10^{-15}$ erg cm^{-2} s^{-1} corresponds to the diffuse X-ray emission.

The best-fit models are compared with the background-subtracted spectrum from the diffuse emission in the 0.2–1.5 keV in Figure 6.10-right, and the parameters are listed in Table 6.2.

6.6 Discussion

Our new *XMM-Newton* observations have discovered very soft X-ray emission in the born-again PN A78. These X-ray observations reveal the existence of a point-like source associated with the CSPN as well as an extended X-ray emission within A78. The spatial distribution of the diffuse X-ray emission does not fill the entire Hα outer shell; instead, this emission can be associated with the H-poor knots and is enclosed by the filamentary shell detected in [O III] narrow band images.

The best-fit model for the CSPN of A78 seems to be the one including only a line emission at ~0.37 keV; models including a plasma component cannot produce an acceptable fit to the data. The estimated total flux for the CSPN, accounting for the fraction of the PSF not included in the source aperture of radius 12″, is $f_{\rm X,CSPN}$=$(1.6\pm0.3)\times10^{-14}$ erg cm^{-2} s^{-1} which corresponds to an X-ray luminosity of $L_{\rm X,CSPN}$=$(3.8\pm0.6)\times10^{30}$ erg s^{-1}.

The X-ray emission from the diffuse component in A78 is better explained with a thermal plasma with temperature of kT=0.11 keV ($T \approx 1.3\times10^6$ K). Its corresponding total flux, also correcting for the region dominated by the CSPN and those regions with aperture radius <17″, is $f_{\rm X,DIFF}$=(8.7±0.3)×10^{-15} erg cm^{-2} s^{-1}, which corresponds to an intrinsic luminosity of $L_{\rm X,DIFF}$=(2.0±0.1)×10^{30} erg s^{-1}. The normalization parameter for the *apec* component (A_1=9.9×10^{-11} cm^{-5}; see Table 6.2) has been used to estimate an electron density of the diffuse X-ray-emitting gas for a distance of 1.4 kpc as $n_{\rm e}$=8.0(ϵ/0.1)$^{1/2}$×10^{-4} cm^{-3}, with ϵ as the volume-filling factor.

6.6.1 Comparison with A30

The four born-again PNe, A30, A58, A78, and Sakurai's object, represent different stages of a common evolutionary path. A30 and A78 are very similar in most ways. The morphology and spectral similarities between A30 and A78 and their central stars are remarkable. Their optical narrow band images show similar limb-brightened outer nebulae which correspond to the expected shell in the canonical formation of a PN (Balick, 1987; Kwok et al., 1978), with estimated dynamical ages, $t_{\rm dy}$[4], of 12,500 and 10,700 yr for A30 and A78, respectively. The processed H-poor material is thought to have been ejected less than a thousand years ago, at least for the case of A30 (Guerrero et al., 2012), which means that the stellar wind velocity must have increased very rapidly within this time span in both cases. The interaction of this stellar wind with the material ejected in the born-again event is responsible of the shaping the cloverleaf and eye-shaped H-poor clumpy distributions in A30 and A78, respectively.

The X-ray properties of A30 and A78 are very alike. They diffuse X-ray emission can be modeled by an optically thin plasma model with similarly low temperatures for both PNe, besides the different relative importance of the O VII emission line at ~0.58 keV. The origin of this hot plasma may be due to pockets of shocked and thermalized stellar wind, as the current fast wind from the CSPNe ($V_\infty \lesssim$4000 km s^{-1}) interacts with the processed material from the born-again ejection. The plasma temperature from an adiabatic shocked stellar wind can be determined by $kT = 3\mu m_{\rm H} V_\infty^2/16$, where μ is the mean particle mass (Dyson & Williams, 1997). Therefore, for the stellar winds of A30 and A78, the temperature expected from the shocked material would be $T \lesssim 5\times10^8$ K, in sharp contrast with the observed temperatures. This discrepancy is found in all PNe in which diffuse X-ray emission is detected (see Ruiz et al., 2013, and references therein) and it is always argued that thermal conduction is able to reduce the temperature of the shocked stellar wind and to increase its density to observable values (Soker, 1994). Even though one-dimension radiative-hydrodynamic models on the formation and X-ray emission from hot bubbles in PNe as those presented by Steffen et al. (2008) and Steffen et al. (2012) are able to explain this discrepancy, they are not tailored to the specific evolution of a star

[4]The dynamical age can be estimated as $t_{\rm dy} = R/v_{\rm exp}$, where R and $v_{\rm exp}$ are the radius and velocity of the outer optical shell, respectively.

that experiences a VLTP and creates a born-again PN. The fact that the diffuse X-ray emission of A30 and A78 is confined within filamentary and clumpy H-poor shells is a clear indication that a variety of physical processes are taking place to reduce its temperature. These processes may include mass-loading and photoevaporation from the H-poor clumps (Meaburn & Redman, 2003), which mix the cold nebular material with the thermalized shocked wind. The realization of numerical simulations on the formation of born-again PNe including these complex interactions and accounting for their anomalous abundances is most needed to understand the puzzling X-ray emission in these objects (Toalá & Arthur in prep.).

The X-ray emission from the point sources at the CSPNe of A30 and A78 is dominated by the C VI line. As discussed by Guerrero et al. (2012), the origin of the X-ray emission associated with the CSPNe of born-again PNe is inconclusive. Several mechanism are capable of producing this X-ray emission (e.g., charge transfer reactions from highly ionized species of carbon, oxygen, and nitrogen), but the present observations cannot provide a definite answer. However, it is clear that this X-ray emission is dominated by the 0.37 keV C VI emission line. This reinforces the idea that the X-ray emission is directly related to the born-again phenomenon, as the very late helium shell flash will dredge-up carbon to the stellar surface where it can be ejected by the stellar wind (see Montez & Kastner, 2013). Given the large opacity of this material (see Figure 11 in Guerrero et al., 2012), the C VI 0.37 keV emitting-region must be located at least a few stellar radii above the surface of the CSPN, CSPN, which is consistent with the carbon-rich wind implies by our optical and UV spectral modeling.

6.7 Summary and conclusions

We have presented *XMM-Newton* observations of the X-ray emission from the born-again PN A78. We report the discovery of hot diffuse X-ray emission associated with the H-poor knots and filamentary cavity inside the PN and a point-like source at the position of the CSPN. The spectral properties and distribution of the X-ray emission detected towards A78 are very similar as those reported for A30 by Guerrero et al. (2012). In particular we find:

- The analysis of the optical and UV spectra of A78 helped us to constrain the abundances from the central star. These abundances are very similar as those of A30.

- The distribution of diffuse X-ray emission in A78 does not fill the outer nebular shell detected in Hα, instead it seems to trace the H-poor clumps and eye-shaped structure detected in [O III] narrow band images. An apparent maximum in the diffuse X-ray emission is detected at the location of one H-poor clump toward the southwest.

- The main X-ray spectral feature of the CSPN in A78 is the C VI emission line, as revealed by the EPIC and RGS spectra. Its estimated flux in the 0.2–2.0 keV energy band is $f_{\rm X,CSPN}$=(1.6±0.3)×10^{-14} erg cm^{-2} s^{-1} which corresponds to a luminosity of $L_{\rm X,CSPN}$=(3.8±0.6)×10^{30}

erg s^{-1}. The physical mechanisms for the production of the emission associated with the CSPN of A78 are elusive.

- The best-fit model for the diffuse X-ray emission resulted in a plasma temperature of kT=0.11 keV ($T \approx 1.3\times10^6$ K) with an estimated absorbed flux of $f_{\rm X,DIFF}=(8.7\pm0.3)\times10^{-15}$ erg cm^{-2} s^{-1}. The estimated X-ray luminosity is $L_{\rm X,DIFF}=(2.0\pm0.1)\times10^{30}$ erg s^{-1}. These results are not reproduced by the current one-dimensional theoretical models as mixing, ablation and photoevaporation seem to be playing important roles in lowering the plasma temperature.

Table 6.2: Best-fit models for the X-ray emission in A78

Region	kT (keV)	A_1^* (cm^{-5})	E (keV)	ΔE (keV)	A_2^* (cm^{-5})	f_X (erg cm^{-2} s^{-1})	χ^2/dof
A78	$0.090^{+0.026}_{-0.016}$	2.53×10^{-11}	0.37	4.0×10^{-2}	4.0×10^{-5}	2.50×10^{-14}	77.44/77=1.00
CSPN	$0.086^{+0.004}_{-0.007}$	2.15×10^{-10}	...	...	...	1.6×10^{-14}	30.95/17=1.82
	...	...	$0.37^{+0.012}_{-0.018}$	2.9×10^{-2}	1.9×10^{-5}	1.1×10^{-14}	20.78/16=1.30
	1–64	4.20×10^{-10}	$0.37^{+0.011}_{-0.016}$	1.7×10^{-2}	1.7×10^{-5}	1.3×10^{-14}	8.29/14=0.59
Diffuse emission	$0.100^{+0.013}_{-0.012}$	1.60×10^{-10}	...	...	...	1.3×10^{-14}	35.19/26=1.43
	...	...	$0.37^{+0.018}_{-0.027}$	3.6×10^{-2}	1.5×10^{-5}	9.1×10^{-15}	34.07/25=1.36
	$0.137^{+0.02}_{-0.02}$	3.60×10^{-11}	0.37	3.0×10^{-2}	1.2×10^{-5}	1.0×10^{-14}	31.64/25=1.26
Net diffuse emission	$0.110^{+0.02}_{-0.02}$	9.90×10^{-11}	0.37	3.6×10^{-2}	5.5×10^{-6}	1.1×10^{-14}	33.53/26=1.29

*The normalization parameter A is defined as $A=1\times10^{-14}\int n_e n_H dV/4\pi d^2$, where d is the distance, n_e is the electron number density, and V the volume in cgs units.

CHAPTER 7

FORMATION AND EVOLUTION OF HOT BUBBLES IN PLANETARY NEBULAE

We carry out high resolution two-dimensional radiation-hydrodynamic numerical simulations to study the formation and evolution of hot bubbles inside planetary nebulae (PNe). We take into account the evolution of the stellar parameters, wind velocity and mass-loss rate from the final thermal pulses during the asymptotic giant branch (AGB) through to the post-AGB stage for a range of initial stellar masses. The instabilities that form at the interface between the hot bubble and the swept-up AGB wind shell lead to hydrodynamical interactions, photoevaporation flows and opacity variations. We explore the effects of hydrodynamical mixing combined with thermal conduction at this interface on the dynamics, photoionization and observational properties of our models. We find that even models without thermal conduction mix sufficient mass into the hot bubble to raise the predicted soft X-ray emissivity to observable values. When thermal conduction is not included, hot gas can leak through the gaps between clumps and filaments in the broken swept-up AGB shell and this depressurises the bubble. The inclusion of thermal conduction evaporates and heats material from the clumpy shell, which expands to seal the gaps, preventing a loss in bubble pressure. The pressure in bubbles without conduction is dominated by the photoionized shell, while for bubbles with thermal conduction it is dominated by the hot, shocked wind.

7.1 Introduction

Planetary nebulae (PNe) are formed as the result of the evolution of low- and intermediate-mass stars ($M_{\rm ZAMS} \sim 1$–$8 M_{\odot}$). In the most simple scenario of the formation of PNe, the star evolves to the asymptotic giant branch (AGB) phase developing a dusty, slow, and dense wind that interacts with the interstellar medium (ISM; e.g., Cox et al., 2012; Mauron et al., 2013). After the star

evolves off the AGB phase towards hotter effective temperatures, the post-AGB star develops a high ultraviolet flux that photoionizes the AGB material. This phase is also characterized by a fast wind that is able to sweep up, shock, and compress the photoionized AGB envelope (Balick, 1987; Kwok et al., 1978).

The first report of the detection of X-ray emission associated with a PN was made by de Korte et al. (1985) using observations from the *EXOSAT* satellite. Since then a great number of PNe have been observed to harbor X-ray emission. A comprehensive review of the PNe reported with the *old* X-ray facilities (*Einstein*, *EXOSAT*, *ROSAT*, and *ASCA*) was presented by Chu et al. (2003b). Given the capabilities of those satellites, it was not possible to unambiguously disentangle the photospheric emission from the central star (CSPN) from that of the nebular diffuse emission. With the unprecedented sensitivity and angular resolution of the *Chandra* and *XMM-Newton* X-ray observatories this problem can finally be resolved. By 2009, diffuse X-ray emission delimited by bright optical bubbles had been reported for ten PNe (Kastner et al., 2008, and references therein). More recently, Kastner et al. (2012) reported that of the 35 PNe observed to that time with *Chandra*, $\sim 30\%$ display diffuse X-ray emission. In all positive detections, the X-ray emission comes from a hot bubble inside an optical shell.

The nature of the diffuse X-ray emission from hot bubbles in PNe is still a matter of discussion. The main problem is that in the wind-wind interaction scenario the shocked plasma would possess temperatures of $T \sim 10^7 - 10^8$ K as expected from an adiabatic shocked wind with terminal velocities of $v_\infty \gtrsim 10^3$ km s^{-1} and plasma densities $\lesssim 10^{-2}$ cm^{-3}. Measured central star wind velocities using P Cygni profiles of UV lines indicate that CSPN wind velocities are generally above 1000 km s^{-1} and can be as high as 4000 km s^{-1} (see Guerrero & De Marco, 2013). However, the X-ray observations suggest plasma temperatures of $T_{\rm X} \sim 10^6$ K and electron densities of 1–10^2 cm^{-3} (Kastner et al., 2012, and references therein)[1]. It should be noted that the same temperature and density discrepancy is found in hot plasmas detected towards H II regions and Wolf-Rayet (WR) bubbles (e.g., Güdel et al., 2008; Toalá et al., 2012).

Mellema & Frank (1995) and Mellema (1995) studied the hot bubbles produced in 2D radiation-hydrodynamic simulations of the formation and evolution of aspherical planetary nebulae. This pioneering work showed that the interface between the hot bubble and the swept-up shell of AGB material is unstable, but unfortunately the numerical resolution of these simulations was not high enough to fully develop the instabilities. These papers also estimated the soft X-ray emission predicted by the simulations and found that it came from the thin interface between the hot bubble and the surrounding photoionized material where numerical diffusion spreads the temperature and density jumps across 4 or 5 computational cells.

More recent numerical models have studied different aspects of the formation of hot bubbles inside PNe and their associated X-ray emission. The influence of the central star stellar wind

[1]The temperature in an adiabatically shocked stellar wind is defined by the terminal velocity as $kT = 3\mu m_{\rm H} V_\infty^2/16$, where k, μ, and $m_{\rm H}$ are the Boltzmann constant, the mean particle mass, and hydrogen mass, respectively.

parameters during the post-AGB phase was studied in purely hydrodynamical, one-dimensional models by Stute & Sahai (2006) and Akashi et al. (2007). They concluded that in this phase the fast wind velocity must be below 10^3 km s^{-1} in order to explain such low temperatures in the X-ray-emitting plasma, however, this is not consistent with the results from the observed P Cygni profiles of UV lines of central star winds. A different explanation for the diffuse emission was put forward in an analytical approach proposed by Lou & Zhai (2010). One difficulty in these works is that they do not take into account the time evolution of the stellar wind properties (velocity and mass-loss rate) and the star's ionizing photon rate.

A more detailed treatment of the evolution of the stellar wind parameters of the central star and the evolution of the X-ray emission from the hot bubble was presented by the Potsdam group in Steffen et al. (2008). They started their 1D study of the evolution of PNe with a parameter study (see Perinotto et al., 1998, 2004) in which they included a large set of initial models from the AGB phase to hot white dwarf (WD) using post-AGB stellar evolution models from Blöcker (1995) and Schönberner (1983). They used three different numerical approaches to the AGB wind evolution: a fixed density profile $\rho(r) \propto r^{-2}$, a kinematical approach, and an hydrodynamic calculation. In the two latter cases the AGB density and velocity profiles depend directly on the evolutionary track used. Specifically, they found that for the hydrodynamical approach, the dependence of the density profile $\rho(r)$ might vary depending on the initial mass from r^{-1} to $r^{-2.5}$ with an even steeper gradient ($r^{-3.5}$) farther from the central star. The transition phase between the AGB and WD phase was developed using the Reimers formulation (Reimers, 1975), but they concluded that the dynamical impact of this short-lived phase is rather small. One of their conclusions is that PNe formed from massive central stars will never become optically thin in the high-luminosity phase unless a low-density AGB envelope is developed.

In Steffen et al. (2008), one-dimensional radiation-hydrodynamic models were used to study the effect of classical and saturated thermal conduction on the soft X-ray emission from PNe. The *CHIANTI* software was used to generate synthetic spectra and study the time variation of the luminosities and surface brightness profiles. They concluded that thermal conduction must be taken into account in order to reproduce the observed X-ray luminosities in closed inner cavities in PNe. Since thermal conduction is suppressed perpendicular to the magnetic field direction, this implies that magnetic fields in PNe must be absent or weak (e.g., Soker, 1994). These results are consistent both with wind velocities greater than 1000 km s^{-1} and with the observed soft X-ray emission in PNe having temperatures of a few times $T \sim 10^6$ K. However, the low X-ray temperatures are only obtained if thermal conduction is included—models without conduction fail to reproduce the observations.

An interesting scenario has been presented by Akashi et al. (2008) in which the soft X-ray-emitting gas can be explained as the result of the interaction of a jet with a spherical AGB wind. This model does not take into account the evolution of the central star in any phase nor the ionizing photon flux in the post-AGB phase. The extended soft X-ray emission predicted by this

model comes from an expanding bubble of adiabatically cooling shocked jet material, where the jet velocities can lie between ~ 500 and 3000 km s^{-1}. The source of the jet is a collimated wind from a binary companion.

Our main goal in the present chapter is to use 2D axisymmetric numerical simulations to study the formation of the hydrodynamical and ionization instabilities created in the wind-wind interaction between the fast wind and the previously ejected AGB slow wind, and the rôle played by these instabilities in reducing the temperature at the edge of the diffuse hot bubble. The importance of these instabilities has been downplayed by other authors in earlier one-dimensional numerical treatments of this problem (Perinotto et al., 2004; Steffen et al., 2008; Villaver et al., 2002a,b). We find that the instabilities result in density inhomogeneities that become enhanced and can form dense clumps in the region of the contact discontinuity between the shocked fast wind and the swept-up AGB material. Secondary shocks, photoevaporation flows and photoionization shadows are some of the phenomena associated with the interaction of the fast wind and the ionizing photon flux with these clumps, with consequences both for the hot bubble and for the external photoionized shell. We argue that this highly dynamic mixing region is an important source of diffuse soft X-ray emission in PNe. When thermal conduction is taken into consideration the soft X-ray emission is enhanced. We compare the characteristics of models with different initial masses, as more massive stars evolve faster.

7.2 Numerical Method

The radiation-hydrodynamics numerical scheme used in this work is similar as that used in Toalá & Arthur (2011) and Arthur (2012). The main difference between that scheme and the one used in this thesis is the way in which the stellar wind is injected into the computational domain.

7.2.1 Overview

First, the AGB wind is modelled in 1D spherical symmetry. This is a slow, dense wind expanding at subsonic velocities into the surrounding medium, which results in a r^{-2} density distribution bounded by a thin, dense shell, located at $\lesssim$2 pc that will not be relevant for the PN formation (see Villaver et al., 2002a,b). Variations in the AGB wind parameters during this stage due to thermal pulses can produce internal density structure superimposed on the general r^{-2} distribution (see Fig. 7.1). We do not consider proper motion of the star during this stage, which could lead to anisotropy in the circumstellar medium (see Esquivel et al., 2010; Mohamed et al., 2012; Villaver et al., 2012) prior to the onset of the fast wind.

At the end of the AGB stage, the 1D spherically symmetric results are remapped onto a 2D axisymmetric (r,z) grid to continue the evolution through the PN stage, where the effective temperature of the central star increases, resulting in a two-orders of magnitude increase in

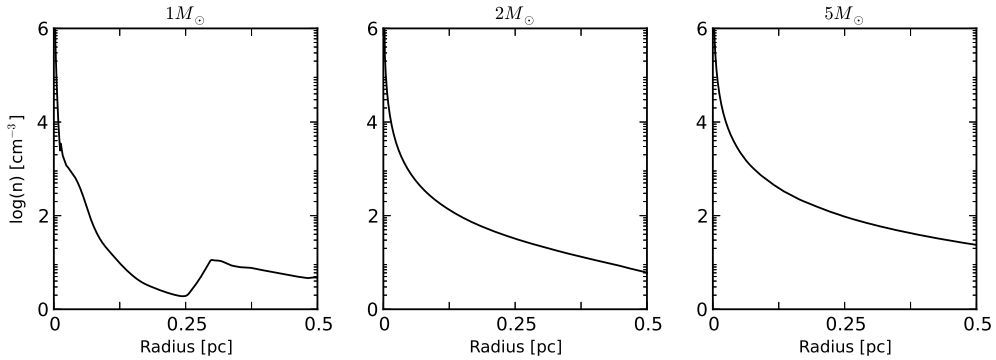

Figure 7.1: Radial distribution of the number density at the end of the AGB phase for models with initial masses ($M_{\rm ZAMS}$) of 1, 2, and 5 $M_\odot$ zoomed at the inner 0.5 pc as obtained from 1D simulations.

the stellar wind velocity and the onset of an ionizing photon flux. The combined effects of the fast wind–AGB-wind interaction, the density gradient, and the ionizing photon flux lead to the formation of structures at the contact discontinuity due to Rayleigh-Taylor, thin-shell and shadowing instabilities (e.g., García-Segura et al., 1999). These phenomena cannot be modelled in 1D spherical symmetry. The dense clumps formed as a result of these instabilities are ablated and photoevaporated by their interaction with the shocked fast wind and the ionizing photon flux. This leads to a complex scenario in which the densities and temperatures of the material at the edge of the hot, shocked wind bubble do not mark a sharp transition as in the 1D case. In our models the large surface area presented by these structures formed at the contact discontinuity enhances the evaporation of material from the dense, cold clumps into the hot, tenuous bubble.

7.2.2 Code Description

In 1D spherical symmetry, the appropriate Eulerian conservation equations are

$$\frac{\partial \mathbf{U}}{\partial t} + \frac{1}{r^2}\frac{\partial r^2 \mathbf{F}}{\partial r} = \mathbf{S}\,, \tag{7.1}$$

where $\mathbf{U} = \left[\rho, \rho u, e\right]$ is the vector of conserved quantities, $\mathbf{F} = \left[\rho u, p + \rho u^2, u(e+p)\right]$ is the vector of fluxes and $\mathbf{S} = [0, 2p/r, G - L]$ is the vector of source terms, both physical and geometrical. Here, ρ, u, p are the mass density, radial velocity and pressure, respectively, and e is the total energy, where

$$e = \frac{p}{\gamma - 1} + \frac{1}{2}\rho u^2\,. \tag{7.2}$$

The energy source terms G and L are the heating and cooling rates, respectively, and γ is the ratio of specific heats. The neutral hydrogen fraction is advected through the computational

domain according to the equation

$$\frac{\partial \rho y_0}{\partial t} + \frac{1}{r^2}\frac{\partial}{\partial r} r^2 \rho y_0 u = 0 \,, \tag{7.3}$$

where y_0 is the H I fraction.

The hydrodynamic conservation equations are solved using a second-order, finite volume Godunov-type scheme with outflow-only boundary conditions at the outer boundary. At every time step, the density, momentum and energy in an inner spherical region are reset with a free-flowing stellar wind, whose parameters are interpolated from a table according to the current time values derived from stellar evolution models. The hydrogen ionizing photon rate is also interpolated from these tables and the transfer of ionizing radiation is performed by the method of short characteristics (Raga et al., 1999) in spherical symmetry. A single frequency of ionizing radiation is assumed in these calculations.

The time-dependent hydrogen ionization balance equation takes into account both photoionization and collisional ionization together with recombination:

$$\frac{\partial y_{\rm i}}{\partial t} = n_e C_0 y_0 + P_0 y_0 - n_e R_{\rm i} y_{\rm i} \,, \tag{7.4}$$

where y_0 and $y_{\rm i}$ are the neutral and ionized hydrogen fractions and n_e is the electron density. The collisional ionization rate of neutral hydrogen, C_0, and the radiative recombination rate of ionized hydrogen, $R_{\rm i}$, are functions of temperature only and are obtained from analytic fits. The photoionization rate , P_0, is obtained from the radiation transport procedure at each cell. The ionization update is performed after the main hydrodynamic evolution step using operator splitting.

The hydrodynamic and ionization equations are coupled through the pressure term in the momentum and energy equations (since the gas pressure depends on the total number of particles, i.e., ions, neutrals and electrons), and also through the heating and cooling source terms in the energy equation. Other elements are assumed to be in ionization equilibrium at the temperature and radiation conditions for each computational cell. Although this procedure is not as accurate as taking into account the fully time-dependent ionization of the most important ions (Steffen et al., 2008), it has the benefit of being computationally efficient and is easily extended to two (or more) dimensions.

The radiative cooling term L takes into account abundances appropriate to PNe, via the Cloudy PN abundance set (Ferland et al., 2013, see Table 7.1). These abundances are also used to calculate the appropriate mean nucleon mass. Since H I is not present in 10^4 K photoionized gas, and therefore cannot contribute to cooling for $T < 3 \times 10^4$ K, we have generated a table of cooling rates using the Cloudy photoionization code for a hot central star with an effective temperature of 100 kK, a mean gas density of 10^3 cm^{-3}, and an ionizing flux $\phi = Q_{\rm H0}/4\pi r^2 = 10^{11}$

Table 7.1: Abundance set for a PN and the interstellar medium (ISM) in Cloudy[a]

Atom	PN (Log$X$+12)	ISM (Log$X$+12)
He	11.0	10.991
C	8.892	8.399
N	8.255	7.899
O	8.643	8.504
F	5.477	4.301
Ne	8.041	8.090
Na	6.279	5.500
Mg	6.204	7.100
Al	5.431	4.900
Si	7.00	6.500
P	5.301	5.204
S	7.00	7.511
Cl	5.230	5.000
Ar	6.431	6.450
K	5.079	4.041
Ca	4.079	2.612
Fe	5.699	5.800
Ni	4.255	4.266

[a] From Ferland et al. (2013)

(see Figure 7.2)[2] Cooling rates in photoionized gas at temperatures 10^4–$10^{4.5}$ K are less than in collisionally ionized gas since there will be little Lyα cooling due to the absence of neutral hydrogen. The heating term, G, depends on the local photoionization rate and the current stellar effective temperature. In order to avoid spurious cooling due to numerical diffusion at contact discontinuities, we limit cooling in cells whose cooling is more than double that of its neighbours, as described in García-Arredondo et al. (2002).

Thermal conduction is optionally included through the diffusion equation

$$\rho c_{\rm V} \frac{\partial T_e}{\partial t} = \nabla \cdot (D \nabla T_e) \ , \tag{7.5}$$

where T_e is the electron thermal temperature, $c_{\rm V}$ is the specific heat at constant volume and $D \propto T_e^{5/2}$ is the diffusion coefficient. A Crank-Nicholson type scheme (Press et al., 1992) is used to solve the diffusion equation through operator splitting after the main hydrodynamic and radiation transport steps. Full details of the thermal conduction scheme can be found in Arthur (2012).

The 1D numerical scheme is used to simulate the evolution through the AGB stage. The AGB stage is deemed to end once the stellar effective temperature is more than 10^4 K and the ionizing photon rate rises steeply. At this point, the 1D distributions of density, momentum and total energy are remapped to a 2D cylindrically symmetric grid using a volume-weighted averaging procedure to ensure conservation of these quantities. The calculation then proceeds in 2D but we also continue the 1D calculation for comparison.

[2]The most accurate way of doing this would be tailoring the cooling rate to the effective temperature of the central star at each time and the ionizing flux at each position in the nebula, but this procedure would be very time consuming. Nevertheless, Figure 7.2 shows that the cooling curves for stars between 50 and 150 kK are very similar.

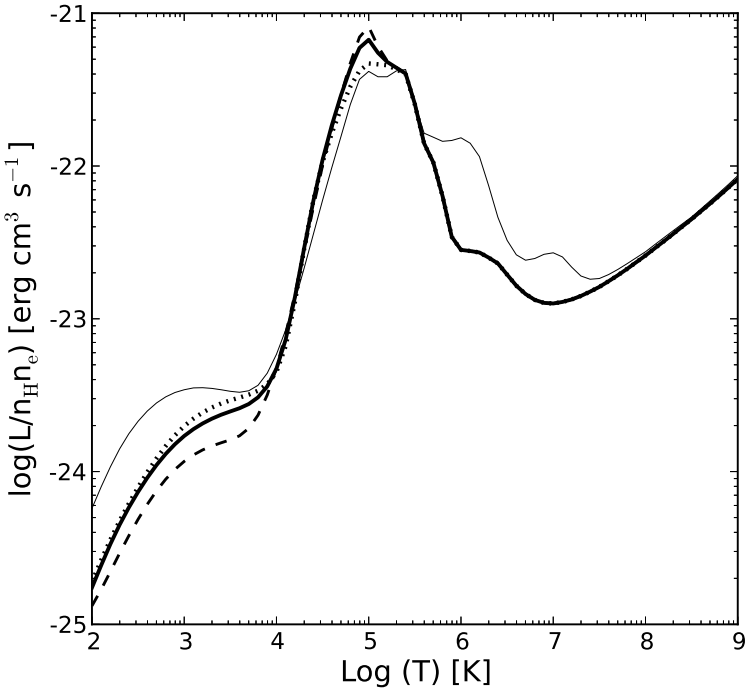

Figure 7.2: Cooling rate per hydrogen nucleon for gas in a photoionizing radiation field obtained from Cloudy (see text for details). Solid, dotted, and dashed lines correspond to stars with effective temperatures of 100, 50, and 150 kK, respectively, computed with typical PNe abundances (see Table 7.1). The thin line corresponds to a stellar effective temperature of 40 kK and ISM abundances.

In 2D cylindrical symmetry, the conservation equations in the $r-z$ plane can be written

$$\frac{\partial \mathbf{U}}{\partial t} + \frac{1}{r}\frac{\partial r\mathbf{R}}{\partial r} + \frac{\partial \mathbf{Z}}{\partial z} = \mathbf{S} \tag{7.6}$$

where, in an analogous fashion to the spherically symmetric case, $\mathbf{U} = \left[\rho, \rho u, \rho v, e\right]$ is the vector of conserved quantities (mass, momenta and energy), $\mathbf{R} = \left[\rho u, p + \rho u^2, \rho uv, u(e+p)\right]$ and $\mathbf{Z} = \left[\rho v, \rho uv, p + \rho v^2, v(e+p)\right]$ are the flux vectors, and $S = [0, p/r, 0.G - L]$ is the vector of geometrical and physical source terms. Here, u is the radial velocity, v is the azimuthal velocity, and the total energy e is now defined by

$$e = \frac{p}{\gamma - 1} + \frac{1}{2}\rho(u^2 + v^2)\,. \tag{7.7}$$

The r and z directions are dealt with separately using operator splitting.

The 2D cylindrically symmetric hydrodynamic conservation equations, are solved using a hybrid scheme, in which alternate time steps are calculated by a second-order Godunov-type

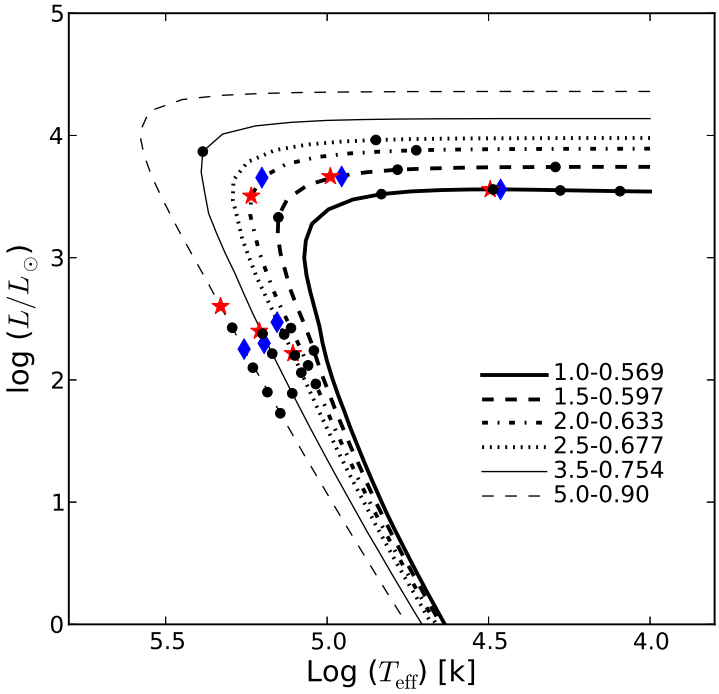

Figure 7.3: Evolutionary tracks for the WD models from Vassiliadis & Wood (1994) used in this work. The positions of the (black) circles mark times at [1, 5, 10, and 20]$\times 10^3$ yr on the tracks. Stars (red) and diamonds (blue) indicate the positions on the tracks when the hot bubble has a mean radius of ~ 0.2 pc (or the maximum extension in the case of the massive models), for cases without and with thermal conduction, respectively.

method and the van Leer flux-vector splitting method (van Leer, 1982). The outer r and z boundaries are outflow only, while the radial fluxes are zero at the symmetry axis.

In an analogous fashion to the 1D case, the stellar wind is input into the computational domain as a free-flowing wind in an inner spherical region, which is reset at every time step with the appropriate values interpolated from the stellar evolution table. The radiation transport is performed by the 2D axisymmetric version of the same short characteristics method and the source of ionization (the star) is taken to be positioned on the symmetry axis. In the same way, the hydrodynamic and ionization equations are coupled through the pressure term in the momenta and energy equations and through the source term in the energy equation. We again solve the time-dependent hydrogen ionization equation (Eq. 7.4) and employ the 2D advection equation to describe the transport of the neutral hydrogen fraction through the computational domain. We use the same radiative cooling source term and again limit the cooling in a cell whose cooling is more than double that of its neighbours in an effort to avoid spurious cooling due to numerical diffusion in the vicinity of contact discontinuities. We optionally include ther-

mal conduction through the axisymmetric diffusion equation (Eq. 7.5), which is again solved by appropriate numerical techniques through operator splitting after the main hydrodynamic and radiation transport steps.

7.2.3 Computational grid and initial conditions

For the 1D spherically symmetric calculations, the initial conditions for the interstellar medium were a density of $n_0 = 1$ cm^{-3} and a temperature of $T_0 = 100$ K. The initial grid has 2000 uniformly spaced radial cells δr and the initial spatial size is 0.5 pc. The wind injection zone comprises the innermost 10 cells. The computer code automatically detects when the outer edge of the expanding AGB wind has become close to the outer boundary and incrementally extends the computational grid with more cells at the original initial conditions of density and temperature whenever necessary. This procedure avoids large computational domains at the beginning of the simulation and also means that the final size depends on the particular stellar evolution model being calculated without needing to compromise the initial resolution.

The 2D axisymmetric calculations are performed on a fixed grid of 1000 radial by 2000 z-direction cells of uniform cell size and total grid spatial size 0.5×1 pc^2. The initial conditions for these calculations are the remapped results of the innermost 0.5 pc of the 1D calculations, which entirely fill the 2D computational domain. The free-wind injection region has a radius of 40 cells, corresponding to 0.02 pc. With this number of cells, the spherical free-wind injection region can be adequately represented on the axisymmetric grid. The use of a fixed-size grid has the disadvantage that, for the lowest initial stellar mass models, the outer photoionized shell leaves the computational domain at late times. However, since we are primarily interested in the formation of hot bubbles and their potential for emitting soft X-rays, we have decided to focus on the region $\left(r^2 + z^2\right)^{0.5} < 0.5$ pc.

The remap to the 2D grid also downgrades the numerical resolution since the 2D calculations are computationally far more expensive than the 1D calculations. In order to provide a meaningful comparison with 1D results, we also downgrade the resolution of the continuing 1D simulations and fix the total number of radial cells to 1000.

7.3 Stellar Evolution Models

In this thesis we use publicly available stellar evolution models with initial masses of 1, 1.5, 2, 2.5, 3.5, and 5 $M_\odot$ at solar metallicity ($Z = 0.016$) from Vassiliadis & Wood (1993) for the AGB phase and from Vassiliadis & Wood (1994) for the WD phase (see Figure 7.3. These models correspond to final WD masses of 0.569, 0.597, 0.633, 0.677, 0.754, and 0.90 $M_\odot$. We will label each set of simulation as a combination of their initial masses and the final WD mass, for example, the model with initial mass of 1 $M_\odot$ and final WD mass of 0.569 $M_\odot$ will be called 1.0-0.569. Thus, all models will be referred as 1.0-0.569, 1.5-0.597, 2.0-0.633, 2.5-0.677, 3.5-0.754, and 5.0-0.90.

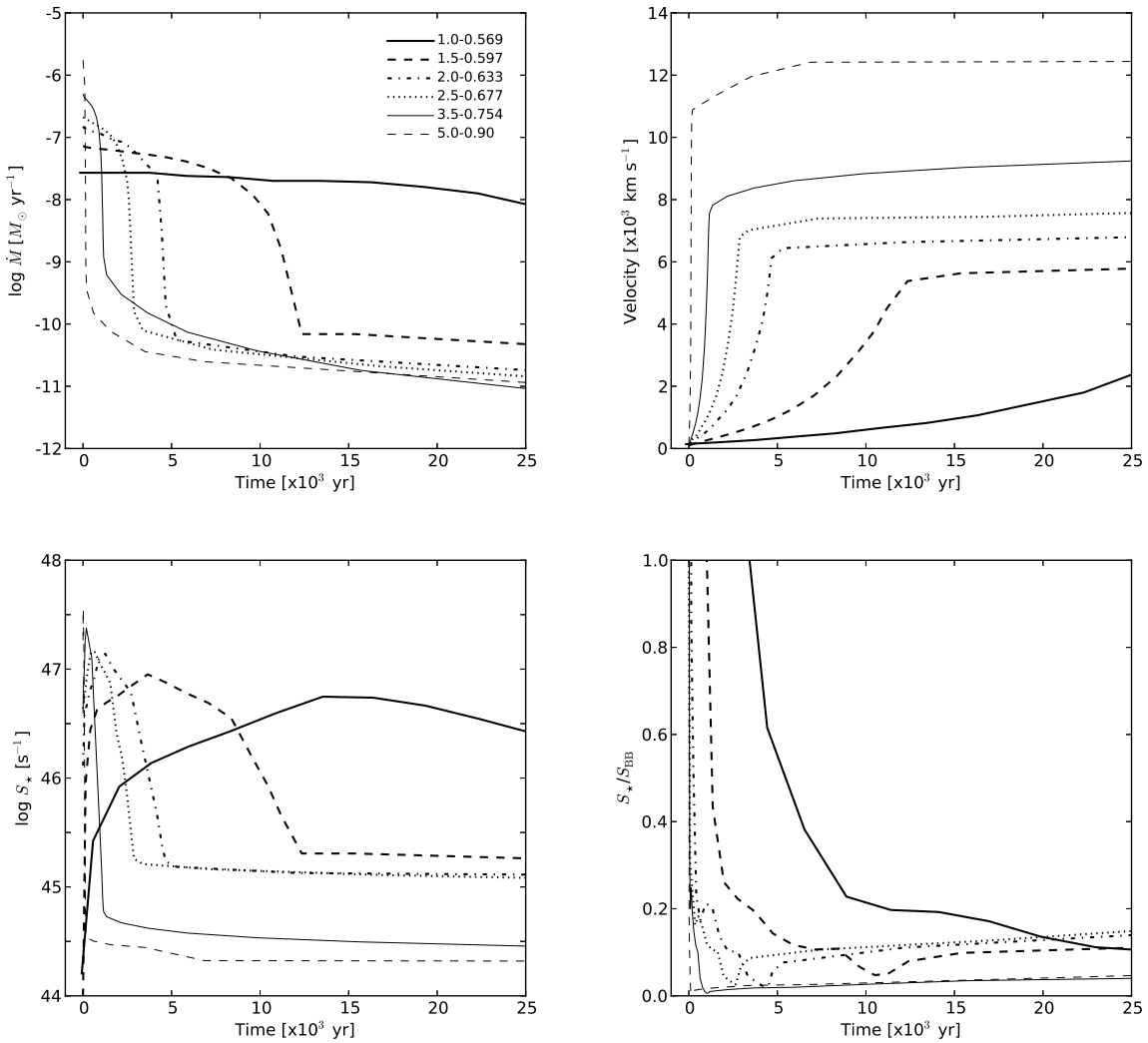

Figure 7.4: (Top-left) Mass-loss rate, (top-right) stellar wind velocity, and (bottom-left) ionizing photon flux for the different stellar models. (Bottom-right) Ratio of the ionizing photon flux over that expected from a black body model. The initial mass of each model is marked on top-left panel.

The AGB wind parameters (velocity and mass-loss rate) are empirical relations derived by Vassiliadis & Wood (1993) from observations of Galactic and Large Magellanic Cloud Mira variables and dust-enshrouded AGB stars and are the same as those used by Villaver et al. (2002a). The stellar wind parameters and ionizing photon flux during the hot CSPN stage were computed using the WM-basic hot star stellar atmosphere code (Pauldrach et al., 2012, 2001, 1994; Pauldrach, 1987; Pauldrach et al., 1986) using the stellar effective temperature, radius and surface gravity taken at discrete times from the stellar evolution models from Vassiliadis & Wood (1994). Figure 7.4 (top panels) shows the mass-loss rates and velocity profiles corresponding to the CSPN stage for the six evolution models. An improvement between our stellar parameters and those from previous numerical studies is that we do not model the ionizing photon flux as black body radiation. With the use of WM-basic we obtained realistic spectra at different evolution times of the star and we integrated them to compute the ionizing photon rate. Figure 7.4 (bottom-left panel) shows the resultant integrated ionizing photon flux for the six models studied here. As the star becomes hotter and more compact, the opacity increases and the ionizing photon flux diminishes considerably compared to a black body (see Figure 7.4 bottom-right panel).

As can be seen from Figure 7.4, the potential lifetime of a PN produced by a star of initial mass 5.0-0.90 $M_{\odot}$ is considerably shorter than that of a 1.0-0.569 $M_{\odot}$ star.

In common with Villaver et al. (2002b), we assume that the post-AGB stage starts when the star's effective temperature has reached 10^4 K and we do not model the short transition phase between the superwind and the post-AGB phase. We are aware that the inclusion of this transition may affect the hydrodynamics at the edge of the hot bubble (Perinotto et al., 2004).

7.4 Results

We will separate the presentation of the results into two groups according to similarities in the morphological evolution. This is mainly a consequence of the density structure at the end of the AGB stage (see Fig. 7.1) and the duration of the CSPN stage. Group A comprises the results from 1.0-0.569$M_{\odot}$, 1.5-0.597 $M_{\odot}$, 2.0-0.633 $M_{\odot}$, and 2.5-0.677 $M_{\odot}$ stars, while Group B consists of the 3.5-0.754 $M_{\odot}$ and 5.0-0.90 $M_{\odot}$ stars. The Group A models start with a circumstellar medium whose density falls off quite steeply with distance from the star. Group B models have a less steep fall off in the initial density distribution and are therefore denser at a given radius. At early times, all the models create well-defined hot bubbles with sharp shells but soon differences in the stellar wind parameters, the circumstellar medium left by the AGB stage, the ionizing photon rate variation and the different evolution timescales lead to significant morphological differences. We first describe the results without thermal conduction, and then discuss the main features of the inclusion of this physical effect.

All our models focus on the innermost 0.5 pc of the PN, since this is the region that hosts the hot bubble. As a result, we do not follow the complete evolution of the PN, since at late times

the photoionized outer shell leaves the computational domain. We present a series of images for each model, corresponding to the inner hot shocked wind bubble having mean radius 0.05, 0.1 and 0.2 pc for Group A models, and for the Group B models we show results corresponding to the maximum radius of the hot, shocked bubble, since in these cases the hot bubble stalls before it reaches 0.2 pc and then begins to collapse.

In each set of images, the total ionized number density, temperature, and Hα emitting region are shown[3]. Although the calculations are performed on the full $r-z$ plane, the results are symmetric about the midplane and for reasons of space, we show only half of the computational domain.

7.4.1 Group A

Models 1.0-0.569, 1.5-0.597, 2.0-0.633, and 2.5-0.677 (Figures 7.5, 7.6, 7.7, and 7.8) evolve in very similar ways due to the similarity of the initial circumstellar medium density distribution and velocity at the start of the post-AGB phase (see Fig. 7.1). These models follow the classic PNe formation scheme: the fast CSPN wind expands into the slowly expanding $v_{\rm exp} \lesssim 15$ km s^{-1}, smooth $\rho \propto r^{-2}$ (or steeper) density profile left after the AGB stage. The interaction between the fast wind and the slow wind forms a two-shock pattern: the outer shock sweeps up and compresses the AGB material, while the inner shock brakes and heats the fast wind. The two shocks are separated by a contact discontinuity. Behind the outer shock, the density is very high and cooling is efficient. The thin-shell instability (Vishniac, 1983; Vishniac & Ryu, 1989) acts at early times to corrugate the contact discontinuity separating the cold, dense material from the hot bubble and clumps begin to form.

The ionization front is initially trapped close to the thin shell, but as the shell moves outwards the opacity falls and the ionization front progress outwards. The clumps formed by the instability lead to variations in the opacity and as a consequence the shadowing instability becomes important at later times (Williams, 1999). Characteristic rays of alternating ionized and neutral material form at intermediate times. These can be visualized as bright streaks in the Hα emission trailing from bright Hα clumps, as can be seen in the central panels of Figs.7.5, 7.6, 7.7, and 7.8. At later times, the opacity in the ring of clumps drops as they expand outwards, and the whole outer region becomes photoionized and more homogeneous.

The continued acceleration of the fast stellar wind means that the swept-up shell is accelerated down the density gradient and Rayleigh-Taylor instabilities become important at the contact discontinuity between the low density, shocked fast wind material and the dense, swept-up shell. This leads to the formation of elongated, dense, partially ionized structures pointing inwards into the hot bubble. Neutral, dense material inside these filaments can be photoevaporated by the ionizing flux. The expanding, photoevaporated gas flows away from the head of the neutral filament, towards the central star. It then interacts dynamically with the radially

[3]All 2D images were produced with the matplotlib Python routines developed by Hunter (2007)

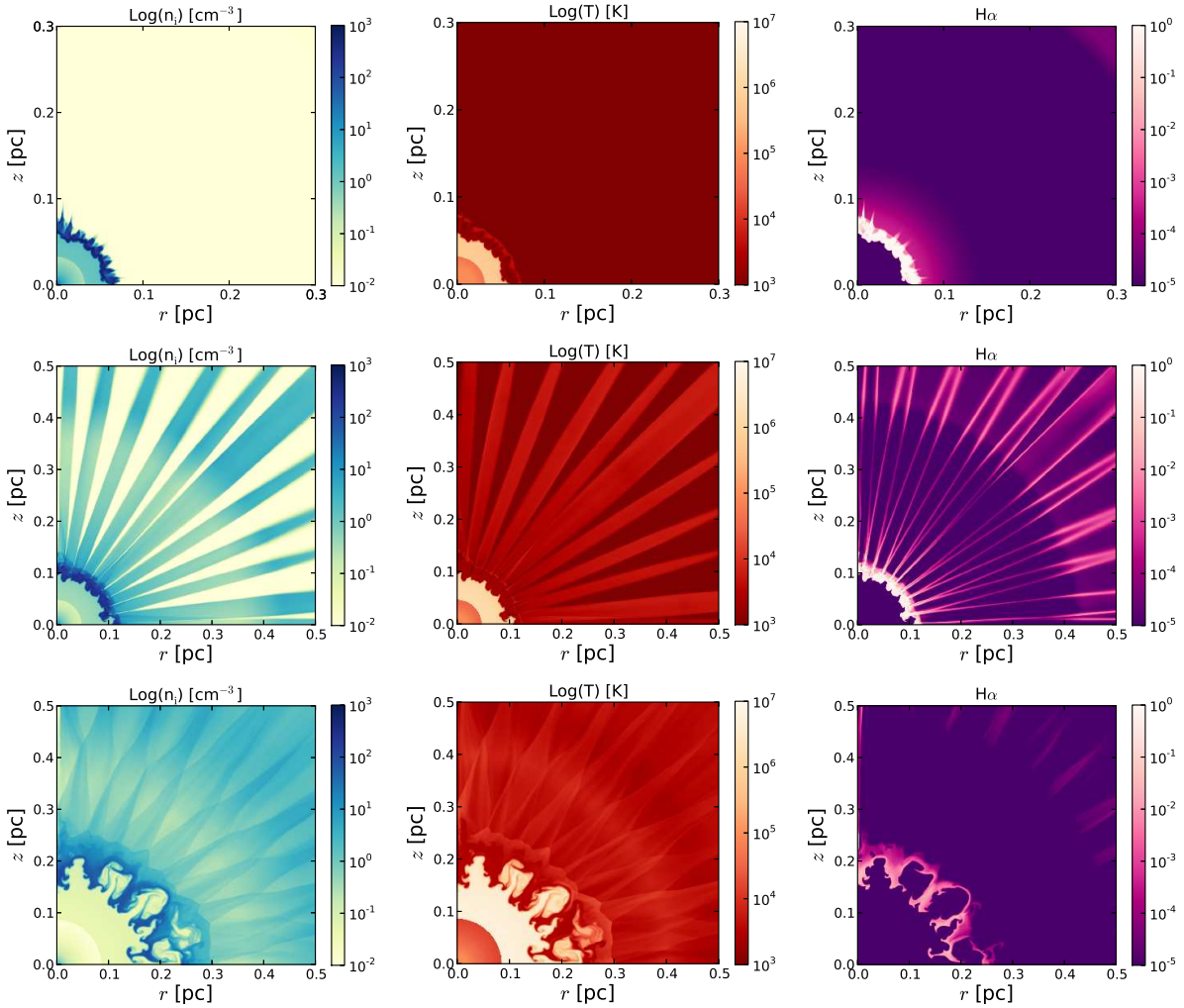

Figure 7.5: Total ionized number density (left panels), temperature(middle panels) and normalized Hα volume emissivity (right panels) for the PN formation for the 1.0-0.569 model 2D simulations without thermal conduction. The three rows correspond to the hot bubble having a mean radius of, from top to bottom, 0.05, 0.1 and 0.2 pc. These are equivalent to 2200, 5200 and 10700 yrs of post-AGB evolution, respectively. The bottom row corresponds to the time when the central star has an effective temperature and luminosity of $T_{\rm eff} = 31260$ K and $L = 3615 L_{\odot}$.

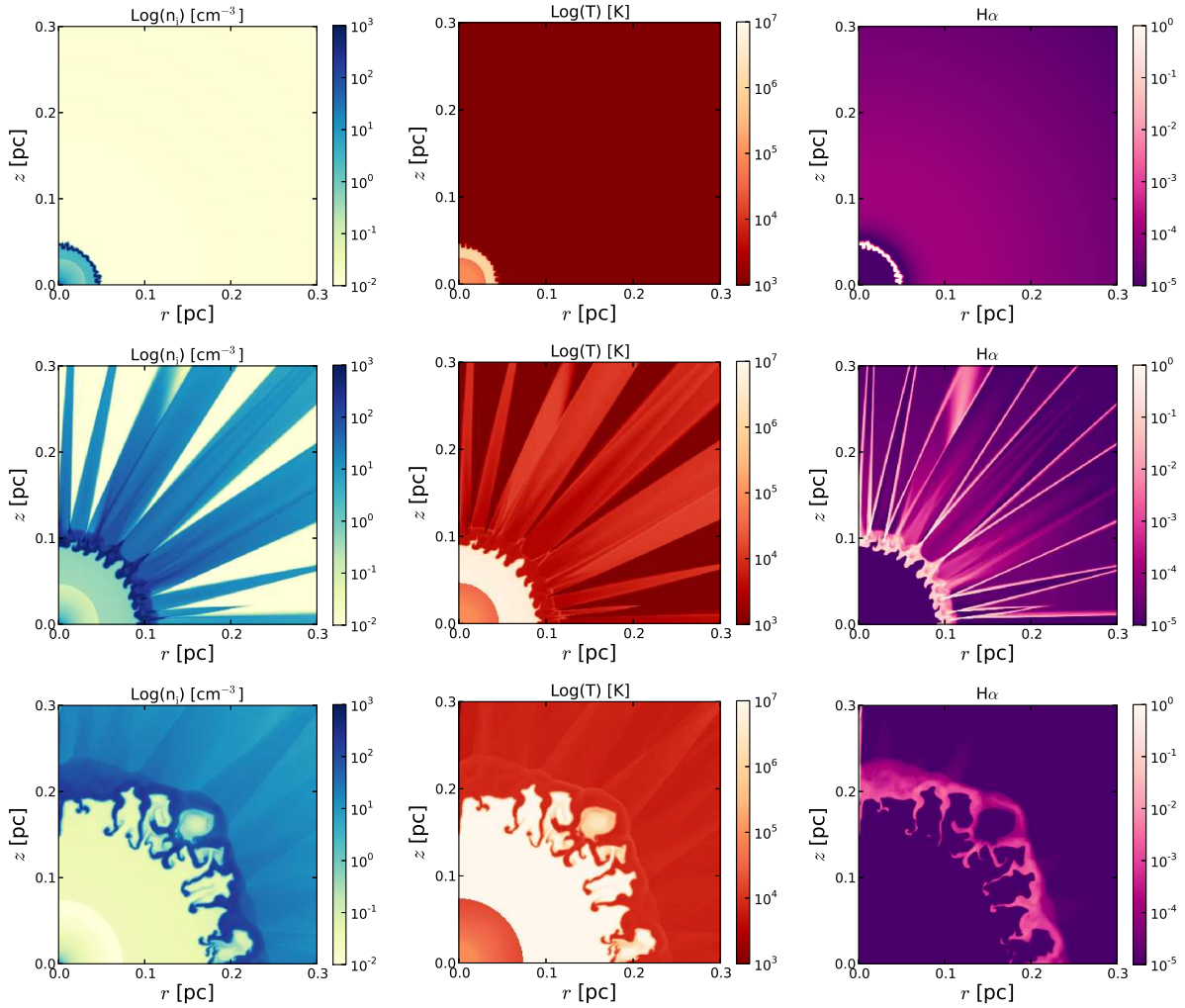

Figure 7.6: Same as Figure 7.5 but for the case of the 1.5-0.597 model 2D simulations without thermal conduction. The rows correspond to the hot bubble having a mean radius of, from top to bottom, 0.05, 0.1 and 0.2 pc. These are equivalent to 1000, 3500, and 7400 yrs of post-AGB evolution for this CSPN. The bottom row corresponds to the time when the central star has an effective temperature and luminosity of $T_{\rm eff} = 97720$ K and $L = 4310 L_{\odot}$.

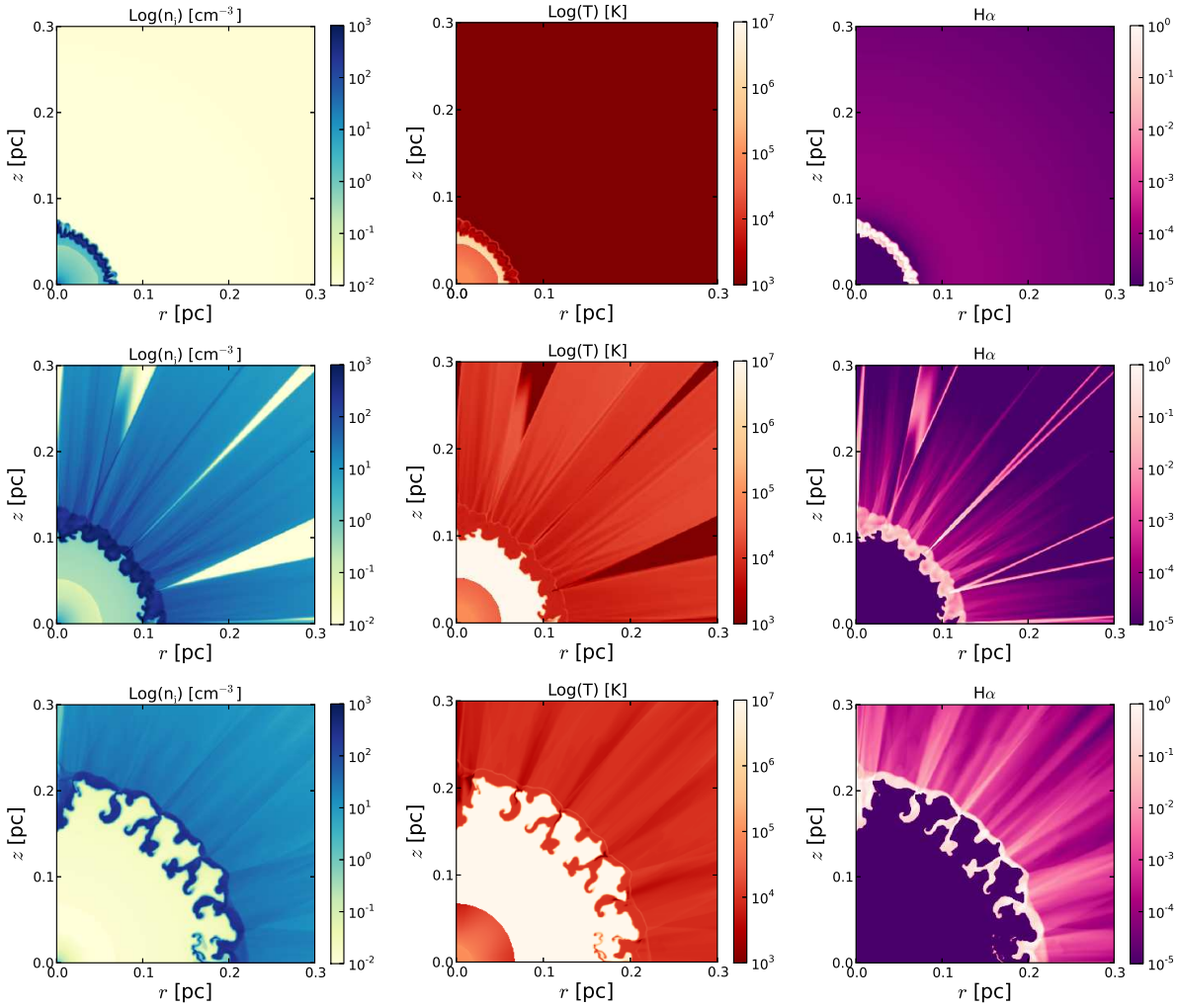

Figure 7.7: Same as Figure 7.5 but for the case of 2.0-0.633 model without thermal conduction. The rows correspond to the hot bubble having a mean radius of, from top to bottom, 0.05, 0.1 and 0.2 pc. These are equivalent to 600, 2000, and 4200 yrs of post-AGB evolution for this central star. The bottom row corresponds to the time when the central star has an effective temperature and luminosity of $T_{\rm eff} = 171790$ K and $L = 3200 L_{\odot}$.

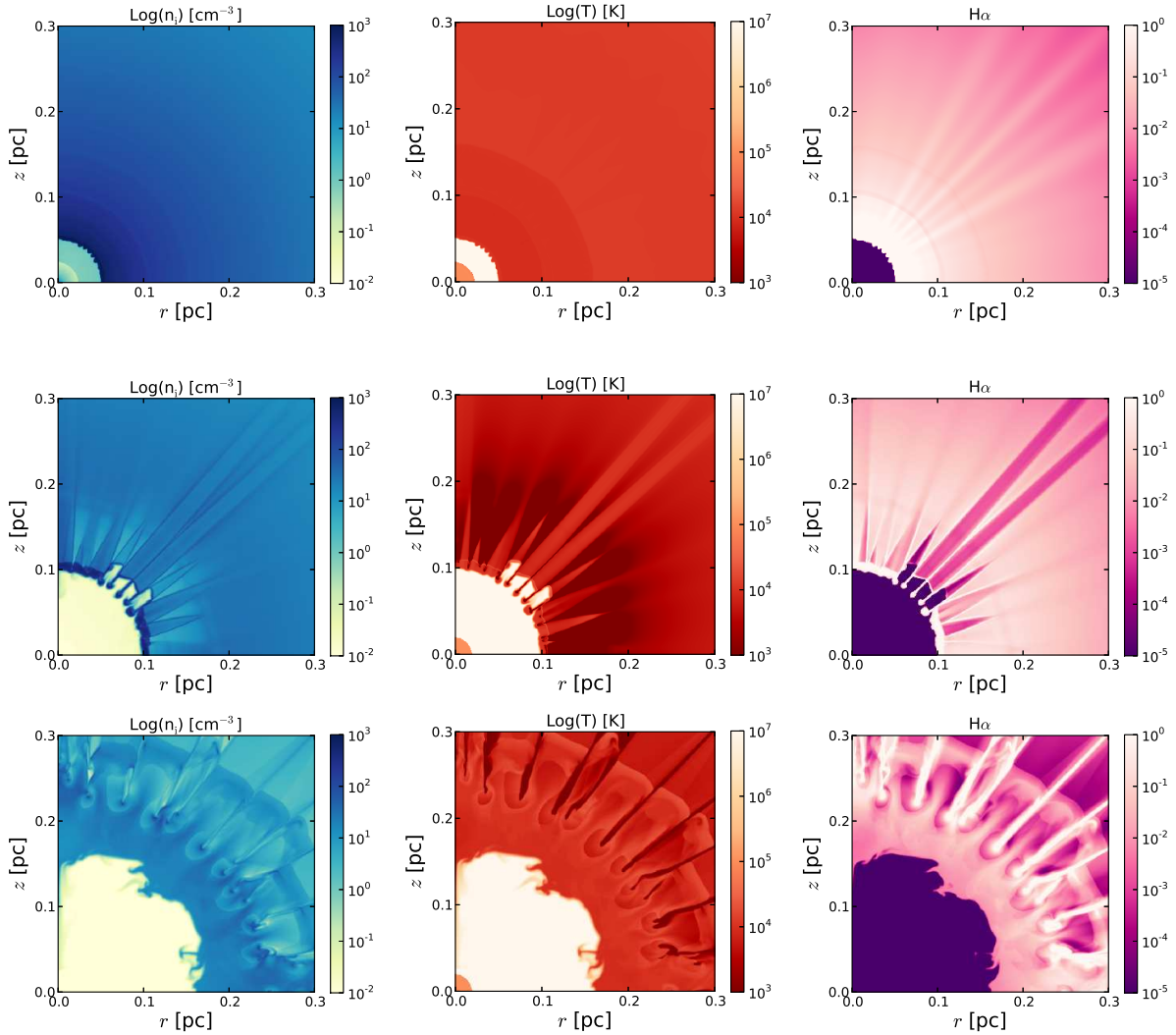

Figure 7.8: Same as Figure 7.5 but for the case of 2.5-0.677 model without thermal conduction. The rows correspond to the hot bubble having a mean radius of, from top to bottom, 0.05, 0.1 and 0.2 pc. These are equivalent to 1800, 2930, and 7300 yrs of post-AGB evolution for this CSPN. The bottom row corresponds to the time when the central star has an effective temperature and luminosity of $T_{\rm eff} = 127640$ K and $L = 165 L_{\odot}$.

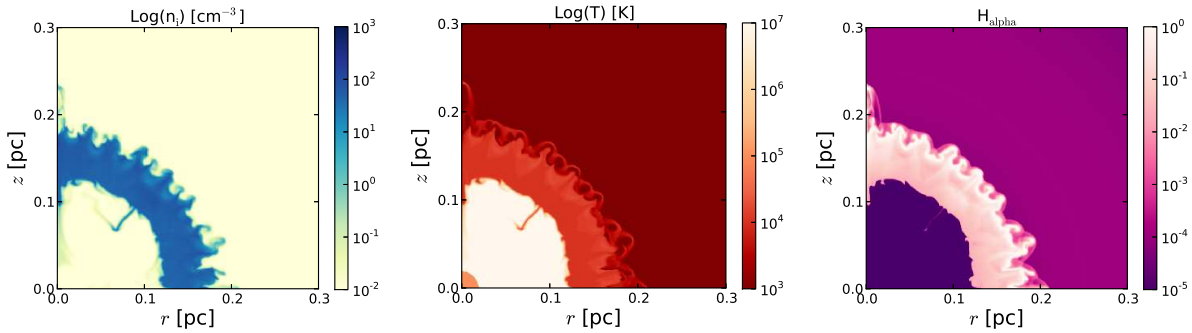

Figure 7.9: Same as Figure 7.5 but for the case of 3.5-0.754 model without thermal conduction. This set of panels corresponds to the maximum radius of the hot bubble, which occurs after 4900 yrs of post-AGB evolution for this CSPN. The panels corresponds to the time when the central star has an effective temperature and luminosity of $T_{\rm eff} = 162180$ K and $L = 250 L_{\odot}$.

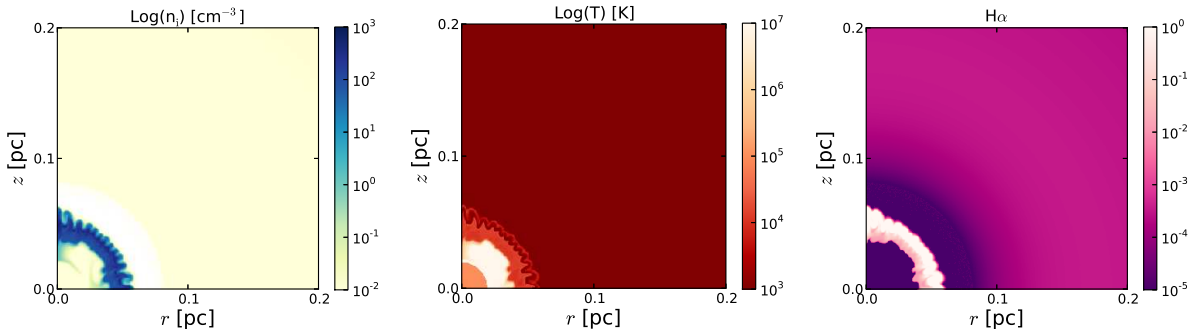

Figure 7.10: Same as Figure 7.5 but for the case of 5.0-0.90 model without thermal conduction. This set of panels corresponds to the maximum radius of the hot bubble, which occurs after 770 yrs of post-AGB evolution for this central star. The bottom row corresponds to the time when the central star has an effective temperature and luminosity of $T_{\rm eff} = 213800$ K and $L = 400 L_{\odot}$.

outflowing, shocked fast wind, giving rise to pockets of $\sim 10^6$ K gas with densities in the range $0.1 < n_{\rm i} < 1.0$ cm^{-3}. The hot bubble, on the other hand, has temperature $> 10^7$ K and density $n < 0.01$ cm^{-3}. Even when there is no neutral material inside the dense filaments to generate photoevaporated flows, the diversion of the shocked fast wind material around the dense obstacles leads to hydrodynamic ablation and the mixing of cooler, dense material into the faster, hot flow (see, e.g., Hartquist et al., 1986). In general, the models that evolve more slowly generate longer filamentary structures, simply because they have had a much longer time to grow by the time the hot bubble has expanded to 0.2 pc radius.

The 2.5-0.677 case is particularly interesting. The ring of clumps forms due to the thin-shell instability as for the other cases in this group. However, the faster acceleration of the stellar wind and the resulting higher pressure in the hot bubble mean that the clumps are pushed out to about 0.1 pc before the photoionization has the opportunity to cause this shell of swept-up

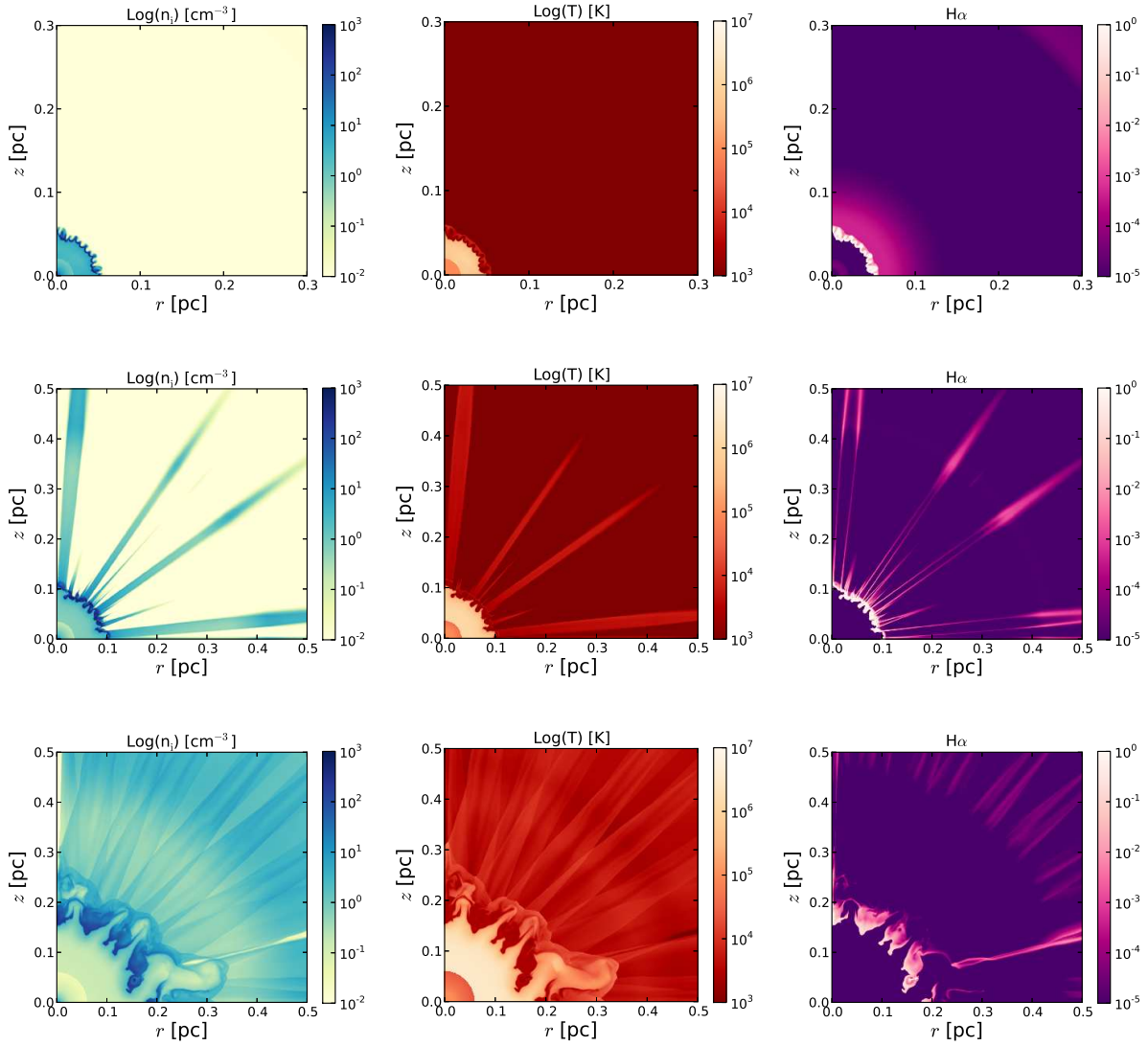

Figure 7.11: Same as Figure 7.5 but for the case of 1.0-0.569 model with thermal conduction. The rows correspond to the hot bubble having a mean radius of, from top to bottom, 0.05, 0.1 and 0.2 pc. These are equivalent to 1200, 4200, and 8700 yrs of post-AGB evolution for this central star. The bottom row corresponds to the time when the central star has an effective temperature and luminosity of $T_{\rm eff} = 29040$ K and $L = 3622 L_{\odot}$.

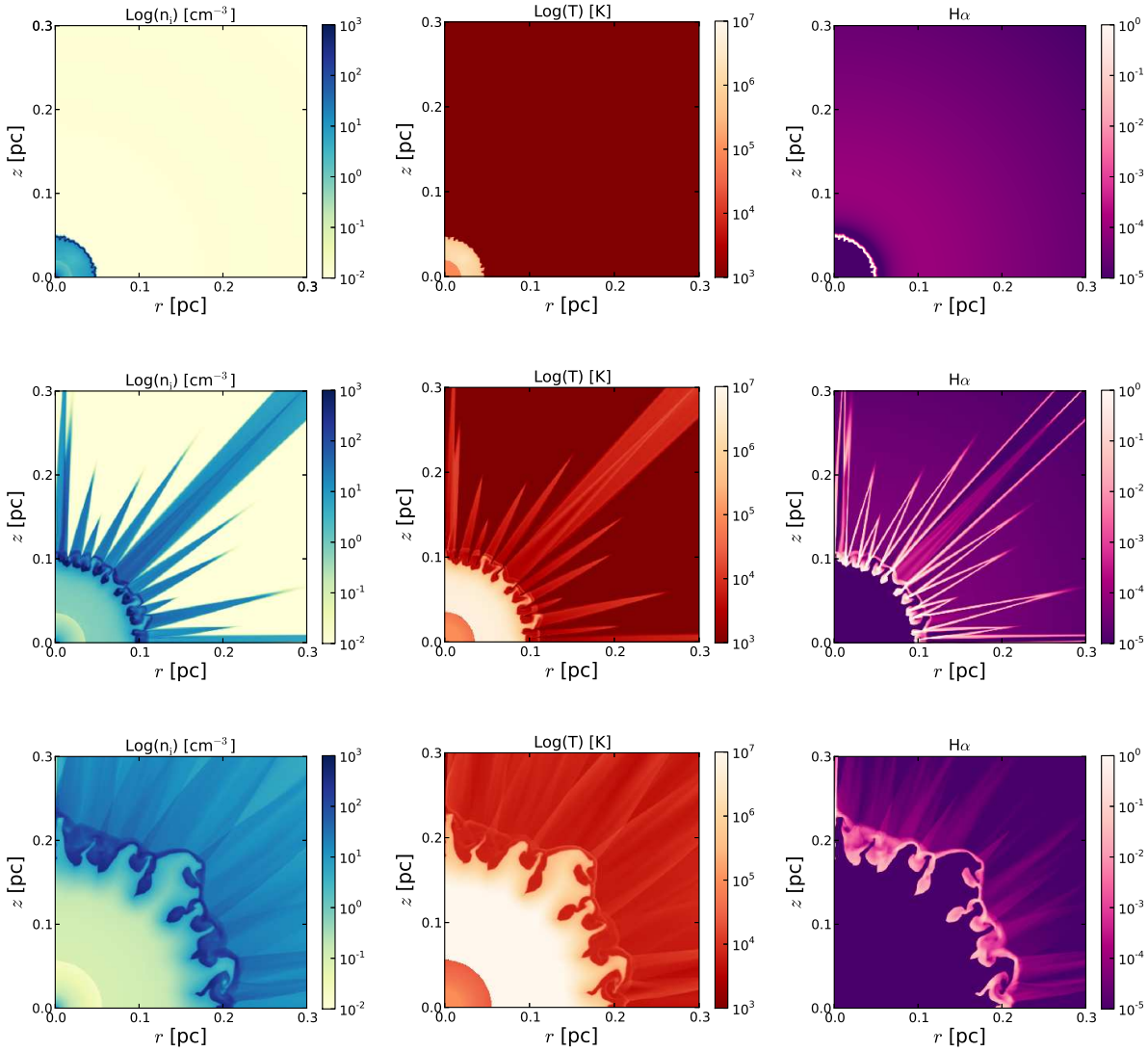

Figure 7.12: Same as Figure 7.5 but for the 1.5-0.597 model with thermal conduction. The rows correspond to the hot bubble having a mean radius of, from top to bottom, 0.05, 0.1 and 0.2 pc. These are equivalent to 1000, 3200, and 6200 yrs of post-AGB evolution for this CSPN. The bottom row corresponds to the time when the central star has an effective temperature and luminosity of $T_{\rm eff} = 90160$ K and $L = 4610 L_{\odot}$.

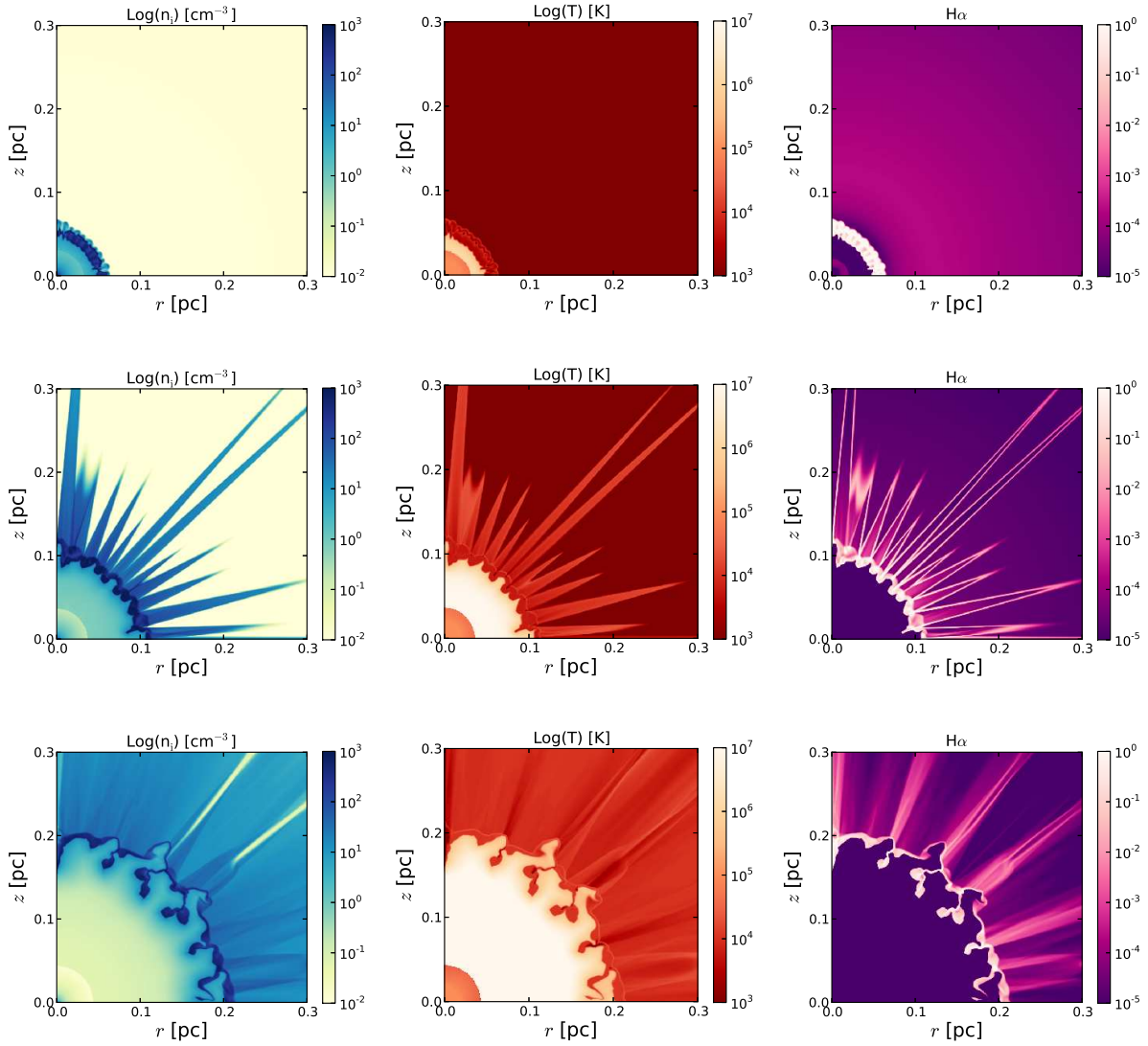

Figure 7.13: Same as Figure 7.5 but for the case of 2.0-0.633 model with thermal conduction. The rows correspond to the hot bubble having a mean radius of, from top to bottom, 0.05, 0.1 and 0.2 pc. These are equivalent to 800, 1600, and 3600 yrs of post-AGB evolution for this central star. The bottom row corresponds to the time when the central star has an effective temperature and luminosity of $T_{\rm eff} = 159220$ K and $L = 4520 L_{\odot}$.

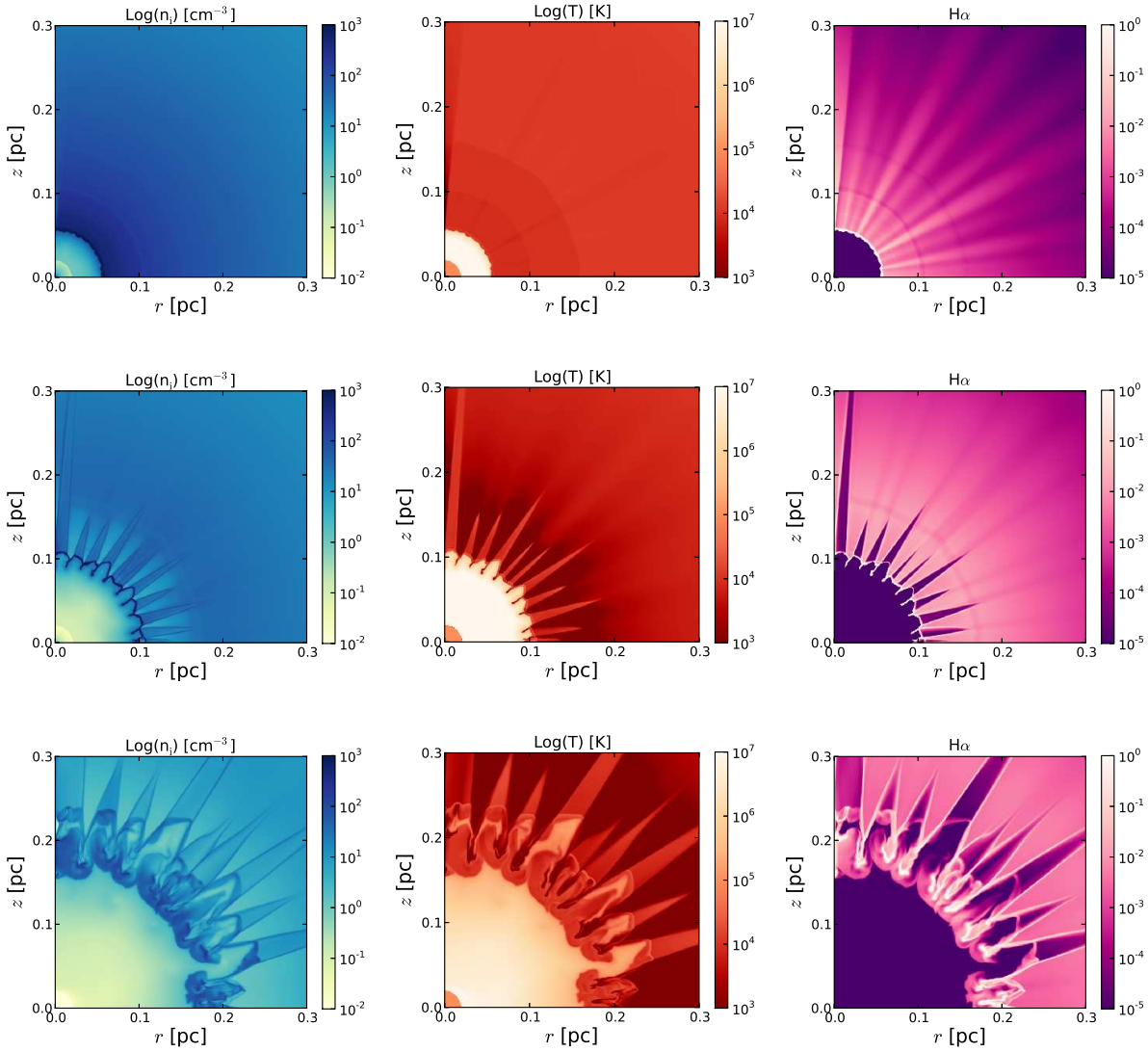

Figure 7.14: Same as Figure 7.5 but for the case of 2.5-0.677 model with thermal conduction. The rows correspond to the hot bubble having a mean radius of, from top to bottom, 0.05, 0.1 and 0.2 pc. These are equivalent to 1800, 2500, and 4300 yrs of post-AGB evolution for this CSPN. The bottom row corresponds to the time when the central star has an effective temperature and luminosity of $T_{\rm eff} = 142900$ K and $L = 295 L_{\odot}$.

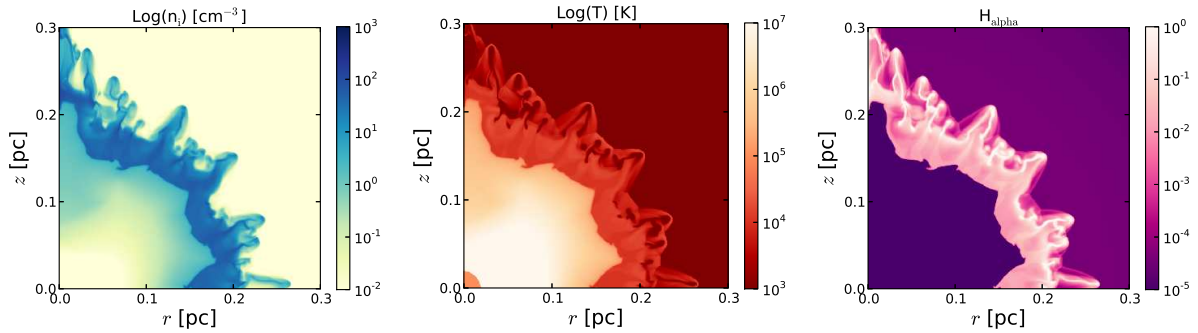

Figure 7.15: Same as Figure 7.5 but for the case of 3.5-0.754 model with thermal conduction. This set of panels corresponds to the maximum radius of the hot bubble, which occurs after 4900 yrs of post-AGB evolution for this CSPN. The panels corresponds to the time when the central star has an effective temperature and luminosity of $T_{\rm eff} = 162180$ K and $L = 250 L_{\odot}$.

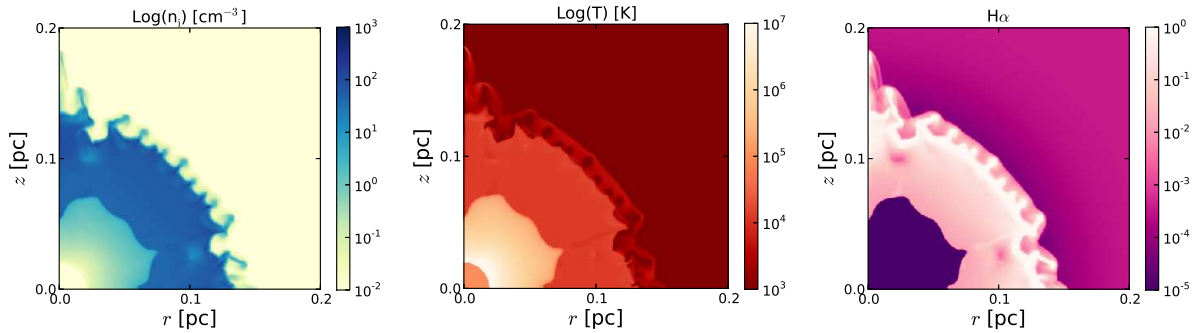

Figure 7.16: Same as Figure 7.5 but for the case of 5.0-0.90 model with thermal conduction. This set of panels corresponds to the maximum radius of the hot bubble, which occurs after 3370 yrs of post-AGB evolution for this central star. The bottom row corresponds to the time when the central star has an effective temperature and luminosity of $T_{\rm eff} = 180720$ K and $L = 180 L_{\odot}$.

material to expand. The clumps are therefore denser in this model at this radius than for other models. The ionizing photon rate of the central star now drops sharply and so the dense clump material recombines. This leads to the situation where the heads of the now neutral clumps develop ionization fronts and photoevaporation flows pointing towards the central star. Initially, the pressure of the hot bubble is higher than the pressure in the photoionized material, and the photoevaporated material is pushed back into the shell. As the whole structure expands slowly outwards, however, and the mass-loss rate of the central star drops sharply, the pressure in the photoevaporated flows becomes greater than that in the hot bubble and starts to expand away from the neutral clumps, back towards the central star after passing through a termination shock. This leads to the situation in the final row of Figure 7.8, where the hot bubble is surrounded by a thick shell of photoionized material, within which are embedded neutral clumps. The thick shell is slowly moving outwards, broadening as it goes, and the hot bubble is confined

by the slowly decreasing pressure of the photoionized gas.

Structures similar to those shown in Figures 7.5,7.6,7.7, and 7.8, i.e. a hot inner cavity surrounded by lacy structures in turn surrounded by a smooth photoionized shell, are observed in *Hubble Space Telescope* (HST) images of, e.g., IC 418, NGC 2392, NGC 6826, and NGC 7662, which also display inner diffuse X-ray emission surrounded by a photoionized shell detected with *Chandra* (Kastner et al., 2012; Ruiz et al., 2013).

7.4.2 Group B

Models from Group B are the result of the evolution of the most massive stars of our sample. The density distribution around these stars at the end of the AGB stage does not have such a steep radial dependence. This means that the fast wind expands into a denser medium and the swept-up shell of AGB material is correspondingly denser. In fact, the ionization front becomes trapped in the shell and does not manage to break out and hence the surrounding medium remains neutral throughout the evolution. The photoionized shell has a high thermal pressure and effectively confines the hot bubble to small radii. This effect is enhanced by the sharp CSPN mass-loss rate fall off (see Fig. 7.4 top-left panel) and as a consequence, the thermal pressure of the hot bubble decreases with time. There comes a point when the pressure inside the hot bubble becomes lower than that in the surrounding photoionized shell. This marks the point at which the hot bubble ceases to expand and starts to collapse. In Figures 7.9 and 7.10 we show the maximum extent of the hot bubble for these models. As can be seen, the hot bubble is surrounded by a thick photoionized shell and this is embedded within a dense neutral envelope.

7.4.3 Thermal Conduction Results

Figures 7.11, 7.12, 7.13, 7.14, 7.15, and 7.16 show the corresponding results for the cases with thermal conduction. Conduction by thermal electrons heats material from the dense, cool swept-up AGB shell and it then expands into the hot bubble. The evaporation process results in a sheath of comparatively dense ($n_{\rm i} \sim 1$ cm^{-3}), but hot ($10^5 < T < 10^6$ K) material around the fingers and clumps that were formed by the different instabilities at the interface between the hot bubble and dense swept-up shell. The total surface area of the conducting layer is very large because of these instabilities and substantial amounts of AGB shell material are evaporated into the hot bubble.

We find that the pressure in the hot bubble is higher in the models with conduction and so the expansion for all models is more rapid than for the models without conduction. This is because the evaporated material expands into the interclump region between the clumps and filaments in the broken shell and the bubble does not depressurize. At a given time, the instabilities are much more developed for the models with conduction than those without. The swept-up photoionized shells in the models with conduction are thinner because the hot bubble dominates the dynamics. The higher pressure means that these PNe are essentially wind-blown

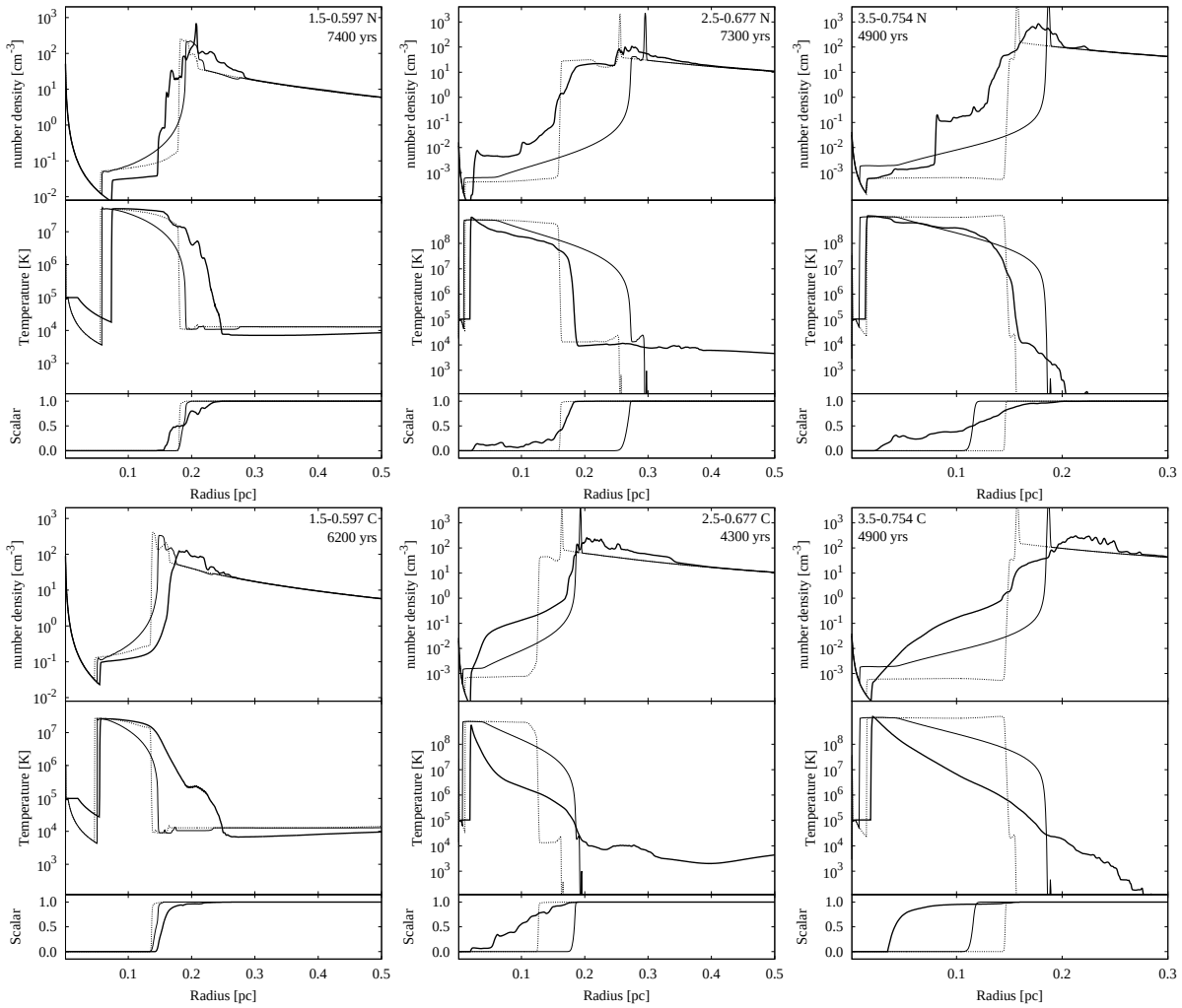

Figure 7.17: Comparison of 2D results with 1D results. Top row—2D results without thermal conduction. Bottom row—2D results with thermal conduction. In each plot the upper panel shows the total number density and the centre panel shows the temperature. The lower panel shows the value of a passive advected scalar. The thick solid line is the 2D simulation as a function of radius averaged over all angles from the stellar position. The thin solid line is the 1D result with thermal conduction and the dotted line is the 1D result without thermal conduction, both at the same evolution time as the corresponding 2D result.

bubbles surrounded by thin swept-up shells. The models without conduction, on the other hand, have their dynamics dictated by the pressure in the broad photoionized shell (see, e.g., Arthur, 2012; Raga et al., 2012).

7.4.4 Comparison between 2D and 1D results

In Figure 7.17 we compare the 2D results shown in the previous sections to the corresponding 1D results calculated at the same numerical resolution and with the same physical processes.

In order to make the comparison, we plot the 2D results as a function of radial distance from the star averaged over all angles. The top row of figures shows the averaged 2D results without conduction for the three principal models: 1.5-0.597, 2.5-0.677 and 3.5-0.754 and the bottom row shows the results when thermal conduction is included. Each figure also shows the 1D simulation results both with and without conduction at the same evolution times. The upper panel in each figure is the total number density, the centre panel is the temperature, and the lower panel shows the value of a passive advected scalar. This scalar has a value of one in the AGB wind material and is zero in the post-AGB fast wind material. Intermediate values indicate mixed regions: for the 1D simulations this is an indication of a cooling region, for the 2D simulations it is a result of the averaging process. The scalar shows how far the evaporated dense shell material has penetrated into the hot bubble.

We begin with an explanation of the 1D results. The classical description of a stellar wind bubble divides it into distinct regions (see e.g., Dyson & Williams, 1997, Arthur, 2012). Closest to the star, there is an inner region of unshocked, free-flowing stellar wind, which is separated from the hot bubble by an inward-facing shock. The hot bubble comprises hot, shocked stellar wind material and is separated by a contact discontinuity from the swept-up shell. This shell is composed of swept-up ambient medium, which for our models is AGB material. There can be a photoionized region inside the swept-up shell, in which case there will be an ionization front preceded by a shock in the neutral medium within the shell. External to the shell is undisturbed ambient medium. For a steady stellar wind, the pressure between the inner stellar wind shock and the outer neutral shock will be uniform. The contact discontinuity between the hot, shocked stellar wind and the swept-up, photoionized shell separates diffuse gas at $\sim 10^7$ K from dense gas at $\sim 10^4$ K. If magnetic fields are not important at this interface, conduction due to thermal electrons from the hot gas can lead to diffusion of heat across the contact discontinuity (see Eq. 7.5). For the hot, diffuse gas, the heat diffusion leads to a loss of thermal energy and hence a reduction of temperature in this gas together with a corresponding increase in density, since the pressure remains constant. For the cooler, dense gas, there is an increase in temperature. Depending on the details of the radiative cooling, the stellar wind, and the ionizing photon rate, one of the following must occur:

1. The cooling timescale for the heated dense material is so short that it cools immediately back to its original state. We remark that this case is also likely to occur if there is over-cooling at the contact discontinuity as a result of numerical diffusion.

2. The heated dense gas expands at constant pressure, where the pressure is dictated by conditions in the hot shocked wind bubble. The increase in volume (and corresponding decrease in density) in this gas pushes the shell outwards.

3. The heated dense gas cannot expand outwards and instead pushes inwards, increasing the pressure inside the hot, shocked bubble and pushing the inner stellar-wind shock closer

to the star. This occurs particularly if the stellar wind mechanical energy is decreasing rapidly with time.

After a cooling time has elapsed in the heated dense region, this gas begins to cool and its volume decreases (since the pressure must remain constant). The evolution timescales of these planetary nebula models are rather short, and hence cooling is not necessarily complete on the timescale of the simulation. If the simulation timescales are long enough, there can also be cooling in the reduced temperature diffuse gas. This sort of behaviour is seen in the long timescale H II region simulations of Arthur (2012).

Figure 7.17 shows examples of the second and third types of situations listed above. For example, the 1.5-0.597 models are examples of the second case, where in the models with conduction, the heated, dense gas expands and pushes the dense shell outwards, in comparison with the models without conduction. In these models, the ambient medium gas is photoionized beyond the swept-up shell. The 3.5-0.754 models, on the other hand, are examples of the third case, where the heated dense gas expands quite a long way back towards the star, pushing the inner stellar wind shock to smaller radii in the models with conduction, in comparison with the models without conduction. In these models, the swept-up shell of ambient medium gas is mainly neutral, since the ionizing photon rate falls off rapidly within the first 1000 yrs of the planetary nebula evolution. The scalar in these figures indicates the position of the interface between the wind material and the ambient material. The 2.5-0.677 models are more complicated, since the swept-up shell contains the ionization front and preceding neutral shock and is mainly, though not completely, photoionized. The photoionized gas regulates the pressure throughout the planetary nebula once the stellar wind mechanical luminosity begins to decline.

We now examine the differences between the 2D and 1D simulations[4]. For the 1.5-0.597 case without conduction we immediately notice that the inner stellar wind shock for the angle-averaged 2D results is at a larger radius than for the equivalent 1D models. This means that the density, and hence the pressure in the hot, shocked wind bubble is lower in the 2D case, since the post-shock temperature is the same in all cases because it depends only on the stellar wind velocity. The reason for the lower pressure can be appreciated by looking at (e.g.) Figure 7.6. The swept-up shell in this figure has broken up due to instabilities and the hot wind can find its way through the gaps, depressurising the hot bubble. Although the peak velocity occurs at roughly the same radius as in the 1D models, warm ($T > 10^4$ K) gas extends beyond the shell as a result of mass pick-up from the clumps and filaments by the hot wind as it flows through the gaps in the leaky bubble. For the 1.5-0.597 2D model with conduction, the inner stellar wind shock coincides more-or-less with the 1D results. This is because conduction heats the gas at the surface of the cold, dense filaments and the expansion of this gas seals the gaps in the bubble. The result is a broad, roughly uniform density shell with a temperature of a few times 10^5 K.

[4]The obvious difference at small radii is due to the difference in size of the wind injection region in the 2D and 1D cases.

The averaged locations of the interface between hot bubble and swept-up shell in 2.5-0.677 2D models with and without conduction correspond roughly to their 1D counterparts. However, the average density as a function of radius within the hot bubble is an order of magnitude higher in both cases. This is a result of hydrodynamical mixing of dense material into the hot diffuse gas at the irregular interface. Non-radial motions thoroughly mix the ablated, cool, dense gas throughout the hot bubble, thereby raising the average density and lowering the average temperature. This is in contrast to the 1D conduction results, where the temperature in the hot bubble is reduced solely as a result of heat loss due to diffusion of heat, with no corresponding diffusion of material. The averaged 2D models have lower density, broader, swept-up shells than the 1D models, and opacity variations in these shells between the clump and interclump gas mean than photons can leak through into the surrounding ambient medium. In the 1D cases, the photoionized region remains trapped in the swept-up shell.

The results for the 3.5-0.754 2D model without conduction are similar to their 1D counterpart. The average density inside the hot bubble is dominated by the long, dense filament that can be seen in Figure 7.9 extending inwards from the interface. The swept-up shell is far broader and has a much lower density than in the 1D models and is partially ionized. In the 2D model with conduction, the interface is extremely distorted (see Fig. 7.15) and this makes it difficult to identify in the averaged density and temperature plots.

7.4.5 Hot bubble mass

The clumps and filaments formed by the instabilities at the interface between the hot, shocked fast wind and the dense, photoionized shell are sources of mass for the hot bubble. Hydrodynamic ablation and photoevaporation remove material from the dense structures, which then shocks against and mixes into the hot shocked wind (Steffen & López, 2004). The mass of hot gas (where we consider $T > 8 \times 10^4$ K to be "hot") is thus not solely due to the mass lost by the post-AGB star. Thermal conduction can also enhance the mass of gas in the hot bubble by directly evaporating photoionized shell material at the interface. The increased surface area due to the corrugations in the interface facilitates the mixing processes.

To illustrate this, we compute the mass of hot gas in the bubble as a function of time for the 1.5-0.597 and 2.0-0.633 models (the other cases are similar) for the first 8000 yr of the PNe. Figure 7.18 shows the total mass injected by the post-AGB wind, obtained by integrating the mass-loss rates shown in Figure 7.4 and the actual mass of hot gas in the numerical simulation for both models and for the simulations with and without thermal conduction. It is clear that the hot bubble becomes dominated by mixed-in mass even in the simulations without conduction. The mixed-in mass is one order of magnitude higher than the mass injected by the hot central star wind in the simulations without conduction, and two orders of magnitude higher in the simulations with conduction. It must be emphasized that the hot bubble masses from our 2D simulations without thermal conduction are comparable to those obtained by Steffen et al.

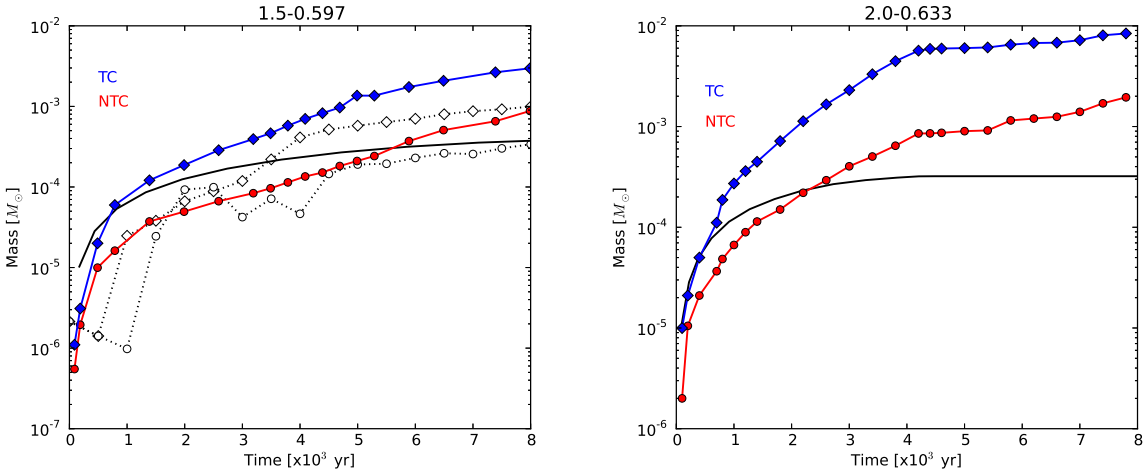

Figure 7.18: The hot bubble mass as a function of time for the 1.5-0.597 and 2.0-0.633 models. The solid lines without symbols represent the amount of mass injected by the fast wind. The lines with circles (red) represent the total mass of the hot bubble without thermal conduction, while the diamonds (blue) represent the model with thermal conduction.

(2008) for 1D models with thermal conduction.

The increase in the mass of hot gas in the PNe in these 2D simulations as compared to our 1D models (see also the 1D simulations of Steffen et al., 2008) suggests that detection in soft X-rays is likely even when thermal conduction is not present. We address this issue in the following chapter.

7.4.6 Hot bubble expansion velocity

The radial velocity of the photoionized shell is of observational and theoretical interest (García-Segura et al., 2006; Pereyra et al., 2013; Perinotto et al., 2004; Schönberner et al., 2005b; Villaver et al., 2002b) since it provides a link between observable properties of the PN and the evolution of the central star. The photoionized shell kinematics depends on the initial density distribution left by the AGB star, the stellar wind mechanical energy and the stellar ionizing photon luminosity. Our simulations are focused on the formation of the hot bubble (see § 2.3), and our spatial domain extends only to 0.5 pc radius from the star. As a result, we lose information about the outer shell that results from the ionization front and its interaction with the outer rim of the AGB material. However, we can study the expansion velocity of the dense shell created in the fast wind-AGB-wind interaction. This dense shell, or W-shell (see Mellema, 1995), is created by the expansion of the hot shocked wind into the photoionized AGB material.

Since the fast wind-AGB-wind interaction provokes the instabilities, we include them as part of the W-shell for the velocity calculation. We define the velocity as the mass-weighted

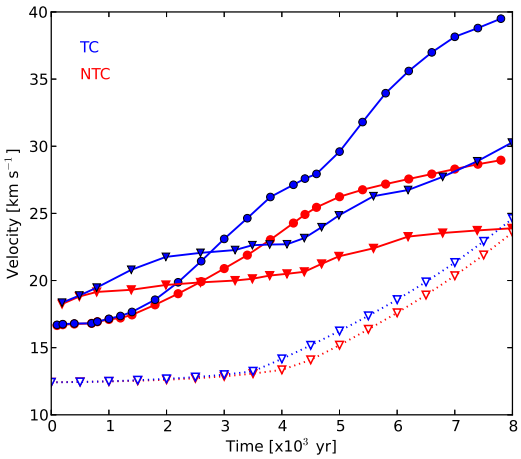

Figure 7.19: W-shell velocity as a function of time for the 1.5-0.597 (triangles) and 2.0-0.633 (circles) models. Models including thermal conduction are represented with filled (red) markers.

mean radial velocity of the photoionized gas in the W-shell by

$$\bar{v} = \frac{\int \rho_{\rm i} v dV}{\int \rho_{\rm i} dV} \ , \tag{7.8}$$

where the integrals are performed over all photoionized gas with a number density in excess of 200 cm^{-3}.

Figure 7.19 shows the W-shell velocity as a function of time for the 1.5-0.597 and 2.0-0.633 models with and without thermal conduction. All models show a steady increase of the W-shell velocity with time, which is consistent with previous numerical results by Schönberner et al. (2005b). Observational results (Pereyra et al., 2013) suggest that the nebular shells decelerate as the central star luminosity decreases, however, we do not find this from our models. Our models with thermal conduction have, in general, faster expansion rates, since the pressure in the hot bubble is higher in these models than in those without conduction. We do not calculate the nebular expansion for the 3.5-0.754 and 5.0-0.90 models as these would not be observationally detected since they are ionization bounded and enshrouded by dense neutral material.

7.5 Discussion

The results presented in §8.3 illustrate the formation of hot bubbles for different initial mass stellar evolution models. Instabilities corrugate the interface between the hot bubble and the surrounding dense shell and lead to the formation of filaments and clumps. The properties of these clumps depend on the interplay between the initial AGB density profile and the time-dependence of the stellar wind and ionizing photon rate in the post-AGB phase. The stellar wind

velocity increases steadily with time for CSPN masses $< 0.754 M_{\odot}$), and so the temperature of the hot, shocked stellar wind increases during the PN lifetime. In the case of the 1.0-0.569 $M_{\odot}$ model, the velocity increases extremely slowly, and the temperature in the hot bubble is only $T \sim 10^6$ K even after 5000 yrs of PN evolution. On the other hand, the velocity increase in the 2.0-0.633 $M_{\odot}$ model is much more rapid, and after 5000 yrs, the hot shocked wind temperature is $T > 10^8$ K. For the most massive star models (3.5-0.754 and 5.0-0.90), the velocity almost instantaneously increases to $V_w > 6000$ km s^{-1} but after only ~ 1000 yrs the mechanical energy of post-AGB wind decays dramatically and the bubble starts to collapse.

Rayleigh-Taylor instabilities are important at the contact discontinuity between the hot bubble and the dense shell, due to the continued acceleration of the stellar wind, together with expansion in a radially decreasing density distribution. The swept-up AGB material also cools rapidly and forms a thin, dense shell which is unstable to thin shell instabilities (Vishniac, 1983). Once dense clumps have begun to form, the shadowing instability (Williams, 1999) comes into play due to the variations in opacity, and the density contrasts between clump and interclump regions can become even more enhanced. If the density becomes high enough, the clumps become opaque to photoionizing radiation and the gas within them can recombine. We speculate that neutral clumps such as those formed in our 2.5-0.677 simulations could be precursors of molecular clumps observed in PNe such as NGC 6053 and NGC 6720 (Lupu et al., 2006; van Hoof et al., 2010). However, in the present simulations our treatment of the neutral gas is not sufficiently detailed to follow the formation of molecules and dust.

Another important factor in the formation of the clumps and filaments is the cooling curve used (see Fig 7.2), which for photoionized regions depends on the abundances in the gas and on the ionization parameter (ϕ/n). Our cooling curve was calibrated using the Cloudy photoionization code for standard PN abundances (see Table 7.1), mean stellar effective temperature $T_{\rm eff} = 10^5$ K, gas density 10^3 cm^{-3} and ionizing photon flux $\phi = 10^{11}$ cm^{-2}s^{-1}. There are differences between results obtained using this cooling curve and cooling curves for different abundance sets and ionization parameters.

As an illustration, in Figure 7.20 we compare the total ionized number density resulting from a simulation for a 1.0-0.569 model without thermal conduction using our usual PN cooling curve with that of a simulation using a cooling curve calibrated for a cooler star ($T_{\rm eff} = 40$ kK) with standard ISM abundances taken from Cloudy (see Table 7.1), gas density 1 cm^{-3} and ionizing photon flux $\phi = 10^9$ cm^{-2}s^{-1} (Fig. 7.2–thin-solid line). The appearance of the interface is very different: there are fewer clumps and the instability appears to be more a pure Rayleigh-Taylor type. The density of the clumps at the interface is not large enough to trap the ionizing photons and so the region beyond the swept-up shell is completely photoionized. The differences due to the adopted cooling curves are most important in the temperature range 10^4K $< T < 10^5$K, and cooling at higher temperatures is independent of the stellar parameters, since the hot gas is collisionally ionized, although the metallicity remains an important factor (see Steffen et al.,

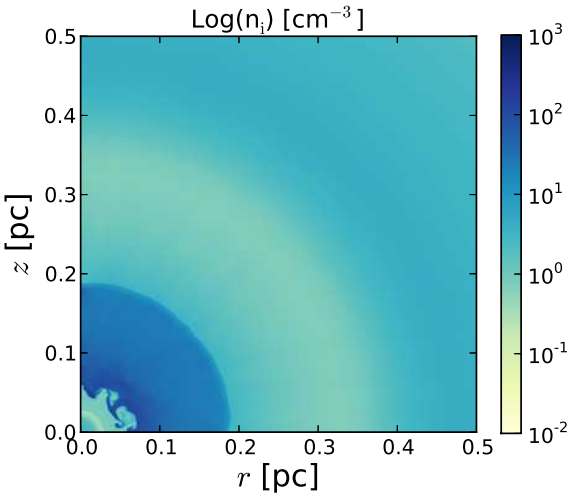

Figure 7.20: Ionized number density for the 1.0-0.569 model without thermal conduction at 5200 yr. Upper panel: simulation using the planetary nebula cooling curve described in § 7.2. Lower panel: simulation using a cooling curve for standard ISM abundances, stellar effective temperature $T_{\rm eff} = 40000$ K and ionizing flux $\phi = 10^9$ cm^{-2}s^{-1} (see Fig. 7.2).

2012). While the cooling curve used in the present simulation is a clear improvement over the standard ISM CIE cooling curve typically used in hydrodynamical simulations, it would be more accurate to tailor the cooling to the evolving stellar parameters, ionization parameter and abundance set. Finally, our cooling assumes ionization equilibrium but cooling can also be modified if nonequilibrium ionization is taken into account (see Steffen et al., 2008).

The clumps and filaments are sources of mixing due to hydrodynamic ablation, shock diffraction and photoevaporation and the large surface area leads to substantial quantities of dense material being shocked and incorporated into the hot bubble. For models without thermal conduction, the breakup of the dense shell can cause hot gas to leak out of the bubble, flowing between the clumps and filaments and thereby depressurising the hot bubble. The inclusion of thermal conduction leads to evaporation of material at the interface, which fills in the inter-clump region in the broken shell and reseals the bubble. This results in higher pressures in the conduction models than in those without conduction. Indeed, the expansion of the models without thermal conduction is dominated by the pressure of the thick shell of photoionized gas around the hot bubble, while the models with thermal conduction are more similar to wind-blown bubbles, surrounded by thin shells of swept-up photoionized material.

We have investigated the extent to which numerical diffusion is responsible for mixing across the interface by running a test simulation consisting of an inner, circular region of hot, diffuse gas in pressure equilibrium with a surrounding envelope of dense, cool gas. Both gases were assumed to be at rest, but radiative cooling was taken into account. After 10,000 yrs, the interface between the two fluids was only 4 cells wide and was not growing with time. This gives

us confidence that the mixing seen in our simulations without conduction is a real, hydrodynamical effect rather than a numerical one. We have also undertaken studies of the effect of increasing and decreasing the numerical resolution and the size of the wind injection region. The qualitative results are the same, although small details do vary.

7.5.1 Comparison with previous works

There are some differences that are worth noting between our numerical calculations and the referenced works mentioned in § 7.1. We limit our comparison to those works that have taken into account a detailed treatment of the evolution of the stellar wind parameters and show the formation of hot bubbles, principally those studies presented by Villaver et al. (2002a,b), Perinotto et al. (2004) and Steffen et al. (2008).

Potential differences are due to the stellar evolution models, which determine both the initial conditions defined by the final few thermal pulses of the AGB state and the stellar wind parameters in the post-AGB phase, the numerical method and the physics included in the model.

We adopt the same AGB wind parameters as (Villaver et al., 2002a), i.e., those calculated by Vassiliadis & Wood (1993) and so do not expect large departures from their results. Indeed, the density profiles we arrive at at the end of the TP-AGB stage are very similar, particularly the innermost 0.5 pc, which is of most interest to us. We find steep density profiles ($\rho \propto r^{<-2}$) for low initial stellar mass models and shallow density profiles ($\rho \propto r^{>-2}$) for the high initial stellar mass models. Perinotto et al. (2004) and Steffen et al. (2008) consider two types of AGB winds: a constant mass-loss rate and wind velocity "kinematical" model, which gives a $\rho \propto r^{-2}$ density profile, and a "hydrodynamical" model, where the mass-loss rate and wind velocity are based on the AGB mass-loss prescription of Blöcker (1995), which leads to a variety of density gradients. As pointed out in these previous works, once the photoionization switches the fine details of the initial density and velocity profiles are quickly erased by the shock that passes through the neutral gas ahead of the ionization front.

For the post-AGB evolution, we use the same stellar evolution models as Villaver et al. (2002b). However, we calculate the stellar wind mass loss and terminal velocity velocity using the WM-Basic code (Pauldrach et al., 1986, and subsequent papers.). We also obtained the ionizing photon flux from WM-Basic instead of using a black body. Our stellar wind parameters differ from those of Villaver et al. (2002b), who use the empirical fits of Vassiliadis & Wood (1994) to the data compiled by Pauldrach et al. (1988). The resulting mass-loss rates are in the same range of values with very similar temporal dependence. On the other hand, the terminal wind velocities obtained by Villaver et al. (2002b) are a factor of approximately 2 higher than ours for all stellar models presented in our Figure 7.4 (top-right panel).

Perinotto et al. (2004) and Steffen et al. (2008) use different evolutionary models for the post-AGB stage (Blöcker, 1995; Schönberner, 1983). Moreover, for stellar effective temperatures below 25 kK they use the Reimers (1975) prescription for the stellar wind mass-loss rate. Their stel-

lar wind properties are therefore not quite the same as those used in this work—our mass-loss rates are slightly higher and our wind terminal velocity is slightly lower—but the differences are not significant since the stellar wind mechanical luminosity $L_{\rm w} = 0.5\dot{M}V_{\rm w}^2$ is the important quantity. Once again, a black body spectrum is used to calculate the ionizing photon rate.

The minor differences in the stellar wind parameters and ionizing photon rate between our models and previously published work are dynamically not that important. The duration of the transition from the AGB to the white dwarf stage is the main indicator of whether the planetary nebula will be density bounded (as seen for the models with initial mass $M < 2.5M_{\odot}$) or ionization bounded (as seen for the 3.5-0.754 and 5.0-0.90 models). Our results agree broadly with those of Villaver et al. (2002b) and Perinotto et al. (2004) in this regard but the fact that our simulations are 2D allows the possibility that the shell of AGB material swept up by the fast wind in the early stages of the PN evolution breaks up due to instabilities. For the lower initial stellar mass models, this creates regions of higher opacity (clumps) that may even recombine and become neutral condensations embedded in a surrounding photoionized flow, and regions of lower opacity through which the ionizing photons may pass to photoionize the material beyond the shell. The formation of these clumps starts with the thin shell instability and depends on the metallicity of the gas and on the form of the cooling curve. The evolution of the photoionized gas within and beyond the shell depends on the radiative transfer model. Our code includes a self-consistent treatment of the radiative transfer and we are able to follow regions of partially ionized, recombining gas (see also Perinotto et al., 2004; Steffen et al., 2008), in contrast to Villaver et al. (2002b) who use the Strömgren approximation.

Unlike Steffen et al. (2008), we find that in our 2D models the thermal conduction does have a dynamical effect on the planetary nebula system. For the lower mass CSPN ($M_{\rm WD} < 0.677M_{\odot}$), models without conduction have leaky bubbles, whereas thermal conduction reseals the gaps between the clumps and filaments in the broken shell. The gas between the clumps and filaments is material which has been evaporated from the filaments and has expanded as it is heated. The hot bubble in these models grows much more quickly, reaching our "target" distance of 0.2 pc much sooner than in the models without conduction, since there is no loss of pressure, and the interclump material has temperatures $T \sim 10^5$ K. The interclump material in the models without conduction, on the other hand, is hot gas with $T > 10^6$ K escaping from the bubble.

Figure 7.17 shows that for the higher mass models, the positions of the inner and outer shock waves and the interface between the hot bubble and swept-up shell for models both with and without conduction for the 2D simulations averaged over angle coincide reasonably well with their 1D counterparts. However, in the 2D cases, a substantial amount of dense shell material is shed from the clumps and filaments by hydrodynamic interaction, photoevaporation and thermal evaporation and is thoroughly mixed throughout the hot bubble by non-radial motions. At later times, once the dynamical time has become as large as the cooling time, cooling will become important inside the hot bubble. This will occur much earlier in the 2D simulations than in the

1D simulations because the density is much higher in the former.

While cooling is still unimportant, the effect of thermal conduction is to raise the temperature in the cool, dense gas at the interface with the hot bubble. In both 1D and 2D simulations, the heated gas expands and pushes the swept-up shell outwards. This is particularly the case with the higher-mass CSPN models $M_{\rm WD} > 0.677 M_{\odot}$). These models have larger hot bubbles than their counterparts without conduction, although they still remain enshrouded by neutral material and would not be detectable.

Our 2.5-0.677 model shows intermediate behaviour. The simulation without conduction has "leaky bubble" characteristics, while the simulation with conduction mixes quite a lot of dense shell material back into the bubble. In these models, the clumps in the broken shell recombine and photoevaporated material flows off the heads of these clumps back towards the star.

The effect of thermal conduction on the dynamics is also evident in Figure 7.19, where we show the W-shell (dense shell formed by the fast wind-AGB wind interaction) velocity as a function of time for two of our lower mass CSPN models, 1.5-0.597 and 2.0-0.633. For these models, the simulations without conduction are of the "leaky bubble" type, where hot, shocked gas pushes its way between the clumps and filaments of the broken shell. The reduced pressure in the hot bubble results in lower expansion velocities for the external photoionized shell. The corresponding models with conduction remain pressurised, since the gaps in the shell are sealed by material evaporated from the filaments. The expansion velocities in the surrounding photoionized shell are correspondingly higher.

Mellema & Frank (1995) and Mellema (1995) performed 2D axisymmetric radiation-hydrodynamics simulations of the formation of aspherical planetary nebulae through an interacting winds model. Their models took into account the density distribution of the circumstellar AGB stage material and although Mellema & Frank (1995) considers constant fast wind parameters, Mellema (1995) takes into account the time evolution of the post-AGB wind and ionizing photons. Unfortunately, the resolution of these simulations is very low (80x80 computational cells at best), and although the formation of instabilities at the interface between the hot shocked fast wind and the swept-up photoionized AGB material is hinted at, the numerical resolution is simply not adequate to follow their development. Mellema & Frank (1995) estimate the soft X-ray emission from their models and find it to come from a thin layer just inside the photoionized shell. However, this is an artefact due to numerical diffusion at the contact discontinuity and the low resolution of the simulations converts it into an appreciably amount of soft X-ray emission. Other 2D, purely hydrodynamic simulations by Stute & Sahai (2006) show the formation of instabilities at the contact discontinuity, but these remain confined to a thin layer and do not grow. In our simulations, the resolution is much higher and the instabilities can be characterised and are well developed. Moreover, the strong radiative cooling and the proper treatment of the radiative transfer in our models mean that once the instabilities form they become enhanced and grow in size so that the surface area they present becomes quite large.

We only follow the evolution of our models up until the hot bubble has achieved a radius of ~ 0.2 pc. For the 1.0-0.569, 1.5-0.597, and 2.0-0.633 models this occurs before the mass-loss rate and ionizing photon luminosity have dropped off completely and so it can be expected that these hot bubbles will expand further. The 2.5-0.677 model reaches 0.2 pc only very slowly, since the mass-loss rate and ionizing photon luminosity decline sharply after 3000 yrs and it is the residual pressure of the hot bubble that is driving the expansion against the diminishing pressure of the expanding photoionized shell. Our most massive star models, 3.5-0.754 and 5.0-0.90, have such a fast evolution that the hot bubble reaches a maximum radius before the pressure in the hot shocked gas falls below the pressure of the surrounding photoionized shell and the hot bubble collapses back towards the star. This is a natural way of explaining the back-filling of gas in PNe, such as is seen in the Helix nebula (García-Segura et al., 2006; Meaburn et al., 2005).

Finally, we speculate that in the case of 3D simulations the instabilities in the wind-wind interaction zone would develop faster than the formation of clumps in 2D simulations (see Young et al., 2001). This was explored in numerical simulations for the analogous case of the formation of (hot bubbles in) WR nebulae by van Marle & Keppens (2012). They found that 3D simulations show more structure than 2D simulations, although the differences are relatively small. In 3D, there will be a larger surface area of dense AGB material available to be hydrodynamically ablated or evaporated and we therefore expect that the mixing of material into the hot bubble would be even more effective than in the present 2D results.

7.6 Summary and conclusions

We have presented high-resolution 2D radiation-hydrodynamic numerical simulations of the formation and evolution of hot bubbles in planetary nebulae (PNe). We considered six different stellar evolution models with initial masses of 1, 1.5, 2, 2.5, 3.5, and $5 M_{\odot}$ at solar metallicity ($Z = 0.016$ Vassiliadis & Wood, 1993, 1994), which correspond to final WD masses of 0.569, 0.597, 0.633, 0.677, 0.754, and 0.90 $M_{\odot}$. The initial circumstellar conditions are obtained from 1D simulations of the final few thermal pulses of the AGB phase and are the same as those used in Villaver et al. (2002a), but in the case of the post-AGB phase the stellar wind velocity, mass-loss rate, and ionizing photon rate are computed self-consistently using the WM-Basic stellar atmosphere code (Pauldrach et al., 2012, and references therein). From our results we find that:

- The formation and evolution of hot bubbles in PNe depend on different factors: the density distribution of the previously ejected AGB material, the time-evolution of the stellar wind parameters in the post-AGB phase, and the metallicity and cooling rate used in the calculations. Differences between models create different patterns of instabilities in the wind-wind interaction zone. The most important factors are the length of time before the mass-loss rate and ionizing photon rate decline sharply, and the acceleration timescale for the stellar wind.

- The breakup of the shell of swept-up AGB material due to instabilities complicates the wind-wind interaction region and none of our models exhibits a clear double-shell pattern such as those observed by Guerrero et al. (1998). This is principally because the outer ionized shell leaves the computational domain during the simulation for the lower mass models. The formation of clumps leads to dynamic opacity variations in the photoionized shell, which in turn lead to a ray-like distribution of photoionized gas in the AGB envelope, which varies with time.

- The formation and distribution of clumps and filaments has been shown to depend strongly on the cooling rate curve used and the ionization and temperature history of these clumps should be a function of the evolving stellar parameters and radiation field. Although we take into account planetary nebula abundances and a representative radiation field when calculating the radiative losses, we do not take into account the time evolution of the stellar parameters nor do we include molecules or dust in our treatment of the neutral gas.

- The creation of hydrodynamical instabilities results in mixing of AGB material into the hot bubble, even for cases in which thermal conduction is not included. The temperature and density of the mixing zone are favourable for the emission of soft X-rays.

- The inclusion of thermal conduction has several effects: it stops the bubble leaking hot gas through the gaps between the clumps and filaments by sealing them with evaporated material, and it increases the amount of AGB material mixed into the hot bubble. Models without conduction were found to form leaking bubbles with pressures dominated by the photoionized shell, whereas models with conduction resemble wind-blown bubbles surrounded by thin swept-up shells. This changes the appearance of the clumps around the edge of the hot bubble in the two cases.

CHAPTER 8

SYNTHETIC X-RAY EMISSION FROM PLANETARY NEBULAE

We present a study of the synthetic X-ray emission from hot bubbles in planetary nebulae (PNe). We use high resolution two-dimensional radiative-hydrodynamical results of the formation of hot bubbles in PNe with and without thermal conduction to compute their corresponding X-ray emission (e.g., spectra, luminosities, and plasma temperatures) and study the time-dependence of these parameters. We use the CHIANTI software to compute synthetic spectra for the models and compute their corresponding luminosities. We find that even models without thermal conduction can achieve the observed plasma temperature and luminosity values as those observed as contrary as found by previous authors. Instabilities formed in the wind-wind interaction zone are a natural consequence for the inclusion of material from the cold ionized nebula into the hot bubble and increase the X-ray emissivity up to observable values. We discuss the resultant synthetic surface brightness to compare with current X-ray observations towards PNe.

8.1 Introduction

The formation scenario of a hot bubble in a planetary nebula (PN) is related to the evolution of the stellar wind parameters and to the formation of the PN itselft. In the generalized interacting winds scenario (Balick, 1987; Kwok et al., 1978), a low- or intermediate-mass star ($M_{\rm ZAMS}$ ~1–8 $M_{\odot}$) evolves through the asymptotic giant branch (AGB) phase developing a dense and slow wind. This phase creates a cold and dusty envelope that interacts with the interstellar medium (e.g., Mauron et al., 2013, and references therein), which at later times is sweep up by the fast wind developed in the post-AGB phase. This wind-wind interaction creates a two-shock pattern, one that sweeps up and compresses the AGB material, and a second one traveling inwards that brakes and heats the fast wind, creating a diffuse and hot bubble.

The characteristic temperature of the plasma derived from X-ray observations of hot bubbles in PNe is around $T \sim 10^6$ K with electronic densities of the order of 1–10^2 cm^{-3}. Observations performed with the X-ray satellites *Chandra* and *XMM-Newton* report X-ray luminosities of the order of 10^{30}–10^{32} erg s^{-1} in the 0.3–2.0 energy range (e.g., see Table 2 in Ruiz et al., 2013). These values are in contrast with analytical calculations from the expected temperatures of adiabatically shocked stellar wind, as the temperature can be expressed as (Dyson & Williams, 1997)

$$T = \frac{3}{16}\frac{\mu m_{\rm H}}{k} V_\infty^2, \tag{8.1}$$

where k, μ, $m_{\rm H}$, and V_∞ are the Boltzmann constant, the mean particle mass, hydrogen mass, and the terminal wind velocity. Thus, terminal wind velocities of $\gtrsim$1000 km s^{-1} as those find from central stars of PNe (CSPNe; Guerrero & De Marco, 2013) would imply shocked plasma temperature of $T \gtrsim 10^7$–10^8 K. On the other hand, analytical solutions of the formation of hot bubbles as that from the oft-used model form Weaver et al. (1977), which assume classical thermal conduction between the hot bubble and the cold ($T \sim 10^4$ K) ionized shell, predicts X-ray luminosities greater that the observed values ($L_{\rm X} \gtrsim 10^{35}$ erg s^{-1}). In the case of PNe, heat conduction by thermal electrons evaporates material from the dense swept-up AGB shell into the hot bubble which reduces the temperature at the edge of the bubble to values $< 10^7$ K (Soker, 1994).

There have been several numerical works on the diffuse X-ray emission from PNe. To our knowledge, Mellema (1995) were the first to study the synthetic X-ray emission from PNe by means of 2D radiative-hydrodynamic simulations (see Frank & Mellema, 1994, and references therein). That work showed that the interface in the wind-wind interaction is able to create instabilities. They also estimated the X-ray emission predicted by these simulations and found that is mainly coming from this interface. Even though they did not include thermal conduction into their simulations, they could mimic the soft X-ray emission from PNe due to the low resolution of their grid. Because of this, they could not resolve numerically the clumps that could be created by instabilities in the wind-wind interaciton zone.

Numerical studies reported by Stute & Sahai (2006) and Akashi et al. (2007) presented one-dimension hydrodynamical simulations without accounting for the ionization photon flux from the central star nor the evolution of the stellar wind parameters. Their work concentrates in the study of parcels of shocked gas that was produced by wind velocities below 1000 km s^{-1}, at the begining of the post-AGB phase. Such results do not agree with PNe in which X-ray emission is present and the CSPN has a high stellar wind velocity.

The most accurate numerical study of X-ray emission from PNe has been developed by Steffen et al. (2008). They presented 1D radiative-hydrodynamic numerical calculations following in detail the evolution of the stellar wind parameters and include the effects of thermal conduction. They use classic and saturated thermal conduction scheme (method 1; Cowie & McKee, 1977; Spitzer, 1962), and a new formulation of this physical effect according to an interpolation

formula (see method 2 in Steffen et al., 2008). The main difference between these two methods is that method 2 is more *aggressive*, injecting more mass from the AGB shell into the hot bubble in less time. They used this last method to estimate luminosities and synthetic spectra to compare with observations and discard those results from method 1 arguing that those results create limb brightened X-ray profiles. Within their main conclusions is that models without thermal conduction will not be able to explain the soft X-ray emission from PNe, and that mixing due to instabilities created in the wind-wind interaction zone will never become important to explain the X-ray-emitting gas distribution as they would be restricted only at this interphase zone.

In Chapter 7 (see Toalá & Arthur, 2014) we presented high resolution two-dimension (2D) radiative-hydrodynamical numerical simulations on the formation of hot bubbles inside PNe for different stellar initial masses. We used the stellar evolution models at solar metallicities (Z = 0.016) from Vassiliadis & Wood (1993) for the AGB phase and those models from Vassiliadis & Wood (1994) for the stellar parameters in the post-AGB phase. We computed the stellar wind parameters from the post-AGB phase with WM-basic code (Pauldrach et al., 2012, 2001, 1994; Pauldrach, 1987; Pauldrach et al., 1986). We found that the instabilities created in the wind-AGB-wind interaction zone are a natural way in inject material into the hot bubble, which can lower the temperature of the hot bubble and raise the density. Specifically, we found that those cases without thermal conduction can inject mass via clumps to levels as those shown by models with a modify thermal conduction (method 2) from Steffen et al. (2008).

In this Chapter we use the results from Chapter 7 and study the time-variation of the X-ray spectra, luminosities, and surface brightness for models with different masses and models with/without thermal conduction. The structure of the present Chapter is as follows. In § 2 we describe the procedure of the numerical approach, in § 3 we present our results (differential emission measure, synthetic spectra, luminosities, etc.). In § 4 we discuss our findings and compare to previous works. Finally, we summarize in § 5.

8.2 Numerical Approach

We use the radiative-hydrodynamic results on the formation of hot bubbles in PNe from Chapter 7 to perform the calculation of their corresponding synthetic X-ray emission. We use models corresponding to stellar initial masses ($M_{\rm ZAMS}$) of 1, 1.5, 2, and 2.5 $M_{\odot}$ with and without thermal conduction. These models correspond to final white dwarf (WD) masses of 0.569, 0.597, 0.633, and 0.677 $M_{\odot}$ but for simplicity and consistency with Chapter 7 we will refer to these models by a combination of their initial mass and their final WD masses. For example, the stellar model with initial mass of 1 $M_{\odot}$ and final WD mass of 0.569 $M_{\odot}$ will be labeled as 1.0-0.569. Thus, the labels of the other models are 1.5-0.597, 2.0-0.633, and 2.5-0.677.

All these results create hot bubbles in which instabilities in the wind-wind interaction zone become important. Models with initial masses of 3.5 and 5 $M_{\odot}$ are not used as they only create

ionized-bounded PNe which never become optically thin (see Perinotto et al., 2004; Villaver et al., 2002b, and Chapter 7).

We use the *CHIANTI* software version 7.1.3 (Landi et al., 2013, and references therein) to compute synthetic X-ray spectra for the different models at different times for cases with and without thermal conduction. The synthetic spectra are integrated for selected times and integrated to compute their corresponding luminosities.

We want to remark here that the spectra, luminosities, and surface brightness are studied in the 0.3–2.0 keV energy range at a standard distance of 1 kpc.

8.3 Results

8.3.1 Differential emission measure

Prior to the use of *CHIANTI* software we must compute the corresponding differential emission measure (DEM) at each time for the different models used here. We assume a 100 bin array in the temperature range of 10^5–10^9 K, and for each bin we compute the DEM as

$$\mathrm{DEM}(T) = \int n_{\mathrm{H}} n_{\mathrm{e}} dV, \tag{8.2}$$

where n_{H},n_{e}, and V are the hydrogen and electron number density, and the volume of gas with temperatures $\geqslant 10^5$ K.

As a result of the evolution of the hot gas inside the PN (temperature, density, and volume), the DEM histogram changes with time. We show in Figure 8.1 the time-evolution of the DEM for the cases of the 1.0-0.569 and 1.5-0.597 models with and without thermal conduction. Models without thermal conduction (left column) show a prominent peak at higher temperatures on each corresponding histogram. In particular, the case of the 1.0-0.569 model do not show a contribution at temperatures above 10^7 K because at ~10,000 yr the velocity is still <800 km s^{-1}. The case of 1.5-0.597 model has a terminal velocity >3000 km s^{-1} after 10^4 yr of evolution (see Figure 7.4 from Chapter 7) and it has a significant temperature component at 10^8 K. The time-evolution of these cases show that at earlier times the softer and higher temperatures in the distribution have almost the same contribution to the DEM, but as the stellar wind parameters evolve, the contribution to higher temperatures diminishes.

On the other hand, models with thermal conduction show a higher contribution at lower temperatures (right column in Figure 8.1 and the peak at higher temperatures is smoothed at all times. The lower contributions to the DEM around higher temperatures, and the fact that the density in the hot bubble is raised due to the conductive effect, will be naturally translated into softer synthetic spectra. Furthermore, the DEMs in the cases with thermal conduction cases have higher values, thus, their corresponding spectra will be more intense than their corresponding cases without this effect.

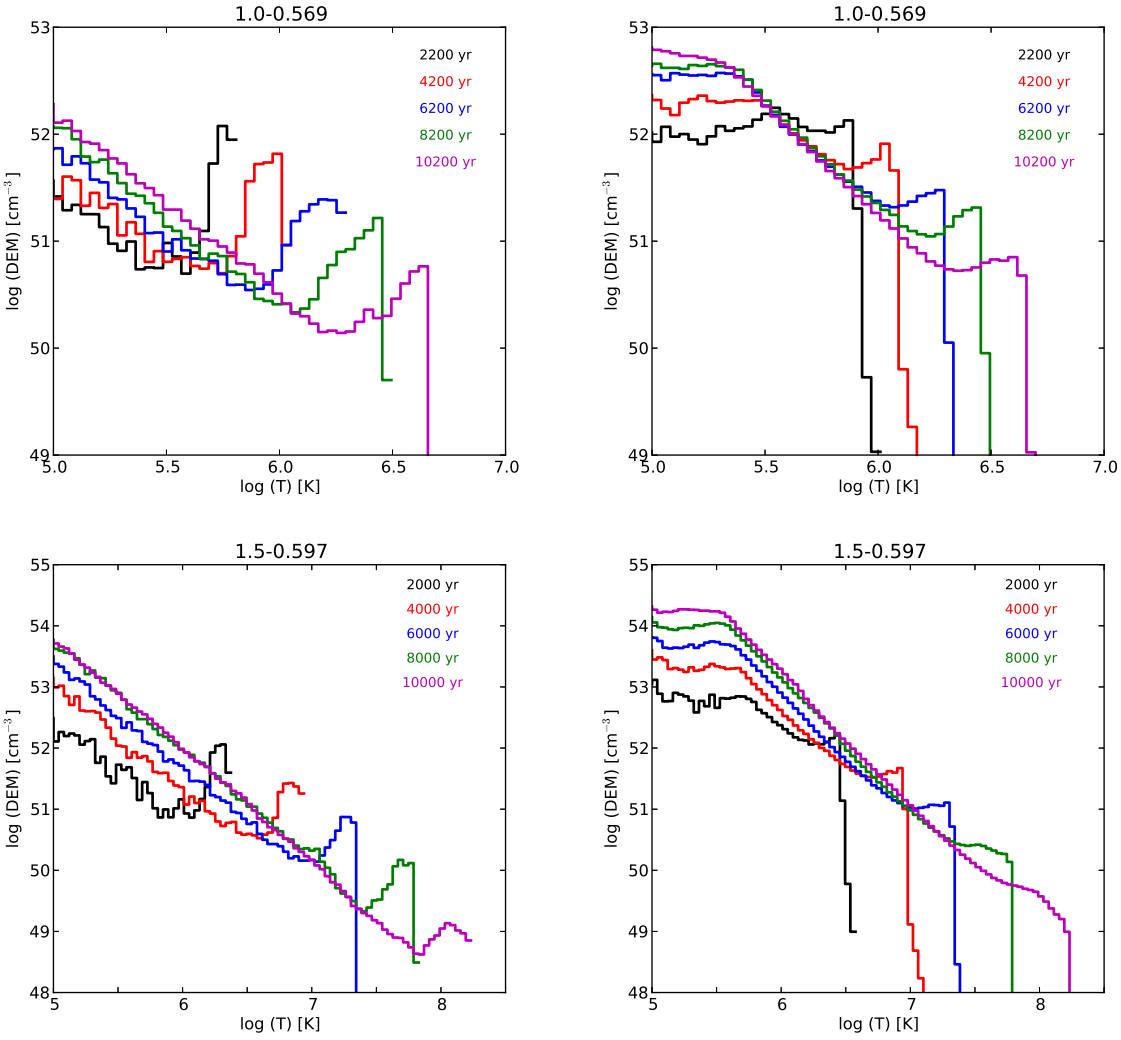

Figure 8.1: Differential emission measure (DEM) for the first ~10,000 yr for the evolution of hot bubbles in models 1.0-0.569 (upper panels) and 1.5-0.597 (lower panels) models. Left column corresponds to results without thermal conduction, and right column models with thermal conduction. Each time is marked on the panels.

8.3.2 Synthetic X-ray spectra

The calculation of the corresponding synthetic X-ray emission for each model at each time was done using the extensively tested *CHIANTI* (version 7.1.3) software package. The calculation performed by *CHIANTI* includes the contribution due to lines and to free-free, free-bound, and two-photon continuum.

All synthetic spectra were computed in the 0.1–2.0 keV, corresponding to 6–120 Å in the wavelength range, with a spectral bin of 0.01 Å and the spectral line FWHM is assumed to be 0.1 Å. The abundances used to compute the spectra are those defined for standard PN composition in Cloudy version 13.0 (Ferland et al., 2013) for consistency with Chapter 7. For comparison with observations we will only show spectra in the 0.3–2.0 keV energy range (see Section 8.4).

Figure 8.2 shows different spectra for the 1.5-0.597 model with and without thermal conduction at different times after the onset of the post-AGB phase. All spectra show a great number of spectral lines but there is a noticeable difference between models with and without thermal conduction. The case without thermal conduction (Figure 8.2-top panel) shows a change in the slope of the continuum with time (for times greater than 2000 yr), from a more less flat continuum to a spectrum with greater slope towards lower energies at latter times. This is a consequence of the mixing due to the clumps created by the instabilities, the spectrum gets more dominated by gas at temperatures below 10^7 K. On the other hand, the evolution of the spectrum in the case with thermal conduction is dominated by lower temperatures at all times and the slope does not change considerably. To illustrate this, we show in Figure 8.3 the variation of the hardness ratio of the soft band (0.3–1.0 keV) to the hard band (1.0–2.0 keV) for the models 1.5-0.597 and 2.0-0.633. At early times all models have low wind velocities, i.e., diffuse hot bubbles that contribute mainly to the soft band, this is clearly seen in both panels in Figure 8.3. After some time, the velocity increases and in the case of models without thermal conduction this is translated in the increase of the temperature of the hot bubble, this is, $F_{\rm soft}/F_{\rm hard}$ decreases. But after some time, instabilities in the wind-wind interaction became important and reduce again the temperature, raising $F_{\rm soft}/F_{\rm hard}$. On the cases with thermal conduction the hardness ratios is more less constant. Other models show similar trends.

8.3.3 Luminosities

To obtain a measurement of the luminosity $L_{\rm X}$, we integrated each synthetic spectrum in the 0.3–2.0 energy range to facilitate comparison with observations.

In Figure 8.4 we show the evolution with time of the X-ray luminosity for all models used in the present paper. The first thing to notice is that all models result in a wide range of X-ray luminosities below 10^{33} erg s^{-1}. As it is expected, models without thermal conduction (dashed lines) have lower X-ray luminosities at all times compared to their corresponding models with thermal conduction (solid lines).

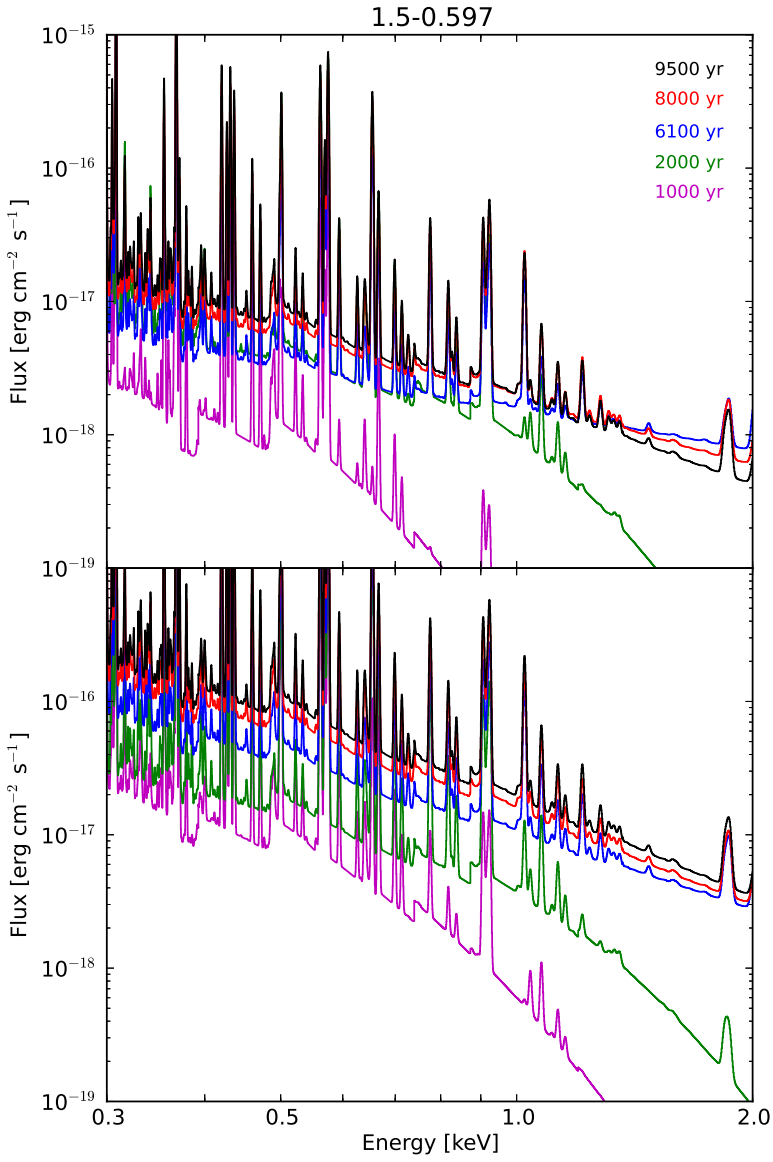

Figure 8.2: Time evolution of the spectra in the 0.3-2.0 keV energy range for the 1.5-0.597 model at different times after the onset of the post-AGB phase. Top: Without thermal conduction. Bottom: With thermal conduction. The times are marked on the top panel.

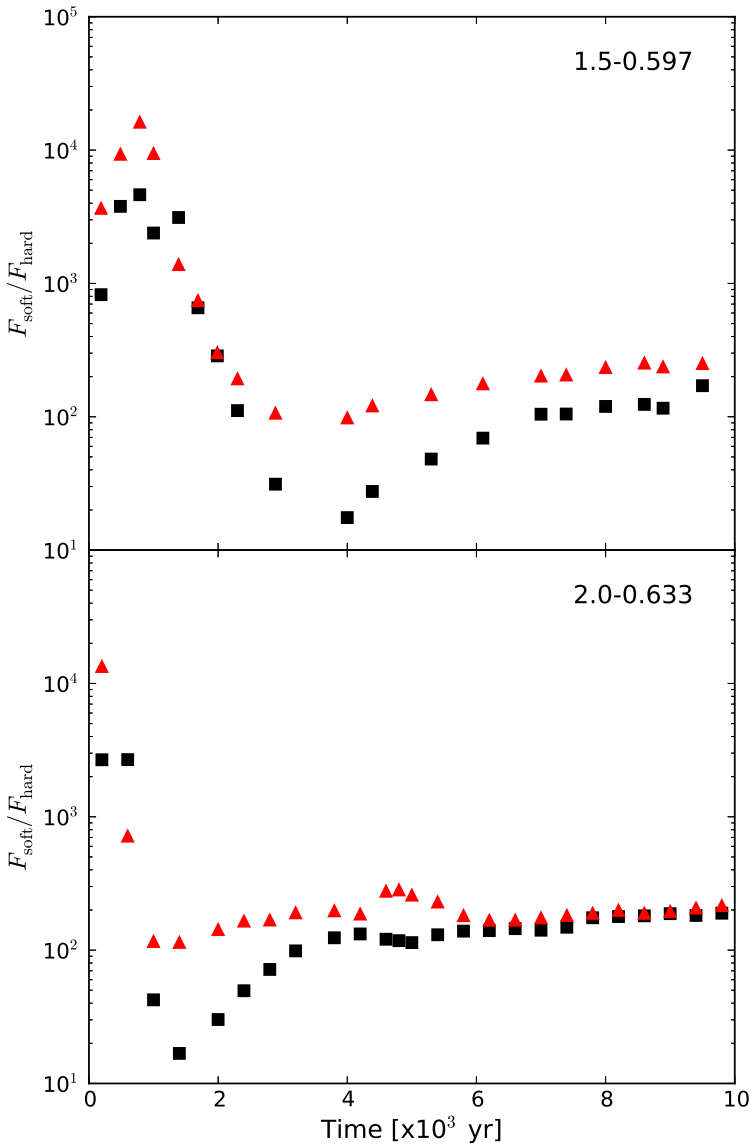

Figure 8.3: Variation of the ratio of soft (0.3-1.0 keV) to hard (1.0–2.0 keV) X-ray fluxes with time for cases of 1.5-0.597 (top) and 2.0-0.633 (bottom) models. Triangles (red) and squares (black) represent results with and without thermal conduction, respectively.

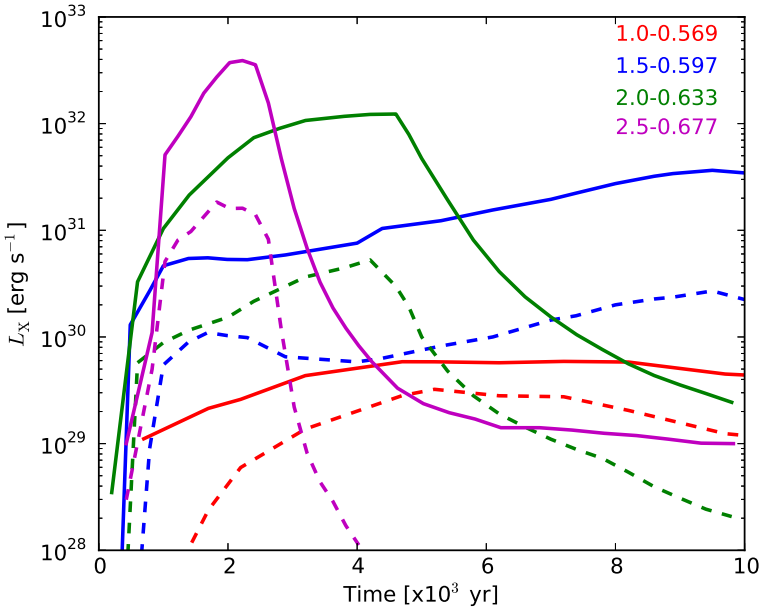

Figure 8.4: Evolution of the X-ray luminosity with time for the models used in the present paper. Solid and dashed lines represent models with and without thermal conduction, respectively. The luminosities are computed in the 0.3–2.0 keV energy range.

The evolution of the X-ray luminosity curves resemble those reported by Steffen et al. (2008) using their thermal conduction model 2, soft increasing curves with a maximum and an abrupt decay. More massive stars have rapidly decaying curves, while lower mass stars have less changing curves within 10^4 yr.

Our models without thermal conduction do not resemble the luminosity curves reported by models without thermal conduction from Steffen et al. (2008). Their models present broken lines while our models present a soft increasing in the luminosity more less like their corresponding cases with thermal conduction. Furthermore, our results without the conductivity effect can also reproduce the luminosity values as reported by observations.

8.3.4 Plasma Temperatures

Another important parameter that it is obtained from observations, apart from the luminosities from the hot interior in PNe, is the plasma temperature. With the use of the DEM (see Section 8.3) we can compute the averaged plasma temperature at each time. The most accurate procedure to do this is defining an average temperature as

$$\langle T \rangle = \frac{\int \mathrm{DEM}(T) T dT}{\int \mathrm{DEM}(T) dT}. \tag{8.3}$$

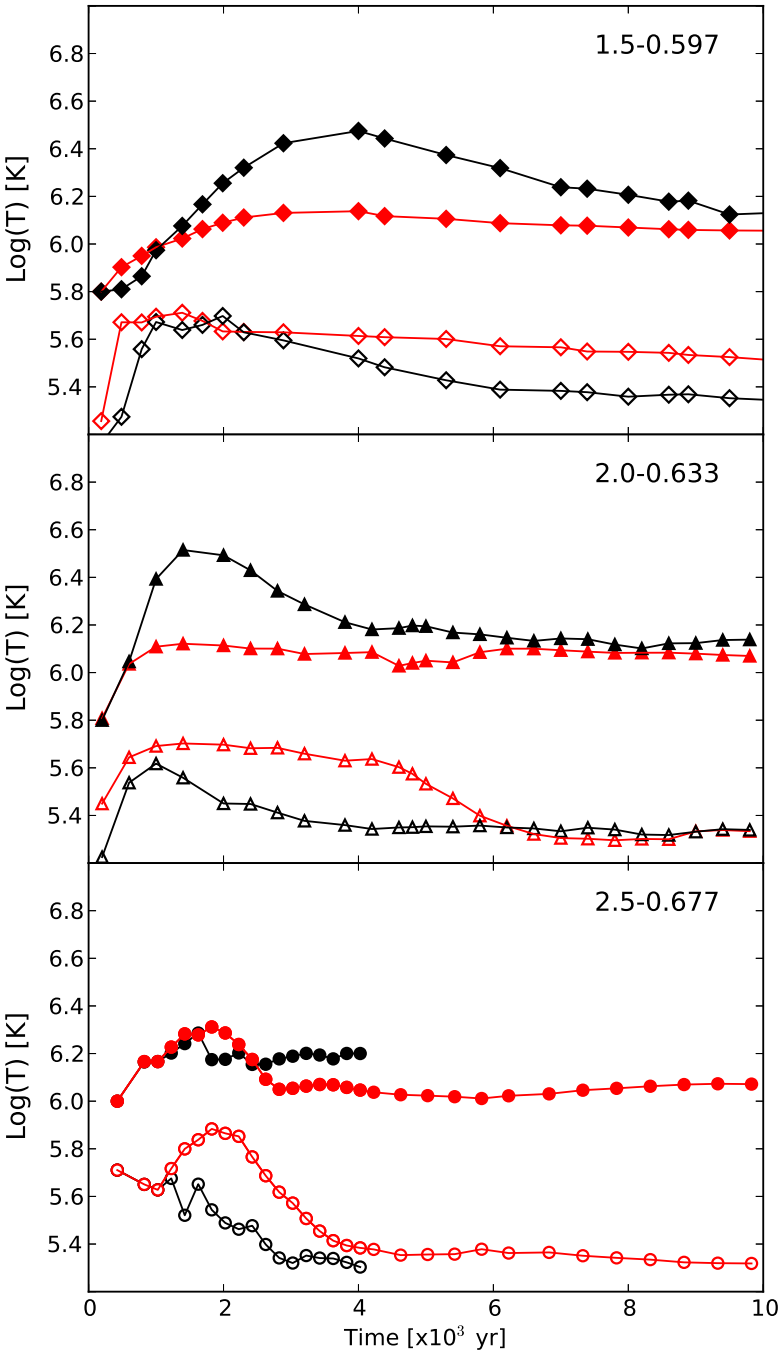

Figure 8.5: Averaged plasma temperature $\langle T \rangle$ in the hot bubbles for different models empty symbols represent the values obtained from integrating the entire temperature range (10^5–10^9 K). Filled symbols represent the calculation with a temperature lower limit of Log(T)=5.8.

This is done by integrating the whole defined range for the DEM(T), this is, temperature values above 10^5 K. The results of doing this are illustrated for the cases of 1.5-0.597, 2.0-0.633, and 2.5-0.677 in Figure 8.5 with empty symbols. Note that all this values do not exceed the temperature value of Log(T)=5.9. This is because all DEMs have their major contribution towards lower temperature values. Furthermore, the cases without thermal conduction have higher averaged temperature as they have a meaningful component at higher temperatures. In particular, in the case of the 2.5-0.677 model we stopped the calculation of the temperature as after 4,000 yr of evolution the luminosity drops considerably to unobservable values.

To assess a more realistic averaged temperature we must apply a lower limit to the integration. To do so, we evaluated the differences in the spectral shape computing spectra with single temperatures and the same differential emission measures, making use of *CHIANTI* software assuming nebular abundances as in Section 8.3.2. Figure 8.6 shows the differences in their spectral shape for different plasma temperatures from Log(T)=5.2 to 7.5. It is important to notice that the peak intensity in the continuum emission is shifted towards higher energies for plasmas with greater temperatures. The lower energy limit for the current X-ray satellites (*Chandra* and *XMM-Newton*) is around 0.25-0.3 keV, thus, we conclude that a temperature of Log(T)=5.8 is a good lower limit to perform the averaged plasma temperature. Even though extinction plays an important rôle in diminishing the intensity of the spectrum at lower energies (see Section 8.4), there are some PNe in which an important count rate has been made towards these energies (e.g., NGC 6543 and BD +30° 3639; Chu et al., 2001; Yu et al., 2009).

With this in mind, we recomputed $\langle T \rangle$ for Log(T)>5.8. The results are plotted in Figure 8.5 with filled symbols. These new averaged temperature values are in agreement with those summarized by Ruiz et al. (2013, see Table 2 in that paper) even for cases in which thermal conduction is not included. Furthermore, the specific case of NGC 7027 which has a plasma temperature of kT=0.26 keV(=3×10^6 K) is achieved by model without thermal conduction such as 1.5-0.597 and 2.0-0.633.

8.4 Comparison with observations

Before comparing our synthetic spectra with observations we have to perform two corrections to the spectra obtained in Section 8.3. First, we have to correct the spectra with absorption by the interstellar material in the line of sight, and secondly, we have to convolve the spectra with the satellite response matrices.

Figure 8.7 shows the absorption affects to an intrinsic spectrum from a 1.5-0.597 model with thermal conduction at 8000 yr after the onset of the fast wind as seen at 1 kpc using the photoelectric absorption cross sections from Balucińska-Church & McCammon (1992). We used a moderated ($N_{\rm H}$=8×10^{20} cm^{-2}) and a high ($N_{\rm H}$=5×10^{21} cm^{-2}) column density to show this effect. This figure shows how the most X-ray-emitting part of the spectrum is absorbed

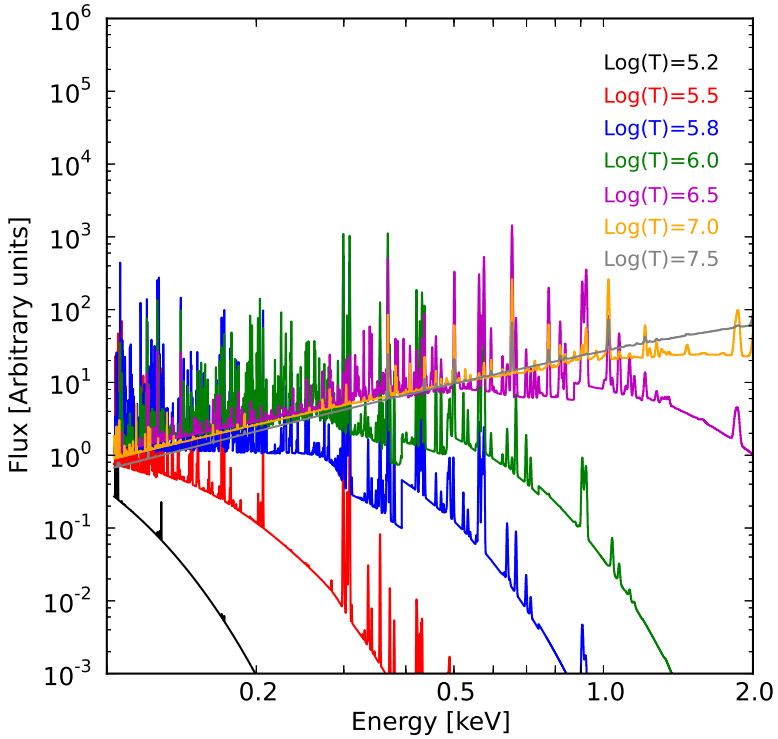

Figure 8.6: Comparison between synthetic spectra for single temperature models assuming nebular abundances.

by extinction. For example, the emission below 0.3 keV is diminished more than an order of magnitude and is even greater for lower energies (not showed here).

In Figure 8.8 we show how a spectrum from a 2.0-0.633 model with thermal conduction at 1600 yr looks after the convolution with the response matrices from the *Chandra* and *XMM-Newton*[1] X-ray satellites binned with a resolution of 60 keV with an interstellar absorption of $N_{\rm H}$=8×10^{20} cm^{-2}. All spectral lines are *erased* and a few spectral features can be identified in the spectrum. For example the $\lesssim$0.6 keV O VII(?) and 0.9 keV features (?).

As a result of the evolution of the hot bubble in the PN, the spectral shape changes with time as shown in Section 3.2 and this is also seen in the convolved spectra. For example, we show in Figure 8.9 the evolution with time of the spectrum for the 1.5-0.597 model using a column density of $N_{\rm H}$=8×10^{20} cm^{-2} until 8000 yr for the cases with and without thermal conduction. Two major peaks can be identify in the spectra, one at energies below 0.5 keV and another at 0.5–0.6 keV, with a secondary feature line at ~0.9 keV. Similarly, we show in Figure 8.10 the equivalent time evolution of the spectra but of the 2.5-0.677 model with an interstellar absorption of $N_{\rm H}$=5×10^{21} cm^{-2} until 4000 yr. No significant emission is detected below 0.4 keV.

[1]Assuming the EPIC-pn camera with the medium optical filter

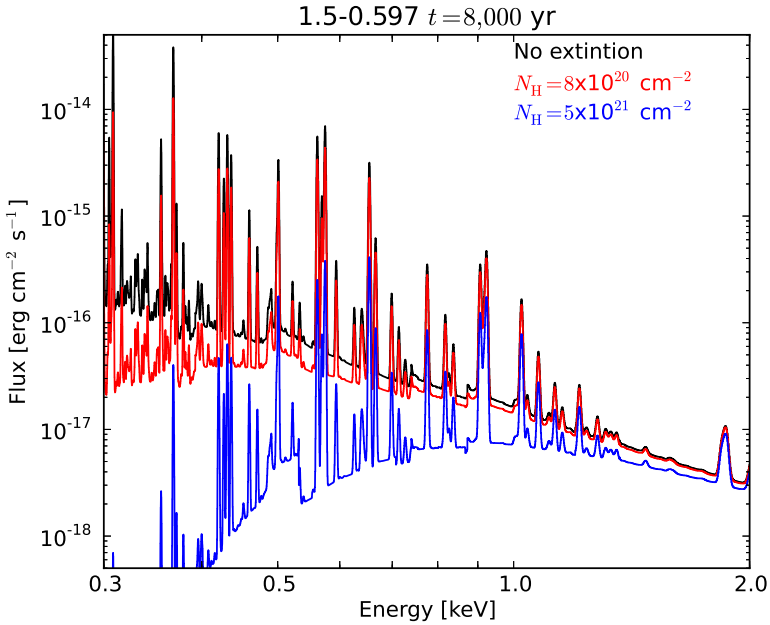

Figure 8.7: Synthetic spectra generated with CHIANTI for the 1.5-0.597 model at 8000 yr of post-AGB evolution with thermal conduction with different interstellar absorptions applied.

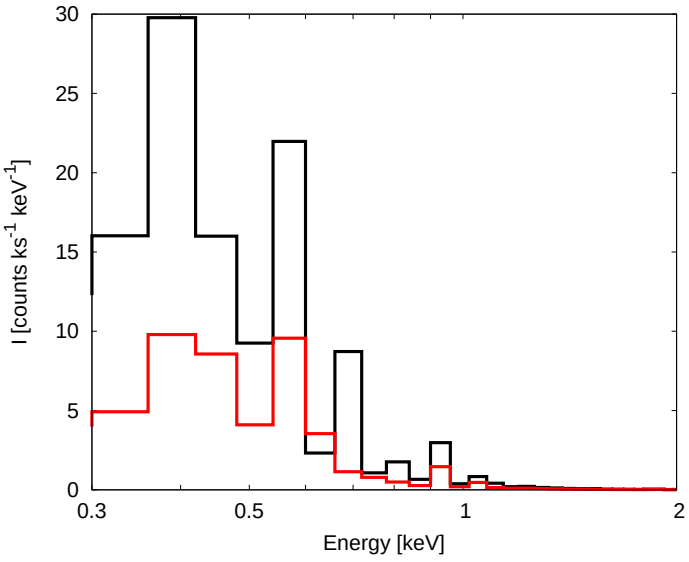

Figure 8.8: Simulated spectra for the case of the 2.0-0.633 model at 1600 yr after the onset of the post-AGB wind convolved with the *Chandra* (red) and *XMM-Newton* EPIC-pn camera with the medium optical filter (black) response matrices with spectral bin of 60 eV using a column density $N_{\rm H}$=8×10^{20} cm^{-2}.

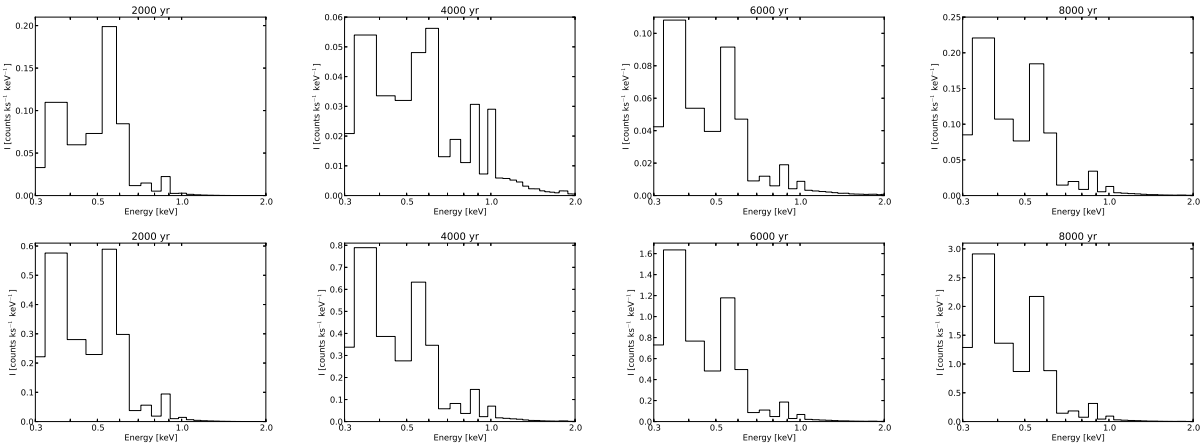

Figure 8.9: Evolution with time of the spectrum for the 1.5-0.597 model. Top row: without thermal conduction. Bottom row: with thermal conduction. Time is marked on each panel. All spectra were computed with an absorption of $N_{\rm H}$=8×10^{20} cm^{-2} and binned with 60 eV.

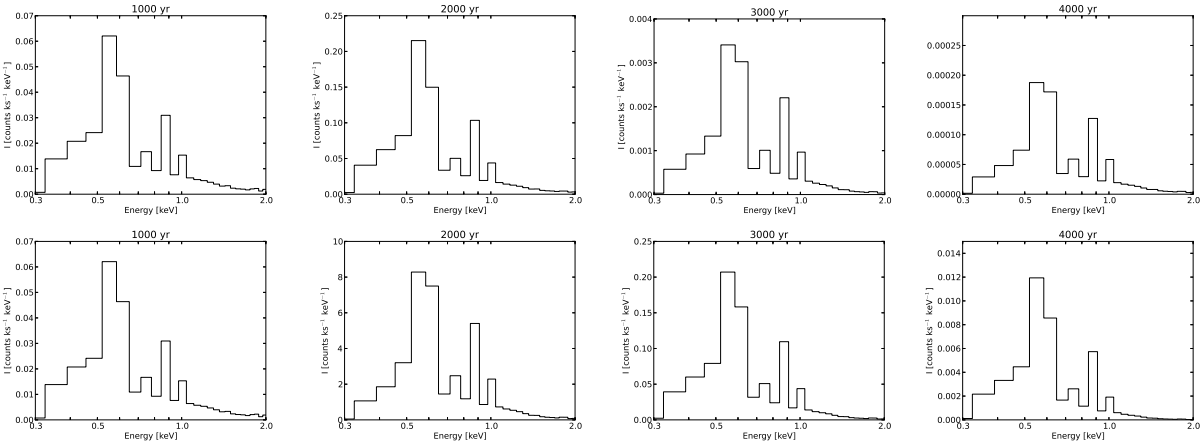

Figure 8.10: Evolution with time of the spectrum for the 2.5-0.677 model. Top row: without thermal conduction. Bottom row: with thermal conduction. Time is marked on each panel. All spectra were were computed with an absorption of $N_{\rm H}$=5×10^{21} cm^{-2} and binned with 60 eV.

The main emission is detected around 0.5–0.6 keV and secondary emission around 1.0 keV.

It is worth mentioning here that even though we are not tailoring the abundances or morphology to any PNe, we obtain spectra similar to *Chandra* observations reported by Chu et al. (2001), Gruendl et al. (2006), and Ruiz et al. (2013) for the cases of NGC 6543, NGC7026, IC 418 and NGC 2392, respectively.

8.4.1 X-ray surface brightness

As a final step in the comparison with observations we have to create surface brightness profiles. For this, we have integrated the X-ray intensity in the 0.3–2.0 keV energy band taking into account the absorption by the interstellar medium. Furthermore, all profiles must be convolved with a Gaussian to simulate the creation of the exposure-corrected maps of the X-ray-emitting gas in PNe.

Figure 8.11 (top panel) presents the resulting surface brightness from a 1.5-0.597 model with and without thermal conduction at the time when the hot bubble has an equivalent radius of ~0.2 pc assuming a column density of $N_{\rm H}$=8×10^{20} cm^{-2}. The peaks of the profiles appear shifted toward the center because cooler gas is more affected by absorption than hotter gas as illustrated in Figure 8.7 (see section 5.1 in Steffen et al., 2008). Moreover, the case with thermal conduction is even more shifted because the extension of the soft gas is broader than the case without thermal conduction. Anyhow, the difference in distance between the peaks of the models shown in this figure is <0.02 pc.

The other panels in Figure 8.11 show different results from applying different Gaussians with different FWHM to the same profiles shown in the top panel. Each value of the FWHM represents a fraction of the effective radius of the hot bubble. The effect of applying a strong smoothing process (higher FWHM) can give the appearance that the X-ray-emitting gas is distributed with a maximum at the center of the hot bubble.

8.5 Discussion

Our results presented in Section 3 and 4 confirm that instabilities created in the wind-wind interaction zone are important in injecting mass into the hot bubble to the point of enhancing the production of soft X-ray emission. Luminosities and averaged plasma temperatures are in agreement with those reported by observations for both cases with and without thermal conduction (e.g., Ruiz et al., 2013). We can also produce synthetic absorbed spectra very similar as those reported for several PNe.

The obtained averaged plasma temperatures from cases with and without thermal conduction are a little different between them but not dramatically, this is attributed to the fact that cases without thermal conduction present an important contribution towards higher tempera-

tures in their DEMs. But after some time, they converge to similar values (e.g., middle panel in Figure 8.5).

One of our main results that we would like to enhance in this discussion is the surface brightness profile obtained for the X-ray-emitting gas. With the convolved profiles shown in Figure 8.11, we would like to illustrate a very important point: it is a mistaken idea to compare unconvolved surface brightness profiles with those presented by observational works. The production of the X-ray-emitting gas images of PNe depend on different factors. To start, the angular size of the PN combined with the point spread function (PSF) of the X-ray satellite. For example, NGC 3242 displays different morphologies when comparing the *XMM-Newton* and *Chandra* observations presented by Ruiz et al. (2011) and Kastner et al. (2012). The PSF of the EPIC *XMM-Newton* X-ray detectors is not able to resolve the structure resolved by the back-illuminated ACIS-S CCD3 in *Chandra* (see figure 3 in Kastner et al., 2012).

In the cases in which the count rate is low the convolution (smoothing) process is equivalent to applying Gaussians with big FWHM (see lower panel in Figure 8.11. This process get things worse for cases in which the hot bubble's size is of a few arcsec even for high angular resolution observations as in the case of the *Chandra* observations of NGC 6826 (Kastner et al., 2012; Ruiz et al., 2013). On the other hand, those cases in which a sufficient count rate is detected or the PN has big angular size (compared to the angular resolution of the detector), this smoothing process may finally end up showing some structure, and even a limb-brightened morphologies as in NGC 40, NGC 6543, NGC 7009, NGC 7026, NGC 7027, and NGC 7662 (e.g., Gruendl et al., 2006; Kastner et al., 2012). Thus, it is an incomplete idea to assume that all PNe have a flat X-ray surface brightness, as the production of the exposure-corrected images from observations depend on mathematical tools, the angular size of the nebula as seen by the PSF of the instrument, and the count rate (which depends on the exposure time of the observation).

8.5.1 Comparison with previous numerical studies

We have described the possible differences that may take place due to different numerical treatment, the use of different stellar evolution models, and the detailed treatment of the stellar wind parameters on the formation of hot bubbles in Chapter 7, here we will give a short summary of those works that address the production of synthetic X-ray emission (spectra, luminosities, and surface brightness) and the differences with our results.

A milestone paper that discussed the X-ray emission from PNe was presented by Soker (1994). This work was the first to suggest that thermal conduction was responsible for the production of the soft X-ray emission related to plasma temperatures of $T \sim 10^6$ K which can be related to a conductive layer, and not to the hot bubble created by the adiabatically shocked stellar wind. This is, that cold material from the photoionized shell ($T \sim 10^4$ K) was injected into the hot bubble. Since then, several analytical and 1D numerical works have addressed the effects of thermal conductivity on the X-ray emission for hot bubbles in PNe (e.g., Akashi et al., 2007,

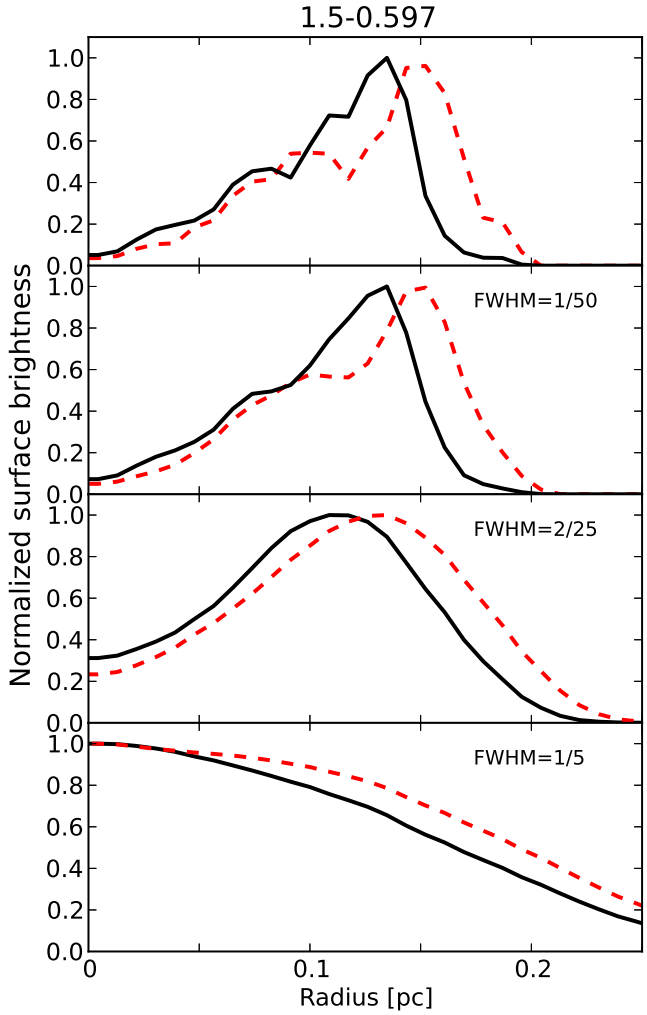

Figure 8.11: Normalized surface brightness profiles for the 1.5-0.597 model for the time when the rim-shell is ~0.2 pc with interstellar absorption of $N_{\rm H}$=8×10^{20} cm^{-2} for different Gaussian convolutions. Dashed (red) lines represent the results without thermal conduction and solid lines results with thermal conduction.

2006; Stute & Sahai, 2006; Zhekov & Perinotto, 1996, 1998). But non of those works follow in detail the time-dependence on the stellar wind parameters and the ionizing photon flux from the CSPN. This has only been done by Steffen et al. (2008).

Steffen et al. (2008) proposed that in order to agree with the high velocities reported by the CSPN in PNe, thermal conduction must be affecting the structure of the whole bubble. This is only achieved by limiting their electron mean free path with method 2, a more *aggressive* thermal conduction. Their results lead them to conclude that the X-ray surface brightness distribution should be flat and that instabilities in the wind-wind interaction zone should not be important. In fact, this is one of their reasons to discard models obtained with thermal conduction method 1. Furthermore, these authors compute the plasma temperature for a range of energies of 0.45–2.5 keV, which is too high, without justifying it. Surprisingly, they obtain plasma temperatures similar as those obtained by the present work.

On the other hand, 2D numerical simulations to study the X-ray emission in PNe were first presented by Mellema (1995). Due to the low resolution simulations they suffered from numerical high-velocity disturbances which make the hot bubble turbulent. Furthermore, the soft X-ray surface brightness is mimic by their numerical diffusion. Even though their results lack of resolution, they argue that the X-ray emission in PNe must come from a thin shell just inside the optical counterpart, a limb-brightened morphology was expected.

Zhekov & Myasnikov (2000) presented the first 2D numerical study that modeled an asymmetric thermal conduction to study the effects that a magnetic field could produce in the formation of a hot bubble. They do this by assuming that the conductivity coefficient depends on the polar angle. This work assumes a constant density profile before starting the fast wind, they did not take into account radiative losses and do not form instabilities only in the direction of the thermal conduction. Unfortunately, the authors do not compute spectra or surface brightness profiles.

8.6 Summary and conclusions

We presented calculations of the synthetic X-ray emission from hot bubbles in PNe from high resolution radiative-hydrodynamic results presented in Chapter 7. The numerical results correspond to models with initial masses ($M_{\rm ZAMS}$) of 1, 1.5, 2, and 2.5 $M_{\odot}$ which correspond to WD masses of 0.569, 0.597, 0.633, and 0.677 $M_{\odot}$. We computed their corresponding DEMs and studied the time-evolution. These were used to compute their synthetic spectra in the 0.3–2.0 keV energy range making use of *CHIANTI* software. This allow us to study the evolution with time of the spectrum of each model. Luminosities were obtained from integrating the spectra.

Our main findings can be summarized as follows:

- Instabilities created in the wind-wind interaction zone are able to inject mass into the hot bubble and produce soft X-ray emission, e.g., the cases without thermal conduction. Their

corresponding spectra and luminosities agree nicely with observations. Cases in which thermal conduction is included have higher fluxes and luminosities. There is no need to modify the thermal conduction formula (classic and saturated) to increase the emissivity of the hot bubble.

- The DEMs from models without thermal conduction present a peak in the distribution at hotter temperatures. The contribution of this peak is diminished with time as the mixing of the instabilities becomes important. In cases with thermal conduction, there is no significant contribution towards higher temperatures to the DEMs. These models, present a plato in the DEM distribution for temperatures below 10^6 K.

- The flux ratio between the soft (0.3–1.0 keV) and hard (1.0–2.0 keV) energy bands is always dominated by the soft contribution of the spectrum.

- The averaged plasma temperatures of all cases lay withing observable values.

- Even though we are not tailoring the abundances or morphologies, our simulated spectra (convolved with the *Chandra* response matrices) resemble those observed in several PNe.

- Discarding models that do not produce flat X-ray surface brightness profiles is an incomplete interpretation and should not be done. Surface brightness are obtained as the result of the smoothing of the observed distribution of the X-ray-emitting gas and the production of the exposure-corrected maps. A combination of effects must be taken into account when comparing simulated profiles with those obtained from observations: the angular size of the hot bubble in the PN, the PSF of the X-ray satellite, and the smoothing process of the X-ray images.

CHAPTER 9

CONCLUSIONS AND GENERAL DISCUSSION

This thesis has presented observational and theoretical results on the X-ray emission from hot bubbles in WR nebulae and PNe. In this chapter we present the main conclusions of our study and describe future work related to this thesis.

Our main observational results are:

- The WR nebula S 308 has been mapped using with four *XMM-Newton* observations which cover ≈90% of its nebular extent. The temperature of the hot plasma in the nebula was estimated to be 1.1×10^6 K with a luminosity of $L_{\rm X}$=2×10^{33}erg s^{-1}. The electron density of the hot gas is estimated to be $n_{\rm e}$=0.1 cm^{-3}. The X-ray emission from this nebula presents a clear limb-brightened morphology. These factors point out that cold gas has been injected to the interiors which have increase the electron temperature and reduce the temperature.

- NGC 6888 was partially observed with *Chandra*, but the unprecedented high spatial resolution of the observations allowed us to excise point-like sources whose emission plagued previous X-ray studies towards this WR nebula. The estimated plasma temperature and luminosity of this nebula are 1.4×10^6 K and $L_{\rm X}$=7.7×10^{33}erg s^{-1}. These observations suggest that the X-ray-emitting gas is distributed in three maxima, two corresponding to the caps and another to the blowout detected towards the northwest. The electron density of the hot gas is estimated to be $n_{\rm e}\gtrsim$0.4 cm^{-3}. The formation scenario of NGC 6888 is complex and its probably interacting with the ISM.

- We have used archived *XMM-Newton* observations to study the WR nebula around WR 16. Even though diffuse X-ray emission was expected from a close-morphology nebula such as this, no hot gas is detected towards this nebula. We estimated an upper limit for the X-ray luminosity of $L_{\rm X}$=7.4×10^{32}erg s^{-1} assuming that the temperature and chemical abun-

dances of the hot gas are similar to those detected in S 308 and NGC 6888. This would imply an upper limit to the electron density of n_e <0.6 cm^{-3}.

- We have analyzed *XMM-Newton* RGS observations of the Cat's Eye PN (a.k.a. NGC 6543). We are able to detect emission lines from carbon, nitrogen, and oxygen (C V, C VI, N VI, N VII, and O VII). This makes NGC 6543 the second PN with high resolution spectroscopy. The line ratio has allowed us to estimate a plasma temperature lower than that derived by previous studies.

- We presented an *XMM-Newton* discovery of X-ray emission from A78, the second born-again PN to display diffuse and point-like X-ray emission apart from A30. The diffuse X-ray emission is spatially correlated to the H-poor knots and filaments detected in the optical [O III] line. This suggests a complex mixing scenario that has not been reproduced by the current 1D radiative-hydrodynamic simulations on the X-ray emission from PNe. The diffuse X-ray emission can be modeled by a plasma temperature of 1.3×10^6 K which corresponds to an X-ray luminosity of L_X=2×10^{30}erg s^{-1}. The CSPN displays a soft X-ray emission modeled by a C VI emission line at 33.7Å (0.37 keV). The origin of this emission is inconclusive, but the presence of this line reinforces the idea that its X-ray emission is directly related to the born-again phenomenon and this region must be located at least a few stellar radii above the surface of the CSPN.

We have performed 2D radiative-hydrodinamic numerical simulations to study the formation, evolution, and X-ray emission from hot bubbles in PNe. Our main findings are:

- The formation of the hot bubble in PNe depend on different factors: the density distribution left by the previous AGB phase, the time-evolution of the stellar wind parameters in the post-AGB phase, the metalicity and cooling rate used in the calculations. The important difference in our models is that these variations create different patterns of instabilities in the wind-wind interaction zone.

- The breakup of the shell of swept-up AGB material due to instabilities adds more complexity to the wind-wind interaction region. The formation of clumps leads to dynamic opacity variations in the photoionized shell, which in turn lead to a ray-like distribution of photoionized gas in the AGB envelope, which varies with time.

- The creation of hydrodynamical instabilities results in mixing of AGB material into the hot bubble, even for cases in which thermal conduction is not included. The temperature and density of the mixing zone are favourable for the emission of soft X-rays.

- The inclusion of thermal conduction has several effects: it stops the bubble leaking hot gas through the gaps between the clumps and filaments by sealing them with evaporated

material, and it increases the amount of AGB material mixed into the hot bubble. Models without conduction were found to form leaking bubbles with pressures dominated by the photoionized shell, whereas models with conduction resemble wind-blown bubbles surrounded by thin swept-up shells. This changes the appearance of the clumps around the edge of the hot bubble in the two cases.

- We can reproduce observable values for the luminosities and plasma temperature estimates reported in the literature even for cases without thermal conduction.

9.1 Future work

There are a few works that can be pursuit as a continuation of the observational and theoretical results presented in this thesis. For example, it is important to increase the number of observed WR nebulae with X-ray satellites in order to expand further the differences (or similarities) in these objects. For this, we have proposed to observe NGC 6888 and NGC 3199 (around WR 18) with *XMM-Newton*. Both WR nebulae have been accepted as priority C targets. Nevertheless, NGC 6888 was observed on April 2014.

The born-again PNe A30, A58, A78, and the Sakurai's object will be studied with a multiwavelegth observational campaign in which we are involved (optical, infrared, and radio). Furthermore, our 2D radiative-hydrodynamic simulations will be tailored to the study of the formation, evolution, and X-ray emission from these objects.

9.1.1 *XMM-Newton* observations of NGC 6888

The present thesis has put in context the current observational view of the X-ray emission from WR nebulae. Of the 4 WR nebulae observed to date (S 308, NGC 6888, RCW 58 and that around WR 16)[1], only two of them harbor diffuse X-ray emission. Furthermore, S 308 presents a limb-brightened morphology while NGC 6888 seems to have three maxima in the X-ray-emitting gas distribution. X-ray observations of WR nebulae are dearly deficitary and this field needs to be expanded.

As stated in Chapter 4, *XMM-Newton* observations towards NGC 6888 were most needed to study the complete morphology of this WR nebula. We have been awarded with these observations on 2014 April 5 (Observation ID 0721570101; PI: J.A.Toalá) using EPIC and the RGS observations for a total exposure time of 75.9 ks. Figure 9.1 presents the resultant exposure-map-corrected, background-subtracted EPIC images in three different energy bands bands, namely 0.3–0.7 keV (soft), 0.7–1.2 keV (medium), and 1.2–3.0 keV (hard), as well as a color-composite image of the three bands. A quick analysis of this figure confirms the findings of the *Chandra*

[1]During the last months of the realization of this thesis, Zhekov (2014) reported the discovery of the X-ray emission from the WR nebula NGC 2359 around WR 7.

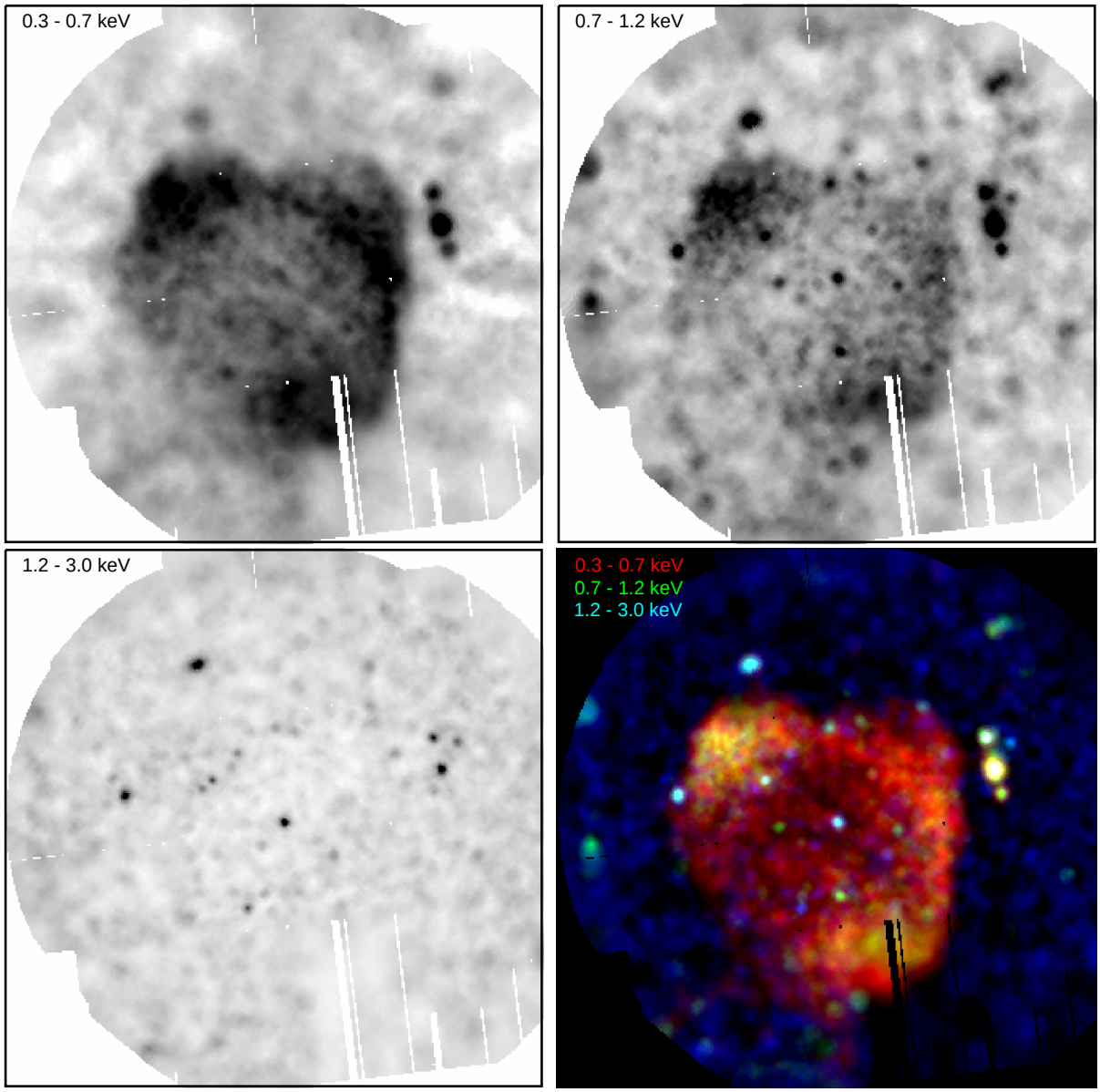

Figure 9.1: *XMM-Newton* EPIC (MOS1, MOS2, and pn) exposure-corrected X-ray images in three different energy bands of the field of view of NGC 6888. Bottom-right panel corresponds to a color-composite picture of the three different energy band images shown in the other panels. The central star in NGC 6888 (WR 136) is located at the center of each image. Note that no point-sources have been excised from the observations. North is up, east to the left.

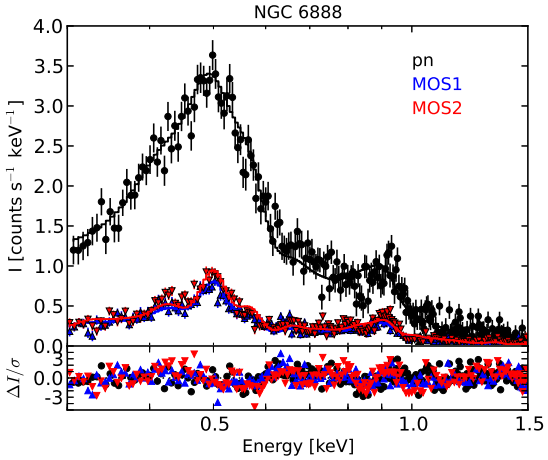

Figure 9.2: Background-subtracted spectra of NGC 6888 from the three EPIC cameras (pn, MOS1, and MOS2) overplotted with their best-fit two- temperature *apec* model (solid lines) in the 0.3–1.5 keV energy range.

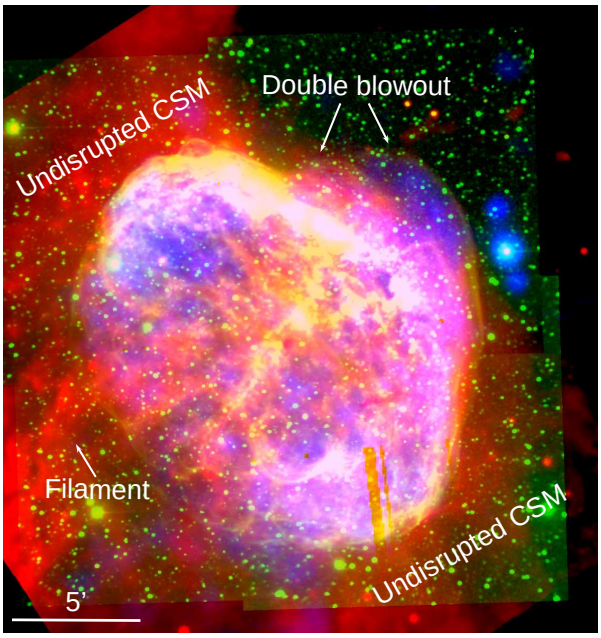

Figure 9.3: *Spitzer* MIPS 24 μm (red), [O III] (green), and EPIC 0.3–0.7 keV (blue) images of NGC 6888. Different features are shown.

Table 9.1: Stellar parameters used in the born-again simulation

Phase	Duration (yr)	$\log(\dot{M})$ ($M_\odot$ yr^{-1})	v_∞ (km s^{-1})
AGB	10^5	-5.5	15
WD_1	1.1×10^4	-7	$\lesssim$3000
Born-again	20	-4	20
WD_2	...	-7	4000

observations and the presence of a third maximum in the soft X-ray emission towards the northwest.

We have also excised all point-like sources in the field of view of the nebula and have extracted an X-ray spectrum. The background-subtracted spectra of the three different EPIC cameras is shown in Figure 9.2. The analysis of the global spectrum of NGC 6888 was obtained from an optically thin plasma model and the parameters are in good agreement with those found and reported in Chapter 4.

A comparison between X-rays, optical, and IR images of NGC 6888 can help us understand the morphology and distribution of the hot gas in this WR nebula. Figure 9.3 shows that this WR is evolving at the edge of a molecular cloud, and the northwest blowout formed is due to the low density towards this direction.

A more sophisticated analysis of the spatial and spectral properties of the X-ray emission in this WR nebula is under way.

9.1.2 Simulations on the formation of born-again PNe

A first approach of the formation of a born-again PN has been presented by Xuan et al. (2014). We have used the code presented in the present thesis to study the complex interaction of the material ejected during the born-again event with the fast wind developed afterwards. The stellar wind parameters assumed in these calculations are presented in Table 9.1.

The 2D cylindrically symmetric calculations were performed on a fixed grid of 1000 radial by 2000 z-direction cells of uniform cell size and total grid spatial size of 0.5×1.0 pc^2. The free-wind injection zone has a radius of 40 cells, corresponding to 0.02 pc, and the initial conditions for the ISM were a number density n_0=1 cm^{-3} and a temperature of T_0=100 K.

We assume that the star evolves through the AGB and WD phases with durations of 10^5 and 11 000 yr, respectively, before reaching the born-again event. Even though the born-again phase is not completely understood, calculations presented by Miller Bertolami et al. (2006) helped us constrain the time lapse as high as 20 yr. Details of the wind properties on the different phases are presented in Table 9.1 and Figure 9.4.

Figure 9.5 presents the numerical results at two different times after the born-again event. It can be seen that after 500 yr the fast stellar wind has disrupted the dense shell left by the

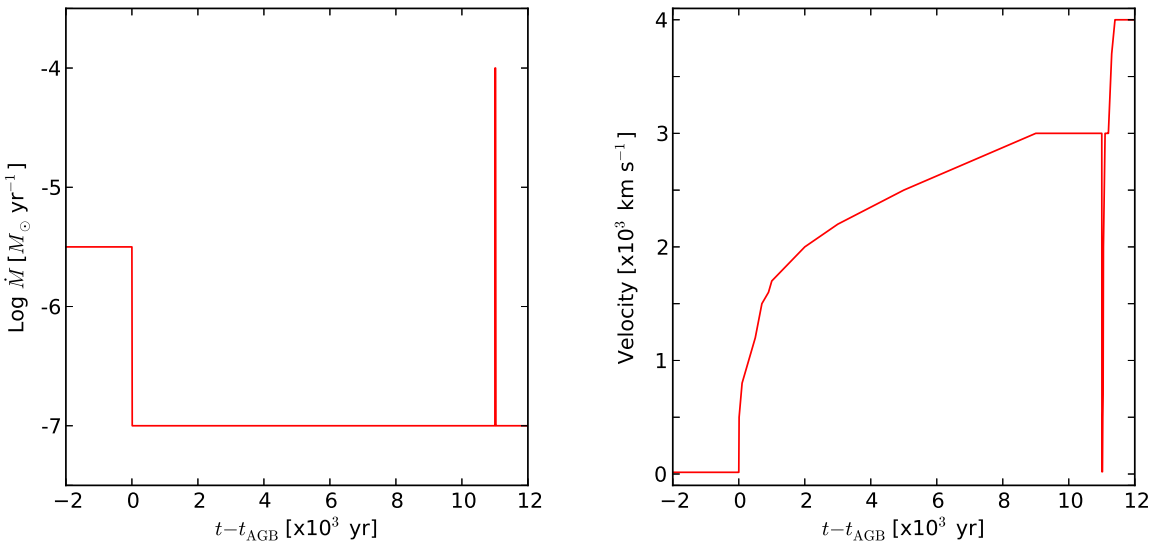

Figure 9.4: Mass-loss rate and wind velocity profiles used for the simulations of the born-again PN. $t_{\rm AGB}$ corresponds to the duration of the AGB phase.

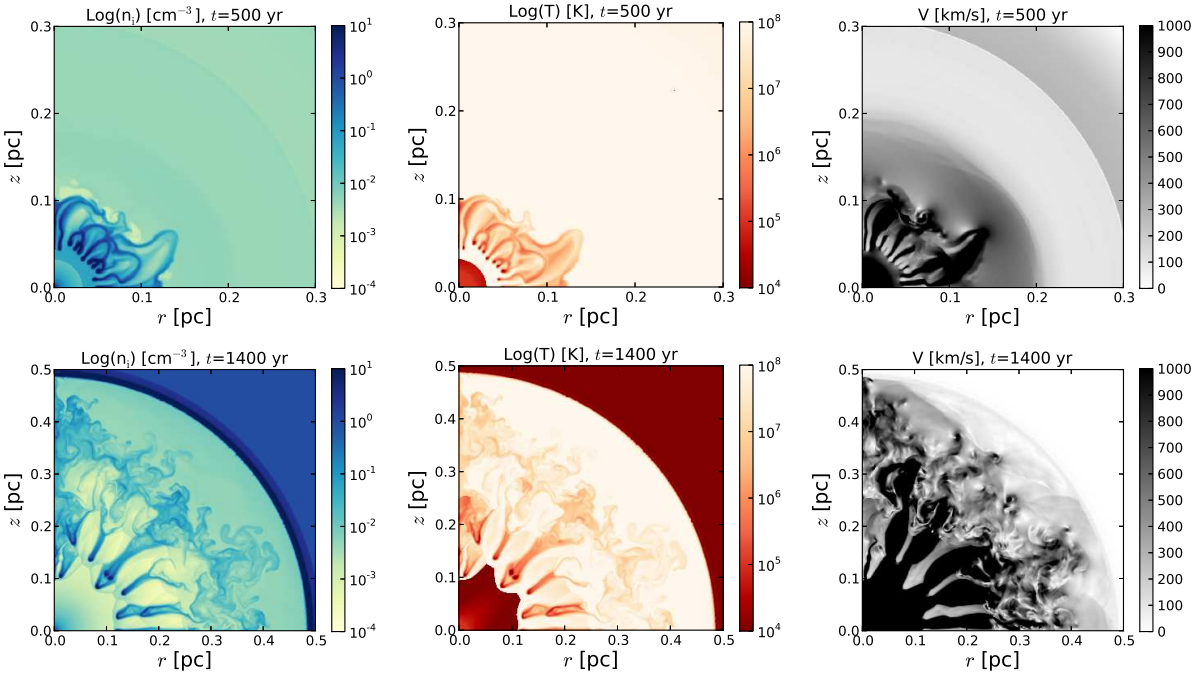

Figure 9.5: Total ionized number density (left panels), temperature (middle panels), and velocity (right panels) for the evolution of the PN after the born-again event. The rows correspond to different times marked on each panel.

born-again ejection and photoionized clumps are formed. These clumps have cometary shape, with dense, cold (10^4 K) heads pointing toward the central star as seen in *HST* observations. Note that the tails extend further as they have greater velocities as a result of the interaction of the clump material and the shocked fast wind, creating multiple interacting shocks. This last effect heats the ablated clump gas and might be the cause of the X-ray emission detected toward A30 and A78.

After 1400 yr (Figure 9.5-bottom panels), the densest clumps are still close to the star while the rest of the material that has been eroded fills the rest of the old PN. It is important to remark here that with only a single and short born-again event we are able to sweep up material at different distances from the CSPN as a result of the complex evolution.

These simulations have to be rerun taking into account the unique abundances of the H-poor knots and filaments because, as concluded in the present thesis, the chemical composition of the gas changes the cooling rate of the gas and affects the formation of clumps in the wind-wind interaction zone. Synthetic X-ray emission (spectra and luminosities) of these simulations will be also created.

BIBLIOGRAPHY

Abbott, D. C., Beiging, J. H., Churchwell, E., & Torres, A. V. 1986, ApJ, 303, 239

Akashi, M., Meiron, Y., & Soker, N. 2008, New Astron., 13, 563

Akashi, M., Soker, N., Behar, E., & Blondin, J. 2007, MNRAS, 375, 137

Akashi, M., Soker, N., & Behar, E. 2006, MNRAS, 368, 1706

Althaus, L. G., Serenelli, A. M., Panei, J. A., et al. 2005, A&A, 435, 631

Anders, E., & Grevesse, N. 1989, Geochim. Cosmochim. Acta, 53, 197

Arnal, E. M., & Cappa, C. E. 1996, MNRAS, 279, 788

Arnaud, K. A. 1996, Astronomical Data Analysis Software and Systems V, 101, 17

Arthur, S. J. 2007a, Diffuse Matter from Star Forming Regions to Active Galaxies, 183

Arthur, S. J. 2012, MNRAS, 421, 1283

Arthur, S. J., & Hoare, M. G. 2006, ApJS, 165, 283

Asensio Ramos, A., Martínez González, M. J., Manso Sainz, R., Corradi, R. L. M., & Leone, F. 2014, ApJ, 787, 111

Balick, B. 1987, AJ, 94, 671

Balucińska-Church, M., & McCammon, D. 1992, ApJ, 400, 699

Barstow, M.A., Boyce, D.D., Welsh, B.Y. et al. 2010, ApJ, 723, 1762

Berghöfer, T. W., & Christian, D. J. 2002, A&A, 384, 890

Bernard-Salas, J., Pottasch, S. R., Wesselius, P. R., & Feibelman, W. A. 2003, A&A, 406, 165

Blöcker, T. 1995, A&A, 299, 755

Blöcker, T., & Schönberner, D. 1993, Planetary Nebulae, 155, 479

Bochkarev, N. G. 1988, Nature, 332, 518

Bohlin, R. C., Savage, B. D., & Drake, J. F. 1978, ApJ, 224, 132

Borkowski, K. J., Harrington, J. P., Tsvetanov, Z., & Clegg, R. E. S. 1993, ApJL, 415, L47

Cardelli, J. A., Clayton, G. C., & Mathis, J. S. 1989, ApJ, 345, 245

Carter, J. A., & Read, A. M. 2007, A&A, 464, 1155

Castor, J., McCray, R., & Weaver, R. 1975, ApJl, 200, L107

Cassinelli, J. P., Waldron, W. L., Sanders, W. T., et al. 1981, ApJ, 250, 677

Chu, Y.-H. 1981, ApJ, 249, 195

Chu, Y.-H. 2008, IAU Symposium, 250, 341

Chu, Y.-H., & Ho, C.-H. 1995, ApJl, 448, L127

Chu, Y.-H., Troland, T. H., Gull, T. R., Treffers, R. R., & Kwitter, K. B. 1982, ApJ, 254, 562

Chu, Y.-H., Treffers, R. R., & Kwitter, K. B. 1983, ApJs, 53, 937

Chu, Y.-H., Chang, T. H., & Conway, G. M. 1997, ApJ, 482, 891

Chu, Y.-H., Guerrero, M. A., Gruendl, R. A., Williams, R. M., & Kaler, J. B. 2001, ApJl, 553, L69

Chu, Y.-H., Guerrero, M. A., Gruendl, R. A., García-Segura, G., & Wendker, H. J. 2003a, ApJ, 599, 1189

Chu, Y.-H., Guerrero, M. A., & Gruendl, R. A. 2003b, Planetary Nebulae: Their Evolution and Role in the Universe, 209, 415

Chu, Y.-H., Gruendl, R. A., & Guerrero, M. A. 2006, The X-ray Universe 2005, 604, 363

Conti, P. S. 1975, Memoires of the Societe Royale des Sciences de Liege, 9, 193

Corcoran, M. F., Waldron, W. L., Macfarlane, J. J., et al. 1994, ApJl, 436, L95

Cowie, L. L., & McKee, C. F. 1977, ApJ, 211, 135

Cox, N. L. J., Kerschbaum, F., van Marle, A.-J., et al. 2012, A&A, 537, A35

Damineli, A. 1996, ApJL, 460, L49

de Avillez, M. A., & Breitschwerdt, D. 2012, ApJl, 761, L19

de Korte, P. A. J., Claas, J. J., Jansen, F. A., & McKechnie, S. P. 1985, Advances in Space Research, 5, 57

Dere, K. P., Landi, E., Young, P. R., et al. 2009, A&A, 498, 915

Dixon, W. V., Sahnow, D. J., Barrett, P. E., et al. 2007, PASP, 119, 527

Dixon, W. V. D., & Sankrit, R. 2008, ApJ, 686, 1162

Dunne, B. C., Chu, Y.-H., Chen, C.-H. R., Lowry, J. D., Townsley, L., Gruendl, R. A., Guerrero, M. A., & Rosado, M. 2003, ApJ, 590, 306

Duronea, N. U., Arnal, E. M., & Bronfman, L. 2013, A&A, 551, A71

Drout, M. R., Massey, P., Meynet, G., Tokarz, S., & Caldwell, N. 2009, ApJ, 703, 441

Dwarkadas, V. V., & Rosenberg, D. L. 2013, High Energy Density Physics, 9, 226

Dyson, J. E., & Williams, D. A. 1997, The physics of the interstellar medium. Edition: 2nd ed. Publisher: Bristol: Institute of Physics Publishing, 1997. Edited by J. E. Dyson and D. A. Williams. Series: The graduate series in astronomy

Eggleton, P. P. 1971, MNRAS, 151, 351

Ekström, S., Georgy, C., Eggenberger, P., et al. 2012, A&A, 537, A146

Eldridge, J. J., & Tout, C. A. 2004, MNRAS, 353, 87

Esteban, C., Vílchez, J. M., Smith, L. J., & Clegg, R. E. S. 1992, A&A, 259, 629

Esteban, C., Smith, L. J., Vilchez, J. M., & Clegg, R. E. S. 1993, A&A, 272, 299

Esquivel, A., Raga, A. C., Cantó, J., et al. 2010, ApJ, 725, 1466

Evans, A., Tyne, V. H., van Loon, J. T., et al. 2006, MNRAS, 373, L75

Ferland, G. J., Korista, K. T., Verner, D. A., et al. 1998, PASP, 110, 761

Ferland, G. J., Porter, R. L., van Hoof, P. A. M., et al. 2013, RevMexAA, 49, 137

Fernández-Martín, A., Martín-Gordón, D., Vílchez, J. M., et al. 2012, A&A, 541, A119

Frank, A., & Mellema, G. 1994, ApJ, 430, 800

Freyer, T., Hensler, G., & Yorke, H. W. 2003, ApJ, 594, 888

Freyer, T., Hensler, G., & Yorke, H. W. 2006, ApJ, 638, 262

García-Arredondo, F., Arthur, S. J., & Henney, W. J. 2002, RevMexAA, 38, 51

García-Segura, G., & Mac Low, M.-M. 1995, ApJ, 455, 145

García-Segura, G., Mac Low, M.-M., & Langer, N. 1996a, A&A, 305, 229

García-Segura, G., Langer, N., & Mac Low, M.-M. 1996b, A&A, 316, 133

García-Segura G., Langer N., Różyczka M., Franco J., 1999, ApJ, 517, 767

García-Segura, G., López, J. A., Steffen, W., Meaburn, J., & Manchado, A. 2006, ApJL, 646, L61

Georgiev, L. N., Peimbert, M., Hillier, D. J., et al. 2008, ApJ, 681, 333

Georgy, C., Ekström, S., Meynet, G., et al. 2012, A&A, 542, A29

Girardi, L., Bressan, A., Bertelli, G., & Chiosi, C. 2000, A&ASS, 141, 371

Gosset, E., Nazé, Y., Claeskens, J.-F., et al. 2005, A&A, 429, 685

Gosset, E., De Becker, M., Nazé, Y., et al. 2011, A&A, 527, A66

Gräfener, G., Koesterke, L., & Hamann, W.-R. 2002, A&A, 387, 244

Gruendl, R. A., Chu, Y.-H., Dunne, B. C., & Points, S. D. 2000, AJ, 120, 2670

Gruendl, R. A., Chu, Y.-H., & Guerrero, M. A. 2004, ApJl, 617, L127

Gruendl, R. A., Guerrero, M. A., Chu, Y.-H., & Williams, R. M. 2006, ApJ, 653, 339

Güdel, M., Briggs, K. R., Montmerle, T., et al. 2008, Science, 319, 309

Guerrero, M. A., & De Marco, O. 2013, A&A, 553, A126

Guerrero, M. A., Villaver, E., & Manchado, A. 1998, ApJ, 507, 889

Guerrero, M. A., Chu, Y.-H., & Gruendl, R. A. 2000, ApJS, 129, 295

Guerrero, M. A., Chu, Y.-H., Gruendl, R. A., & Meixner, M. 2005, A&A, 430, L69

Guerrero, M. A., Ruiz, N., Hamann, W.-R., et al. 2012, ApJ, 755, 129

Hamann, W.-R., & Gräfener, G. 2004, A&A, 427, 697

Hamann, W.-R., Wessolowski, U., & Koesterke, L. 1994, A&A, 281, 184

Hamann, W.-R., Gräfener, G., & Liermann, A. 2006, A&A, 457, 1015

Hamann, W.-R., & Koesterke, L. 1998, A&A, 333, 251

Harrington, J. P., Borkowski, K. J., & Tsvetanov, Z. 1995, ApJ, 439, 264

Hartquist, T. W., Dyson, J. E., Pettini, M., & Smith, L. J. 1986, MNRAS, 221, 715

Herald, J. E., Bianchi, L., & Hillier, D. J. 2005, ApJ, 627, 424

Herwig, F., Blöcker, T., Langer, N., & Driebe, T. 1999, A&A, 349, L5

Hinkle, K. H., & Joyce, R. R. 2014, ApJ, 785, 146

Hinkle, K. H., Lebzelter, T., Joyce, R. R., et al. 2008, A&A, 479, 817

Howk, J.C., Sembach, K.R., Savaga, B.D., et al. 2002, ApJ, 569, 214

Humphreys, R. M. 2010, Hot and Cool: Bridging Gaps in Massive Star Evolution, 425, 247

Hunter, J. D., 2007, *Computing Science and Engineering*, Vol. 9, No. 3, pp. 90

Jacoby, G. H. 1979, PASP, 91, 754

Jeffery, C. S. 1995, A&A, 299, 135

Johnson, H. M., & Hogg, D. E. 1965, ApJ, 142, 1033

Kastner, J. H., Montez, R., Jr., Balick, B., & De Marco, O. 2008, ApJ, 672, 957

Kastner, J. H., Montez, R., Jr., Balick, B., et al. 2012, AJ, 144, 58

Kimeswenger, S., Kerber, F., & Weinberger, R. 1998, MNRAS, 296, 614

Koesterke, L., & Werner, K. 1998, ApJl, 500, L55

Kreysing, H. C., Diesch, C., Zweigle, J., et al. 1992, A&, 264, 623

Kuntz, K. D., & Snowden, S. L. 2008, A&A, 478, 575

Kwok, S., Purton, C. R., & Fitzgerald, P. M. 1978, ApJl, 219, L125

Landi, E., Young, P. R., Dere, K. P., Del Zanna, G., & Mason, H. E. 2013, ApJ, 763, 86

Lawlor, T. M., & MacDonald, J. 2006, MNRAS, 371, 263

Leone, F., Corradi, R. L. M., Martínez González, M. J., Asensio Ramos, A., & Manso Sainz, R. 2014, A&A, 563, A43

Leuenhagen, U., Koesterke, L., & Hamann, W.-R. 1993, Acta Astron., 43, 329

Lou, Y.-Q., & Zhai, X. 2010, MNRAS, 408, 436

Lupu, R. E., France, K., & McCandliss, S. R. 2006, ApJ, 644, 981

Maness, H., & Vrtilek, S. D. 2003, PASP, 115, 1002

Marston, A. P., Yocum, D. R., García-Segura, G., & Chu, Y.-H. 1994, ApJs, 95, 151

Marston, A. P. 1995, AJ, 109, 1839

Marston, A. P., Welzmiller, J., Bransford, M. A., Black, J. H., & Bergman, P. 1999, ApJ, 518, 769

Mauron, N., Huggins, P. J., & Cheung, C.-L. 2013, A&A, 551, A110

Meaburn, J., & Lopez, J. A. 1996, ApJl, 472, L45

Meaburn, J., & Redman, M. P. 2003, Revista Mexicana de Astronomia y Astrofisica Conference Series, 15, 1

Meaburn, J., Lopez, J. A., Bryce, M., & Redman, M. P. 1998, A&A, 334, 670

Meaburn, J., Boumis, P., López, J. A., et al. 2005, MNRAS, 360, 963

Mellema, G. 1995, MNRAS, 277, 173

Mellema, G., & Frank, A. 1995, MNRAS, 273, 401

Meynet, G., & Maeder, A. 2003, A&A, 404, 975

Miller Bertolami, M. M., & Althaus, L. G. 2007, MNRAS, 380, 763

Miller Bertolami, M. M., & Althaus, L. G. 2006, A&A, 454, 845

Miller Bertolami, M. M., Althaus, L. G., Serenelli, A. M., & Panei, J. A. 2006, A&A, 449, 313

Mohamed, S., Mackey, J., & Langer, N. 2012, A&A, 541, A1

Montez, R., Jr., & Kastner, J. H. 2013, ApJ, 766, 26

Moore, B. D., Walter, D. K., Hester, J. J., et al. 2002, AJ, 124, 3313

Moore, B. D., Hester, J. J., & Scowen, P. A. 2000, AJ, 119, 2991

Moos, H. W., Cash, W. C., Cowie, L. L., et al. 2000, ApJl, 538, L1

Nazé, Y. 2009, A&A, 506, 1055

Nugis, T., & Lamers, H. J. G. L. M. 2000, A&A, 360, 227

Palen, S., Balick, B., Hajian, A. R., et al. 2002, AJ, 123, 2666

Parker, Q. A., Phillipps, S., Pierce, M. J., et al. 2005, MNRAS, 362, 689

Pathak, A., Pradhan, A. C., Sujatha, N. V., & Murthy, J. 2011, MNRAS, 412, 1105

Patriarchi, P., & Perinotto, M. 1991, A&AS, 91, 325

Pauldrach, A. W. A., Vanbeveren, D., & Hoffmann, T. L. 2012, A&A, 538, A75

Pauldrach, A. W. A., Hoffmann, T. L., & Lennon, M. 2001, A&A, 375, 161

Pauldrach, A. W. A., Kudritzki, R. P., Puls, J., Butler, K., & Hunsinger, J. 1994, A&A, 283, 525

Pauldrach, A., Puls, J., Kudritzki, R. P., Mendez, R. H., & Heap, S. R. 1988, A&A, 207, 123

Pauldrach, A. 1987, A&A, 183, 295

Pauldrach, A., Puls, J., & Kudritzki, R. P. 1986, A&A, 164, 86

Pereyra, M., Richer, M. G., & López, J. A. 2013, ApJ, 771, 114

Perinotto, M., Kifonidis, K., Schönberner, D., & Marten, H. 1998, A&A, 332, 1044

Perinotto, M., Schönberner, D., Steffen, M., & Calonaci, C. 2004, A&A, 414, 993

Pittard, J. M. 2007, Diffuse Matter from Star Forming Regions to Active Galaxies, 245

Pittard, J. M., Dyson, J. E., & Hartquist, T. W. 2001, A&A, 367, 1000

Phillips, J. P., & Ramos-Larios, G. 2007, AJ, 133, 347

Pols, O. R., Tout, C. A., Eggleton, P. P., & Han, Z. 1995, MNRAS, 274, 964

Pottasch, S. R. 1984, Astrophysics and Space Science Library, Vol. 107, Planetary Nebulae - A study of late stages of stellar evolution

Press, W. H., Teukolsky, S. A., Vetterling, W. T., & Flannery, B. P. 1992, Cambridge: University Press, 1992, 2nd ed.

Raga, A. C., Mellema, G., Arthur, S. J., et al. 1999, RevMexAA, 35, 123

Raga, A. C., Cantó, J., & Rodríguez, L. F. 2012, RevMexAA, 48, 199

Reimers, D. 1975, Problems in stellar atmospheres and envelopes., 229

Rogers, H., & Pittard, J. M. 2013, MNRAS, 431, 1337

Ruiz, N., Chu, Y.-H., Gruendl, R. A., et al. 2013, ApJ, 767, 35

Ruiz, N., Guerrero, M. A., Chu, Y.-H., & Gruendl, R. A. 2011, AJ, 142, 91

Sabin, L., Zhang, Q., Zijlstra, A. A., et al. 2014, MNRAS, 438, 1794

Sahnow, D. J., Moos, H. W., Ake, T. B., et al. 2000, ApJl, 538, L7

Sarazin, C. L. 1988, X-ray emission from clusters of galaxies, Cambridge Astrophysics Series, Cambridge: Cambridge University Press, 1988

Savage, B. D., & Sembach, K. R. 1991, ApJ, 379, 245

Schönberner, D. 1983, ApJ, 272, 708

Schönberner, D., Jacob, R., Steffen, M., et al. 2005, A&A, 431, 963

Schönberner, D., Jacob, R., & Steffen, M. 2005, A&A, 441, 573

Sharpless, S. 1959, ApJs, 4, 257

Skinner, S., Nagase, F., Ozawa, H., & Itoh, M. 1996, Bulletin of the American Astronomical Society, 28, 1375

Skinner, S. L., Zhekov, S. A., Güdel, M., & Schmutz, W. 2002, ApJ, 579, 764

Skinner, S. L., Zhekov, S. A., Güdel, M., Schmutz, W., & Sokal, K. R. 2010, AJ, 139, 825

Skinner, S. L., Zhekov, S. A., Güdel, M., Schmutz, W., & Sokal, K. R. 2012, AJ, 143, 116

Smith, R. K., &Hughes, J. P. 2010, ApJ, 718, 583

Snowden, S.L., Egger, R., Freyberg, M.J., McCammon, D., Plucinsky, P.P., Sanders, W.T., Schmitt, J.H.M.M., Trümper, J., & Voges, W. 1997, ApJ 485, 125

Snowden, S.L., Collier, M.R., & Kuntz, K.D. 2004, ApJ, 610, 1182

Snowden, S. L., Mushotzky, R. F., Kuntz, K. D., & Davis, D. S. 2008, A&A, 478, 615

Snowden, S. L., & Kuntz, K. D. 2011, Bulletin of the American Astronomical Society, 43, #344.17

Soker, N. 1994, AJ, 107, 276

Spitzer, L. 1962, Physics of Fully Ionized Gases, New York: Interscience (2nd edition), 1962

Steffen, W., & López, J. A. 2004, ApJ, 612, 319

Steffen, M., Schönberner, D., & Warmuth, A. 2008, A&A, 489, 173

Steffen, M., Sandin, C., Jacob, R., & Schönberner, D. 2012, IAU Symposium, 283, 215

Stock, D. J., & Barlow, M. J. 2010, MNRAS, 409, 1429

Stute, M., & Sahai, R. 2006, ApJ, 651, 882

Tarafdar, S. P., & Apparao, K. M. V. 1988, ApJ, 327, 342

Toalá, J. A., & Arthur, S. J. 2011, ApJ, 737, 100

Toalá, J. A., & Arthur, S. J. 2014, accepted to MNRAS

Toalá, J. A., Guerrero, M. A., Chu, Y.-H., et al. 2012, ApJ, 755, 77

Townsley, L. K., Feigelson, E. D., Montmerle, T., Broos, P. S., Chu, Y.-H., & Garmire, G. P. 2003, ApJ, 593, 874

van der Hucht, K. A., Cassinelli, J. P., & Williams, P. M. 1986, A&A, 168, 111

van der Hucht, K. A. 2001, New A Rev., 45, 135

van der Hucht, K. A., Hidayat, B., Admiranto, A. G., Supelli, K. R., & Doom, C. 1988, A&A, 199, 217

van der Hucht, K. A., Cassinelli, J. P., & Williams, P. M. 1986, A&A, 168, 111

van Hoof, P. A. M., van de Steene, G. C., Barlow, M. J., et al. 2010, A&A, 518, L137

van Leer, B. 1982, Numerical Methods in Fluid Dynamics, 170, 507

van Marle, A. J., & Keppens, R. 2012, A&A, 547, A3

Vassiliadis, E., & Wood, P. R. 1993, ApJ, 413, 641

Vassiliadis, E., & Wood, P. R. 1994, ApJSS, 92, 125

Villaver, E., García-Segura, G., & Manchado, A. 2002a, ApJ, 571, 880

Villaver, E., Manchado, A., & García-Segura, G. 2002b, ApJ, 581, 1204

Villaver, E., Manchado, A., & García-Segura, G. 2012, ApJ, 748, 94

Vishniac, E. T. 1983, ApJ, 274, 152

Vishniac, E. T., & Ryu, D. 1989, ApJ, 337, 917

Weaver, R., McCray, R., Castor, J., Shapiro, P., & Moore, R. 1977, ApJ, 218, 377

Welsh, B.Y., & Lallement, R. 2008, A&A, 490, 707

Wendker, H. J., Smith, L. F., Israel, F. P., Habing, H. J., & Dickel, H. R. 1975, A&A, 42, 173

Werner, K., & Koesterke, L. 1992, The Atmospheres of Early-Type Stars, 401, 288

Werner, K., Rauch, T., & Kruk, J. W. 2005, A&A, 433, 641

Williams, R. J. R. 1999, MNRAS, 310, 789

Wrigge, M. 1999, A&A, 343, 599

Wrigge, M., Wendker, H. J., & Wisotzki, L. 1994, A&A, 286, 219

Wrigge, M., Chu, Y.-H., Magnier, E. A., & Kamata, Y. 1998, IAU Colloq. 166: The Local Bubble and Beyond, 506, 425

Wrigge, M., & Wendker, H. J. 2002, A&A, 391, 287

Wrigge, M., Chu, Y.-H., Magnier, E. A., & Wendker, H. J. 2005, ApJ, 633, 248

Young, Y.-N., Tufo, H., Dubey, A., & Rosner, R. 2001, Journal of Fluid Mechanics, 447, 377

Yu, Y. S., Nordon, R., Kastner, J. H., et al. 2009, ApJ, 690, 440

Zhekov, S. A. 2014, arXiv:1406.2463

Zhekov, S. A., & Myasnikov, A. V. 1998, New A., 3, 57

Zhekov, S. A., & Myasnikov, A. V. 2000, ApJL, 543, L53

Zhekov, S. A., & Park, S. 2011, ApJ, 728, 135

Zhekov, S. A., & Perinotto, M. 1996, A&A, 309, 648

Zhekov, S. A., & Perinotto, M. 1998, A&A, 334, 239

Zsargó, J., Hillier, D. J., Bouret, J.-C., et al. 2008, ApJl, 685, L149